Western Graduate&PostdoctoralStudies

Western University
Scholarship@Western

Electronic Thesis and Dissertation Repository

January 2019

# Properties of Si quantum dots

Carolyn C. F Cadogan
*The University of Western Ontario*

Supervisor
Simpson, Peter J.
*The University of Western Ontario*

Joint Supervisor
Goncharova, Lyudmila V.
*The University of Western Ontario*

Graduate Program in Physics

A thesis submitted in partial fulfillment of the requirements for the degree in Doctor of Philosophy

© Carolyn C. F Cadogan 2018

Follow this and additional works at: https://ir.lib.uwo.ca/etd

Part of the Condensed Matter Physics Commons

## Recommended Citation

Cadogan, Carolyn C. F, "Properties of Si quantum dots" (2018). *Electronic Thesis and Dissertation Repository*. 5920.
https://ir.lib.uwo.ca/etd/5920

This Dissertation/Thesis is brought to you for free and open access by Scholarship@Western. It has been accepted for inclusion in Electronic Thesis and Dissertation Repository by an authorized administrator of Scholarship@Western. For more information, please contact tadam@uwo.ca, wlswadmin@uwo.ca.

# Abstract

Silicon (Si) is a material extensively used in the manufacturing of electronic and photovoltaic devices. However, the poor light emission of the material limits its use in optical and optoelectronic devices. In comparison to bulk Si, silicon quantum dots (Si-QDs) have been shown to display improved luminescence. However, there is still a need to increase the light emission of Si-QDs for this material to be commercially viable. Therefore, the aim of this thesis is to improve the light emission of Si-QDs and to understand the mechanism behind it.

In several different but interconnected parts of this thesis, the optical properties of Si-QDs embedded in $Si_3N_4$ and the role of crystallinity on the optical properties and formation of Si-QDs in $Al_2O_3$ were investigated. This work examined the role of (1) annealing temperature and the composition of the nitride film, (2) Al doping of the host $Si_3N_4$ film, (3) doping Si-QDs and (4) Al and P passivation of Si-QDs on the PL intensity of Si-QDs embedded in $Si_3N_4$. We have found that using an annealing temperature greater than 600°C significantly decreases the PL intensity for Si-rich silicon nitride samples due to the loss of hydrogen and nitrogen from the film. Al doping of the host $Si_3N_4$ film was found to increase the PL intensity when an Al dose equal to or greater than $5\times10^{14}$ ions/cm$^2$ followed by annealing at 600°C was used. This increase in PL intensity was attributed to the formation of Si-Al and to a lesser extent N-Al bonds. The doping of Si-QDs was determined not to be influential when Al was incorporated into the Si-QDs/$Si_3N_4$ system. On the other hand, the passivation of Si-QDs by Al and P was found to increase the PL intensity of the system significantly.

For $Al_2O_3$ samples, we found that the growth of Si-QDs was strongly dependent on the crystallinity of the $Al_2O_3$ film. From XANES measurements, it was found that Si-QDs formed more readily in a disordered and crystalline matrix. In addition, the luminescence of Si-QDs was not observed due to the presence of oxygen vacancies and impurities dominating the luminescence.

**Keywords:** Silicon, quantum dots, silicon nitride, X-ray absorption spectroscopy, positron annihilation spectroscopy, aluminium oxide, aluminium, phosphorus, ion implantation

# Co-authorship Statement

The following thesis contents work which has been previously published in a peer-review journal. Chapter 3 of the thesis was previously published and co-authored by Dr. Lyudmila Goncharova, Dr. Peter Simpson, Dr. Tsun-Kong Sham, Dr. Zhiqiang Wang and Peter Nguyen. For this publication, Carolyn Cadogan was the primary author responsible for the majority of experimental work and writing the final manuscript. Dr. Tsun-Kong Sham and Dr. Zhiqiang Wang collected and analysed the X-ray absorption near edge spectroscopy measurements presented in this work. Peter Nguyen, of University of Alberta, assisted with film characterization and in the drafting of the manuscript.

The work presented in all chapters were primarily analysed by Carolyn Cadogan with assistance from Dr. Lyudmila Goncharova and Dr. Peter Simpson. The majority of sample preparation and measurements presented in this thesis were conducted by Carolyn Cadogan. Some positron results presented in chapter 4 were collected by Joshua Rideout, who was also responsible for helping update the positron annihilation system used in this thesis. Some films used in this study were made by summer students Victoria Karner and Alexander Tavares. Particle-induced X-ray emission (PIXE) and X-ray diffraction (XRD) data presented in Appendix A4 were collected by Victoria Karner who is currently associated with the chemistry department at the University of British Colombia. Some X-ray excited optical luminescence measurements presented in Appendix A4 were collected by Dr. Zhiqiang Wang. Scanning electron microscope images presented in Appendix B2 were collected by Dr. Todd Simpson of the Western Nanofabrication Facility. The assistance of all who are mentioned above was greatly appreciated.

# Acknowledgements

I would like to thank my supervisors Dr. Lyudmila Goncharova and Dr. Peter Simpson for their continued help throughout my Ph.D. I am very thankful for their assistance with writing of this thesis and the many corrections they provided to help me improve the quality of my writing. I am very grateful for all the support they have given me throughout this journey. I would also like to thank Dr. Giovanni Fanchini for his assistance with some experiments conducted in his lab and for helping me to realize the type of dedication needed to be a true academic.

During my degree, I have had the pleasure of working in the Tandetron Facility with Jack Hendrix without whom running my RBS and ERD measurements would not have been possible. I really appreciated the wealth of advice he provided during experiments and the many conversations we have had. I have also had the pleasure of working in the Western Nanofabrication Facility and would like to thank Dr. Todd Simpson and Tim Goldhawk for all their help. I would also like to thank Liz Chapman, at the CLS residence, who always went above and beyond to make me feel at home while I was in Saskatoon.

I have also had the pleasure of interacting with Phin Perquin at the Physics Stores during my many visits to order equipment and supplies. He always made sure that orders were placed in a timely fashion and with whom I would have great conversations with while I waited around to place my orders. I would like to especially thank Jodi Guthrie and Clara Buma for their encouragement throughout my degree and their support of my accomplishments which I truly appreciated. I would also like to thank Shaliesh Nene for being a great mentor during my time in the first-year physics labs.

I would also like to thank my friends and family for all their support. I would like to dedicate my Ph.D. thesis to my wonderful parents, Carson and Coralene Cadogan, who have been with me through it all. Through the good times and through the hard times with their many words of encouragement. No matter what happened and will happen I always know they have my back and I will never forget this.

# Table of Contents

Abstract....ii

Co-Authorship Statement....iv

Acknowledgements....v

Table of Contents....vi

List of Tables....xi

List of Figures....xii

List of Abbreviations....xxiii

Chapter 1. Introduction....1

1.1 Motivation....1

1.2 Silicon Quantum Dots....5

1.2.1 Luminescence of Silicon Quantum Dots....5

1.2.2 Overview of Fabrication Techniques for Silicon Quantum Dots....11

1.2.2a Silicon Quantum Dot Growth....11

1.2.2b Synthesis using Plasma Enhanced Chemical Vapour Deposition....13

1.2.2c Synthesis using Ion Implantation....14

1.3 Fundamentals of Materials Examined....16

1.3.1 PECVD Silicon Nitride……………..……………………….....................16

1.3.1a Impurity Doping…………………...................................................19

1.3.2 Aluminum Oxide…….………………..……………………….....................20

1.4 Thesis Outline……………………….........................................................................24

1.5 References....……………………….......................................................................26

Chapter 2. Experimental Techniques.......................................................................33

2.1 Photoluminescence (PL) Spectroscopy ……………………………..……...................33

2.2 Time-Resolved Photoluminescence (TR-PL) .........................................................34

2.3 Fourier Transform Infrared Spectroscopy (FT-IR) ………..……………………............35

2.4 X-ray Absorption Spectroscopy.........................................................................37

2.4.1 X-ray Absorption Near-Edge Structure (XANES)…………………………......39

2.4.2 X-ray Excited Optical Luminescence (XEOL)...............................................42

2.4.3 XAS Beamlines at the Canadian Light Source Synchrotron Facility………...43

2.5 Rutherford Backscattering Spectroscopy (RBS).......................................................44

2.6 Elastic Recoil Detection (ERD)…..………………………………………….............46

2.7 Particle Induced X-ray Emission (PIXE)…………………….……….....................48

2.8 Ion Implantation……………………………………………………………...............49

2.8.1 Stopping Power………........................................................................50

2.8.2 Ion Range and Straggle……………………………………………………51

2.8.3 Displacements and Radiation Damage.....………………..……...................52

2.8.4 Defects due to Ion implantation………………………………………………53

2.8.5 Diffusion of Implanted Ions…………………………………………………..55

2.8.6 Irradiation-Enhanced Diffusion………………………………………………56

2.9 Positron Annihilation Spectroscopy (PAS) …………………………………………..56

2.9.1 Positron Source……………………………………………………………57

2.9.2 Interaction of Positrons with Matter……………………………………….58

2.9.3 Positronium Formation……………………………………………………59

2.9.4 Doppler Broadening Method………………………………………………60

2.10 References………………………………………………………………………..63

Chapter 3. The influence of hydrogen passivation on the luminescence of Si quantum dots embedded in $Si_3N_x$……………………………………………………………………………………66

3.1 Introduction……………………………………………………………………......66

3.2 Experimental………………………………………………………………………67

3.2.1 Sample Preparation …………………………………………………...67

3.2.2 Sample Characterization…………………………………………………68

3.3 Results and Discussion ……………………………………………………………70

3.3.1 Results ……………………………………………………………………70

3.3.2 Discussion ……………………………………………………………...78

3.4 Summary and Conclusions…………………………………………………………81

3.5 References…………………………………………………………………………82

Chapter 4 Optical Properties and Defect Concentration of Al Implanted Stoichiometric Silicon Nitride…………………………………………………………………………………88

4.1 Introduction………………………………………………………………………..88

4.2 Experimental Details………………………………………………………………90

4.2.1 Samples preparation………………………………………………………90

4.2.2 Sample Characterization…………………………………………………..91

4.3 Results…………………………………………………………………………..93

4.4 Discussion………………………………………………..…………………103

4.5 Conclusion……………………………………………………………………..106

4.6 References……………………………………………………………….......107

Chapter 5 Optical Properties of Al- and P- Implanted Silicon-Rich Silicon Nitride..........110

5.1 Introduction……………………………………………………………………110

5.2 Experimental…………………………………………………………………...112

5.3 Results…………………………………………………………………………114

5.4 Discussion……………………………………………………………...…124

5.5 Conclusion……………………………………………………………………..129

5.6 References……………………………………………………………………..130

Chapter 6 The Influence of Matrix Crystallinity on the Optical Properties of Si Implanted Aluminium Oxide.......................................................................................................135

6.1 Introduction……………………………………………………………………135

6.2 Experimental Details…………………………………………………………..139

6.3 Results…………………………………………………………………………142

6.4 Discussion……………………………………………………………………...151

6.5 Conclusion……………………………………………………………………..153

6.6 References……………………………………………………………………..155

Chapter 7 Conclusion and Future Work ………...........................................................162

7.1 Conclusion……………………………………………………………………..162

7.2 Future Work……………………………………………………………………165

7.3 References……………………………………………………………………..168

Appendices

Appendix A1……………………………………………………………………169

Appendix A2……………………………………………………………………170

Appendix A3……………………………………………………………………172

Appendix A4…..........................................................................................................178

Appendix B1…………………………………………………………………….191

Appendix B2…………………………………………………………………….193

# List of Tables

5.1 Hydrogen content (in at.%) based on elastic recoil detection measurements for SRSN_asis and SRSN_annealed in comparison to SRSN samples implanted with Al and P. SRSN_annealed, SRSN_Al_5e15 and SRSN_P_5e15 were all annealed in forming gas at 600°C for 30mins. ….. 123

6.1 Table of defect centres found in $Al_2O_3$ ….. 138

# List of Figures

1.1 The calculated energy band structure of bulk Si with energy, E(eV), vs wavevector (k). ….. 6

1.2 Diagram illustrating a quasi-direct band gap, where the increase in momentum uncertainty is shown as red dashed circles for the charge carriers in the valence (VB) and conduction (CB) band. ….. 8

1.3 Band gap alignment of crystalline Si (c-Si) with SiC, $Si_3N_4$ and $SiO_2$. The band gap energy of c-Si is shown using red dashed lines. ….. 13

1.4 Illustration of cluster growth after ion implantation as a function of annealing time. After ion implantation the matrix is in a supersaturated state followed by nucleation as time of annealing increases. As the time of annealing increases clusters grow larger and larger as according to the Ostwald ripening process. ….. 15

1.5 Illustration of the crystal structure of (a) α-$Si_3N_4$ and (b) β-$Si_3N_4$ consisting of layer sequence ABCDAB… and ABAB… respectively. Si atoms are in dark blue and N atoms are in light blue. The structure of AB and CD layers are shown in (c) and (d). Crystal structures were made using Crystal Maker software. ….. 17

1.6 Illustration of the possible defects present in $Si_3N_4$ based on results by Mo et al. ….. 19

1.7 Crystal structure of α-$Al_2O_3$, γ- $Al_2O_3$ and θ-$Al_2O_3$ with Al atoms in green and O atoms depicted in red. ….. 21

1.8 Illustration of (a) barrier-type $Al_2O_3$ and (b) porous $Al_2O_3$. ….. 23

1.9 Schematic of the formation of porous $Al_2O_3$. (a) Starting with the formation of barrier-type $Al_2O_3$, followed by (b) surface fluctuations causing electric field distribution with electric field shown as red arrows and (c) the field-enhanced dissolution and stable growth of pores. ….. 23

2.1 Schematic of synchrotron facility (modified image from CLS website see ref. 7). ….. 39

2.2 Illustration of normalized X-ray absorption spectrum showing the pre-edge, rising edge, XANES region and EXAFS region. ….. 40

2.3 Schematic of different XAS detection modes (a) transmission, (b) fluorescence and (c) electron yield mode. ….. 42

2.4 Layout of (a) SGM beamline, (b) VLS-PGM and (c) SXRMB beamline at the CLS. ….. 43

2.5 Schematic of RBS and example of RBS spectrum for a sample with two elements A and B. The RBS system consists of an incident ion of mass $M_1$ while $K_B$ and $K_A$ are the kinematic factors of the elements A and B, respectively. The mass of A is greater than B hence the energy of the backscattered ion from A is higher than B. From ref. 14. ….. 45

2.6 Schematic of ERD setup with incident He ions in red and detected H ions in blue. ….. 47

2.7 Schematic of the ion implantation system ….. 49

2.8 Decay scheme of $^{22}Na$ to $^{22}Ne$. ….. 58

2.9 The penetration depth profile $P(z,E)$ for positrons with four different energies in Si. Dotted lines show the mean penetration depth ($\bar{z}$) with the associated energy written next to it. ….. 59

2.10 Schematic of a typical Doppler broadening setup using the coincidence technique. Emitted gamma rays are collected using liquid nitrogen cooled Ge detectors. Based on ref.29. ….. 61

2.11 Illustration of Doppler broadening peak highlighting the regions of the spectrum used for determining the S and W parameters. The total number of counts ($N_p$) is shown in red and is used for calculating the S parameter while the number of counts in the wing regions ($N_{w1}$ and $N_{w2}$) shown in blue are used for calculating the W-parameter. ….. 62

3.1 XPS Si 2p spectra from an $Si_3N_{3.00}$ sample annealed at 500°C. ….. 71

3.2 (a) Normalized PL spectra for samples annealed at 500°C, (b) change in Si-QD size with annealing temperature and (c) the variation in PL intensity with annealing temperature. Samples not post-annealed are indicated by 300°C (growth temperature). ….. 73

3.3 Percentage of hydrogen remaining after annealing (blue), and PL intensity (red) vs annealing temperature for composition $Si_3N_{3.00}$. Samples not post-annealed are indicated by 300°C (growth temperature). ….. 74

3.4 (a) FT-IR spectra and (b) extracted parameters for $Si_3N_{3.00}$ films before and after annealing. ….. 75

3.5 (a) X-ray absorption near edge spectroscopy (XANES) for the Si-K edge, for $Si_3N_{3.00}$, and the normalized intensity of the (b) ….. 77

Si-O bond and (c) Si-Si bond, as a function of annealing temperature.

4.1 Normalized photoluminescence spectra of the samples examined including $Si_3N_4$ films before and after annealing labelled asis and annealed, respectively, implanted $Si_3N_4$ films labelled 5e13, 5e14 and 5e15 based on the Al implantation dose. Spectra are normalized to a common but arbitrary scale. ….. 94

4.2 (a) S parameter of PAS measurements (black squares) and integrated PL intensity (blue dots) as a function of annealing temperature for $Si_3N_4$ sample implanted with $5\times10^{15}$ Al atoms/cm$^2$. The S parameter value and integrated PL intensity for the asis sample are included as a reference. (b) S parameter for ex-situ samples (black square), which are those annealed in vacuum followed by PAS measurements, are compared with in-situ samples (red dots), which are those heated on the PAS stage during PAS measurements. The uncertainty is calculated based on the S parameter value ($S$) and the total number of counts ($N$) and given by $S(1-S)\sqrt{N}$. ….. 95

4.3 (a) Difference spectra for samples minus the PAS spectrum for a Si wafer. For the subtraction, all PAS spectra used had an equal number of total counts. (b) The integrated area under the middle peak of difference spectra shown in (a). In (b) the grey dashed line indicates the integrated area for the asis sample. The annealing temperature of 0°C is used to indicate an unannealed but implanted sample. ….. 97

4.4 Integrated absorbance (black dots) and wavenumber (blue squares) of the (a) Si-H and (b) N-H absorbance peak as a function implantation dose. Error bars for integrated absorbance ….. 99

is 9% based on the signal-to-noise ratio while the error bars for wavenumber are $\pm 0.5 cm^{-1}$.

4.5 (a) FLY XANES spectra at the Si $L_{2,3}$-edge from 99 to 106.5 eV for asis, annealed, and implanted (implanted with Al doses of $5\times10^{13}$, $5\times10^{14}$ and $5\times10^{15}$ atom/cm$^2$ ) silicon nitride samples. (b) 1st derivative of the normalized spectra that are shown in (a). ….. 100

4.6 TEY XANES spectra at the N K-edge for annealed $Si_3N_4$ and $Si_3N_4$ films implanted with Al doses of $5\times10^{13}$, $5\times10^{14}$ and $5\times10^{15}$ atom/cm$^2$. ….. 101

4.7 (a) Normalized XANES spectra of $Si_3N_4$ implanted with $5\times10^{15}$ ions/cm$^2$ of Al. (b) Raw XANES spectra at the Al K-edge for $Si_3N_4$ implanted with a dose of $5\times10^{11}$ and $5\times10^{13}$ ions/cm$^2$ of Al. ….. 102

5.1 Photoluminescence spectra of Si-rich silicon nitride (SRSN) and stoichiometric silicon nitride (SiN) samples. PL intensity has been normalised to a common but arbitrary scale. (a) Shows the PL spectra of SRSN before and after annealing at 600°C in forming gas in comparison to SRSN samples that have been implanted with different doses of Al ranging from $5\times10^{13}$ to $5\times10^{15}$ ions/cm$^2$ (labeled Al_5e13, Al_5e14 and Al_5e15, respectively) followed by annealing at 600°C in forming gas. (b) PL spectra of SiN samples after annealing at 600°C in forming gas compared to SiN samples that have been implanted using the same Al dose range as SRSN samples followed by annealing at 600°C in forming gas. ….. 115

5.2 Maximum PL intensity for SRSN samples implanted with Al (black squares) and P (red dots) followed by 600°C anneal in ….. 117

forming gas compared to SRSN that is unimplanted but annealed under the same conditions (0 atoms/cm$^2$).

5.3 Fluorescence yield (FLY) XANES at the Si $L_{2,3}$-edge for SiN and SRSN samples. The Si-N peak at the Si $L_{2,3}$ edge is highlighted using grey dashed line, and the dose range of implanted samples is $5\times10^{13}$ to $5\times10^{15}$ atoms/cm$^2$. (a) The FLY XANES spectra of Al implanted and annealed SiN samples are compared to the unimplanted and annealed SiN. The XANES of (b) Al implanted and (c) P implanted SRSN samples compared to unimplanted and annealed SRSN. ….. 119

5.4 (a) The TEY XANES of Al implanted SRSN samples and SiN implanted with Al dose of $5\times10^{15}$atoms/cm$^2$ at the Al K-edge with inset showing the peak at 1566eV. (b) The first derivative of XANES spectra shown in (a). ….. 121

5.5 Bond density of Si-H (squares) and N-H (dots) for implanted and unimplanted samples. FTIR spectra for unimplanted and unannealed sample SRSN_Asis. (insert) The first point on both curves is for SRSN_Asis which is an unannealed and unimplanted SRSN sample. All other points are for samples that have been annealed at 600°C in forming gas for 30mins. ….. 122

6.1 Structure of $\alpha$-$Al_2O_3$, projected on (2110) plane with oxygen monovacancies ($F^+$ and F centres) and the oxygen divacancies ($F_2$, $F_2^+$ and $F_2^{2+}$ centres). All Al (filled small circles) are in the plane of the paper, while the oxygen atoms are located above (thick open circles) or below (thin open large circles) this plane. Adapted from reference 11. ….. 137

6.2 Schematic of the (a) electropolishing, (b) anodization, and (c) Al etching processes used for growing the amorphous aluminium oxide film. ….. 139

6.3 Scanning electron microscopy (SEM) images of anodized nanoporous aluminium oxide films. (a) The cross-sectional view of the film. (b) The top view of the film with the outline of the pores in grey. ….. 140

6.4 Photoluminescence spectra of a-$Al_2O_3$ (solid black line), d-$Al_2O_3$ (solid blue line) and c-$Al_2O_3$ (solid red line) samples implanted with Si ions and annealed at 1000°C (with a vertical offset and magnified where indicated for clarity). The matrix before implantation and anneal are labelled blank. ….. 143

6.5 PL lifetime curve for samples *c*-$Al_2O_3$ fitted with a multi-exponential decay function. ….. 144

6.6 XEOL spectra at (a, b) 540eV and (c, d) 1566eV for samples a-$Al_2O_3$, d-$Al_2O_3$ and c-$Al_2O_3$. In (c) the XEOL spectra for a-$Al_2O_3$ and d-$Al_2O_3$ have been magnified by a factor 5 for the clarity. While at (e, f) 1841eV only the XEOL spectra for samples d-$Al_2O_3$ and c-$Al_2O_3$ are presented since a-$Al_2O_3$ had no XEOL emission at the Si K-edge. In (e), the XEOL spectra of d-$Al_2O_3$ is magnified by a factor of five for clarity.. ….. 145

6.7 XANES spectra at (a) O K-edge, (b) Al K-edge and (c) Si K-edge, for a-$Al_2O_3$, d-$Al_2O_3$ and c-$Al_2O_3$ implanted with Si and annealed at 1000ºC. ….. 149

A1.1 Partial fluorescence yield X-ray absorption near edge spectroscopy (PFY-XANES) for the Si-K edge for $Si_3N_{3.00}$ ….. 169

annealed from 400 to 1000°C. The XANES spectra for a Si wafer is included as a reference.

A2.1 FT-IR spectra for asis $Si_3N_4$ and $Si_3N_4$ implanted with $5\times10^{11}$ atoms/cm$^2$ (labelled 5e11). For clarity, a y-offset of 0.1 is applied to the spectra. ..... 170

A2.2 XANES spectra at the Si K-edge in TEY mode for implanted and unimplanted samples annealed at the same temperature. ..... 171

A3.1 Normalized PL spectra for annealed SRSN and P doped SRSN samples. ..... 172

A3.2 TEY XANES at the Si K-edge for SRSN_Annealaed, SRSN_5e13, SRSN_5e14 and SRSN_5e15 samples. For clarity the spectra for SRSN_5e11 and SRSN_5e12 are omitted from this plot. ..... 174

A3.3 TEY XANES at the Si K-edge of (a) SiN_Annealed and SRSN_Annealed are compared to (b) SiN_5e15 and SRSN_5e15. The spectra of SRSN samples are plotted using solid lines and SiN samples are plotted using dash lines. ..... 175

A3.4 The XANES spectra at the N K-edge in (a) TEY mode and (b) FLY mode for Al and P imlplanted SRSN samples. The spectra for Al implanted samples are plotted using solid lines while for P implanted samples the spectra are plotted using dashed line. The XANES spectra of our unimplanted and annealed sample is plotted for comparison. The spectra for samples 5e11 and 5e12 are not plotted for clarity as the N K-edge spectra for all implanted samples the same. ..... 176

A3.5 Elastic recoil detection spectra for SRSN samples ..... 177

A4.1 PIXE spectra for (a) $Al_2O_3$ film after removal from the Al film, (b) Al film, and (c) $Al_2O_3$ film on Al. ….. 178

A4.2 PIXE Spectra for (a) 5×5 mm sapphire (polished side), and (b) 5×5 mm sapphire (unpolished side). ….. 179

A4.3 XEOL spectra of *c*-$Al_2O_3$ before Si implantation from 200 to 650nm along the (a) O K-edge and from 200 to 500nm along (b) Al K-edge. ….. 180

A4.4 XEOL spectra of *c*-$Al_2O_3$ prior to Si implantation from 600 to 1000nm along the (a) O K-edge and (b) Al K-edge. ….. 181

A4.5 XEOL spectra of *d*-$Al_2O_3$ prior to Si implantation from 200 to 650nm along (a) O K-edge and (b) Al K-edge. ….. 182

A4.6 XEOL spectra of *d*-$Al_2O_3$ before Si implantation from 600 to 1000nm along the (a) O K-edge and (b) Al K-edge. ….. 183

A4.7 XEOL spectra of Si-implanted (a) *a*-$Al_2O_3$. (b) *d*-$Al_2O_3$ and (c) *c*-$Al_2O_3$ along the O K-edge. ….. 184

A4.8 XEOL spectra of Si-implanted (a) *a*-$Al_2O_3$. (b) *d*-$Al_2O_3$ and (c) *c*-$Al_2O_3$ along the Al K-edge. ….. 185

A4.9 XEOL spectra of Si-implanted (a) *a*-$Al_2O_3$ (b) *d*-$Al_2O_3$ and (c) *c*-$Al_2O_3$ along the Si K-edge. ….. 186

A4.10 XEOL spectra of Si-implanted *d*-$Al_2O_3$ along the O K-edge. This spectrum is fitted using two gaussian peaks centred at 694nm and 740nm. The cumulative fit of these two peaks is shown with an orange dashed line ….. 187

A4.11 X-ray diffraction spectra for unimplanted (black) and unimplanted (red) amorphous $Al_2O_3$ films. Sapphire reference points are included to compare the amorphous $Al_2O_3$ sample with crystalline $Al_2O_3$. ….. 188

A4.12 Images of amorphous$Al_2O_3$ samples (a) before and (b) after annealing. Samples were supported on a Si wafer to reduce material fractures caused by annealing. ….. 189

A4.13 PL Lifetime curve for samples *a*-Al2O3 (black), *d*-Al2O3 (blue) *c*-al2O3 (red). ….. 190

B1.1 Schematic of (a) Al deposition mask used for depositing Al front contacts and (b) silicon nitride films with front Al contacts and Ag back contact. ….. 192

B1.2 Current-voltage curves for Si-rich silicon nitride (SRSN) samples asis (black dash) and implanted samples with Al doses of $5\times10^{14}$atoms/cm$^2$ (red dash) and $5\times10^{15}$atoms/cm$^2$. ….. 192

B2.1 Diagram illustrating the fabrication of Al nanostructures. (1) Polystyrene microspheres are dispersed on the water surface, (2) microspheres are deposited on to the sample surface, (3) microsphere mask is allowed to dry and (4) Al film is deposited through the microsphere mask. ….. 194

B2.2 Photoluminescence intensity of Si-rich silicon nitride sample with Al nanostructure deposited on the surface. Al nanostructures were produced using different Al film thicknesses. ….. 195

B2.3 SEM images of Si-rich silicon nitride films with Al nanostructures where (a) shows the region that clearly shows the ….. 196

type of Al nanostructures formed. In (a) we observe that there are regions where the microsphere film had gaps as we can observe elevated regions of Al. A region where microspheres were not completely removed is shown in (b).

# List of Abbreviations

| | |
|---|---|
| ***a*-$Al_2O_3$** | Amorphous $Al_2O_3$ |
| ***c*-$Al_2O_3$** | Crystalline $Al_2O_3$ |
| **CB** | Conduction band |
| **CLS** | Canadian Light Source |
| ***d*- $Al_2O_3$** | Disordered $Al_2O_3$ |
| **DOS** | Density of states |
| **EL** | Electroluminescence |
| **ERD** | Elastic Recoil Detection |
| **EXAFS** | Extended X-ray absorption fine structure |
| **FLY** | Fluorescence yield |
| **FT-IR** | Fourier transform infrared |
| **$I_0$** | Incident beam |
| **NEXAFS** | Near edge X-ray absorption fine structure |
| **o-Ps** | Ortho-positronium |
| **PAS** | Positron Annihilation Spectroscopy |
| **PDOS** | Partial DOS |
| **PECVD** | Plasma enhanced chemical vapour deposition |
| **PFY** | Partial fluorescence yield |
| **PL** | Photoluminescence |
| **p-Ps** | Positronium |
| **Ps** | Positronium |

| | |
|---|---|
| **RBS** | Rutherford Backscattering Spectroscopy |
| **SEM** | Scanning electron microscope |
| **$Si_3N_4$** | Silicon nitride |
| **$Si_3N_x$** | Non-stoichiometric silicon nitride |
| **SiN** | Stoichiometric silicon nitride |
| **Si-QDs** | Silicon quantum dots |
| **SRSN** | Silicon-rich silicon nitride |
| **STEM** | Scanning transmission electron microscopy |
| **STEM EELS** | STEM electron energy loss spectrum |
| **SXRMB** | Soft X-ray Microcharacterization Beamline |
| **TEM** | Transmission electron microscope |
| **TEY** | Total electron yield |
| **VLS-PGM** | Variable line spacing plane grating monochromator |
| **XANES** | X-ray absorption near edge structure |
| **XAS** | X-ray absorption spectroscopy |
| **XEOL** | X-ray excited optical luminescence |
| **XPS** | X-ray photoelectron spectroscopy |

# Chapter 1

# Introduction

## 1.1 Motivation

Silicon (Si) is a material used extensively in modern electronic and photovoltaic devices. However, its use in photonic and optoelectronic devices has been limited by the material's poor light emitting properties. This limitation of Si is because of the material's indirect band gap structure which causes the material to have a long radiative lifetime. In general, the relaxation pathway of an excited carrier can either be non-radiative (no light is produced) or radiative (light is produced). As these two pathways are competing, the long radiative lifetime of Si decreases the probability of radiative recombination, which in turn causes the material to be a poor light emitter.

In 1956, porous Si (por-Si) was discovered by Uhlir while he was electropolishing a Si wafer using a HF-based electrolyte.[1] Uhlir discovered that the partial electrochemical dissolution of the Si wafer produced an array of narrow pores in the Si wafer. These pores had diameters that ranged from a few nanometers up to several micrometers and were micrometers deep. The pore arrangement could be either disordered or ordered depending on etching conditions. It was not until 1990 that Leigh Canham and his group at the Royal Signals and Radar Establishment in England demonstrated that visible light could be emitted from por-Si. This lead to intense research into the various properties of this material. The luminescence of por-Si was found to vary with porosity which was attributed to 2-D quantum confinement of the charge carriers in the por-Si.[2, 3] Details on the quantum confinement effect can be found in section 1.2.1. But in brief it is the restriction of the

motion of charge carriers within the material by the placing “walls”, known as potential barriers, to prevent free movement in that given direction. The highly reactive surface of por-Si was found to be a major disadvantage as it would cause rapid aging of por-Si LEDs. To combat this, researchers passivated the por-Si surface which came at a tremendous loss of LED efficiency.[4, 5]

As a result, researchers have explored the use of other nanoscale Si materials that would display the variable luminescence which was achieved with por-Si without the drawbacks that were associated with this material. Researchers have explored numerous methods to produce nanoscale Si particles. One popular method has been the production of Si quantum dots (Si-QDs) embedded in a silica ($SiO_2$) matrix. The name quantum dot comes from the fact these nanoscale Si particles are three-dimensional quantum confinement structures. Further details on these structures can be found in section 1.2.1.

These Si-QDs exploit the stability provided by the Si-QD/$SiO_2$ interface, which was a major issue for por-Si, while also exploiting the improved size-dependent tunable emission of the quantum confined Si. Though there has been intense research into the properties of Si-QDs embedded in $SiO_2$ there is great concern with regard to the limited emission energy range as well as the difficulty for charge carriers to traverse the potential barrier of $SiO_2$. This is because, even though a wide band gap material like $SiO_2$ is needed for strong confinement of the charge carriers, for optoelectronic applications there is still a need for the potential barrier to allow for efficient charge transport without the need for an excessively high device bias.

The wide band gap of $SiO_2$ makes it difficult for carrier transport, leading to a need to replace it with other matrix materials. One of the reasons for exploring materials such as silicon nitride ($Si_3N_4$) and silicon carbide (SiC) is to lower the potential barrier of the

system, which is needed for producing electroluminescence (EL) as well as for optoelectronic applications. Our group and other researchers have demonstrated that amorphous Si-QDs can be produced in $Si_3N_4$ using plasma enhanced chemical vapour deposition and that the emission wavelength of these Si-QDs can be controlled by varying the composition of the sub-stoichiometric silicon nitride film.[6, 7]

Though researchers have demonstrated that Si-QDs embedded in $Si_3N_4$ produce photoluminescence (PL) and EL.[6, 7] The light emitted from Si-QDs in $Si_3N_4$ is still very low in intensity for commercial applications and more research is still required. To increase charge transport in these types of systems, researchers have explored introducing dopants into the system. The technique of doping has been a common method used for semiconductors to modify their electrical and structural properties. Dopants such as P and B have been explored to modify the optical and electrical properties of Si-QDs, which mostly stems from their common use in doping bulk Si.[8-11]

Thus far the majority of work in this area has focused on Si-QDs in $SiO_2$. With interest shifting to Si-QDs embedded in materials like $Si_3N_4$, studies on the optical and electrical properties of dopant incorporation in Si-QDs/$Si_3N_4$ systems are gaining interest. This thesis will explore the use of Al as a potential dopant for Si-QDs embedded $Si_3N_4$ and compare the optical properties of this system with that of one doped using P.

Aluminum oxide ($Al_2O_3$) has also been explored by some researchers as an alternative to $SiO_2$, but for different reasons to materials like $Si_3N_4$ and SiC. The interest in $Al_2O_3$ stems not from an effort to decrease the potential barrier formed by the material but rather from a desire to reduce device size while still maintaining the high dielectric constant of the host material which is needed for charge storage devices. The ideal material is one that can maintain a large enough potential barrier for strong confinement but also maintain

a high dielectric constant as the thickness of the film decreases. $Al_2O_3$ has a wide band gap like $SiO_2$ and it has a dielectric constant that is twice that of $SiO_2$. Since it has been shown that the effective dielectric constant of thin films decreases with decreasing thickness,[12] for thinner storage devices the material used should have a high dielectric constant. It is for this reason we explore the growth of Si-QDs and their optical properties as a function of film crystallinity. We would like to compare our results to existing literature on this type of system and explore the phenomenon responsible for the growth or lack of growth of Si-QDs and what properties hinder or enhance the luminescence of the Si-QDs in a Si-QDs/$Al_2O_3$ system.

Furthermore, the luminescence of Si-QDs systems can be the result of numerous light emitting mechanisms such as (1) quantum confinement, (2) interface interaction and (3) radiative recombination at defect sites.[13, 14] Considering the possible mechanisms occurring within a Si-QD system, there is still a need to examine the role these various mechanisms play in the process of luminescence and explore means of improving the luminescence of Si-QDs systems.

The versatility of Si-QDs and the many avenues of Si-QDs research that are still left to explore are the motivating factors of this thesis. This thesis is focused on the structure-property relationship of Si-QDs in various dielectric matrices, in particular we study local chemical environment in Si-QDs and their interfaces with the dielectric and their luminescence. We also study the factors that affect the growth of embedded Si-QDs in $Si_3N_4$ and $Al_2O_3$; and the use of dopant ions on the material's optical properties.

## 1.2 Silicon Quantum Dots

### 1.2.1 Luminescence of Silicon Quantum Dots

Si is one of the most abundant bulk materials harvested from the earth's crust. Atoms in crystalline Si are arranged in a diamond lattice structure with a lattice constant of 5.43Å.[15] The crystal structure of a material is one factor which plays a role in the energy band structure of the material, which is basically a relationship between the energy (E) and momentum (k) of charge carriers ( either electrons or holes) in the material. The energy band structure is also dependent on the type of bonding and the chemical species of the crystal. It is the difference in the energy band structure of materials that results in the differences in optical and electronic properties observed. In semiconductors like Si, the valence band (VB) has a maximum at the center of the Brillouin zone (Γ point where k=0). The lowest point of the conduction band (CB) can occur at a different wave vector in the Brillouin zone. The energy difference between the CB minimum and the VB maximum is known as the energy band gap.

In Si, the VB maximum occurs at the $\Gamma_{25'}$ band while the CB minimum occurs near X point ($X_1$) as shown in Fig.1.1.[16] This type of band gap is termed an indirect band gap due to the difference in the k value for the VB maximum and CB minimum. Since for optical transitions one must conserve both energy and momentum, in indirect band gap materials like Si the electron momentum is transferred to a phonon (quanta of vibrational energy) with a momentum value that is equal but opposite to that of the CB. This is followed by recombination with the hole in the VB. This three-particle (electron-hole-phonon) process is very inefficient and causes indirect band gap materials like Si to have a long radiative lifetime on the order of a few milliseconds.[17]

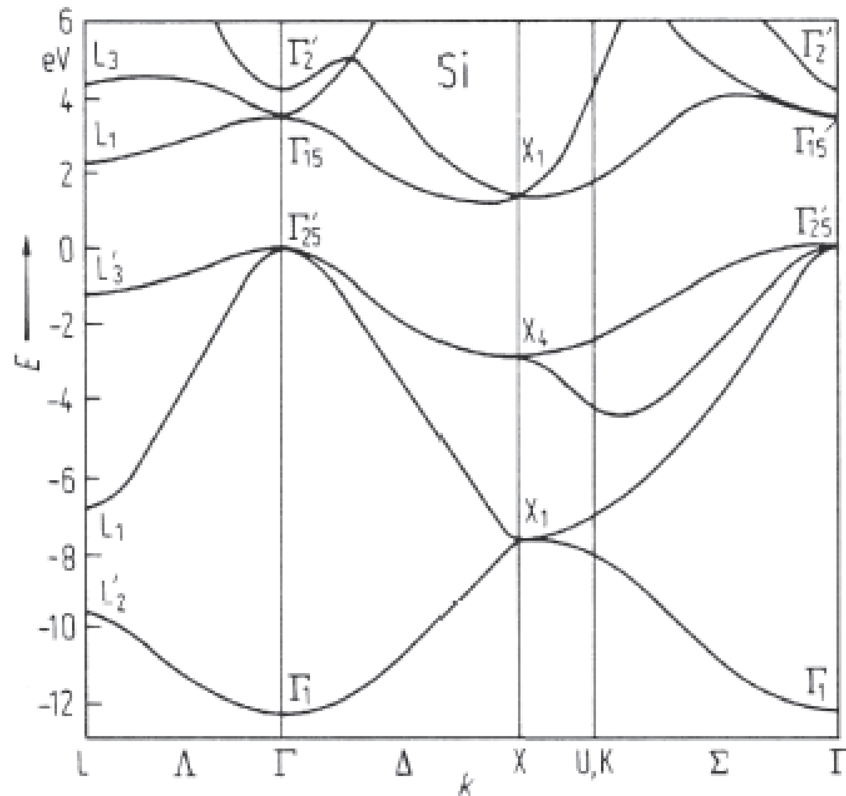


**Fig.1.1:**The calculated energy band structure of bulk Si with energy, *E*, (eV) vs wavevector (k). Adapted from Ref.18 based on Ref.19. [18, 19]

Luminescence is characterized by three parameters: (1) the wavelength (energy) of the maximum emission intensity (λ), (2) the luminescence quantum yield (Φ) or radiative efficiency, and (3) the excited state decay time (τ). The wavelength of luminescence is determined by the energy difference between excited and ground states. The luminescence quantum yield (Φ) or radiative efficiency is the ratio of the number of photons absorbed by a material to the number emitted. It is related to the rate constants for radiative ($k_r$) and non-radiative ($k_{nr}$) excited state processes, and therefore the quantum yield of a material is dependent on both the lifetime of radiative and non-radiative recombination,

$$\Phi = \frac{\frac{1}{\tau_r}}{\frac{1}{\tau_r} + \frac{1}{\tau_{nr}}} \tag{1. 1}$$

where $\tau_r = 1/k_r$ and $\tau_{nr} = 1/k_{nr}$ are the radiative and non-radiative recombination lifetimes, respectively. Based on equation 1.1, a long radiative lifetime in comparison to a short (several orders of magnitude shorter) non-radiative lifetime would result in a low luminescence quantum yield. For Si, it is well established that the radiative lifetime of the material is a few milliseconds while non-radiative lifetimes are of the order of pico- and nanoseconds. It is this significant difference between the competing recombination processes that is responsible for the poor emission from Si.

For Si-QDs, the principle governing the luminescence can be understood by a basic understanding of the quantum size effects and the Heisenberg uncertainty principle. As the dimensions of the material approach the atomic scale there is a transition from classical laws to quantum-mechanical laws of physics to describe the material's behavior. In quantum mechanics, wave-particle duality is a concept that states that every particle can be viewed as both a particle and a wave. A particle in the classical regime is point-like while in quantum mechanics a particle is viewed as wave-like. Analogous to Newton's equations of motion in classical mechanics, the Schrodinger equation is used to describe the behavior of a particle in quantum mechanics and will be referred to later to explain the difference in band gap energy between bulk materials and quantum dots.

Heisenberg established that, based on the concept of wave-particle duality, there is a limit to which the position ($\sigma_x$) and momentum ($\sigma_p$) of a particle can be precisely measured and this is known as the Heisenberg uncertainty principle which is given as:

$$\sigma_x \cdot \sigma_p \geq \frac{h}{2} \tag{1. 2}$$

where $h$ is Planck's constant.

Therefore, reducing the dimensions of the material decreases the position uncertainty of the charge carriers of the structure which in turn increases the uncertainty of their momenta. At the point where the dimensions of Si are reduced sufficiently enough that the momentum uncertainty is greater than the difference in the momentum of CB and VB, the material is said to possesses a quasi-direct band gap as illustrated in Fig.1.2. This quasi-direct band gap structure therefore increases the probability of radiative recombination because no phonon is required which increases the material's radiative efficiency.

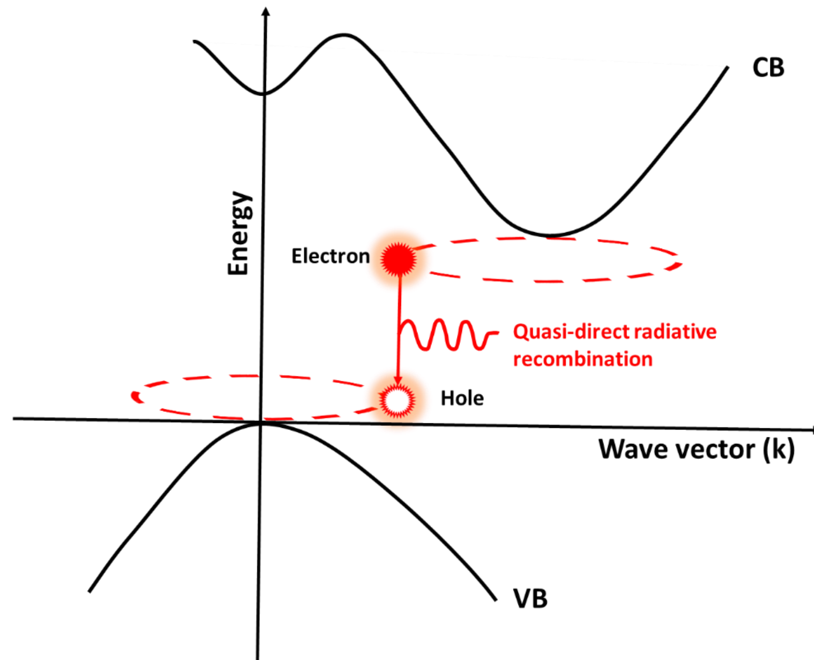


**Fig.1.2:** Diagram illustrating a quasi-direct band gap, where the increase in momentum uncertainty is shown as red dashed circles for the charge carriers in the valence (VB) and conduction (CB) band.

To understand why different size Si-QDs emit at different energies would require us to briefly discuss the quantum size effect. As the size (or dimensions) of the material decreases to the materials exciton Bohr radius (distance between the electron and hole pair) quantum confinement effects are observed. As mentioned earlier, quantum confinement is simply a restriction of the degrees of freedom in which the charge carrier can move in either one, two or three dimensions (1-D, 2-D or 3-D). In the case of 3-D confinement, the behaviour of the charge carrier can be described by the quantum mechanical 'particle in a box'. By applying the boundary condition of a 3-D infinite well, which is that at the walls of the well we apply an infinite potential, the energy of the charge carrier can be described by the following:[20]

$$E_{n,m,l} = \frac{\hbar^2\pi^2}{2m_e} \left(\frac{n^2}{a_x^2} + \frac{m^2}{a_y^2} + \frac{l^2}{a_z^2}\right) \tag{1. 3}$$

where $\hbar$ is reduced Plank's constant, $m_e$ is the effective mass of the charge carrier; $a_x$ , $a_y$ and $a_z$ are the dimensions in the $x$, $y$ and $z$ directions with $n$, $m$ and $l$ being their corresponding quantum numbers. From this equation, we can see that there is a strong dependence between the allowed energy levels of the charge carrier and the particle dimensions, i.e. the width of the well in the three dimensions, and that the allowed energy states are discrete. The difference between the equation for the band gap of the system and the energy of the charge carrier would be that instead of using the effective mass of the charge carrier we would use the effective mass of the exciton.

The value of the effective mass of the exciton is determined by the size of the particle. For strong confinement, which occurs when the dimensions of the particle are less than the exciton Bohr radius, the reduced mass is used as the approximate mass of the

exciton which is simply the reciprocal of the sum of the reciprocal of the effective mass of the electron and hole. The consequence of this is that a correction term is added to the energy band gap of the bulk material where the correction term is inversely proportional to the radius of the particle. Therefore, as the particle becomes larger this correction term decreases and the material's band gap tends to approach the bulk band gap.[21] As the size of the particle decreases, the band gap energy would increase which causes in the emission energy to increase. The Brus formula relates the QD's size to its emission energy is given by the following:[22]

$$\Delta E = E_{g(bulk)} + \frac{h^2}{8R^2}\left(\frac{1}{m_e^*} + \frac{1}{m_h^*}\right) \quad (1.4)$$

where $E_{g(bulk)}$ is the band gap of the bulk material, $R$ is the radius of the QD while the effective mass of an excited electron and hole are $m_e^*$ and $m_h^*$, respectively. Depending on the crystallinity of the Si-QDs, its emission energy is can be given by one of the following equations[23]:

$$E_c = 1.12eV + \frac{2.4\ eV\ nm^2}{R^2} \quad (1.5)$$

$$E_a = 1.56eV + \frac{2.4\ eV\ nm^2}{R^2} \quad (1.6)$$

where $E_c$ is the emission energy of crystalline Si-QDs, while $E_a$ is for amorphous Si-QDs. For Si quantum systems, the emission wavelength usually falls in the ultraviolet-visible (UV-Vis) to near-infrared (NIR), i.e. 300-1200nm, spectrum range.

### 1.2.2 Overview of Fabrication Techniques for Silicon Quantum Dots

Synthesis techniques used for producing Si-QDs can be classified as either solid-phase or liquid-phase synthesis. Liquid-phase synthesis is commonly used to produce "free-standing" or colloidal Si-QDs while solid-phase synthesis is commonly used for embedded Si-QDs. As this thesis is focused on embedded Si-QDs, we will discuss the most common techniques that have been used for the synthesis of embedded Si-QDs in a host material.

#### 1.2.2a Silicon Quantum Dot growth

In order to produce embedded Si-QDs, the most common approach is to first produce a film with an excess of Si. This is followed by annealing the film, which causes a phase separation between the host matrix and the excess Si, which results in the growth of Si-QDs in the film. The growth of Si-QDs can be described by the classical nucleation and growth theory which predicts the three stages of QD growth in films with low levels of supersaturation. A supersaturated solid solution is one in which the amount of solute (*e.g.* excess Si) exceeds the solubility of the solution (*i.e.* the host matrix). Since the Gibbs free energy of a supersaturated solution in general is very high, to reduce the overall energy of the system there is a separation of the solute from the solution. As an example, if we have a supersaturated solid solution of $SiO_2$ with excess Si, then the excess Si would be segregated from the host $SiO_2$ in order to reduce the overall energy of the system. If given sufficient atomic mobility, the excess Si atoms then may diffuse and form clusters. It is for this reason that the film is annealed.

The stability of these clusters is dependent on them reaching a critical size which is necessary for them to continue to grow. This critical size is described by the following equation:[24]

$$r_c = -\frac{2\sigma}{\Delta G_v}, \quad (1.7)$$

where $r_c$ is the critical radius, $\sigma$ is the surface free energy per unit area and is a positive term, and $\Delta G_v$ is the change in volume free energy per unit volume and has a negative value. If the size of the cluster is smaller than the critical size, the cluster may disassociate. Clusters that are equal to or greater than the critical size will then attach surrounding Si atoms and continue to grow which is the second stage of the classical nucleation and growth theory. Clusters then enter the final and more competitive growth stage in which larger clusters are grown at the expense of smaller clusters. This stage is described by the theory of coarsening commonly known as Ostwald ripening.

As mentioned in section 1.1, for quantum confinement to occur the size of the particle needs to be close to or less than the exciton Bohr radius of the material. Therefore, the host matrix of the QDs must then have a wide enough band gap to restrict the movement of the charge carriers to cause strong confinement. In addition, due to the competition between radiative and non-radiative processes, discussed in section 1.2.1, the host matrix must also help to reduce defects on the QD surface which would act as non-radiative recombination sites. There are a few Si-based dielectric materials which satisfy these criteria which include $SiO_2$, $Si_3N_4$ and SiC but it should be noted that the dielectric material does not necessarily have to be a Si-based compound. Fig.1.3 shows the band alignment of the Si-QDs and these Si-based compounds.

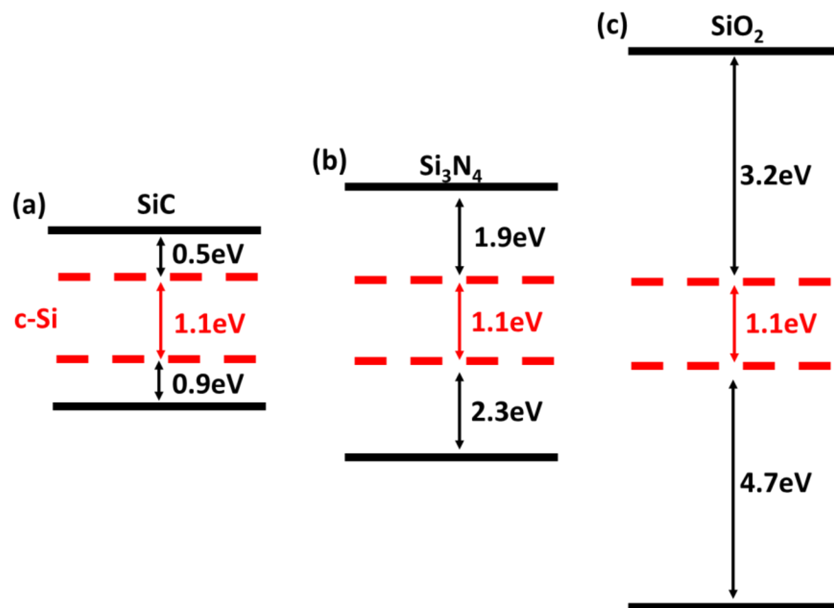


**Fig.1.3:** Band gap alignment of crystalline Si (c-Si) with SiC, $Si_3N_4$ and $SiO_2$. The band gap energy of c-Si is shown using red dashed lines.[25]

### 1.2.2b Synthesis using Plasma Enhanced Chemical Vapour Deposition

Plasma enhanced chemical vapour deposition (PECVD) is one of the common techniques used to produce stoichiometric and non-stoichiometric silicon nitride films. In PECVD, a radio-frequency energized electrode is used to excite the precursor gases into a plasma. The radicals that are produced in the gaseous phase then form a thin film on the desired substrate. It has been shown that the size, crystallinity and optical properties of Si-QDs are dependent on the type of precursors used for deposition of Si-rich silicon nitride film.[26,27] For instance, researchers have shown that the PL intensity of Si-QDs grown in $Si_3N_4$ thin films using $SiH_4$ and ammonia precursors is more intense than those grown using $SiH_4$ and nitrogen.[27] The reason for this increase in PL was associated with the incorporation of more hydrogen into the deposited film which helped to reduce dangling

bonds at the Si-QDs/$Si_3N_4$ interface that would otherwise act as non-radiative recombination sites.

PECVD has also been used to produce superlattices that after annealing have been shown to produce Si-QDs. As an example, Zacharias *et al.* was one of the first groups to demonstrate Si-QDs could be produced by the decomposition of a non-stoichiometric oxide superlattice.[28] In this technique alternating layers of stoichiometric oxide and non-stoichiometric oxide are deposited and a subsequent high temperature anneal leads to the excess Si forming clusters. The size of these Si-QDs is controlled by the thickness of the non-stoichiometric layer. The high temperature annealing treatment used on superlattice structures possess an issue from economical perceptive due to the higher cost that would be incurred to make devices.

### 1.2.2c Synthesis using Ion Implantation

Another common technique used to produce Si-QDs is ion implantation which is a technique that is compatible with existing microelectronics fabrication. The fundamentals of ion implantation will be explained in detail in section 2.8, but in summary ion implantation involves the target material being bombarded by ions to introduce them into the target. For producing Si-QDs, the implanted ions would be Si which would be implanted at a high dose in order to produce excess Si in the film. The need for this excess Si is outlined in section 1.2.2a.

For Si-QDs to form, phase separation of the excess Si must occur. This phase separation can occur if there is sufficient atomic mobility in the matrix or by post-implantation annealing. The annealing step is typically carried out at very high

temperatures (around 800°C–1100°C) for Si-QDs to grow and to repair damage caused by the ion implantation process. Fig.1.4 illustrates the growth process of Si-QDs after ion implantation and annealing. The spatial distribution of the Si atoms causes the size of Si-QDs to vary as a function depth. The simplest approximation to an ion implantation profile is a Gaussian distribution. Larger Si-QDs are typically found around the peak of the Gaussian where the ion concentration is highest while smaller QDs are found at the extremes of the distribution.

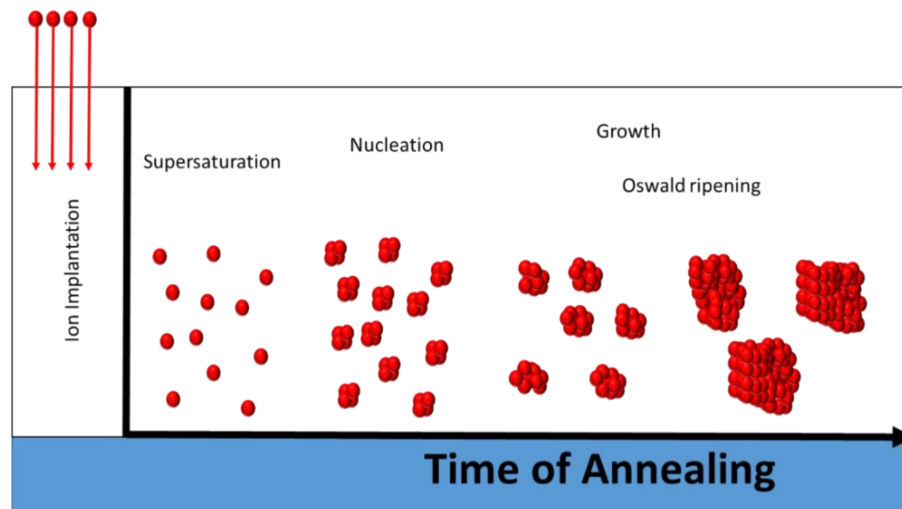


**Fig.1.4:** Illustration of cluster growth after ion implantation as a function of annealing time. After ion implantation the matrix is in a supersaturated state followed by nucleation as time of annealing increases. As the time of annealing increases clusters grow larger and larger as according to the Ostwald ripening process.

Ion implantation has been shown to produce luminescent Si-QDs in $SiO_2$ films as demonstrated by several research groups. For example, Shimizu-Iwayama *et al.* have conducted many studies on the luminescence of Si implanted silica glass and have

demonstrated that at high annealing temperatures (about 1100°C) optically active Si-QDs can be produced.[29] The size of these Si-QDs has been shown to depend on implantation temperature as well as the post annealing time and temperature. This technique is less favourable to produce Si-QDs in $Si_3N_4$ as PECVD has been established as the most common and effective fabrication method. Ion implantation has, however, been explored as a technique for producing Si-QDs in other host materials such as $Al_2O_3$. However, the formation and emissions of Si-QDs have proven challenging for reasons that are explained in chapter 6 of this thesis. In general, the high temperature annealing required for Si-QDs growth and for the repair of implantation damage is a major drawback of ion implantation because it is not suitable for processing low cost devices.

## 1.3 Fundamentals of Materials Examined

### 1.3.1 PECVD Nitride

Silicon nitride is a very important material to various industries due to its high dielectric constant and strength. To name a few examples, $Si_3N_4$ is used in thin film transistors as a gate dielectric and in solar cells as an antireflective coating. $Si_3N_4$ films have also been selected as a suitable host matrix for embedded Si-QDs. This selection is based on an effort to increase charge transport and improve EL by using the lower band gap energy of $Si_3N_4$ compared to $SiO_2$.

$Si_3N_4$ films are either amorphous or can exist in one of two common crystallographic forms, α or β. α-$Si_3N_4$ and β-$Si_3N_4$ are members of the P31c and P63/m space groups, respectively. The crystal structure of these two forms of $Si_3N_4$ are stacked layers of Si-N layers with α-$Si_3N_4$ consist of a layer sequence of ABCDABCD… while

for β-$Si_3N_4$ these layers have a ABAB… sequence.[30] The configuration of the AB and CD layers are shown in Fig.1.5. The lattice parameters for α-$Si_3N_4$ are $a = 7.7$Å and $c = 5.6$Å while for β-$Si_3N_4$ they are $a = 7.58$Å and $c = 2.9$Å. The transformation temperature required for α to become β is in the range of 1573 to 1723K.[31] The band gap of these two phases are 4.67eV and 5.25eV for α and β phases, respectively.[32] In amorphous $Si_3N_4$, there is a lack of long range order however there is short-range order and the Si-N configuration is maintained.[33]

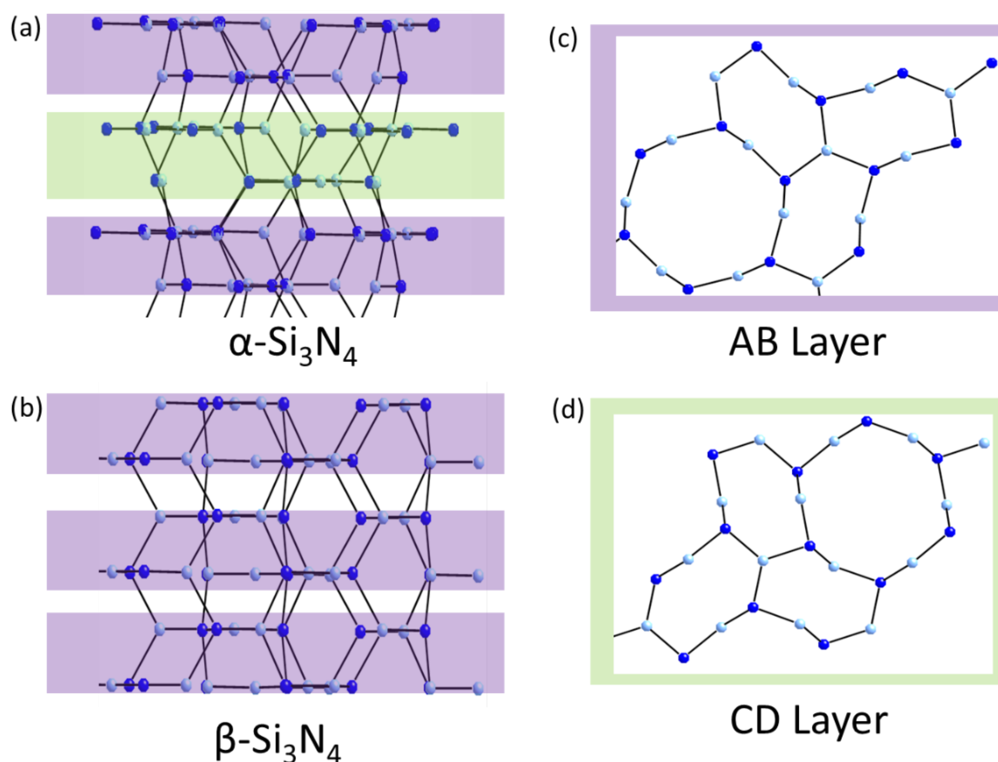


**Fig.1.5:** Illustration of the crystal structure of (a) α-$Si_3N_4$ and (b) β-$Si_3N_4$ consisting of layer sequence ABCDAB… and ABAB… respectively. Si atoms are in dark blue and N atoms are in light blue. The structure of AB and CD layers are shown in (c) and (d). Crystal structures were made using Crystal Maker software.

$Si_3N_4$ thin films deposited using chemical vapour deposition (CVD) or derivatives of this technique such as PECVD and low pressure (LPCVD) tends to be amorphous and has a hydrogen content that is in the range of 10 to 25%.[34] The optical band gap of amorphous $Si_3N_4$ is approximately 5.1 eV but can slightly decrease in samples with high hydrogen content. This type of $Si_3N_4$ consists of an amorphous network that composes Si-N, Si-H, N-H and Si-Si bonds with bond energies of 3.5eV, 3.0eV, 4.0eV and 1.83eV, respectively. During the deposition process structural defects can form within amorphous $Si_3N_4$ with the most common types of defects being Si and N dangling bonds.

The presence of N dangling bonds has been observed by Warren *et al.* for stoichiometric and N-rich $Si_3N_4$ produced by LPCVD and PECVD respectively. In this report, they found that the formation of N dangling bonds was the result of post deposition annealing causing hydrogen evolution from the breaking of N-H bonds.[35] In other work by Warren *et al.*, the researchers observed that the presence of N and Si dangling bonds was dependent on the Si and N concentration in the hydrogenated amorphous silicon nitride (*a*-$SiN_x$:H) films. N dangling bonds were observed for $x > 1.3$ (N-rich $Si_3N_4$) while Si dangling bonds were only observed for $x < 1.3$ (Si-rich $Si_3N_4$).[36]

Notably, the presence of these defects in $Si_3N_4$ results in the formation of the mid-bandgap states. There has been a substantial amount of theoretical and experimental work done to characterize the various defects.[37-39]. Fig.1.6 summarizes the energies of these defects.

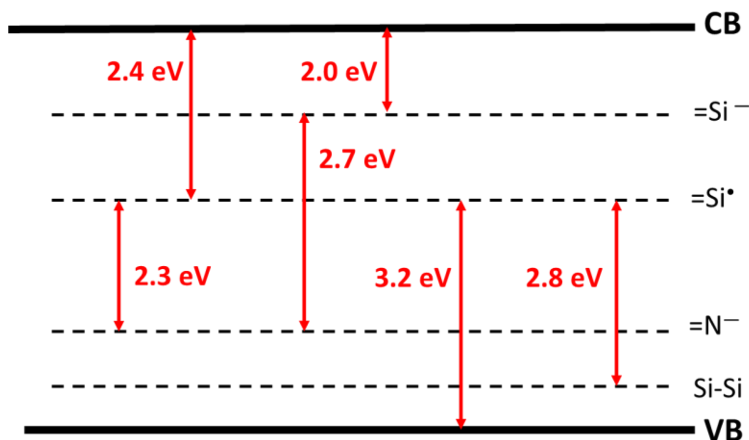


**Fig.1. 6:** Illustration of the possible defects present in $Si_3N_4$ based on results by Mo *et al.*[39]

### 1.3.1a Impurity Doping

Similar to the well-established band gap engineering of semiconductor materials, like ZnO using impurities, researchers have also explored the use of dopants to modify the band gap of $Si_3N_4$. In 1999, F. Munakata *et al.* observed that the incorporation of Al impurities into single crystal β-$Si_3N_4$ introduced an interband state of approximately 2.4 eV.[40] In addition, Z. Mao *et al.* demonstrated that an intermediate state at 2.65 eV was produced in Al-doped α-$Si_3N_4$ micron-belts based on their I-V curve measurements.[41] Later on, in 2016, Z. Huang *et al.* proposed that the electron transition mechanism for their Al-doped system was due to the formation of Al-N and Al-Si mid gap states forming. This resulted in an apparent band gap of 1.99 eV, which was confirmed by their PL measurements.[42] In the study conducted by Z. Huang, the α-$Si_3N_4$ used was single crystalline nanowires produced through the nitriding cryomilled nanocrystalline silicon powder (see the details in Ref.[43]).[43] To the author's knowledge there currently does not exist any publications on the influence of Al doping of $Si_3N_4$ containing Si-QDs. But, based

on the publications cited above, there is great potential for Al incorporation to alter the emission of the $Si_3N_4$ and the Si-QDs.

There has been a recent report on the optical and electrical properties of boron (B) doping Si-QDs contained in $Si_3N_4$ thin films, which has been a common candidate for doping Si-QDs. In a publication by J. Liu, it was shown that the Ar flow rate used during film deposition can be used to alter the properties of Si-QDs in B-doped $Si_3N_4$ because it helped to increase B incorporation into the Si-QDs.[44] These studies on doped $Si_3N_4$ suggest that impurity doping could be used to modify the optical and electrical properties of $Si_3N_4$ thin films and $Si_3N_4$ containing Si-QDs. This thesis will explore the influence of Al dose (concentration) on the optical properties of Si-QDs in $Si_3N_4$.

### 1.3.2 Aluminum oxide

$Al_2O_3$ is a material that is used in a wide range of applications including optics, electronics and metallurgy. The wide band gap (9.2eV) and high dielectric constant of this material make it a promising candidate as a host matrix for Si-QDs. Furthermore, the intrinsic defects and impurities of $Al_2O_3$ can be exploited to further expand the possible applications of Si-QDs systems.

$Al_2O_3$ is a transparent inorganic material that can exist in amorphous and crystalline states. This thesis will examine both amorphous and crystalline $Al_2O_3$. Crystalline $Al_2O_3$ can be subdivided into different crystalline phases with the three most common phases being α, θ and γ. The α-$Al_2O_3$ phase is the most thermodynamically stable phase while θ and γ are metastable phases. The crystal structures of the most common phases γ, θ and α are presented in Fig.1.7.[45-47]

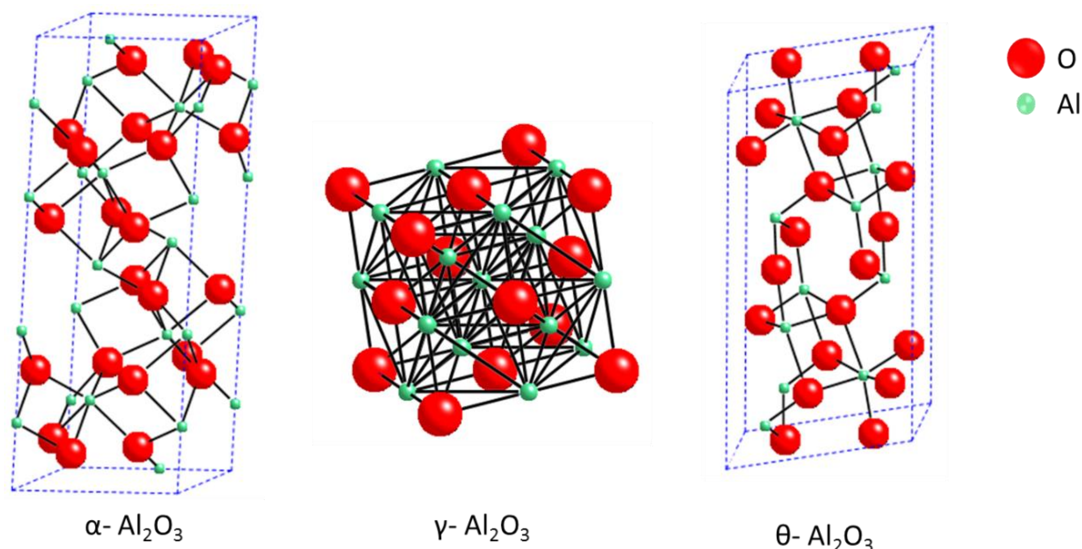


**Fig.1.7:** Crystal structure of α-$Al_2O_3$, γ- $Al_2O_3$ and θ-$Al_2O_3$ with Al atoms in green and O atoms depicted in red.

The crystal structure of γ-$Al_2O_3$ comprises of Al lattice that has octahedral and tetrahedral Al along with an O lattice which is face-centered cubic. θ-$Al_2O_3$ has a hexagonal closed packed Al and face-centered cubic O lattice structure. And finally, α-$Al_2O_3$ comprises of hexagonal close packed O anions with octahedral interstitials of $Al^{3+}$ cations.

The processes that are used for producing α-$Al_2O_3$ involve the transition from intermediate metastable phases to the α phase. For instance, an aluminum hydroxides precursor like AlOOH can be thermally dehydrated or amorphous $Al_2O_3$ (a-$Al_2O_3$) can be heat treated to form crystalline α-$Al_2O_3$. There are several methods for producing a-$Al_2O_3$ thin films, with the most common techniques being CVD and electrochemical anodization. As an example, a-$Al_2O_3$ thin films can be deposited on Si substrates by thermal CVD of aluminum tri-isopropoxide ($Al[OCH(CH_3)_2]_3$) or ATI at 420°C at a pressure of 10mbar.[48]

Anodization is a common technique used for producing $Al_2O_3$ coatings in order to increase the corrosion resistance of aluminum surfaces. Anodization is the controlled

oxidation of an aluminum surface to produce a continuous oxide film. Aluminum is connected to the positive terminal of a power supply acting as the anode in the electrochemical process while another metal, typically tungsten or tantalum, acts the cathode. The two metals are then submerged in an electrolyte such as phosphoric or sulphuric acid.[49] The bias potential splits the water molecules in the acid into hydrogen cations and oxygen anions. The oxygen anions then migrate to the aluminum anode while the hydrogen cations move towards the metal cathode. The reaction at the two electrodes are described below,

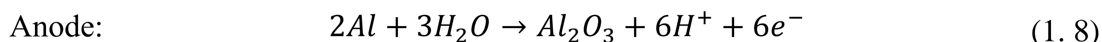

Anode: $$2Al + 3H_2O \rightarrow Al_2O_3 + 6H^+ + 6e^- \quad (1.8)$$

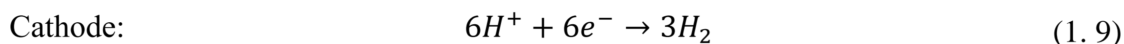

Cathode: $$6H^+ + 6e^- \rightarrow 3H_2 \quad (1.9)$$

There are two types of anodic oxide films that can be formed on aluminum, shown in Fig1.8.[50] One type is known as barrier-type $Al_2O_3$ film were the thickness of the film is very uniform and typically forms in completely insoluble electrolyte solutions with a pH of 5-7 such as neutral boric acid and ammonium tetraborate in ethylene glycol. The other type of film is porous and normally forms in a slightly soluble electrolyte such as oxalic and phosphoric acid.

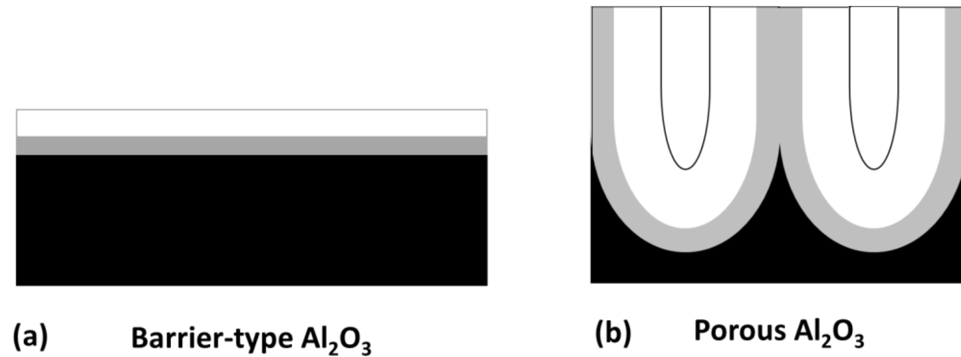


**Fig.1.8:** Illustration of (a) barrier-type $Al_2O_3$ and (b) porous $Al_2O_3$.

For barrier-type $Al_2O_3$ films, the maximum thickness is less than 1μm while porous $Al_2O_3$ films can be made much thicker. The thickness of porous $Al_2O_3$ films is dependent on the anodization time, the electrolyte used and current density. The formation mechanism for porous $Al_2O_3$ is illustrated below in Fig.1.9.

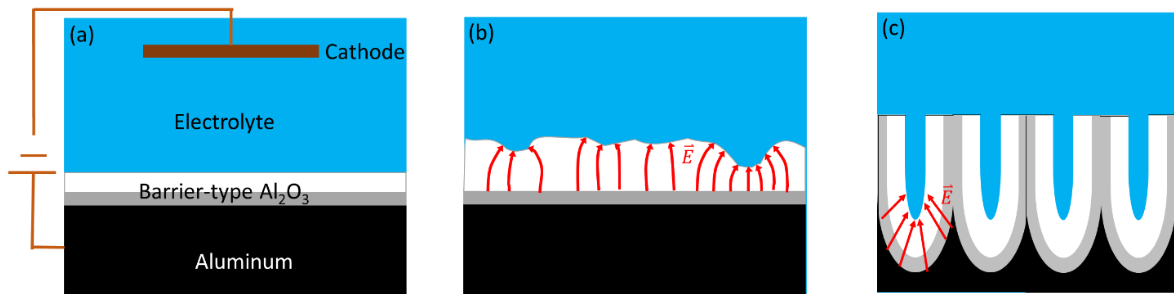


**Fig.1.9:** Schematic of the formation of porous $Al_2O_3$. (a) Starting with the formation of barrier-type $Al_2O_3$, followed by (b) surface fluctuations causing electric field distribution with electric field shown as red arrows and (c) the field-enhanced dissolution and stable growth of pores.

Growth steps can be summarized in the following sequence. First a barrier film is formed that covers the aluminum surface, Fig.1.9(a). Then pores begin to grow due to the field-enhanced and/or temperature enhanced dissolution of the barrier film, as shown in

Fig.1.9(b). The competitive growth of pores causes some of the pores to stop growing while the growth of surviving pores begins to stabilize.

## 1.4 Thesis Outline

The focus of this thesis is to examine the luminescence of Si-QDs in $Si_3N_4$ and $Al_2O_3$. This thesis will examine the luminescence of Si-QDs and examine the effect: (1) different growth conditions have on the emission of Si-QDs in $Si_3N_4$, (2) matrix crystallinity has on the growth and luminescence of Si implanted $Al_2O_3$ as well as (3) impurity doping has on the luminescence of Si-QDs. The content of this thesis is presented as follows:

- Chapter 2: this chapter provides details on sample fabrication and characterization techniques used in this thesis.
- Chapter 3: will examine the influence of hydrogen passivation on the PL intensity of Si-QDs in $Si_3N_4$ and the impact which post-annealing temperature has on the hydrogen content of this system. This chapter explores how sample composition and annealing temperature impact the luminescence of Si-QDs formed in $Si_3N_4$.
- Chapter 4: explores the impact of defect concentration on the light emission of Al implanted stoichiometric $Si_3N_4$. This chapter explores the impact of post-annealing temperature on the light emission of Al implanted stoichiometric $Si_3N_4$. It will also examine the role of dopant concentration on the photoluminescence spectra of this doped system.

- Chapter 5: focuses on the luminescence of Al and P implanted Si-rich $Si_3N_4$. This chapter explores the influence dopant type and concentration have on the luminescence of Si-QDs embedded in $Si_3N_4$.
- Chapter 6: examines the optical properties of Si-implanted $Al_2O_3$. This chapter investigates the influence of $Al_2O_3$ crystallinity on the formation of Si-QDs in a non-Si based matrix.
- Chapter 7: provides a summary of conclusions made in this thesis as well as suggestions for the follow-up research.

## 1.5 References

[1] K. Hiroyuki, H. Masataka, and O. Yukio, "Wide Optical-Gap, Photoconductive a-$Si_x N_{1-x}$:H," *Japanese Journal of Applied Physics,* vol. 20, p. L811, 1981.

[2] L. T. Canham, "Silicon quantum wire array fabrication by electrochemical and chemical dissolution of wafers," *Applied Physics Letters,* vol. 57, pp. 1046-1048, 1990.

[3] A. G. Cullis and L. T. Canham, "Visible light emission due to quantum size effects in highly porous crystalline silicon," *Nature,* vol. 353, p. 335, 1991.

[4] B. Gelloz, H. Sano, R. Boukherroub, D. D. M. Wayner, D. J. Lockwood, and N. Koshida, "Stabilization of porous silicon electroluminescence by surface passivation with controlled covalent bonds," *Applied Physics Letters,* vol. 83, pp. 2342-2344, 2003.

[5] O. Bisi, S. Ossicini, and L. Pavesi, "Porous silicon: a quantum sponge structure for silicon based optoelectronics," *Surface Science Reports,* vol. 38, pp. 1-126, 2000.

[6] D. Li, J. Huang, and D. Yang, "Electroluminescence of silicon-rich silicon nitride light-emitting devices," in *2008 5th IEEE International Conference on Group IV Photonics*, 2008, pp. 119-121.

[7] O. Debieu, R. P. Nalini, J. Cardin, X. Portier, J. Perrière, and F. Gourbilleau, "Structural and optical characterization of pure Si-rich nitride thin films," *Nanoscale Research Letters,* vol. 8, pp. 31-31, 2013.

[8] M. Khelil, S. Kraiem, M. Kraini, C. Vázquez-Vázquez, K. Khirouni, and M. A. López-Quintela, "The effects of doping type on structural and electrical properties of silicon nanocrystals layers grown by plasma enhanced chemical vapor

deposition," *Journal of Materials Science: Materials in Electronics,* vol. 29, pp. 11000-11012, 2018.

[9] I. Marri, E. Degoli, and S. Ossicini, "First Principle Studies of B and P Doped Si Nanocrystals," *Physica status solidi (a),* vol. 215, p. 1700414, 2017.

[10] D. Hiller, J. López-Vidrier, S. Gutsch, M. Zacharias, K. Nomoto, and D. König, "Defect-Induced Luminescence Quenching vs. Charge Carrier Generation of Phosphorus Incorporated in Silicon Nanocrystals as Function of Size," *Scientific Reports,* vol. 7, p. 863, 2017.

[11] L. Dongke, J. Yicheng, L. Jingjing, Z. Pei, X. Jun, L. Wei*, et al.*, "Modulation of surface states by phosphorus to improve the optical properties of ultra-small Si nanocrystals," *Nanotechnology,* vol. 28, p. 475704, 2017.

[12] K. Natori, D. Otani, and N. Sano, "Thickness dependence of the effective dielectric constant in a thin film capacitor," *Applied Physics Letters,* vol. 73, pp. 632-634, 1998.

[13] F. Giorgis, C. Vinegoni, and L. Pavesi, "Optical absorption and photoluminescence properties of films deposited by plasma-enhanced CVD," *Physical Review B,* vol. 61, pp. 4693-4698, 2000.

[14] D. S. Kim, S. G. Yoon, G. E. Jang, S. J. Suh, H. Kim, and D. H. Yoon, "Refractive index properties of SiN thin films and fabrication of SiN optical waveguide," *Journal of Electroceramics,* vol. 17, pp. 315-318, 2006.

[15] M. Balarin, "Properties of Silicon. EMIS Datareviews Series No. 4. Einführung: C. Hilsum, Vorwort: T. H. Ning, INSPEC, The Institution of Electrical Engineering, London, New York 1988, 31 Kapitel, 1100 Seiten, 260 Datareviews, £ 195, ISBN 0-85296-4757," *Crystal Research and Technology,* vol. 24, pp. 386-386, 1989.

[16] R. E. Hummel, *Electronic properties of materials*, 4 ed.: Springer-Verlag New York, 2011.

[17] L. C. Kimerling, K. D. Kolenbrander, J. Michel, and J. Palm, "Light Emission from Silicon," in *Solid State Physics*. vol. 50, H. Ehrenreich and F. Spaepen, Eds., ed: Academic Press, 1996, pp. 333-381.

[18] M. Grundmann, "Band Structure," in *The Physics of Semiconductors: An Introduction Including Devices and Nanophysics*, ed Germany: Springer, Berlin, Heidelberg, p. 111.

[19] J. R. Chelikowsky and M. L. Cohen, "Nonlocal pseudopotential calculations for the electronic structure of eleven diamond and zinc-blende semiconductors," *Physical Review B,* vol. 14, pp. 556-582, 1976.

[20] D. A. Neamen, *Semiconductor physics and devices: basic principles*, 3 ed.: Elizabeth A. Jones 2003.

[21] H. Takagi, H. Ogawa, Y. Yamazaki, A. Ishizaki, and T. Nakagiri, "Quantum size effects on photoluminescence in ultrafine Si particles," *Applied Physics Letters,* vol. 56, pp. 2379-2380, 1990.

[22] L. Brus, "Electronic wave functions in semiconductor clusters: experiment and theory," *The Journal of Physical Chemistry,* vol. 90, pp. 2555-2560, 1986.

[23] H.-S. Kwack, Y. Sun, Y.-H. Cho, N.-M. Park, and S.-J. Park, "Anomalous temperature dependence of optical emission in visible-light-emitting amorphous silicon quantum dots," *Applied Physics Letters,* vol. 83, pp. 2901-2903, 2003.

[24] E. J. Mittemeijer, "Phase Transformations," in *Fundamentals of Materials Science* ed Berlin, Heidelberg: Springer Berlin Heidelberg, 2011, p. 371.

[25] E. Cho, M. Green, G. Conibeer, D. Song, Y.-H. Cho, G. Scardera*, et al.*, *ResearchArticle Silicon Quantum Dots in a Dielectric Matrix for All-Silicon Tandem Solar Cells*, 2018.

[26] A. A. Korkin, J. V. Cole, D. Sengupta, and J. B. Adams, "On the Mechanism of Silicon Nitride Chemical Vapor Deposition from Dichlorosilane and Ammonia," *Journal of The Electrochemical Society,* vol. 146, pp. 4203-4212, 1999.

[27] B.-H. Kim, C.-H. Cho, T.-W. Kim, N.-M. Park, G. Y. Sung, and S.-J. Park, "Photoluminescence of silicon quantum dots in silicon nitride grown by $NH_3$ and $SiH_4$," *Applied Physics Letters,* vol. 86, p. 091908, 2005.

[28] M. Zacharias, J. Heitmann, R. Scholz, U. Kahler, M. Schmidt, and J. Bläsing, "Size-controlled highly luminescent silicon nanocrystals: A $SiO/SiO_2$ superlattice approach," *Applied Physics Letters,* vol. 80, pp. 661-663, 2002.

[29] T. Shimizu-Iwayama, K. Fujita, S. Nakao, K. Saitoh, T. Fujita, and N. Itoh, "Visible photoluminescence in $Si^+$-implanted silica glass," *Journal of Applied Physics,* vol. 75, pp. 7779-7783, 1994.

[30] M. Yashima, Y. Ando, and Y. Tabira, "Crystal Structure and Electron Density of α-Silicon Nitride: Experimental and Theoretical Evidence for the Covalent Bonding and Charge Transfer," *The Journal of Physical Chemistry B,* vol. 111, pp. 3609-3613, 2007.

[31] W. D. Forgeng, "Nitrides of Silicon," *Trans. AIME,* vol. 212, pp. 343-348, 1958.

[32] Y.-N. Xu and W. Y. Ching, "Electronic structure and optical properties of a and b phases of silicon nitride, silicon oxynitride, and with comparison to silicon dioxide," *Physical Review B,* vol. 51, pp. 17379-17389, 1995.

[33] V. A. Gritsenko, R. W. M. Kwok, H. Wong, and J. B. Xu, "Short-range order in non-stoichiometric amorphous silicon oxynitride and silicon-rich nitride," *Journal of Non-Crystalline Solids,* vol. 297, pp. 96-101, 2002.

[34] S. V. Nguyen and S. Fridmann, "Plasma Deposition and Characterization of Thin Silicon-Rich Silicon Nitride Films," *Journal of The Electrochemical Society,* vol. 134, pp. 2324-2329, 1987.

[35] W. L. Warren, C. H. Seager, J. Robertson, J. Kanicki, and E. H. Poindexter, "Creation and Properties of Nitrogen Dangling Bond Defects in Silicon Nitride Thin Films," *Journal of The Electrochemical Society,* vol. 143, pp. 3685-3691, 1996.

[36] W. L. Warren, J. Robertson, and J. Kanicki, "Si and N dangling bond creation in silicon nitride thin films," *Applied Physics Letters,* vol. 63, pp. 2685-2687, 1993.

[37] B. Sain and D. Das, "Tunable photoluminescence from nc-Si/a-$SiN_x$:H quantum dot thin films prepared by ICP-CVD," *Physical Chemistry Chemical Physics,* vol. 15, pp. 3881-3888, 2013.

[38] S. V. Deshpande, E. Gulari, S. W. Brown, and S. C. Rand, "Optical properties of silicon nitride films deposited by hot filament chemical vapor deposition," *Journal of Applied Physics,* vol. 77, pp. 6534-6541, 1995.

[39] C. m. Mo, L. Zhang, C. Xie, and T. Wang, "Luminescence of nanometer-sized amorphous silicon nitride solids," *Journal of Applied Physics,* vol. 73, pp. 5185-5188, 1993.

[40] F. Munakata, K. Matsuo, K. Furuya, Y. Akimune, J. Ye, and I. Ishikawa, "Optical properties of β-$Si_3N_4$ single crystals grown from a Si melt in $N_2$," *Applied Physics Letters,* vol. 74, pp. 3498-3500, 1999.

[41] Z. Mao, Y. Zhu, Y. Zeng, F. Xu, Z. Liu, G. Ma, *et al.*, "Investigation of Al-doped silicon nitride-based semiconductor and its shrinkage mechanism," *CrystEngComm,* vol. 14, pp. 7929-7933, 2012.

[42] Z. Huang, Z. Wang, F. Chen, Q. Shen, and L. Zhang, "Band structures and optical properties of Al-doped α-$Si_3N_4$: theoretical and experimental studies," *Ceramics International,* vol. 42, pp. 3681-3686, 2016.

[43] F. Chen, Y. Li, W. Liu, Q. Shen, L. Zhang, Q. Jiang, *et al.*, "Synthesis of α silicon nitride single-crystalline nanowires by nitriding cryomilled nanocrystalline silicon powder," *Scripta Materialia,* vol. 60, pp. 737-740, 2009.

[44] L. Jia, L. Bin, Z. Xisheng, G. Xiaojia, and L. Shengzhong, "Effect of argon flow on promoting boron doping for in-situ grown silicon nitride thin films containing silicon quantum dots," *Nanotechnology,* vol. 28, p. 285202, 2017.

[45] R. E. Newnham and Y. M. d. Haan, "Refinement of the α $Al_2O_3$, $Ti_2O_3$, $V_2O_3$ and $Cr_2O_3$ structures*," in *Zeitschrift für Kristallographie* vol. 117, ed, 1962, p. 235.

[46] E. J. W. Verwey, "The Structure of the electrolytical oxide Layer on Aluminium," in *Zeitschrift für Kristallographie - Crystalline Materials* vol. 91, ed, 1935, p. 317.

[47] E. Husson and Y. Repelin, *Structural studies of transition aluminas. Theta alumina* vol. 33, 1996.

[48] O. Mekasuwandumrong, P. L. Silveston, P. Praserthdam, M. Inoue, V. Pavarajarn, and W. Tanakulrungsank, "Synthesis of thermally stable micro spherical χ-alumina by thermal decomposition of aluminum isopropoxide in mineral oil," *Inorganic Chemistry Communications,* vol. 6, pp. 930-934, 2003.

[49] P. G. S. Wernick S. Pinner, *The Surface Treatment and Finishing of Aluminium and Its Alloys*, 6 ed. vol. 1: Fininshing Pubns Ltd, 2001.

[50] Y. Peng, T. H. Shen, B. Ashworth, X.-G. Zhao, C. A. Faunce, and Y.-W. Liu, "Magneto-optical characteristics of magnetic nanowire arrays in anodic aluminum oxide templates," *Applied Physics Letters,* vol. 83, pp. 362-364, 2003.

# Chapter 2

# Experimental Techniques

## 2.1 Photoluminescence (PL) Spectroscopy

Photoluminescence is a contactless technique which probes the electronic structure of a material. The sample is illuminated by a light source with photon energy equal to or greater than the band gap of the material. The absorption of light promotes a valence electron from the ground state to an excited state. Eventually, this excited electron recombines with a hole in the valence band (VB). This recombination process can either be radiative (to produce a photon) or non-radiative (to produce a phonon).

In semiconductors, the probability that the recombination process is radiative or non-radiative is strongly dependent on the band gap structure. Semiconductors can have a direct band gap in which the VB and conduction band (CB) occur at the same momentum or an indirect band gap in which the VB and CB are misaligned in reciprocal space. For semiconductors with an indirect band gap (such as bulk Si), the probability that the electron-hole pair recombines radiatively is very low due to the three-particle process required for a photon to be produced. This process has been discussed in section 1.2.1. In contrast, direct band gap semiconductors (such as GaAs) have a higher probability for radiative recombination as no phonon is required.[1] Hence, the PL wavelength and intensity provide information about the de-excitation processes occurring in the material. This information is extracted by examining the wavelength of emission, spectral shape and PL intensity.

A typical PL setup comprises of a light source with a wavelength close to the band gap energy of the target material. The sample is oriented such that the reflected incident beam and the PL emission of the sample are in different directions. A high-pass filter can also be used to prevent scattered incident rays from entering the spectrometer. The emitted light from the sample is collected by the spectrometer which uses a diffraction grating to direct different wavelengths of the light to an array of photodetectors in the spectrometer. The photodetectors in the spectrometer measure the intensity of the different wavelengths and this information is then interpreted by a computer which outputs the PL spectrum of the sample being examined.

The PL spectra presented in this thesis were obtained at room temperature using an in-house PL system. The light source for PL measurements was a 405±10 nm wavelength laser diode with a power input of 120mW. The angle of incidence was 45° relative to the sample surface. The light source was band-pass filtered (405nm), and the emitted photons from the sample were high-pass filtered (> 450nm). PL spectra were collected using a Mightex HRS-BD1-200 spectrometer with a wavelength range of 300-1050 nm and 0.9 nm resolution.

## 2.2 Time-Resolved Photoluminescence (TRPL)

Unlike PL which uses a continuous laser beam, time-resolved photoluminescence (TRPL) uses a short laser pulse for excitation. The subsequent decay of PL intensity as a function of time is measured when the laser is off. Since the light emitted during electron-hole pair recombination is composed of various transitions which have different PL lifetimes, TRPL can provide information about the species responsible for the luminescence of a given system. TRPL spectra are analysed by

fitting the decay curve with a single- or multi-exponential decay function depending on the number of components present. For semiconductors, the characteristic lifetime is dependent on the dimensions and type of material and interfaces involved and can vary from picoseconds to milliseconds. It is important to note that the lifetimes observed in the decay spectra are also dependent on the resolution of the TRPL setup used. Therefore, samples with very short lifetime components (on the order of picoseconds) require a very fast acting laser and ultra-high-speed detector in order for these short lifetimes to be measured.

For time-resolved PL (TRPL) measurements, the 405nm laser diode was pulsed using a 3310A HP function generator. The time resolution of our setup was ~100nsec. Decay curves were acquired using a R7400U-20 Hamamatsu photomultiplier tube (PMT) with a spectral range of 300-900nm and peak sensitivity of 630nm. Decay curves were analysed using OriginLab® and fitted using a multi-component exponential decay function.

## 2.3 Fourier Transform Infrared Spectroscopy (FTIR)

Infrared (IR) spectroscopy is a vibrational spectroscopy technique that is used for identifying chemical compounds in a sample. In this technique, the sample is exposed to an IR beam, and when the energy of the IR beam matches the energy of a specific molecular vibration, absorption occurs. For IR absorption to occur (i.e. for a molecule to be IR active) the vibrations or rotations within a molecule must cause a net change in the dipole moment of the molecule. There are two major types of oscillations that atoms can undergo which are stretching and bending modes known as the normal modes of vibration. The stretching mode can be symmetric or antisymmetric motion along the bond axis. While the bending mode occurs is when there is a change in the

angle between bonds. The number of normal modes of vibration for a molecule with N atoms is given by 3N-5 for linear molecules and 3N-6 for non-linear molecules. Since different molecules absorb specific frequencies, the IR spectrum can be used for identifying (fingerprinting) a sample at a molecular level.[2]

An IR spectrometer can be non-dispersive (fixed wavelength selection), dispersive (uses a grating to vary wavelength) or Fourier transform (uses an interferometer to collect the IR spectrum). The most common type of infrared spectrometer is the Fourier transform infrared (FTIR) spectrometer. The main component of an FTIR spectrometer is the Michelson interferometer. In a Michelson interferometer, a beam passes through a beam splitter which splits the original beam into two beams: one passes through while the second is reflected at 90°. Each of these beams is then reflected by mirrors back towards the beam splitter. One of these mirrors is stationary while the other mirror is movable. The two beams that are reflected from these mirrors then merge to form one beam, which is the product of the interference between the two beams. By changing the position of the movable mirror at constant velocity over a fixed distance, the optical path difference between the two beams is changed. As the mirror is moved each wavelength of the collected beam is modulated as a function of frequency. All the wavelengths that make up the source are collected to form an interferogram. This interferogram is a coded representation of the sample spectrum which is then decoded by applying a Fourier transformation to produce the IR spectrum of the sample. The main advantage of using a FTIR spectrometer is the ability to collect numerous average scans in a short amount of time which helps to increase the signal-to-noise ratio of the final spectrum. More information on the principles of FTIR spectrometer can be found in Ref.3.

## 2.4 X-ray Absorption Spectroscopy

X-ray absorption spectroscopy is a very broad term which refers to several techniques that involve X-ray absorption. This thesis utilises two of these techniques: X-ray absorption near edge structure (XANES) and X-ray excited optical luminescence (XEOL). These measurements were conducted using synchrotron radiation at the Canadian Light Source (CLS). Synchrotron radiation (SR) is highly collimated electromagnetic radiation that is emitted tangentially due to any change in the direction of the relativistically travelling charged particle, typically an electron. The radiated power produced is defined by the Larmor equation:

$$P = \left(\frac{2}{3}\right)\left(\frac{e^2}{m^2c^3}\right)\left(\frac{dp}{dt}\right)^2 \tag{2. 1}$$

where $p$ is the relativistic momentum, $m$ is the mass of the electron, $c$ is the speed of light and $e$ is electron charge. This equation can be expressed in terms of the rest mass of the electron and the relativistic energy $E$ (in GeV) of the electron bent by a magnetic field with a radius of curvature $\rho$ as follows:[4]

$$P = \frac{2e^2cE^4}{3(m_oc^2)^2\rho^2} \tag{2. 2}$$

The theory behind SR can be traced back to the discovery of the electron and the work of Larmor in 1897. Larmor was who derived an expression for the total power radiated by the acceleration of a charged particle. The first observation of SR was at the General Electric Research Laboratory in 1947 where at the time this radiation was viewed as a nuisance since it caused the particles to lose energy during high-energy physics experiments. However, later in the 1960s, it was recognised that SR was superior to X-ray tubes as this type of radiation was extremely bright. Considering the potential use of SR, the first SR source became operational in 1968.[5] This type of

synchrotron facility is referred to as a first generation synchrotron with synchrotron experiments being performed parasitically to high-energy particle physics experiments. The generation of a synchrotron source is determined based on the technology used to produce the SR. Second generation synchrotrons utilised bending magnets to produce SR with the first facility being built in 1980 in Daresbury, UK. The third generation of synchrotron sources utilises an array of magnets known as insertion devices. These insertion devices cause the electrons to wiggle which generates an even brighter light than the previous generation.[6]

The CLS is referred to as a third-generation synchrotron facility as it utilizes these insertion devices. The layout of this facility is shown in Fig.2.1. The electrons are produced using an electron gun. These electrons are then accelerated to 99.999998% of the speed of light using a linear accelerator (LINAC). After passing from the LINAC, the electrons then travel to the booster ring where the energy of the electrons is raised to 2900MeV using a specially designed radio frequency cavity. Afterward, the electrons are then transferred to the storage ring where they emit light every time their path is bent by bending magnets at curved sections of the storage ring. In the straight section of the storage ring, the electrons pass through the insertion devices (such as wigglers and undulators) which increase the beam's brightness before it enters the beamline. Wigglers and undulators are devices that consist of periodically arranged dipole magnets which produce an alternating magnetic field that deflects the electron beam sinusoidally. This oscillation of the electron beam causes the electron to emit radiation at every point within the device that the electron beam direction is changed. These emission cones then add up to increase the intensity of the beam.

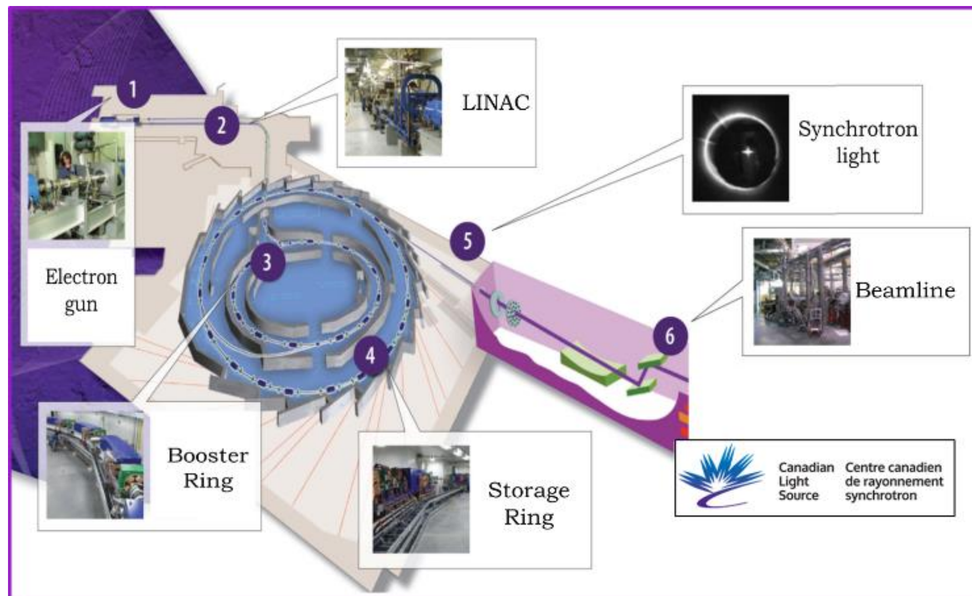


**Fig.2.1:** Schematic of synchrotron facility (modified image from CLS website see ref. 7).[7]

### 2.4.1 X-ray Absorption Near-Edge Structure (XANES)

When light interacts with matter, it can either be scattered, partially or totally absorbed. The absorption of light in matter is defined by Beer's law which relates the incident light intensity to the amount of light transmitted through the material, see equation 2.3.

$$I = I_o e^{-\mu t} \tag{2. 3}$$

where $I_o$ is the incident light intensity, $t$ is the thickness of the material and $\mu$ is the absorption coefficient. X-ray absorption near edge structure (XANES), or near edge X-ray absorption fine structure (NEXAFS) as it is also known, probes the change in the absorption coefficient as a function of the incident X-ray energy.[8] When the incident X-ray energy is equal to or greater than the binding energy of a core electron of the atom of interest, there is a sharp increase in the absorption coefficient ($\mu$). This increase in $\mu$ is referred to as the rising edge and is caused by the promotion of a core electron

to a previously unoccupied bound state, quasi-bound state, or the continuum. The XANES region of the absorption spectra stretches from the rising edge to ~50eV above the rising edge, as shown in Fig.2.2. The region below the rising edge is referred to as the pre-edge region. These pre-edge features are caused by electrons transitioning to empty bound states. Above the XANES region (from ~50eV to ~1000+eV) is known as the extended X-ray absorption fine structure (EXAFS) region.

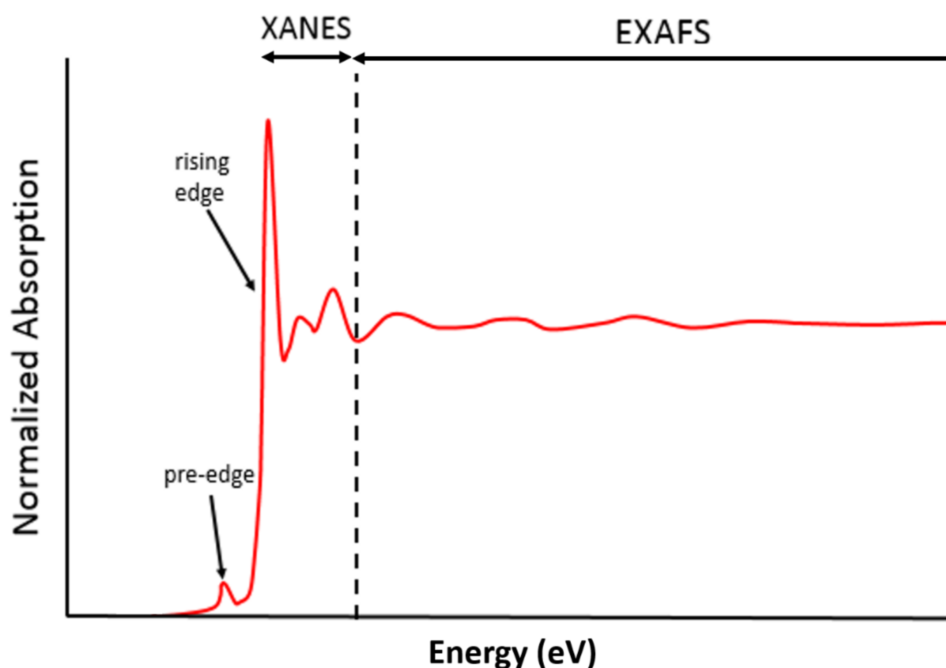


**Fig.2.2:** Illustration of normalized X-ray absorption spectrum showing the pre-edge, rising edge, XANES region and EXAFS region.

The exact location of the rising edge is dependent on many factors, one of which is the orbital location of the excited electron. This is because the X-ray absorption spectroscopy (XAS) spectrum is basically a reflection of the density of states (DOS) of the conduction band (CB) as core electrons are excited to the conduction band (or Fermi level in the case of metals). XANES, in other words, is a probe of the angular

momentum of unoccupied electronic states. Based on quantum selection rules there must be a change in orbital angular momentum quantum number:

$$\Delta l = \pm 1 \; ; \; \Delta n \neq 0 \; ; \; \Delta j = 0, \pm 1 \tag{2.4}$$

where $n$ is the principal quantum number; $l$ is the orbital angular momentum quantum number ($l$ = 0, 1, 2, and 3 refer to the s, p, d, and f orbitals, respectively), and $j$ is the total angular momentum quantum number.

As a consequence of these rules, we are only able to probe the partial DOS (PDOS). In spectroscopic notation, K, L, M, N and O edges refer to the principal quantum number $n$=1, 2, 3, 4 and 5 core levels respectively. An electron from the K-edge, $n$ = 0 and $l$ = 0 (1s orbital), would have a final state of $l$ = 1 (2p orbital). At the L-edge, the initial state is either the 2s or 2p orbital. For 2s transitions, the final state would be a p orbital which is known as the $L_1$ -edge. On the other hand, 2p orbital spin-orbit coupling gives rise to the $2p_{1/2}$ and $2p_{3/2}$ level transition to s and d orbitals. This edge is typically referred to as the $L_{2,3}$-edge as it refers to sublevels of the 2p orbitals.

The absorption coefficient can either be measured directly by taking measurements in transmission mode or indirectly by measuring the electron or fluorescence yield, as shown in Fig.2.3.[8, 9] In transmission mode both the incoming beam and the transmitted beam are measured and the absorption coefficient can be calculated using equation 2.3. For samples not suitable for transmission mode other modes must be used. In fluorescence yield mode, the intensity of fluorescence X-rays ($I_f$), which are a decay product of the absorbed incident beam, is measured using either Si or Ge solid-state detectors. Instead of measuring the fluorescence, the electrons emitted ($I_{ey}$) from the material can be measured in electron yield mode. The electron

yield mode is very surface sensitive due to the short mean free path of the electrons in the solid.

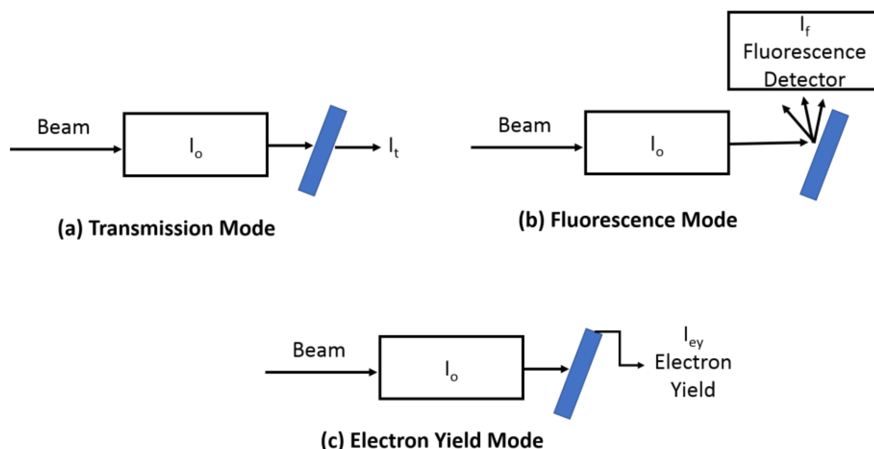


**Fig.2.3:** Schematic of different XAS detection modes (a) transmission, (b) fluorescence and (c) electron yield mode.

### 2.4.2 X-ray Excited Optical Luminescence (XEOL)

XEOL is a measure of the optical emission produced due to radiative recombination. This occurs after an electron is excited to the bottom of the conduction band (CB) by an incident X-ray. This, in turn, produces a hole in the valence band (VB). This electron-hole pair then recombines either radiatively to produce a photon or non-radiatively to produce a phonon. The concept of XEOL is very similar to conventional PL which uses a laser instead of a synchrotron source to excite electrons. Since the X-ray used in XEOL supplies sufficient energy to promote core electrons, the luminescence observed is associated with the absorption process of the core electrons. The tunable X-ray source used in XEOL allows for different deexcitation pathways to be explored.

### 2.4.3 XAS Beamlines at the Canadian Light Source Synchrotron Facility

The results presented in this thesis were conducted at the High Resolution Spherical Grating Monochromator (SGM) 11ID-1 beamline, the Variable Line Spacing Plane Grating Monochromator (VLS PGM) 11ID-2 beamline using end station A or the Soft X-ray Microcharacterization Beamline (SXRMB) beamline. Schematics of these two beamlines are shown in Fig.2.4.[10, 11]

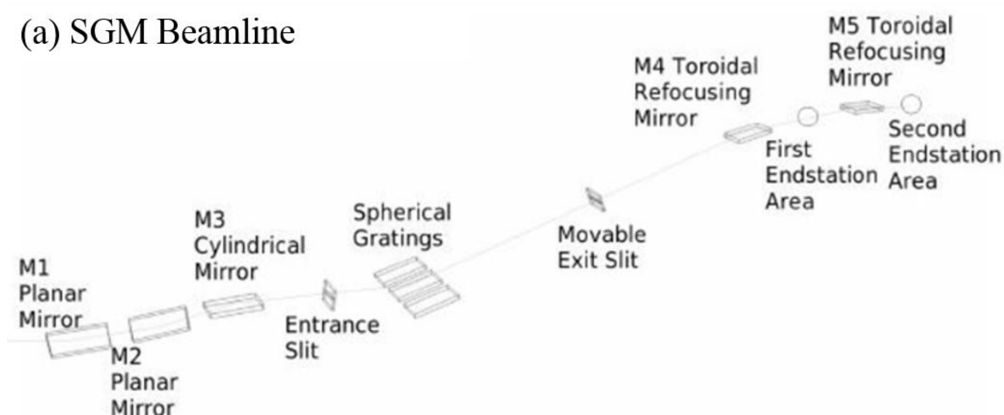


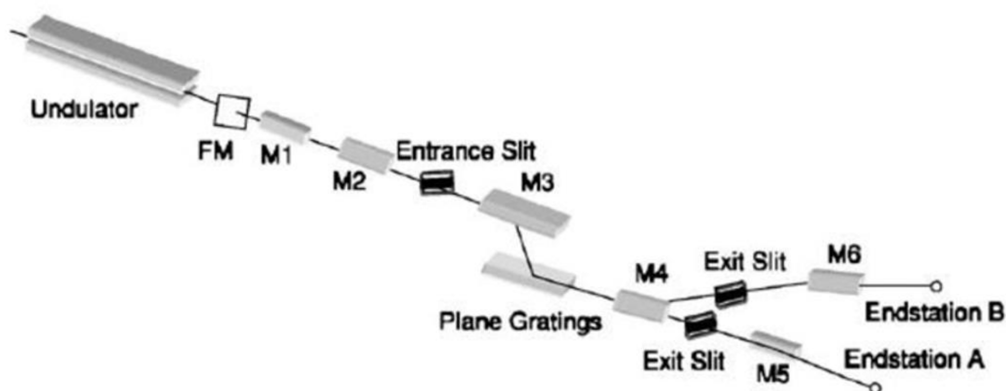


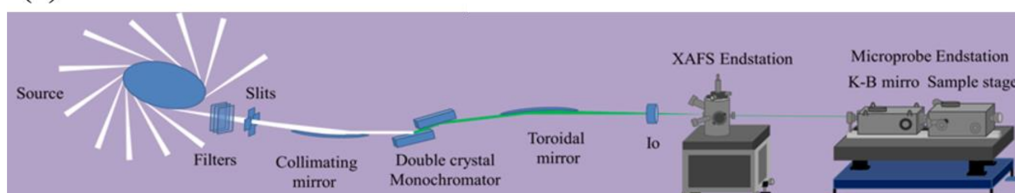


**Fig.2.4:** Layout of (a) SGM beamline, (b) VLS-PGM and (c) SXRMB beamline at the CLS.[11-13]

The SGM beamline at the CLS has an energy range of 250-2000 eV, a typical energy resolution of $2\times10^{-4}$ E/ΔE and beam size of 1000×100μm. This beamline features a 45mm planar undulator and three diffraction gratings: (1) low grating for 250-700 eV, (2) medium grating for 450-1250 eV and (3) high grating for 740-2000 eV. XANES and XEOL measurements at the Si, Al, N and O K-edges were collected using the SGM beamline. For the Si and Al K-edges, the high grating (1700 lines/mm) was used to maximize photon flux. For the N and O K-edges, the low grating was used for similar reasons. For XANES measurements at the Si K-edge, we restricted our measurements to the total electron yield (TEY) to eliminate any signal coming from the Si substrates used in most of the samples studied.

The VLS-PGM beamline has an energy range of 5-250 eV with a typical resolution >10000 E/ΔE and spot size of 500×~500 μm. This beamline is equipped with of three diffraction gratings which are: (1) low grating ranging from 5-38 eV, (2) medium grating for 25-120 eV and (3) high grating for 90-250 eV. On this beamline, the XANES spectra at the Si and Al $L_{2,3}$-edges were measured. For measurements at the Si $L_{2,3}$- edge the high grating was used, while for the Al $L_{2,3}$- edge the medium grating was selected. The SXRMB beamline has an energy range of 1.7 – 10keV with a typical resolution of $3.3 \times 10^{-4}$ E/ΔE and beam spot size of ~1 × 4 mm. This beamline was used for measuring the Si K-edge.

## 2.5 Rutherford Backscattering Spectroscopy (RBS)

Rutherford Backscattering spectroscopy is a non-destructive ion-beam analysis technique that is useful for determining film composition, stoichiometry and thickness. In RBS, samples are bombarded with light ions, such as $H^+$ or $He^+$, at an energy ($E_0$) in

the MeV range, and then the energy of the backscattered ions ($E_1$) is measured. A schematic of this interaction is shown in Fig.2.5.[14]

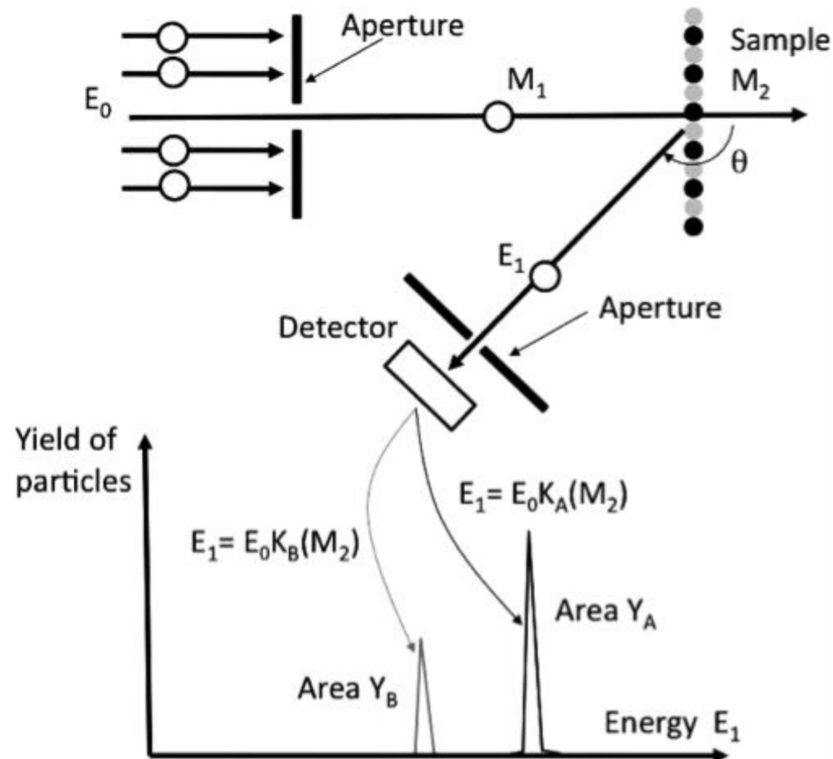


**Fig.2.5:** Schematic of RBS and example of RBS spectrum for a sample with two elements A and B. The RBS system consists of an incident ion of mass $M_1$ while $K_B$ and $K_A$ are the kinematic factors of the elements A and B, respectively. The mass of A is greater than B hence the energy of the backscattered ion from A is higher than B. From ref. 14.

The energy of the backscattered projectile is linearly proportional to the incident energy of the ion ($E_0$):[15, 16]

$$E_1 = KE_0 \tag{2. 5}$$

$$K = \left[\frac{(M_2^2 - M_1^2 \sin^2\theta)^{\frac{1}{2}} + M_1 \cos\theta}{M_2 + M_1}\right]^2 \tag{2. 6}$$

where $K$ is known as the kinematic factor for RBS, $M_1$ is the mass of the lighter incident ion, $M_2$ is the mass of the target atom, and $\theta$ is the backscattering angle. The kinematic factor relates the mass of the incident ion to the mass of the target nucleus which allows for the mass of the target nucleus to be determined. Other physical concepts that need to be taken into account when converting the RBS spectra to a quantitative profile are: (1) the differential scattering cross-section, (2) the stopping power (cross-section), and (3) energy straggling.[16]

The RBS measurements presented in this thesis were taken at the Tandetron Facility at the University of Western Ontario. Spectra were obtained using 500 keV $^4He^+$ ions, with a Si charged particle detector at 170°. In addition to the samples studied in this thesis, the RBS spectra for a Sb-implanted amorphous Si sample with a known total Sb content of $4.82\times10^{15}$ atoms/cm$^2$ was measured to calibrate the detector solid angle. RBS spectra measurements were analysed using SIMNRA software.[17]

## 2.6 Elastic Recoil Detection (ERD)

Elastic recoil detection is an ion-beam analysis technique that uses incident ions to forward scatter light target atoms (atomic number 1 to 9). ERD can be separated into two groups: (1) light ion ERD and (2) heavy ion ERD (Hi-ERD). For light incident ion ERD, typically low energy (~2-3MeV) $^4He+$ ions are used to depth profile hydrogen and deuterium.[18] For Hi-ERD, high energy (hundreds of MeV) heavy ions such as Cl and Au are used. In Hi-ERD, there is also a need for a mass sensitive detector to identify the recoil atoms. The ERD measurements presented in this thesis are light ion ERD. The schematic of ERD is shown in Fig.2.6.

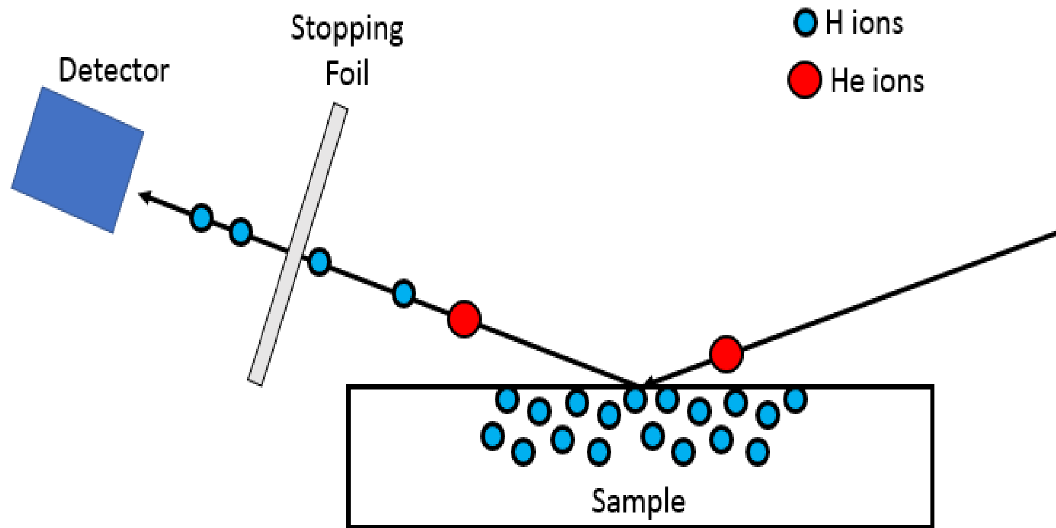


**Fig.2.6:** Schematic of ERD setup with incident He ions in red and detected H ions in blue.

Like RBS, kinematics of ERD is a classic two-body collision problem and the equation relating the incident energy ($E_o$) to scattered energy ($E_1$) is given by:

$$E_1 = \left[\frac{(M_2^2 - M_1^2 \sin^2\theta)^{\frac{1}{2}} \pm M_1 \cos\theta}{M_2 + M_1}\right]^2 E_0 \tag{2.7}$$

when the $M_1 < M_2$, we use the '+' which gives us equation 2.6, for RBS. On the other hand, when $M_1 > M_2$ then we can derive the following equations (details can be found in Ref. 18):[18]

$$E_1 = kE_0 \tag{2.8}$$

$$k = \frac{4M_1 M_2 \cos^2\theta}{(M_1 + M_2)^2} \tag{2.9}$$

where $k$ is known as the kinematic factor for ERD.

ERD measurements were also conducted at the Tandetron facility at The University of Western Ontario. A 1.6 MeV $^{4}He^{+}$ ion beam was used to obtain the H concentrations and depth profiles in samples. For ERD measurements an incident angle of 75°, a recoil angle of 30° and a 6.1 μm Al-coated mylar range foil was used. Kapton ($C_{22}H_{10}N_2O_5$) tape was used as a standard to determine the detector solid angle.

## 2.7 Particle Induced X-ray Emission (PIXE)

PIXE utilizes high energy protons or alpha particles to eject electrons from the innermost shell of the target atoms. This forms a hole in this shell which is later filled by an electron in an outer shell. This may result in either characteristic X-rays being produced or Auger electrons being emitted. PIXE is a spectrum of the emitted X-rays where the energy of the X-ray is equal to the difference between the binding energy of the inner shell electron and that of the outer shell electron. The characteristic X-ray produced in PIXE are collected by a highly sensitive energy dispersive detector. Typically, PIXE is only able to measure elements with an atomic number that is greater than 11. Moseley law relates the X-ray energy to the atomic number of the emitting atom.[19] The energies of the K- and L-series X-ray lines are given by the following equations:

$$E_{K-series} = \left(\frac{3}{4}\right)(Z-\sigma)^2 E_f \tag{2. 10}$$

$$E_{L-series} = \left(\frac{5}{36}\right)(Z-\sigma)^2 E_f \tag{2. 11}$$

where $E_f = 13.6eV$ is the ionization energy of the hydrogen atom, $Z$ is the atomic number of the element in the target and $\sigma$ is the screening constant.

## 2.8 Ion Implantation

Ion implantation is a technique that is used to introduce controlled amounts of impurities ions into a material. In this technique, incident ions are accelerated into the target material. The process of ion implantation can be divided into four parts: (1) source ionization, (2) ion selection, (3) ion acceleration and (4) implantation. The schematic of a typical ion implanter is shown in Fig.2.7.

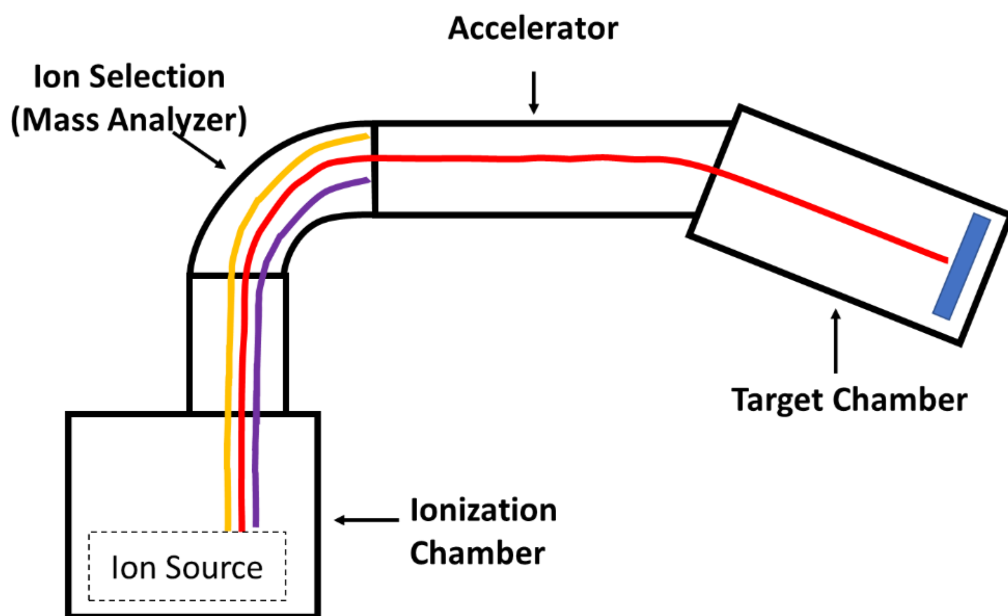


**Fig.2.7:** Schematic of the ion implantation system.

Source ionization requires that the material being implanted is in the gaseous state. This can be done by either using a low-pressure gas source (e.g. boron trifluoride ($BF_3$) gas for boron implantation) or by heating a solid ion source (e.g. phosphorus pentoxide ($P_4O_{10}$) for implanting phosphorous). In the ionization chamber of the ion implanter, a tungsten filament is heated under low pressure. This heated filament then emits electrons, which when hot enough ionize the gaseous ion source. Since other

secondary ions from the gas are produced in addition to the ion of interest, there is a need for ion selection. Ion selection is done by using a bending analyser magnet which selects the ion with the desired charge-to-mass ratio. This is achieved by placing an aperture at the end of the analyser. The desired ion can be selected based on the following equation:

$$r_0 = \left(\frac{1}{H}\right)\left(\frac{2mV_e}{q}\right)^{\frac{1}{2}} \quad (2.\ 12)$$

where $r_0$ is the radius of curvature of the ion in bending analyser magnet, $H$ is the magnetic field, $m$ is the ion mass number, $V_e$ is the applied voltage, and $q$ is the ion charge state. When these desired ions emerge from the analyser, they do not have enough energy to penetrate the sample. For these ions to gain sufficient energy, they must pass through the acceleration tube. The ion beam can then be focused using a quadrupole triplet magnet. For large implantation areas, an electromagnetic two-dimensional beam deflector (X-Y scanner plates) is used to maintain homogeneous exposure of the beam.

### 2.8.1 Stopping Power

When ions are implanted into a target material, it gradually loses energy as it collides with atoms in the target and stops inside of the crystal lattice. There are two stopping mechanisms which are (1) nuclear stopping and (2) electronic stopping. Nuclear stopping occurs when the dopant ion collides with the nuclei of a target atom causing this atom to recoil from its lattice position. This type of stopping produces lattice disorder and is responsible for most of the damage caused to the lattice structure

of the target material. The nuclear stopping power ($S_n$) is given by the following equation:[15]

$$S_n = \left.\frac{dE}{dx}\right|_n = N \int_{T_{min}}^{T_M} T \frac{d\sigma(E)}{dT} dT \tag{2. 13}$$

where $\frac{dE}{dx}$ is the energy-loss rate, $\frac{d\sigma(E)}{dT}$ is the energy-transfer differential cross-section, $T_{min}$ is the minimum energy-transferred, and $T_M = \frac{4M_1M_2E}{(M_1+M_2)^2}$ is the maximum transfer energy.

Electronic stopping occurs when the dopant ion interacts with the electrons of the target atoms. In this type of stopping, energy is transferred through the electron cloud as thermal vibrations. The electronic stopping power is expressed as[15]

$$S_e = \left.\frac{dE}{dx}\right|_e \tag{2. 14}$$

The total stopping power of the target ($S$) is given by the sum of the nuclear and electronic stopping power. Nuclear stopping is dominant at low energy and high atomic number while electronic stopping takes over at high energy and low atomic number.

### 2.8.2 Ion Range and Straggle

The integrated distance that the dopant ion travels before stopping is known as the range ($R$) while the net penetration depth into the material is called the projected range ($R_p$). Since the process of ion stopping is stochastic, the projected range varies from ion to ion even when the implantation conditions are the same. This results in a statistically broad spread in the projected ion range referred to as the range distribution.

The range distribution in cm$^{-2}$, $N(x)$, normalized to the ion implantation dose of $\phi_i$ is given by[15]

$$N(x) = \frac{\phi_i}{\Delta R_p (2\pi)^{\frac{1}{2}}} \exp\left[-\frac{1}{2}\left(\frac{x - R_p}{\Delta R_p}\right)^2\right] \tag{2. 15}$$

where $R_p$ is the projected range, $\Delta R_p$ is the projected range straggling (i.e. standard deviation of the range distribution), and the ion implantation dose $\phi_i$ is related to the ion implantation depth by[15]

$$\phi_i = \int_{-\infty}^{\infty} N(x) dx \tag{2. 16}$$

The peak atomic density for a given ion implantation dose can be determined using the following equation:[15]

$$N(x = R_p) = N_p = \frac{\phi_i}{\Delta R_p (2\pi)^{\frac{1}{2}}} \cong \frac{0.4\phi_i}{\Delta R_p} \tag{2. 17}$$

The concentration of implanted ions ($C_p$) in atomic percentage at the projected range is related to the peak atomic density at a given dose as[15]

$$C_p = \frac{N_p}{N_p + N} \tag{2. 18}$$

### 2.8.3 Displacements and Radiation Damage

When the energy of an incident ion is great enough to displace an atom, the displaced target atom leaves a vacancy and occupies an interstitial site within the target lattice. This type of defect is referred to as a Frenkel defect (or a Frenkel pair). The displaced target atom is referred to as a primary knock-on atom (or PKA) which can, in turn, displace other atoms in the target lattice thus creating a collision cascade. The

following equation can be used to approximate the displacement per atom ($dpa$) for a given dose ($\phi$):[20]

$$dpa \cong \frac{0.8\langle N_d(E)\rangle}{NR}\phi \qquad (2.\,19)$$

where $\langle N_d(E)\rangle$ is the mean number of displacements, $E$ is the energy of the incident ion, $N$ is the atomic density and $R$ is the ion range. When the energy of the PKA is greater than the displacement energy ($E_d$) but less than $2E_d$, then the PKA atom would fill the vacant lattice site left by the displaced target atom which is known as a replacement collision. These replacement collisions cause greater disorder in polyatomic targets than in monoatomic targets.

### 2.8.4 Defects due to Ion implantation

As mentioned previously, ion implantation can cause disorder in the target material. In this section, we will briefly discuss some types of defects that can be present in a material which includes: point defects, line defects, planar defects and volume defects.

*Point Defects*

Point defects can either be intrinsic, meaning that they are formed in the material without any external influence such as irradiation damage or impurity-related defects caused by the introduction of an impurity ion into the material. Intrinsic point defects can either be vacancies, which is an empty lattice site, or self-interstitial which is a native atom that is lodge between lattice sites. Impurity-related defects can be substitutional in which case the impurity is located in a lattice site, or they can occupy interstitial locations.[21]

*Line Defects*

Line defects (or dislocations) are 1-D defects that are irregularities along a line in the crystal structure where there is an abrupt change in the ordering of atoms along a line. Dislocations can be subdivided into edge dislocations and screw dislocations. An edge dislocation can be described as an extra incomplete plane being inserted into the lattice thus atoms above the dislocation line are compressed while those below the dislocation line experience tensile stress.[22] Unlike the edge dislocation which moves parallel to the shear stress, a screw dislocation moves perpendicular to the stress and atom displacement.

*Planar defects*

Planar defects are 2-D imperfections that are discontinuities in the crystal lattice across the plane.[22] This occurs due to the clustering of line defects in the plane. One type of planar defect is a grain boundary, which is where one crystallite ends, and another begins. Grain boundaries can either be subdivided into tilt boundaries or twist boundaries. A tilt boundary arises because of an edge dislocation while a twist boundary is caused by screw dislocations. There are also high and low angle grain boundaries which are defined by the degree of disorientation with angles less than 10° for low angle and great than 15° for high angle grain boundaries.

*Volume defects*

Though volume defects are on a much larger scale than other defects for the sake of completeness, we will briefly discuss this type of defect. Volume defects are 3-D defects which include phase variations and voids (or pores).[22] Phase defects are the result of impurities atoms clustering to form a different phase. Voids occur when many atoms are missing from a region in the lattice.

### 2.8.5 Diffusion of Implanted Ions

During the annealing process, implanted ions would migrate from regions of high concentrations to regions of lower concentration. In a 1-D system, the flux of atoms is defined by Fick's first law of diffusion which is expressed as follows:[23]

$$F = -D\frac{\partial C}{\partial x}, \qquad D = D_o \exp\left(-\frac{E_A}{kT}\right) \tag{2.20}$$

where $\frac{\partial C}{\partial x}$ is the concentration gradient, $D$ is diffusivity, $D_o$ is proportionality constant, $k$ is the Boltzmann constant, $T$ is the absolute temperature, $x$ is depth, and $E_A$ is the activation energy. Fick's second law of diffusion in the case of constant D is expressed as[21]

$$\frac{\delta C}{\delta t} = -D\frac{\delta^2 C}{\delta x^2} \tag{2.21}$$

where $t$ is time and $C$ is concentration. To solve the above equation the appropriate initial boundary conditions must be applied. There are two simplified cases of diffusion. The first of which is constant source diffusion in which the concentration of the dopant is kept constant. The second case is limited source diffusion in which the total quantity of dopants introduced is constant. For ion implantation, the solution of limited source diffusion is used and given by[21]

$$C(x,t) = \frac{Q}{\sqrt{\pi D t}} \exp\left(-\frac{x^2}{4Dt}\right) \tag{2.22}$$

where $Q$ is the total number of dopant atoms.

### 2.8.6 Irradiation-Enhanced Diffusion

The diffusion of dopant ions can be enhanced by ion implantation due to Frenkel pairs produced in this process. This is because the diffusivity is proportional to the defect concentration in the material. The excess vacancies produced during ion implantation aid in atomic motion by the interchange between atoms and neighbouring vacancies. The vacancy-driven atomic diffusion coefficient is defined as follows:[21]

$$D_v = \frac{f_v C_v \Gamma_v d^2}{6} \tag{2.23}$$

where $f_v$ is the correlation factor, $C_v$ is the vacancy concentration, $\Gamma_v$ vacancy jump frequency and $d$ is the atomic jump distance. To account for the diffusion due to the various types of point defects, the diffusion coefficient is given by the general expression:[21]

$$D = f_i C_i D_i + f_v C_v D_v + \cdots \tag{2.24}$$

where $f_i$ , $C_i$ and $D_v$ are correlation factor, vacancy concentration and diffusion coefficient related to interstitials. Based on this equation, it is clear to see that an increase in the number of defects caused by implantation leads to an increased diffusion.

## 2.9 Positron Annihilation Spectroscopy (PAS)

A positron is the antiparticle of the electron. When positron diffuse in a material is can be captured by trapping sites. This trapping occurs because positrons are sensitive to the electron density and the electron momentum distribution in the material. Since the electron density and momentum of defects are different to that of a perfect lattice, positrons provide a means of study the type and concentration of defects in a material.

It is possible for positrons and electrons to annihilate and have their total energy be transferred to photons. The main interaction between positrons and electrons is the two-photon annihilation. Momentum is conserved when the positron-electron pair annihilates by the production of two gamma rays. The energy of each of these gamma rays is 511keV, and they are emitted in opposite directions.[24]

There are three different measuring techniques for positron annihilation spectroscopy (PAS) which are: (1) positron lifetime spectroscopy, (2) angular correlation spectroscopy and (3) Doppler broadening spectroscopy. Positron lifetime spectroscopy utilizes the sensitivity of positrons to the electron density of the sample. While angular correlation and Doppler broadening spectroscopy exploit the sensitivity of the positron to electron momentum distribution. For this thesis, PAS results were collected using the Doppler broadening method which will be discussed below. This section will also discuss the type of positron source used, the interaction of positrons in matter and the Doppler broadening method.

### 2.9.1 Positron Source

Conventionally, positrons for PAS are obtained from the $\beta^{+}$-decay of radioactive isotopes. Typically, the isotope used is a $^{22}Na$ source which gives a high positron yield. The decay process of this isotope is shown in Fig.2.8. To prepare the positron source, a solution of a sodium compound such as $^{22}NaCl$ is deposited on to Kapton film.[25] Once dried this film is then sandwiched between thin metal films. The metal films have two advantages the first of which is that it can prevent the leakage of activity. The other advantage is that the metal has a negative work function on the positron which slows down the fast positrons (from few hundreds of keV to a few keV). These slower

positrons can then be magnetically steered toward the target and electrostatically accelerated to produce a variable-energy positron beam which would allow for depth profiling.[26]

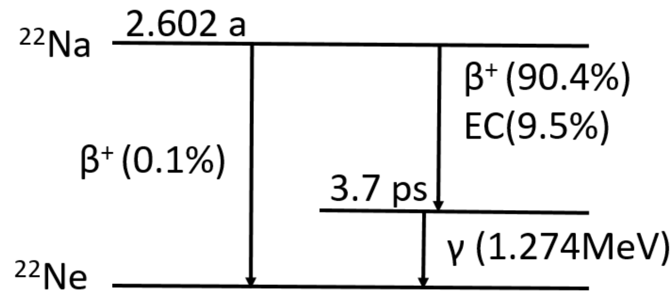


**Fig.2.8:** Decay scheme of $^{22}$Na to $^{22}$Ne.

### 2.9.2 Interaction of Positrons with Matter

A positron incident on a target can either backscatter or penetrate the surface of the material. When the positron of a certain incident energy enters the target material, it will lose energy as it diffuses through the material until it annihilates. The implantation profile of positrons is called the Makhov profile and is defined as follows:[27, 28]

$$P(z,E) = \alpha\, e^{-\alpha x}, \alpha \approx \frac{40}{\rho\left(\frac{g}{cm^2}\right)} E(keV)^{1.6} \tag{2.25}$$

where $P(z,E)$ penetration profile, $\alpha$ absorption coefficient, $\rho$ is the material density (g/cm$^3$), $E$ is the beam energy (keV), and z is the probing depth (nm). As shown in Fig.2.9, the implantation profile is much broader for high energy positrons than low energy positrons. In the presence of point defects within the material, the effective diffusion length is expressed as follows:[21]

$$L_{eff}^{+} = \sqrt{\frac{D^{+}}{\gamma_L + K_d}}, K_d = \mu_d c_d \tag{2.26}$$

where $D^{+}$ is positron diffusivity, $\gamma_L$ is the positron annihilation rate, $K_d$ is the trapping rate of positrons in the point defects, $\mu_d$ is the trapping coefficient, and $c_d$ is the defect concentration. The trapping coefficient is constant for a given defect.

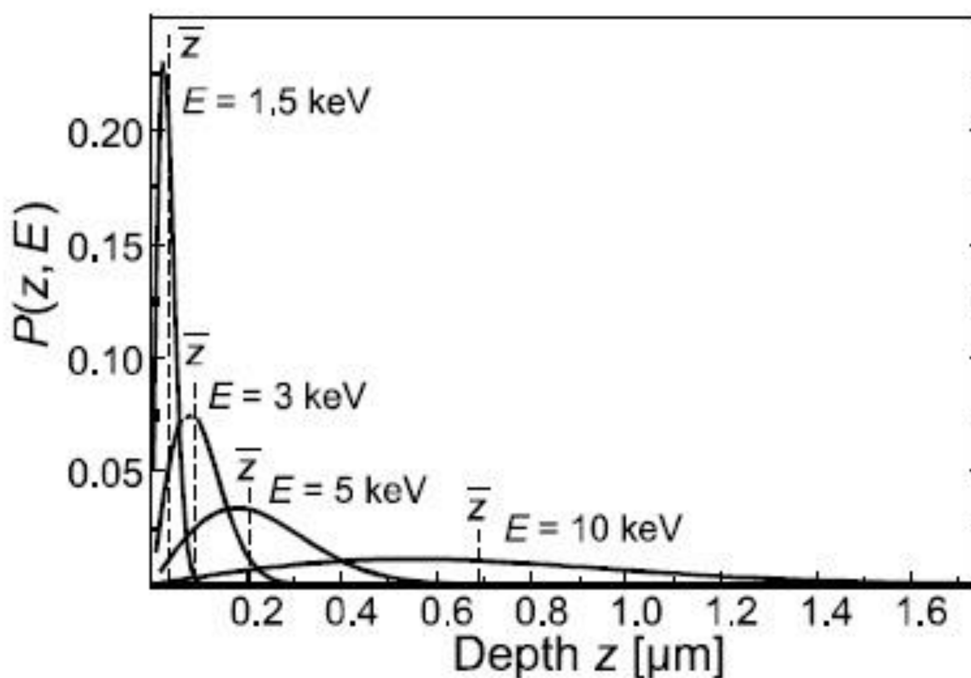


**Fig.2.9:** The penetration depth profile $P(z, E)$ for positrons with four different energies in Si. Dotted lines show the mean penetration depth ($\bar{z}$) with the associated energy written next to it.[24]

### 2.9.3 Positronium Formation

Positronium (Ps) is the bound state of an electron and positron. The formation of positronium occurs when the positron is captured by an electron before the positron and electron can annihilate with each other. Based on the spin orientation of the positron

and electron, two different positronium states are possible, which are ortho-positronium (o-Ps) with parallel spins and para-positronium (p-Ps) with antiparallel spins. In an amorphous material, the o-Ps interacts with electrons outside the positronium and annihilate to produce two gamma rays. This process is called 'pick-off' annihilation.[24]

### 2.9.4 Doppler Broadening Method

As mentioned above the Doppler broadening method relies on the sensitivity of the positron to the electron momentum distribution in the sample. Annihilation radiation is produced to conserve the momentum distribution of the electron-hole pair. The Doppler-broadening spectrum is produced because there is a small Doppler shift in the annihilation energy. The Doppler shift of the annihilation energy is given by[24]:

$$\Delta E = \frac{p_z c}{2} \tag{2.27}$$

where $p_z$ is the momentum component in the propagation direction of the $\gamma$-rays and c is the speed of light. The collection of these annihilation events is what makes up the Doppler-broadening spectrum.

In a Doppler-broadening spectrometer, the annihilation photons are collected using high purity Ge detectors with high energy resolution. The signal from the detectors is processed by the pre-amplifier that is integrated into the detectors. These events are then stored in the multi-channel analyser memory (MCA). To reduce background noise, both gamma rays are collected. The use of a second Ge detector improves the energy resolution by a factor of $\sqrt{2}$. A schematic of a typical Doppler broadening system is shown in Fig.2.10.

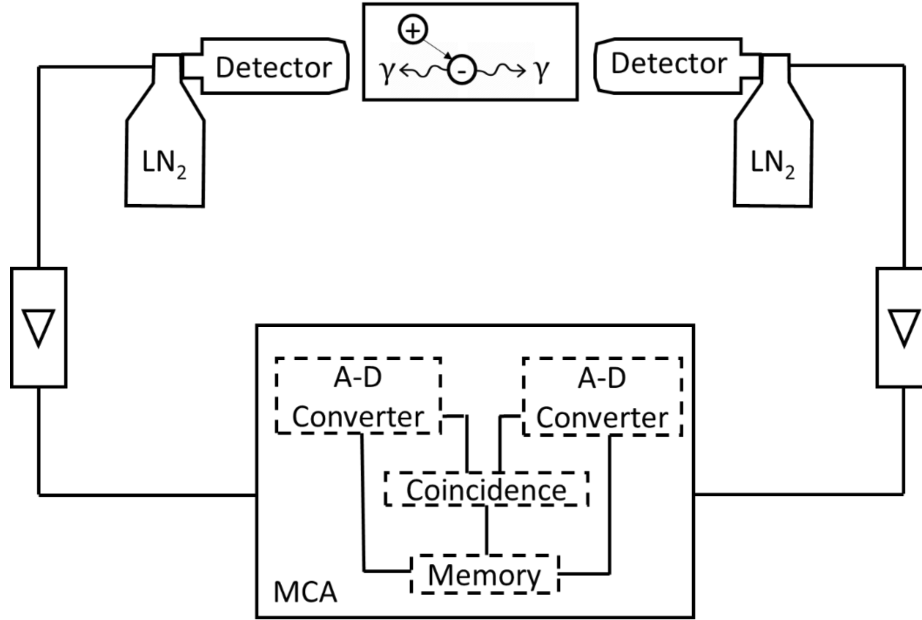


**Fig.2.10:** Schematic of a typical Doppler broadening setup using the coincidence technique. Emitted gamma rays are collected using liquid nitrogen cooled Ge detectors. Based on ref.29.

To extract the information related to the defect concentration in a given sample the Doppler spectrum must be processed. This is carried out by analysing specific line shape parameters known as the S and W parameters. The S parameter is the number of counts in the centre of the spectral peak divided by the number of total counts,[24]

$$S = \frac{N_p}{N_{total}}\,, \qquad N_p = \int_{E_0-\Delta}^{E_0+\Delta} f(E)dE \tag{2.28}$$

where $E_0$ =511keV, $N_p$ is the number of counts in central low-momentum part of the spectrum, and $N_{total}$ is the total number of counts. For calculating the S parameter, symmetric limits are chosen. Typically, limits $E_0 + \Delta$ and $E_0 - \Delta$ are select such that the S parameter value for a close to defect-free material is nearly 0.5.[24] The W-parameter is the number of counts in the two wings of the spectral peak divided by the total number of counts,[24]

$$W = \frac{N_{w1} + N_{w2}}{N_{total}}, \qquad N_{w1,w2} = \int_{E_1}^{E_2} f(E)dE \tag{2.29}$$

where $N_{w1}$ and $N_{w2}$ are the number of counts under the wings as illustrated in Fig.2.11. The W-parameter corresponds to annihilations with core electrons. The limits $E_1$ and $E_2$ must be select such that there is no overlap between these limits and those selected for the determination of the S parameter. In other words, the centroid region used for calculating the S parameter cannot overlap with wing regions used calculating the W parameter, similar to what is illustrated in Fig.2.11. It should be noted that the S and W parameter values collected using different spectrometer cannot be directly compared due to a large statistical error between the resolution of different spectrometers.

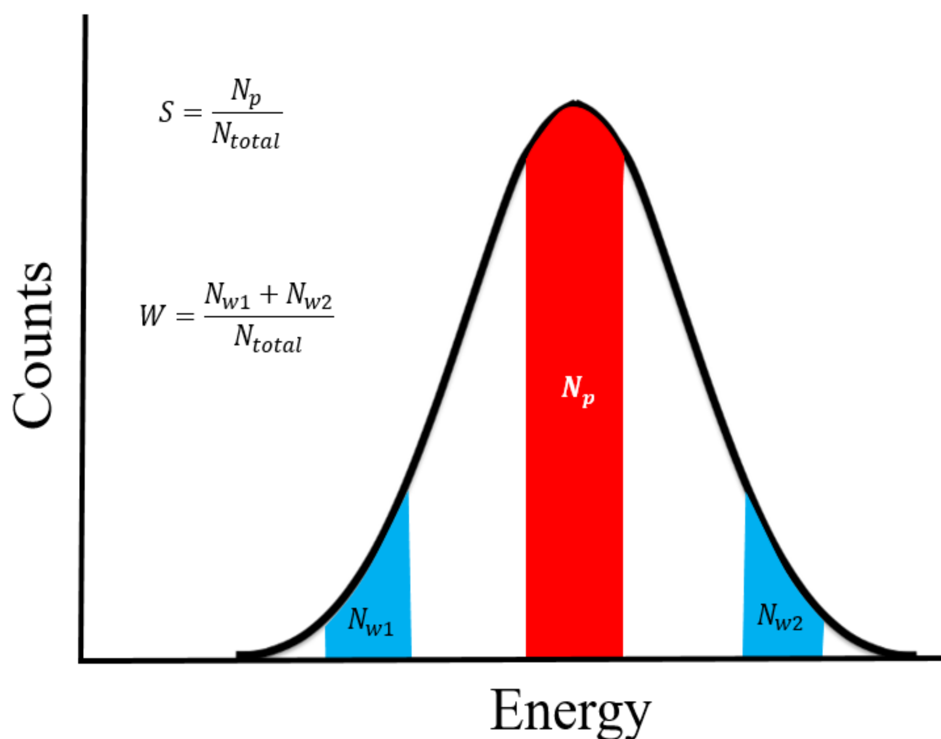


**Fig.2.11:** Illustration of Doppler broadening peak highlighting the regions of the spectrum used for determining the S and W parameters. The total number of counts ($N_p$) is shown in red and is used for calculating the S parameter while the number of counts in the wing regions ($N_{w1}$ and $N_{w2}$) shown in blue are used for calculating the W-parameter.

## 2.10 References

[1] S. Shionoya, "Photoluminescence," in *Luminescence of Solids*, D. R. Vij, Ed., ed Boston, MA: Springer, 1998.

[2] B. Stuart, *Infrared Spectroscopy: Fundamentals and Applications*: wiley, 2004.

[3] W. M. Doyle, "Principles and Applications of Fourier Transform Infra- red (FTIR) Process Analysis," 2017.

[4] P. Willmott, "Synchrotron Physics," in *An Introduction to Synchrotron Radiation*, ed, 2011.

[5] E.-E. Koch, D. E. Eastman, and Y. Farges, "Synchrotron radiation—A powerful tool in science ." in *Handbook on Synchrotron Radiation*. vol. 88, E.-E. Koch, Ed., ed: Wiley-Blackwell, 1984, pp. 591-592.

[6] A. L. Robinson, "History of Synchrotron Radiation," *Synchrotron Radiation News,* vol. 28, pp. 4-9, 2015.

[7] C. L. Source. (2012). *Canadian Light Source Outreach 2012*.

[8] G. Bunker, *Introduction to XAFS A Practical Guide to X-ray Absorption Fine Structure Spectroscopy*: Cambridge: Cambridge University Press, 2010.

[9] C. S. S. M. Ridgway, *X-Ray Absorption Spectroscopy of Semiconductors*: Springer-Verlag Berlin Heidelberg, 2015.

[10] T. Regier, J. Krochak, T. K. Sham, Y. F. Hu, J. Thompson, and R. I. R. Blyth, "Performance and capabilities of the Canadian Dragon: The SGM beamline at the Canadian Light Source," *Nuclear Instruments and Methods in Physics Research Section A: Accelerators, Spectrometers, Detectors and Associated Equipment,* vol. 582, pp. 93-95, 2007.

[11] Y. F. Hu, L. Zuin, G. Wright, R. Igarashi, M. McKibben, T. Wilson*, et al.*, "Commissioning and performance of the variable line spacing plane grating

monochromator beamline at the Canadian Light Source," *Review of Scientific Instruments,* vol. 78, p. 083109, 2007.

[12] R. Blyth, "Spherical Grating Monochromator (SGM) Beamline 11D-1," CLS2008.

[13] C. L. Source. *Soft X-ray Microcharacterization Beamline: About the Beamline*.

[14] R. Hellborg, H.J., and Whitlow, "Industrial Aspects of Ion Beam Analysis," in *Industrial Accelerators and Their Applications*, Robert W Hamm and M. E. Hamm, Eds., ed: World Scientific, 2012, pp. 183-242.

[15] M. Nastasi, J. W. Mayer, and Y. Wang, *Ion Beam Analysis: Fundamentals and Applications*: CRC Press, 2014.

[16] J. R. Tesmer and M. A. Nastasi, *Handbook of Modern Ion Beam Materials Analysis: Materials Research Society Handbook*: Materials Research Society.

[17] M. Mayer, "SIMNRA, a simulation program for the analysis of NRA, RBS and ERDA," *AIP Conference Proceedings,* vol. 475, pp. 541-544, 1999.

[18] T. Som, S. Dhar, N. Banerji, K. Ramakrishnan, and V. N. Kulkarni, "ERD facility for analysis of hydrogen and deuterium in solids," *Bulletin of Materials Science,* vol. 19, pp. 73-82, 1996.

[19] H. G. J. Moseley, "XCIII. The high-frequency spectra of the elements," *The London, Edinburgh, and Dublin Philosophical Magazine and Journal of Science,* vol. 26, pp. 1024-1034, 1913.

[20] "Displacements and Radiation Damage," in *Ion Implantation and Synthesis of Materials*, M. Nastasi and J. W. Mayer, Eds., ed Berlin, Heidelberg: Springer Berlin Heidelberg, 2006, pp. 77-92.

[21] J. W. M. Michael Nastasi, "Doping, Diffusion and Defects in Ion-Implanted Si," in *Ion Implantation and Synthesis of Materials*, ed, 2006.

[22] R. J. D. Tilley, *Understanding Solids : The Science of Materials*. Somerset, UNITED KINGDOM: Wiley, 2013.

[23] G. H. G. D. R. Poirier, "Fick's Law and Diffusivity of Materials," in *Transport Phenomena in Materials Processing*, ed: Springer, 2016.

[24] R. K.-R. H. S. Leipner, *Positron Annihilation in Semiconductors*: Springer 2003.

[25] R. G. Lovas, "Chemical applications of nuclear reactions and radiations," in *Handbook of Nuclear Chemistry:*, S. N. Attila Vértes, Zoltan Klencsár, Rezső G. Lovas, Ed., ed: Kluwer Academic Publishers, 2003.

[26] B. Y. Tong, "Negative Work Function of Thermal Positrons in Metals," *Physical Review B,* vol. 5, pp. 1436-1439, 1972.

[27] S. Valkealahti and R. M. Nieminen, "Monte-Carlo calculations of keV electron and positron slowing down in solids," *Applied Physics A,* vol. 32, pp. 95-106, 1983.

[28] S. Valkealahti and R. M. Nieminen, "Monte Carlo calculations of keV electron and positron slowing down in solids. II," *Applied Physics A,* vol. 35, pp. 51-59, 1984.

[29] H. S. L. Reinhard Krause-Rehberg, *Positron Annihilation in Semi-conductors: Defect Studies*: Springer Berlin Heidelberg, 1999.

# Chapter 3

# The influence of hydrogen passivation on the luminescence of Si quantum dots embedded in $Si_3N_x$

## 3.1 Introduction

Silicon (Si) dominates the photovoltaic and microelectronic industries. The poor light emission of bulk Si makes it unsuitable for fabricating high efficiency optoelectronic devices, [1] however, it has been shown that low-dimensional Si structures such as quantum dots (QDs) have better optical properties than bulk Si.[2] The transition at the Γ-point in crystalline Si-QDs occurs with a lifetime on the order of picoseconds.[3] This phenomenon makes Si-QDs a better candidate for optoelectronic applications compared to bulk Si. Si-QDs also offer advantages of low cost and lack of toxicity over CdSe or GaAs QDs.[4]

In order to improve the luminescence of Si-QDs for the development of optoelectronic devices various approaches have been explored, ranging from different methods of Si-QD fabrication to rare earth doping. The quantum confinement effect (QCE) is not the only mechanism responsible for the photoluminescence (PL) of Si-QDs: matrix defects and radiative interface structures also contribute to the light emission.[5, 6] A number of publications have focused on Si-QDs formed in $SiO_2$ matrices.[7-9] However, the fabrication of Si-QDs/$SiO_2$ typically requires very high annealing temperatures (> 900°C), making it incompatible with other optoelectronic components, especially those

A version of this chapter has been published. [1]C. C. Cadogan, L. V. Goncharova, P. J. Simpson, P. H. Nguyen, Z. Q. Wang, and T. K. Sham, "Influence of hydrogen passivation on the luminescence of Si quantum dots embedded in $Si_3N_x$," *Journal of Vacuum Science and Technology B: Nanotechnology and Microelectronics,* vol. 34, 2016.

based on Si/Ge.[10] On the other hand, Si-QDs in silicon nitride ($Si_3N_x$) films can be fabricated at temperatures as low as 300ºC.[11] From an electrical perspective, $Si/Si_3N_x$ systems have a lower tunneling barrier (~ 1.9eV) compared to that of $SiO_2$ (3.2eV).[12, 13] The luminescence of $Si_3N_x$ systems due to QCE in the 600-850 nm range, combined with defect luminescence in the green (500-570 nm) and blue (400-500 nm) bands, makes it possible to fabricate full-colour devices. The research presented in this chapter explores the optimal conditions for fabricating future light emitting devices. We show the interplay between the QCE and hydrogen passivation, and the effect this interplay has on the luminescence of Si-QDs in $Si_3N_x$.

## 3.2 Experimental

### 3.2.1 Sample Preparation

Si-rich silicon nitride ($Si_3N_x$) films were deposited on As-doped (100) Si wafers ($\rho = 0.001\Omega$cm) using plasma enhanced chemical vapour deposition (PECVD) in an Edwards STS310 system at 750 mTorr and 300°C. Deposition was performed under a constant nitrogen-diluted 5% $SiH_4$ flow rate of 600sccm and a variation in the 99.9999% $NH_3$ gas from 30 to 45sccm. Gases were ionized using a radio frequency source to form $Si_3N_x$ films with stoichiometries from $Si_3N_{2.72}$ to $Si_3N_{3.21}$. $Si_3N_x$ film samples were post annealed for 30 minutes at temperatures ranging from 400°C to 1000°C in forming gas (95% $N_2$, 5% $H_2$) in a Lindberg Blue M Thermo Scientific Furnace. The thickness of the $Si_3N_x$ films was estimated to be 100nm using a Woolam M2000V spectroscopic ellipsometer (SE). The index of refraction was found by ellipsometry to vary from 1.8 to

2.4 for different $Si_3N_x$ stoichiometries, which can be considered an attractive property for fabricating waveguides with tailored characteristics. The observed index of refraction for the stoichiometry $Si_3N_4$ was 1.85, which is consistent with reported values of 1.80-1.92 for hydrogenated $Si_3N_4$.[14]

### 3.2.2 Sample Characterization

The composition of films was determined using Rutherford backscattering spectroscopy (RBS), elastic recoil detection (ERD) and X-ray photoelectron spectroscopy (XPS). RBS and ERD measurements were conducted using $He^{4+}$ at energies of 500keV and 1600keV respectively. RBS was performed at several locations on the surface to confirm the uniformity of the film thickness and composition. A Sb-implanted amorphous Si sample with a known total Sb content of $4.82\times10^{15}$ atoms/cm$^2$ was used to calibrate the detector solid angle. RBS and ERD data were fitted using SIMNRA[15] to determine the elemental composition and film thickness, and to explore changes in hydrogen content for annealed samples. XPS analyses were performed using a Kratos Axis Ultra spectrometer with a monochromatic Al K(α) source (15 mA, 14 kV) at Surface Science Western. High-resolution spectra were obtained using an analysis area of ≈300µm×700µm and either a 10 eV or 20 eV pass energy which corresponds to an Ag $3d_{5/2}$ FWHM of 0.47 eV and 0.55 eV, respectively. In order to perform depth-resolved analysis, the surface of the samples was sputtered with an $Ar^+$ ion beam. Sputter rates were calculated based on an $SiO_2$/Si(001) standard (1.5 nm/min). XPS spectra were fitted using CasaXPS software. [16]

Samples for scanning transmission electron microscopy (STEM) were prepared using a Zeiss NVision 40 focused ion beam system. STEM electron energy loss spectrum

(STEM EELS) images at the Si edge were acquired using a FEI Titan cubed system with a high-resolution Gatan Imaging Filter quantum energy filter. PL spectra were collected at room temperature using a 405±10nm wavelength laser diode with a power output of 120mW. The incident beam was filtered to remove wavelengths longer than 405nm and photons from the sample were filtered to remove wavelengths shorter than 450nm. Emitted photons were collected and analysed using a Mightex HRS-BD1-200 spectrometer with a wavelength range of 300-1050nm.

X-ray absorption near edge structure (XANES) and Fourier Transform Infrared Spectroscopy (FT-IR) measurements were performed to investigate the effects of thermal annealing on the chemical configuration of the samples. XANES measurements were conducted at the Canadian Light Source (CLS) using the Soft X-ray Microcharacterization Beamline (SXRMB) with an energy range of 1.7 to 10 keV. InSb (111) crystals were used as monochromatizing crystals for the Si K-edge XANES measurements with an energy resolution of $3.3\times10^{-4}$ E/ΔE. Detection modes were total electron yield (TEY) and partial fluorescence yield (PFY), which were measured simultaneously, and the spectra were normalized to the incident X-ray intensity ($I_0$). TEY and PFY modes can track surface and bulk information from the sample because of the difference between the mean free paths of electrons and fluorescence photons. FT-IR measurements were performed using a Digilab FTS 7000 Series spectrometer in transmission mode for films deposited on undoped Si substrates, and otherwise prepared under identical conditions as those on doped Si wafers.

## 3.3 Results and Discussion

### 3.3.1 Results

RBS and ERD analyses revealed that as the $NH_3$ flow rate was increased, the Si content of the films decreased. The hydrogen (H) content of the nitride films was unchanged by increasing the $NH_3$ flow rate. The mean percentage of H in the films before annealing was 19$\pm$1 at%. Film compositions of $Si_3N_{2.72}$, $Si_3N_{3.00}$, $Si_3N_{3.15}$ and $Si_3N_{3.21}$ corresponded to $NH_3$ flow rates of 30sccm, 35sccm, 40sccm and 45sccm respectively. Full elemental composition of a set of similar films over a broader range of compositions can be found here.[17]

Energy-filtered STEM images were taken for as-deposited and annealed nitride samples with different compositions ($Si_3N_x$, x=2.72 – 3.21). While the crystalline structure of the Si substrate was imaged very clearly, the non-stoichiometric silicon nitride ($Si_3N_x$) films appeared homogeneous and no individual Si-QDs were resolved. It is possible that the size (d = ≈2-3nm) and amorphous structure of the Si-QDs make them difficult to resolve as they may be below the detection limit of the STEM- EELS system. XPS analysis of the Si 2p core level was conducted to gain further insight into the chemical composition of films. XPS measurements were conducted on samples as-deposited and annealed at 500°C. XPS can be used as an indicator of the presence of Si-QDs, since the binding energy of the $Si^0$ peak in Si-QDs is significantly lower than the $Si^{n+}$ peak in the $SiO_x$ or $Si_3N_x$ matrix.[18] Oxygen was found to be present only on the surface. The Si 2p peaks corresponding to Si in an $SiO_x$ matrix were not detected after sputtering. Fig.3.1 shows XPS data for a $Si_3N_3$ sample annealed at 500°C, after sputtering 9nm (red dotted line) and 45nm (blue dotted line). The spectra were fitted using

CasaXPS, with peaks at 99.7eV, 100.4eV, 101.1eV and 101.7eV (shown in Fig.3.1 by dashed red lines) corresponding to the $Si^{n+}$ (n=0, 1, 2, 3) oxidation states of Si. The peak centered at 99.7eV corresponds to the binding energy of $Si^0$ of Si atoms in a pure Si network, and is considered a signature of the presence of Si-QDs.[18] It should be noted that $Si^0$ was observed in both as-deposited and annealed samples. The peaks at 100.4eV ($Si^{1+}$) and 101.1eV ($Si^{2+}$) correspond to Si subnitride in Si-rich $Si_3N_x$, while $Si^{3+}$ corresponds to Si atoms in a $Si_3N_4$ network.[19-22]

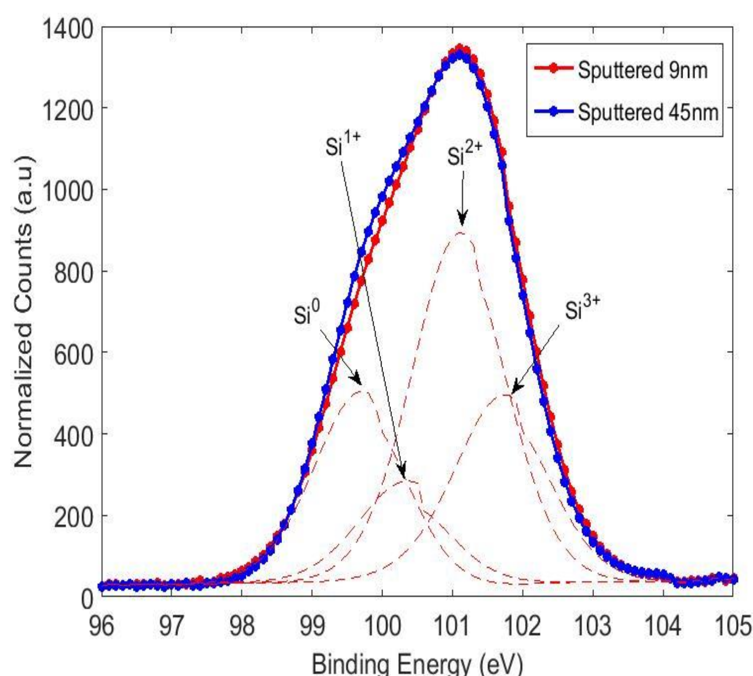


**Fig.3.1:** XPS Si 2p spectra from an $Si_3N_{3.00}$ sample annealed at 500°C.

The PL spectra in Fig.3.2(a) shows the emission from samples annealed at 500°C. PL data shown in Fig.3.2 were normalized with respect to the maximum intensity of brightest sample. A similar trend was observed for as-deposited films. There is a shift in the PL maximum to longer wavelengths as the Si content is increased. The Si-QDs

diameter can be estimated from the PL peak position using the equation:

$$\frac{hc}{\lambda} = E_g + \frac{C}{d^2} \tag{3.1}$$

where $E_g$ is the bandgap of bulk Si, $C$ is the confinement factor ($C =$ 2.4eV for amorphous Si) and λ is the PL peak position.[23, 24] As an example, the position of the PL maximum for the sample with composition $Si_3N_{2.72}$ at 707 nm (1.75 eV) can be used to estimate an average Si-QD diameter of D =3.9nm. We used the confinement factor associated with amorphous Si, due to lack of observed crystallinity for Si-QDs in TEM images. Fig.3.2(b) shows the change in dot size for samples with the same composition annealed at lower temperatures (600°C and below). The dot sizes reported in this figure were calculated using equation 3.1. For samples annealed above 600°C, the reduction in intensity, and broadening, of the PL peaks made the determination of the PL peak position unreliable.

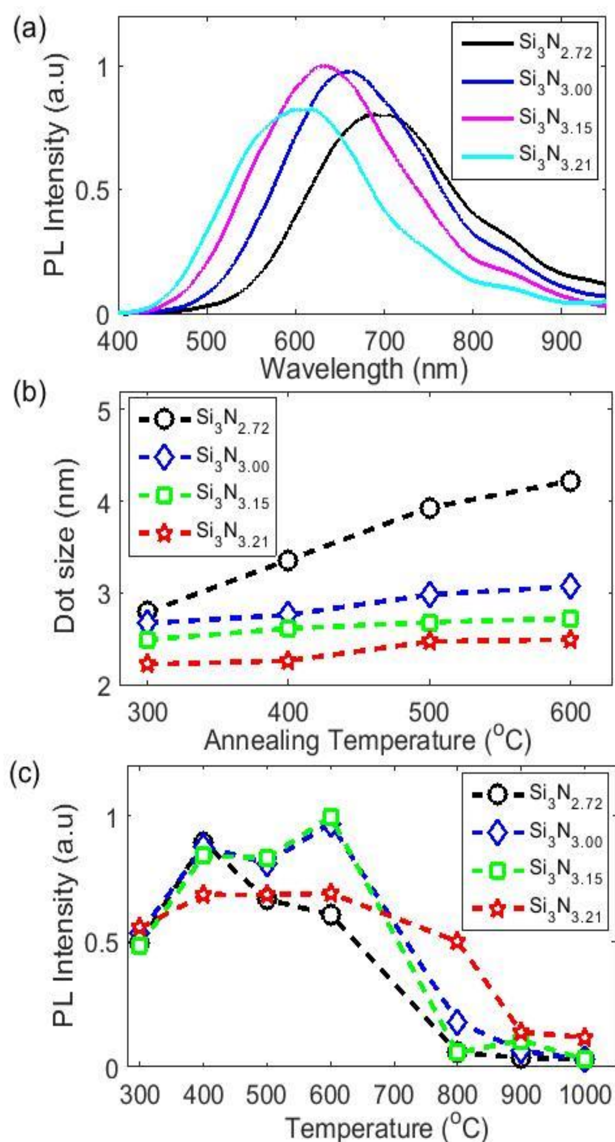


**Fig.3.2:** (a) Normalized PL spectra for samples annealed at 500°C, (b) change in Si-QD size with annealing temperature and (c) the variation in PL intensity with annealing temperature. Samples not post-annealed are indicated by 300°C (growth temperature).

We found that PL intensity was a function of both composition and annealing temperature. The $Si_3N_{2.72}$ film yielded maximum PL intensity after annealing to 400°C, while films of $Si_3N_{3.00}$ and $Si_3N_{3.15}$ showed maximum intensity after annealing at 600°C, and $Si_3N_{3.21}$ showed only slight variations in PL intensity for annealing temperatures

ranging from 400 to 600°C, as seen in Fig.3.2 (c). The PL intensity of the $Si_3N_{2.72}$, $Si_3N_{3.15}$ and $Si_3N_{3.00}$ films was significantly lower for annealing temperatures of 800°C and above. However, for the $Si_3N_{3.21}$ film, which had the highest nitrogen (N) content, the observed decrease in PL intensity was less dramatic, and occurred at 900°C.

To probe changes in the total H content in the films with annealing temperature, ERD analysis was conducted on the $Si_3N_{3.00}$ film. ERD results revealed that the amount of H in the film decreased monotonically with increasing annealing temperatures, as shown in Fig.3.3.

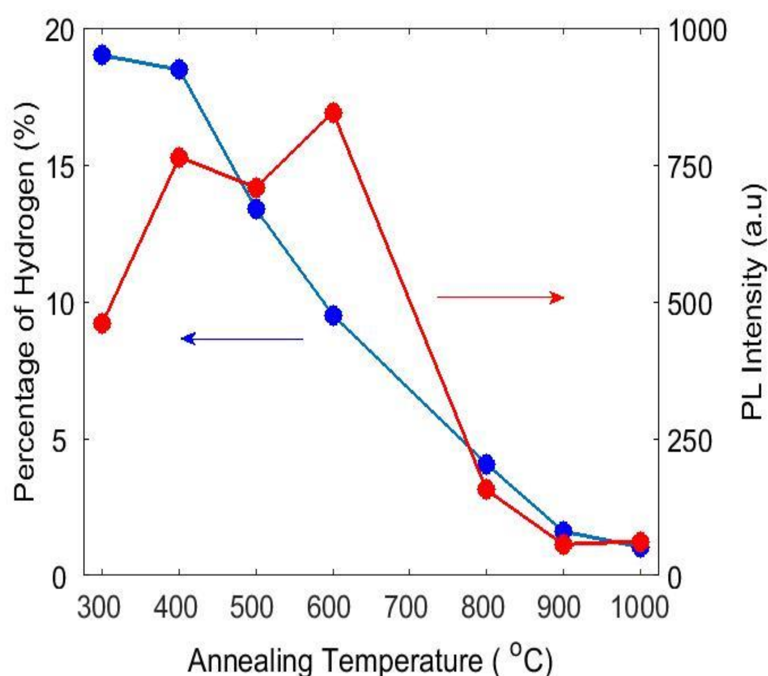


**Fig.3.3:** Percentage of hydrogen remaining after annealing (blue), and PL intensity (red) vs annealing temperature for composition $Si_3N_{3.00}$. Samples not post-annealed are indicated by 300°C (growth temperature).

PL intensity increased for annealing temperatures from 400°C to 600°C, and decreased along with the loss of hydrogen for annealing temperatures of 800°C and

above. It should be noted that standard ERD setups have a detection sensitivity of approximately 10ppm,[25, 26] and therefore, it is possible that some undetected H remains in the film. These trends will also be explained by FT-IR results presented in Fig.3.4.

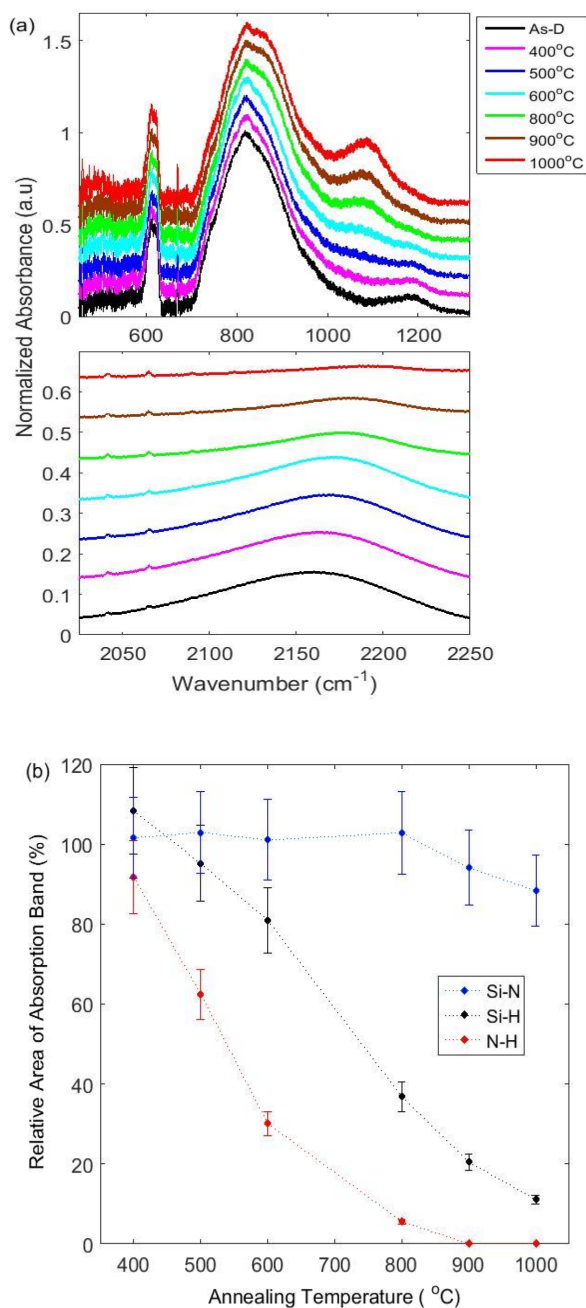


**Fig.3.4:** (a) FT-IR spectra and (b) extracted parameters for $Si_3N_{3.00}$ films before and after annealing.

From Fourier Transform Infrared (FT-IR) spectroscopy measurements six major peaks were observed, as seen in Fig.3.4 (a) for all compositions and temperatures. These peaks were located at 617cm$^{-1}$, 822cm$^{-1}$, 1186cm$^{-1}$and 2160cm$^{-1}$, which correspond to the Si-H wagging mode, Si-N asymmetric stretching, N-H wagging and Si-H stretching respectively. [27-29] Fig.3.4(b) shows the relative area of Si-N asymmetric stretching, Si-H stretching and N-H stretching modes, as a function of annealing temperature. FT-IR spectra for annealed samples revealed that Si-H and N-H bonds decreased with increasing annealing temperature. N-H bonds completely disappeared for temperatures above 800°C. The Si-N bond remained constant (less 5% deviation with respect to an as-deposited sample) for temperatures from 400°C to 800°C, and decreased above 800°C.

XANES measurements were performed at the Si K-edge to explore the chemical and electronic structure of Si in our $Si_3N_x$ films. Fig.3.5(a) shows TEY-XANES spectra of $Si_3N_{3.00}$ films annealed at various temperatures. TEY-XANES is surface and near-surface sensitive (~ 70nm)[30] due to the shallow sampling depth of the photoelectrons. TEY-XANES spectra of $Si_3N_{3.00}$ films annealed at different temperatures exhibit similar features to those of $\beta$-$Si_3N_4$. [31] The feature at 1846 eV corresponds to Si-N bonds, while that at 1848.5 eV corresponds to the Si-O bond, which is due to surface oxidation of the $Si_3N_x$ film or of the Si-QDs. The weak feature at 1842 eV is related to the Si-Si bond, which comes from the Si-QDs and is absent in the spectrum of pure $Si_3N_4$. [31]

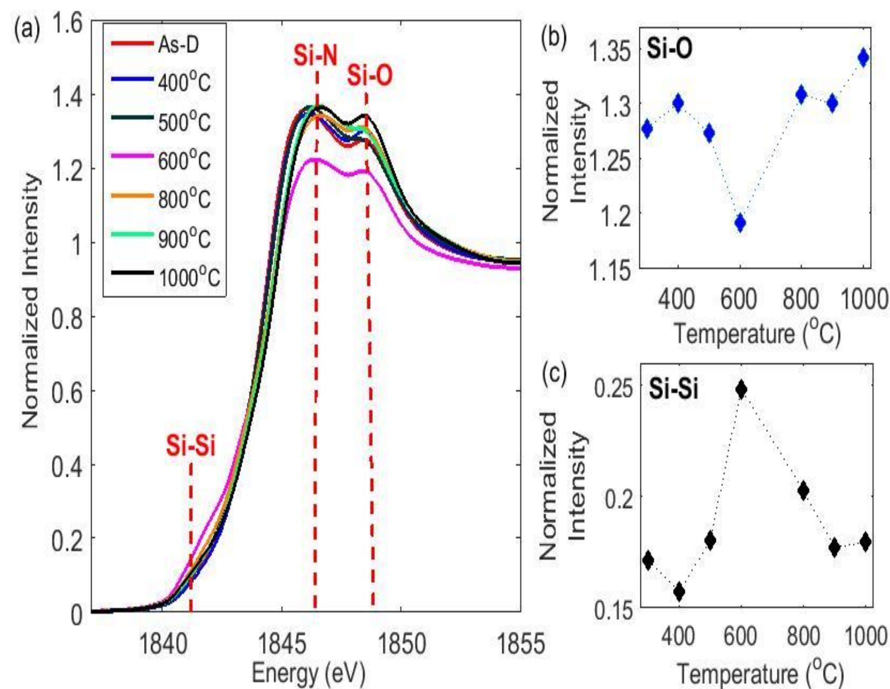


**Fig.3.5:** (a) X-ray absorption near edge spectroscopy (XANES) for the Si-K edge, for $Si_3N_{3.00}$, and the normalized intensity of the (b) Si-O bond and (c) Si-Si bond, as a function of annealing temperature.

A closer examination of the TEY spectra revealed that: (1) the intensity of the Si-O resonance peak decreased with annealing temperature in the range of 400-600°C and significantly increased for annealing temperatures higher than 800°C (as shown in Fig.3.5 (b)); (2) the intensity of the Si-Si resonance peak increased for annealing temperatures up to 600°C and then decreased for higher temperatures (as shown in Fig.3.5 (c)); and (3) the peak position shifted to higher energies as the annealing temperature increased. The presence of the Si-O resonance peak indicates that a layer of $SiO_x$ was formed either on the surface of the Si-QDs or the nitride film during the synthesis process, which was reduced to $Si^0$ when the sample was annealed at 600°C with the presence of H in the nitride film. When the sample was annealed to a temperature higher than 800°C, the

surface of the Si-QDs or of the nitride film was further oxidized. This observation is consistent with the PL results, in which the sample annealed at 600°C shows the strongest luminescence (see Fig.3.3). The bulk-sensitive FLY-XANES spectra from $Si_3N_{3.00}$ films annealed at various temperatures (see appendix A1) show features identical to those of a Si wafer. This is due to the deeper sampling depth of x-rays compared to electrons at the Si K-edge, which resulted in a much greater contribution from the Si wafer beneath the $Si_3N_{3.00}$ film.[30]

### 3.3.2 Discussion

In the literature, the origin of PL from Si-rich $Si_3N_x$ films has been attributed to both radiative recombination at defect sites in the $Si_3N_x$ film and the QCE.[5, 11] The wavelength of defect-based luminescence is only dependent on the energy level of the particular defect and it should not change with the composition of the $Si_3N_x$ film. On the other hand, the QCE PL peak position is dependent on the Si-QD size, and can therefore be manipulated by changing the gas flow rates. [32] Fig.3.2 (a) demonstrates that the PL peak position red-shifts with increased Si content, providing evidence for QCE luminescence.

To increase the intensity of the luminescence from QD systems, hydrogen passivation of dangling bonds has been used by many researchers.[33, 34] The passivation of dangling bonds reduces the number of non-radiative sites within the system, increasing the internal quantum efficiency.[35] Therefore, it would be expected that depletion of hydrogen (H) from the system would reduce the light output. Fig.3.3 shows an initial increase in PL intensity with annealing temperature despite a loss of H from the films,

which appears to contradict this expected result.

During the deposition of $Si_3N_x$ with Si in excess, Si-Si bonds span throughout the nitride film resulting in a rigid and strained structure. The presence of Si-QDs in as-deposited films is evident by the presence of an $Si^0$ peak in XPS and PL of as-deposited samples. The structure of as-deposited films is dependent on a number of factors: the mixture of $Si-N_x$ states present in the film, the arrival species of Si and N atoms; and the combination of these species on the Si substrate surface.[36]

Once the nitride films are annealed, unbonded Si and N atoms in the neighbourhood of Si-QDs diffuse to bond to the Si-QDs. This results in a size increase of the Si-QDs which has been reported by Pei et al.[36] The growth process is Oswald ripening, by which larger particles are grown at the expense of smaller particles. This process occurs because larger particles are thermodynamically favoured over smaller particles.[37] In our samples we observed an increase in dot size, as shown in Fig.3.2(b), however this increase is not as large as was reported by Pei et al.[36] The increase in size of Si-QDs is limited by the supply of surrounding Si atoms because the diffusivity of Si in the nitride films is very low. This is consistent with the larger shift in PL peak position after annealing for samples with higher Si content. In addition, during the annealing process H is lost from the films, as shown in Fig.3.3.The following two reactions are possibly occurring:[38]

$$\text{Si-H} + \text{N-H} \rightarrow \text{Si-N} + H_2(g) \qquad (3.2)$$

$$\text{Si-H} + \text{Si-H} \rightarrow \text{Si-Si} + H_2(g) \qquad (3.3)$$

The reaction in equation 3.2 represents the formation of Si-N bonds and H gas due to dissociation of Si-H and N-H bonds. According to Boeheme *et al*, [39] this process occurs faster at high temperatures. This explains the low intensity of Si-H and N-H peaks after

annealing to temperatures of 800°C and above, as shown in Fig.3.4 (b). In addition to this reaction, the disassociation of Si-H bonds to form Si-Si bonds and H gas is also possible (equation 3.3). This reaction is less probable than the first reaction, due to the higher density of N-H bonds which would surround Si-H bonds when they disassociate, however it is still possible in our Si-rich $Si_3N_x$ films. [40] The second reaction (equation 3.3) facilitates the growth of Si-QDs because the areas in the film where this process occurs act as nucleation sites for Si-QD growth. The formation of these Si-QDs is due to phase separation of excess Si in the nitride film.[41, 42] The shoulder at 1842eV in XANES spectra (Fig.3.5 (a)) and the $Si^0$ peak in XPS (Fig.3.1) are associated with Si-Si bonds.[31, 43] Due to the surface-sensitive nature of TEY XANES, the native oxide present on the nitride films contributes to the features observed in the Si K-edge spectra. By comparing Fig.3.5 (b) and (c) it is evident that the native oxide contributes significantly to the XANES spectra for all annealing temperatures except 600°C. There is clearly a strong contribution due to the Si-QDs for samples annealed at 600°C, which is evident from the rise in intensity of the Si-Si shoulder at 1842eV (as shown in Fig.3.5 (a)). The increased intensity of this shoulder, and the increase in PL intensity, indicate that the increased PL is due to radiative recombination from the Si-QDs. For annealing temperatures above 600°C, there is also a significant decrease in Si-N bonds as shown in Fig.3.4(b). The decrease in Si-N bonds indicates that there is also a loss of N that occurs at higher annealing temperatures. A possible mechanism by which this occurs is the reaction:[44]

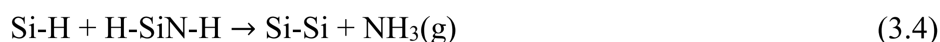

$$\text{Si-H} + \text{H-SiN-H} \rightarrow \text{Si-Si} + NH_3(g) \qquad (3.4)$$

The fairly high bond strength of Si-N bonds explains why this loss of N is not observed at lower temperatures. The loss of both H and N from the film results in the formation of a large number of dangling bonds which act as non-radiative sites.[45] This

increase in non-radiative sites increases the probability of non-radiative recombination and is the reason for the low PL intensity seen following annealing at higher temperatures.

Based on equation 3.4, it is expected that samples with higher N content would be less sensitive to higher annealing temperatures. The results shown in Fig.3.2(c) support such an argument. It is observed that samples with higher N content have higher PL intensity at higher annealing temperatures than those with higher Si content. However, samples with a higher N content would also have smaller Si-QDs because of the lower Si content which would require higher excitation energies in order to luminescence.

## 3.4 Summary and Conclusions

We have shown that the luminescence of Si-QDs in $Si_3N_x$ depends on the interplay between QCE and non-radiative defects formed after desorption of hydrogen from the nitride film. At low annealing temperatures this interplay results in improved luminescence of the Si-QD system. As a result, the light output of Si-QDs increases for annealing temperatures from 400°C to 600°C. However, at higher annealing temperatures (800°C and above) the desorption of hydrogen dominates and results in an increase in the number of non-radiative sites, thus reducing the luminescence of the Si-QD system. We have also demonstrated that N-rich films are less sensitive to this reduction in PL intensity at high annealing temperatures. Our results ultimately show that if Si-QDs in an $Si_3N_x$ matrix are to be integrated in optoelectronic devices, a hydrogenated matrix is needed to achieve high light output.

## 3.5 References

[1] C. Garcia, B. Garrido, P. Pellegrino, R. Ferre, J. A. Moreno, J. R. Morante*, et al.*, "Size dependence of lifetime and absorption cross section of Si nanocrystals embedded in $SiO_2$," *Applied Physics Letters,* vol. 82, pp. 1595-1597, 2003.

[2] A. G. Cullis, L. T. Canham, and P. D. J. Calcott, "The structural and luminescence properties of porous silicon," *Journal of Applied Physics,* vol. 82, pp. 909-965, 1997.

[3] W. D. A. M. de Boer, D. Timmerman, K. Dohnalová, I. N. Yassievich, H. Zhang, W. J. Buma*, et al.*, "Red spectral shift and enhanced quantum efficiency in phonon-free photoluminescence from silicon nanocrystals," *Nature Nanotechnology,* vol. 5, p. 878, 2010.

[4] F. Maier-Flaig, J. Rinck, M. Stephan, T. Bocksrocker, M. Bruns, C. Kübel*, et al.*, "Multicolor Silicon Light-Emitting Diodes (SiLEDs)," *Nano Letters,* vol. 13, pp. 475-480, 2013.

[5] F. Giorgis, C. Vinegoni, and L. Pavesi, "Optical absorption and photoluminescence properties of films deposited by plasma-enhanced CVD," *Physical Review B,* vol. 61, pp. 4693-4698, 2000.

[6] D. T. Jiang, I. Coulthard, T. K. Sham, J. W. Lorimer, S. P. Frigo, X. H. Feng*, et al.*, "Observations on the surface and bulk luminescence of porous silicon," *Journal of Applied Physics,* vol. 74, pp. 6335-6340, 1993.

[7] A. J. Kenyon, P. F. Trwoga, C. W. Pitt, and G. Rehm, "The origin of photoluminescence from thin films of silicon-rich silica," *Journal of Applied Physics,* vol. 79, pp. 9291-9300, 1996.

[8] T. Shimizu-Iwayama, K. Fujita, S. Nakao, K. Saitoh, T. Fujita, and N. Itoh, "Visible photoluminescence in Si+-implanted silica glass," *Journal of Applied Physics,* vol. 75, pp. 7779-7783, 1994.

[9] C. Ternon, F. Gourbilleau, X. Portier, P. Voivenel, and C. Dufour, "An original approach for the fabrication of Si/$SiO_2$ multilayers using reactive magnetron sputtering," *Thin Solid Films,* vol. 419, pp. 5-10, 2002.

[10] D. J. Paul, "Si/SiGe heterostructures: from material and physics to devices and circuits," *Semiconductor Science and Technology,* vol. 19, pp. R75-R108, 2004.

[11] N.-M. Park, C.-J. Choi, T.-Y. Seong, and S.-J. Park, "Quantum Confinement in Amorphous Silicon Quantum Dots Embedded in Silicon Nitride," *Physical Review Letters,* vol. 86, pp. 1355-1357, 2001.

[12] X. D. Pi, O. H. Y. Zalloum, A. P. Knights, P. Mascher, and P. J. Simpson, "Electrical conduction of silicon oxide containing silicon quantum dots," *Journal of Physics: Condensed Matter,* vol. 18, p. 9943, 2006.

[13] C.-W. Jiang and M. A. Green, "Silicon quantum dot superlattices: Modeling of energy bands, densities of states, and mobilities for silicon tandem solar cell applications," *Journal of Applied Physics,* vol. 99, p. 114902, 2006.

[14] Y. Wan, K. R. McIntosh, A. F. Thomson, and A. Cuevas, "Recombination and thin film properties of silicon nitride and amorphous silicon passivated c-Si following ammonia plasma exposure," *Applied Physics Letters,* vol. 106, p. 041607, 2015.

[15] M. Mayer, "SIMNRA User's Guide," vol. version 5.0, ed. Max-Planck-Institut für Plasmaphysik, 1997.

[16] N. Fairley, "CasaXPS," ed: Casa Software Ltd, 2009.

[17] L. V. Goncharova, P. H. Nguyen, V. L. Karner, apos, R. Ortenzio, S. Chaudhary, *et al.*, "Si quantum dots in silicon nitride: Quantum confinement and defects," *Journal of Applied Physics,* vol. 118, p. 224302, 2015.

[18] K. S. Min, K. V. Shcheglov, C. M. Yang, H. A. Atwater, M. L. Brongersma, and A. Polman, "Defect-related versus excitonic visible light emission from ion beam synthesized Si nanocrystals in SiO2," *Applied Physics Letters,* vol. 69, pp. 2033-2035, 1996.

[19] R. Kärcher, L. Ley, and R. L. Johnson, "Electronic structure of hydrogenated and unhydrogenated amorphous $SiN_x$ :($0 \leq x \leq 1.6$): A photoemission study," *Physical Review B,* vol. 30, pp. 1896-1910, 1984.

[20] G. M. Ingo, N. Zacchetti, D. della Sala, and C. Coluzza, "X-ray photoelectron spectroscopy investigation on the chemical structure of amorphous silicon nitride (a-$SiN_x$)," *Journal of Vacuum Science & Technology A,* vol. 7, pp. 3048-3055, 1989.

[21] J. Szepvolgyi, I. Mohai, and J. Gubicza, "Atmospheric ageing of nanosized silicon nitride powders," *Journal of Materials Chemistry,* vol. 11, pp. 859-863, 2001.

[22] P. Cova, S. Poulin, O. Grenier, and R. A. Masut, "A method for the analysis of multiphase bonding structures in amorphous $SiO_xN_y$ films," *Journal of Applied Physics,* vol. 97, p. 073518, 2005.

[23] N.-M. Park, T.-S. Kim, and S.-J. Park, "Band gap engineering of amorphous silicon quantum dots for light-emitting diodes," *Applied Physics Letters,* vol. 78, pp. 2575-2577, 2001.

[24] H.-S. Kwack, Y. Sun, Y.-H. Cho, N.-M. Park, and S.-J. Park, "Anomalous temperature dependence of optical emission in visible-light-emitting amorphous silicon quantum dots," *Applied Physics Letters,* vol. 83, pp. 2901-2903, 2003.

[25] H. R. Verma, "Elastic Recoil Detection," in *Atomic and Nuclear Analytical Methods*, ed: Springer Berlin Heidelberg, 2007, pp. 143-175.

[26] E. Strub, W. Bohne, S. Lindner, and J. Rohrich, "Possibilities and limitations of ERDA: examples from the ERDA ToF set-up at the Hahn-Meitner-Institut," *Surface and Interface Analysis,* vol. 35, pp. 753-756, 2003.

[27] S. Hasegawa, L. He, Y. Amano, and T. Inokuma, "Analysis of SiH and SiN vibrational absorption in amorphous $SiN_x$:H films in terms of a charge-transfer model," *Physical Review B,* vol. 48, pp. 5315-5325, 1993.

[28] G. N. Parsons, J. H. Souk, and J. Batey, "Low hydrogen content stoichiometric silicon nitride films deposited by plasma-enhanced chemical vapor deposition," *Journal of Applied Physics,* vol. 70, pp. 1553-1560, 1991.

[29] G. Lucovsky, J. Yang, S. S. Chao, J. E. Tyler, and W. Czubatyj, "Nitrogen-bonding environments in glow-discharge---deposited a-Si:H films," *Physical Review B,* vol. 28, pp. 3234-3240, 1983.

[30] M. Kasrai, W. N. Lennard, R. W. Brunner, G. M. Bancroft, J. A. Bardwell, and K. H. Tan, "Sampling depth of total electron and fluorescence measurements in Si L- and K-edge absorption spectroscopy," *Applied Surface Science,* vol. 99, pp. 303-312, 1996.

[31] P. Wilson, T. Roschuk, K. Dunn, E. Normand, E. Chelomentsev, O. Zalloum*, et al.*, "Effect of thermal treatment on the growth, structure and luminescence of

nitride-passivated silicon nanoclusters," *Nanoscale Research Letters,* vol. 6, p. 168, 2011.

[32] B.-H. Kim, C.-H. Cho, T.-W. Kim, N.-M. Park, G. Y. Sung, and S.-J. Park, "Photoluminescence of silicon quantum dots in silicon nitride grown by $NH_3$ and $SiH_4$," *Applied Physics Letters,* vol. 86, p. 091908, 2005.

[33] A. I. Yakimov, V. V. Kirienko, V. A. Armbrister, and A. V. Dvurechenskii, "Hydrogen passivation of self-assembled Ge/Si quantum dots," *Semiconductor Science and Technology,* vol. 29, p. 085011, 2014.

[34] A. P. Jacob, Q. X. Zhao, M. Willander, F. Ferdos, M. Sadeghi, and S. M. Wang, "Hydrogen passivation of self assembled InAs quantum dots," *Journal of Applied Physics,* vol. 92, pp. 6794-6798, 2002.

[35] M. Grundmann, *The Physics of Semiconductors: An Introduction Including Nanophysics and Applications*, 2 ed.: Springer-Verlag Berlin Heidelberg, 2010.

[36] Z. Pei and H. L. Hwang, "Formation of silicon nano-dots in luminescent silicon nitride," *Applied Surface Science,* vol. 212–213, pp. 760-764, 2003.

[37] P. W. Voorhees, "The theory of Ostwald ripening," *Journal of Statistical Physics,* vol. 38, pp. 231-252, 1985.

[38] Z. Lu, P. Santos-Filho, G. Stevens, M. J. Williams, and G. Lucovsky, "Fourier transform infrared study of rapid thermal annealing of a-Si:N:H(D) films prepared by remote plasma-enhanced chemical vapor deposition," *Journal of Vacuum Science & Technology A,* vol. 13, pp. 607-613, 1995.

[39] C. Boehme and G. Lucovsky, "Dissociation reactions of hydrogen in remote plasma-enhanced chemical-vapor-deposition silicon nitride," *Journal of Vacuum Science & Technology A: Vacuum, Surfaces, and Films,* vol. 19, p. 2622, 2001.

[40] F. L. Martínez, R. Ruiz-Merino, A. del Prado, E. San Andrés, I. Mártil, G. González-Díaz*, et al.*, "Bonding structure and hydrogen content in silicon nitride thin films deposited by the electron cyclotron resonance plasma method," *Thin Solid Films,* vol. 459, pp. 203-207, 2004.

[41] W. R. T. A. Kumar, R. Sarvanan, P.B. Agarwal, P. Kothari, D. Kumar, "Plasma Enhanced Chemical Vapor Deposited (Pecvd) Silicon-Rich-Nitride Thin Films For Improving Silicon Solar Cells Efficiency," *International Journal of Scientific Engineering and Technology* vol. 1, 2012.

[42] Y. Gong, S. Ishikawa, S.-L. Cheng, M. Gunji, Y. Nishi, and J. Vučković, "Photoluminescence from silicon dioxide photonic crystal cavities with embedded silicon nanocrystals," *Physical Review B,* vol. 81, p. 235317, 2010.

[43] P. R. Wilson, T. Roschuk, K. Dunn, M. Betti, J. Wojcik, and P. Mascher, "The Influence of Structural Ordering on Luminescence from Nitride- and Oxynitride-Passivated Silicon Nanoclusters," *ECS Transactions,* vol. 19, pp. 19-28, 2009.

[44] F. L. Martínez, A. del Prado, I. Mártil, G. González-Diaz, W. Bohne, W. Fuhs*, et al.*, "Molecular models and activation energies for bonding rearrangement in plasma-deposited a-$SiN_x$:H dielectric thin films treated by rapid thermal annealing," *Physical Review B,* vol. 63, p. 245320, 2001.

[45] C. G. Van de Walle and R. A. Street, "Structure, energetics, and dissociation of Si-H bonds at dangling bonds in silicon," *Physical Review B,* vol. 49, pp. 14766-14769, 1994.

# Chapter 4

# Optical Properties and Defects of Al Implanted Stoichiometric Silicon Nitride

## 4.1 Introduction

Silicon nitride ($Si_3N_4$) is used extensively in microelectronics for various applications such as the dielectric material in field effect thin film transistors, and as the passivation material in device packaging. $Si_3N_4$ is also used as an antireflective coating in photovoltaic devices and has been explored as a host material for silicon quantum dots (Si-QDs).[1-4] Due to its numerous applications, there have been many studies on the various optical, electrical and structural properties of $Si_3N_4$, as well as the effect of growth temperature and growth methods on the properties of $Si_3N_4$ thin films.[5-8] To modify the optical properties of Si-QDs researchers have explored the use of dopants such as P and B to modify the optical and electrical properties of Si-QDs in $SiO_2$.[9-11] The shift to the use of $Si_3N_4$ host material, therefore, requires research into the impact of dopants on the optical properties of Si-QDs embedded in $Si_3N_4$.

In the previous chapters, we provided motivation for the use of $Si_3N_4$ as a host material for Si-QDs with a focus on the optical properties of Si-rich $Si_3N_4$. In this chapter, we will examine the impact of incorporating Al impurities in the stoichiometric $Si_3N_4$ film by ion implantation to understand the effects of Al dose and annealing temperature on the optical properties of stoichiometric $Si_3N_4$. These results are the preface to an understanding of the optical properties for Si-QDs in the $Si_3N_4$ system examined in chapter 5.

In this chapter, we explore the optical properties of Al incorporated $Si_3N_4$ thin films made using plasma enhanced chemical vapour deposition (PECVD). This study seeks to examine the influence of Al dose and post-annealing temperature on the photoluminescence (PL) of $Si_3N_4$ thin films. It will also seek to determine the mechanism(s) responsible for the luminescence of this system. The use of ion implantation allows for control of both ion depth and concentration. Previous studies on Al-doped $Si_3N_4$ have examined Al doping at a constant concentration. For instance, one of the first studies of Al-doped $Si_3N_4$ showed that the incorporation of Al impurities into β-$Si_3N_4$ produced midgap energy levels; full details can be found in ref.12. More recent studies have examined the optical properties of Al-doped $Si_3N_4$ of single crystalline $Si_3N_4$ nanowires produced through the nitriding of cryomilled nanocrystalline silicon powder and Al-doped α-$Si_3N_4$ micron-belts.[13, 14]PECVD deposition allows us to produce stoichiometric $Si_3N_4$ and Si-rich $Si_3N_4$ (to be discussed in chapter 5) and is a common growth method for producing Si-QDs embedded $Si_3N_4$ films. As temperature plays an important role in the formation and annihilation of defects produced by ion implantation, we are also focused on the effects of annealing temperature on the optical properties of the implanted material.

Furthermore, based on findings presented in chapter 3, the influence of hydrogen content on the optical properties of the stoichiometric $Si_3N_4$ will be monitored since the hydrogen concentration of the film will likely influence the PL of Si-rich $Si_3N_4$ samples examined in chapter 5. Optical properties of Al implanted $Si_3N_4$ were characterized by photoluminescence (PL), complemented by Fourier transform infrared spectroscopy (FTIR), X-ray absorption near edge spectroscopy (XANES) and positron annihilation

spectroscopy (PAS) to obtain information on the chemical changes and defect concentrations of the material.

## 4.2 Experimental Details

### 4.2.1 Sample preparation

Silicon nitride ($Si_3N_4$) films with 200 nm thickness were deposited on Si (100) wafers using plasma enhanced chemical vapour deposition (PECVD) at 750 mTorr and 300°C. The optimization of film deposition conditions is detailed in a previously published work.[15] $Si_3N_4$ films were then implanted with Al ions at an incident energy of 50 keV at 7° tilt at room temperature with implantation doses ranging from $5\times10^{11}$ to $5\times10^{15}$ ions/cm$^2$. Two sets of samples were prepared, in line with two objectives of this project, which are to investigate the influence of (1) Al dose and (2) post-annealing temperature on photoluminescence. One set of samples had different implantation doses (ranging from $5\times10^{11}$ to $5\times10^{15}$ ions/cm$^2$) followed by annealing at 600°C in forming gas (samples were denoted 5e11 to 5e15). The second set of samples was implanted with $5\times10^{15}$ Al atoms/cm$^2$ and annealed at different temperatures. This second set was further divided into 'ex-situ' and 'in-situ' samples. 'ex-situ' samples were annealed at different temperatures (200°C, 400°C and 600°C) in vacuum for 30mins. 'in-situ' samples were used to study the evolution of defect concentrations with annealing temperatures in comparison to those of samples measured after annealing. 'in-situ' samples were annealed on PAS sample stage in ultra-high vacuum during the collection of positron annihilation spectroscopy measurements from 200°C to 600°C at 200°C intervals for 30mins at each temperature.

### 4.2.2 Sample Characterization

All photoluminescence (PL) spectra were acquired at room temperature using a 405 nm laser diode with a 120mW power input. The incident beam was at 45° to the sample surface, and spectra were collected using a Mightex HRS-BD1-200 spectrometer; see ref.15 for complete details of the PL setup.[15] X-ray absorption near-edge spectroscopy (XANES) measurements were conducted at the Canadian Light Source (CLS) to study the electronic and chemical structure of samples. XANES spectra at the Si, N and Al K-edges were collected at the High Resolution Spherical Grating Monochromator (SGM) 11ID-1 beamline. At the Si K-edge, the total electron yield (TEY) was examined to eliminate any signal from the Si substrate due to the penetration depth at the edge. To maximize photon flux, the high energy grating was used for the Si and Al K-edges while the low energy grating was used for the N K-edge. XANES measurements at the Si $L_{2,3}$-edge were collected at the variable line spacing plane grating monochromator (VLS PGM) 11ID-2 beamline. XANES spectra taken at the Si $L_{2,3}$-edge allow us to examine the bonding of valence electrons in our samples. Due to the short electron mean path (very surface sensitive ~5 nm) at this edge, the TEY measurements were not examined as the signal would be dominated by a $SiO_2$ surface layer. Instead, the fluorescence yield (FLY) is collected, which probes ~70 nm into the film surface. This is deep enough to examine the implanted $Si_3N_4$ film but shallow enough to prevent a signal from the Si substrate affecting our measurements. All XANES spectra except for Si K-edge spectra were normalized to the incident X-ray intensity ($I_0$) using Athena software. Due to beamline mirror contamination, the Si K-edge diode measurements were used for spectra normalization in order to remove absorption caused by the contamination.

In order to study defect concentrations, Doppler broadening positron annihilation spectroscopy (PAS) experiments were conducted using a low energy monoenergetic positron beam at the University of Western Ontario positron facility. PAS is a non-destructive technique often applied to probe the point defects and open volumes in solid materials and thin films. Mono-energetic positrons are directed onto the target material and as the positrons travel through the material annihilation can occur from traps near the surface of the material or from point defects in the material.[16] Due to the conservation of energy and momentum when the electron-positron pair annihilates, two gamma rays travelling in opposite directions are emitted and each has the energy approximately equal to the rest energy of an electron or positron ($m_oc^2$=511 keV). Since the width of the 511 keV gamma ray line is sensitive to the electronic environment of the target material, the origin of the annihilation event can be inferred. The line width of the gamma rays, in high defect regions, is narrower than in low defect regions. The S parameter is a measure of the "sharpness" of the gamma ray line and has a higher value when vacancies are present.[17] The incident positron beam energy and the mean penetration depth of the positron are related according to the following equation:

$$P(x,E) = \alpha\, e^{-\alpha x}\,, x \approx \frac{40}{\rho\left(\frac{g}{cm^3}\right)} E(keV)^{1.6} \tag{4. 1}$$

where $P(x,E)$ penetration profile, $\alpha$ absorption coefficient, $\rho$ is the material density (g/cm$^3$), $E$ is the beam energy (keV) and $x$ is the probing depth (nm). For ex-situ samples, PAS experiments were conducted at room temperature while for in-situ samples the temperatures were controlled by the heated sample stage. An incident positron beam energy of 2 keV (~40 nm) was used in PAS measurements. A FTS 7000 Series DigiLab Fourier

transform infrared (FTIR) spectrometry was used to evaluate chemical bonding. The characteristic IR peaks were then analysed using the integrated absorbance of FTIR spectra.

## 4.3 Results

The room temperature PL spectra for $Si_3N_4$ samples implanted with different doses of Al and annealed at 600°C in forming gas are presented in Fig.4.1. PL spectra of samples 5e11 and 5e12 were similar to sample 5e13 and were omitted for clarity. As shown in Fig.4.1, the PL spectra for samples labelled asis, annealed and 5e13 are very similar. The emission of these samples is very close to the noise level of our spectrometer resulting in some noise in the PL spectra. A significant increase in PL intensity is observed at a dose of $5\times10^{14}$ atoms/cm$^2$ with the PL peak position at 615 nm (2.0eV). When the Al dose is increased to $5\times10^{15}$ atoms/cm$^2$ (labelled 5e15 in Fig.4.1), there is a further increase in PL intensity, accompanied by a blue shift to around 525 nm (2.4eV).

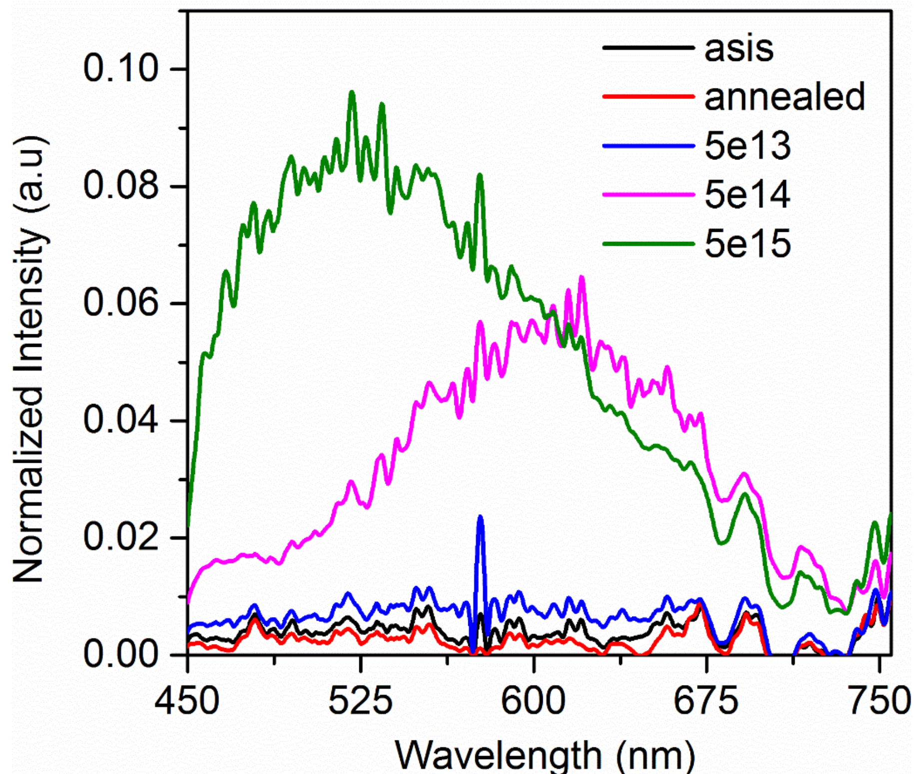


**Fig.4.1:** Normalized photoluminescence spectra of the samples examined including $Si_3N_4$ films before and after annealing labelled asis and annealed, respectively, implanted $Si_3N_4$ films labelled 5e13, 5e14 and 5e15 based on the Al implantation dose. Spectra are normalized to a common but arbitrary scale.

To study the effects of annealing temperature on the luminescence and defect concentrations samples were implanted with $5\times10^{15}$ Al ions/cm$^2$ then annealed at temperatures in the 200-600°C range. Note that annealing was done under vacuum and not in forming gas leading to no additional hydrogen incorporation into the $Si_3N_4$ films. This may affect the comparison of positron annihilation spectroscopy (PAS) results for 'in-situ' and 'ex-situ' samples. Fig.4.2(a) shows the integrated PL intensity and the variation in S parameter values for $Si_3N_4$ samples implanted with $5\times10^{15}$ ions/cm$^2$ of Al as a function of annealing temperature. As shown in Fig.4.2(a), the integrated PL intensity before annealing

(asis sample) is very low. PL intensity increases for implanted samples as the annealing temperature increases.

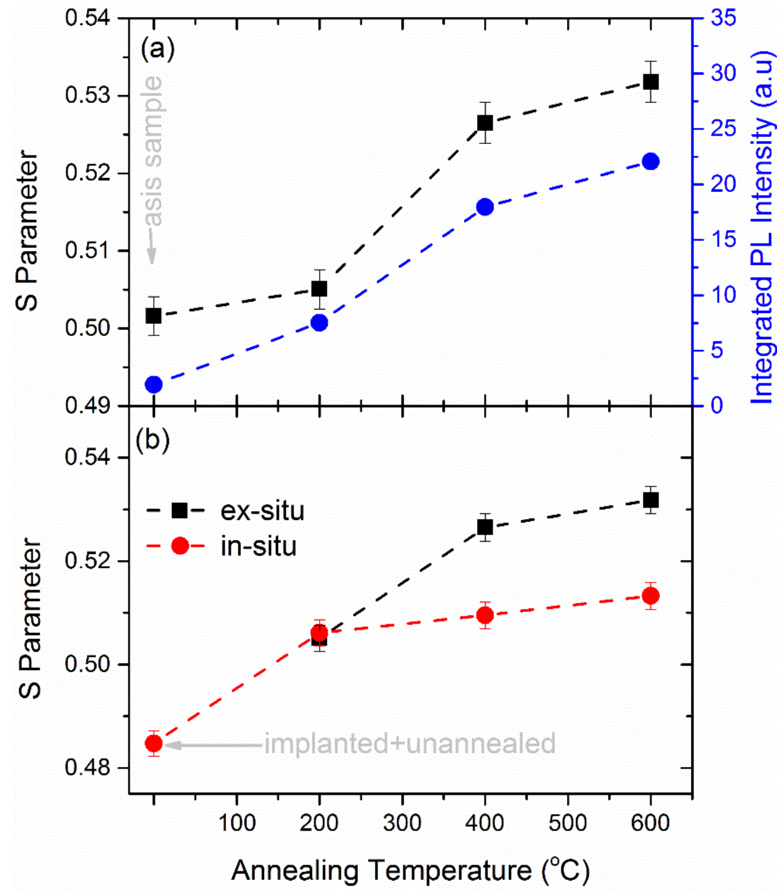


**Fig.4.2:** (a) S parameter of PAS measurements (black squares) and integrated PL intensity (blue dots) as a function of annealing temperature for $Si_3N_4$ sample implanted with $5\times10^{15}$ Al atoms/cm$^2$. The S parameter value and integrated PL intensity for the asis sample are included as a reference. (b) S parameter for ex-situ samples (black square), which are those annealed in vacuum followed by PAS measurements, are compared with in-situ samples (red dots), which are those heated on the PAS stage during PAS measurements. The uncertainty is calculated based on the S parameter value (*S*) and the total number of counts (*N*) and given by $S(1-S)\sqrt{N}$.

We know from previous studies by others and our group that higher annealing temperatures result in a decrease in PL intensity due to hydrogen loss from the films. It should be noted that the integrated PL intensity of vacuum annealed samples compared to those annealed in forming gas was higher (by ~ 20%). PAS measurements show a similar trend to PL results, where the S parameter increases as a function of annealing temperature. Both PL and PAS results will be discussed further in section 4.4.

To monitor the evolution of the S parameter with annealing temperature PAS measurements were taken as sample temperature was raised up to 600°C. It should be noted that the overall temperature profile for these in-situ samples is different to ex-situ samples as the temperature was incrementally increased from room temperature to 600°C. Therefore, samples annealed at 600ºC in-situ had a different thermal history to ex-situ samples. From Fig.4.2(b), we observe that the S parameter value increases with annealing temperature for in-situ samples and is coincidentally the same at 200°C in comparison to ex-situ samples annealed at the same temperature.

The difference spectrum of PAS measurements with respect to a (almost) defect-free Si wafer was taken. The full-width half maximum of the central peak of the difference spectrum can be used to estimate the detector resolution. From our measurements, this value was found to be ~1 keV. Fig.4.3(a) shows the difference of the normalized PAS spectra while Fig.4.3(b) shows the area under 511 keV peak of these spectra. As we can see in Fig.4.3(b), the area under 511 keV peak increases as annealing temperature increases which suggest that the increase in S parameter may be due to changes in the positronium formation.

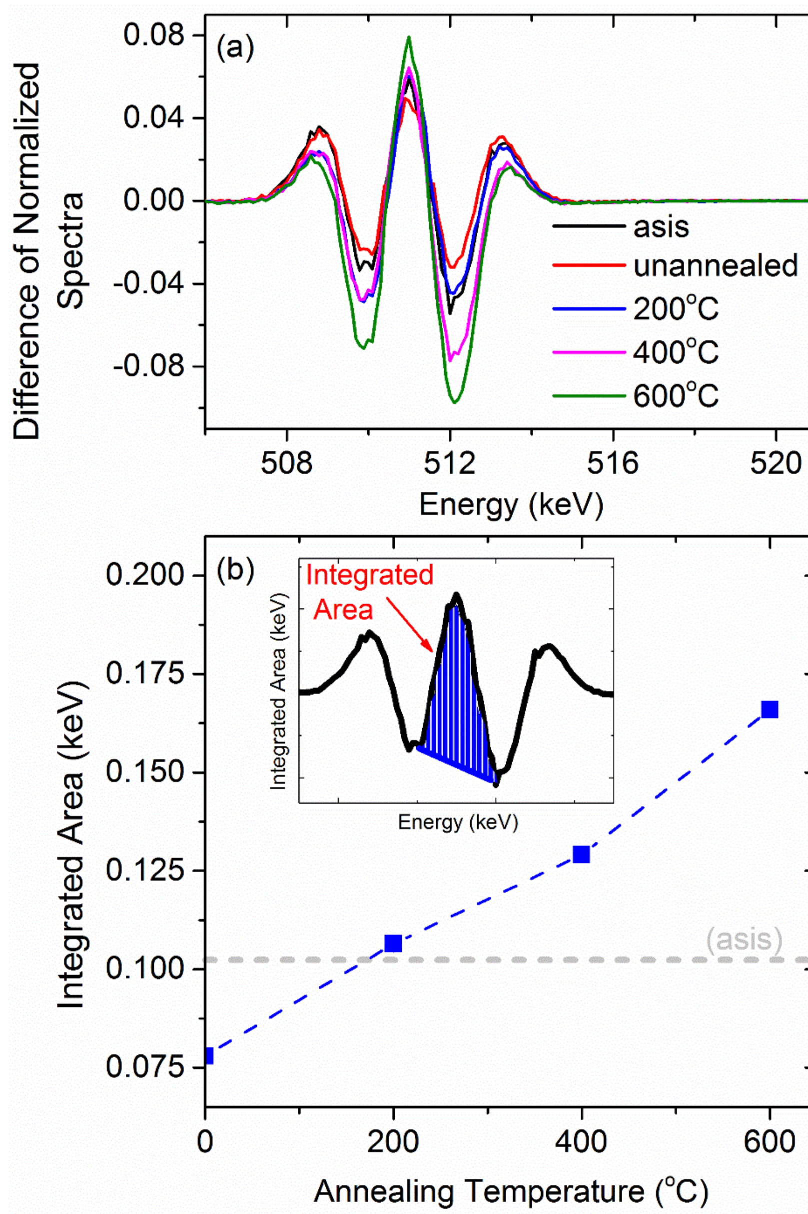


**Fig.4.3:** (a) Difference spectra for samples minus the PAS spectrum for a Si wafer. For the subtraction, all PAS spectra used had an equal number of total counts. (b) The integrated area under the middle peak of difference spectra shown in (a). In (b) the grey dashed line indicates the integrated area for the asis sample. The annealing temperature of 0°C is used to indicate an unannealed but implanted sample.

Fourier transform infrared spectroscopy (FTIR) spectra were collected to examine the changes in Si-H and N-H bonds at different implantation doses. A complete FTIR spectrum can be found in Appendix A2. Fig.4.4 shows the integrated area and absorbance peak positions for Si-H and N-H bonds. As seen in Fig.4.4, the integrated area for Si-H and N-H bonds decreases after implantation and annealing. The decrease in N-H bonds is continuous while for Si-H bonds the maximum decrease is observed at a $5\times10^{12}$ atoms/cm$^2$. At implantation doses greater than $5\times10^{12}$ atoms/cm$^2$, a slight increase is observed. It should be stressed that overall the Si-H bonds decrease after implantation in comparison to the annealed sample. The peak position of the Si-H bond increases by ~20cm$^{-1}$ for the maximum implantation dose. For N-H bonds, the integrated absorbance and peak position both decreases with increasing implantation dose.

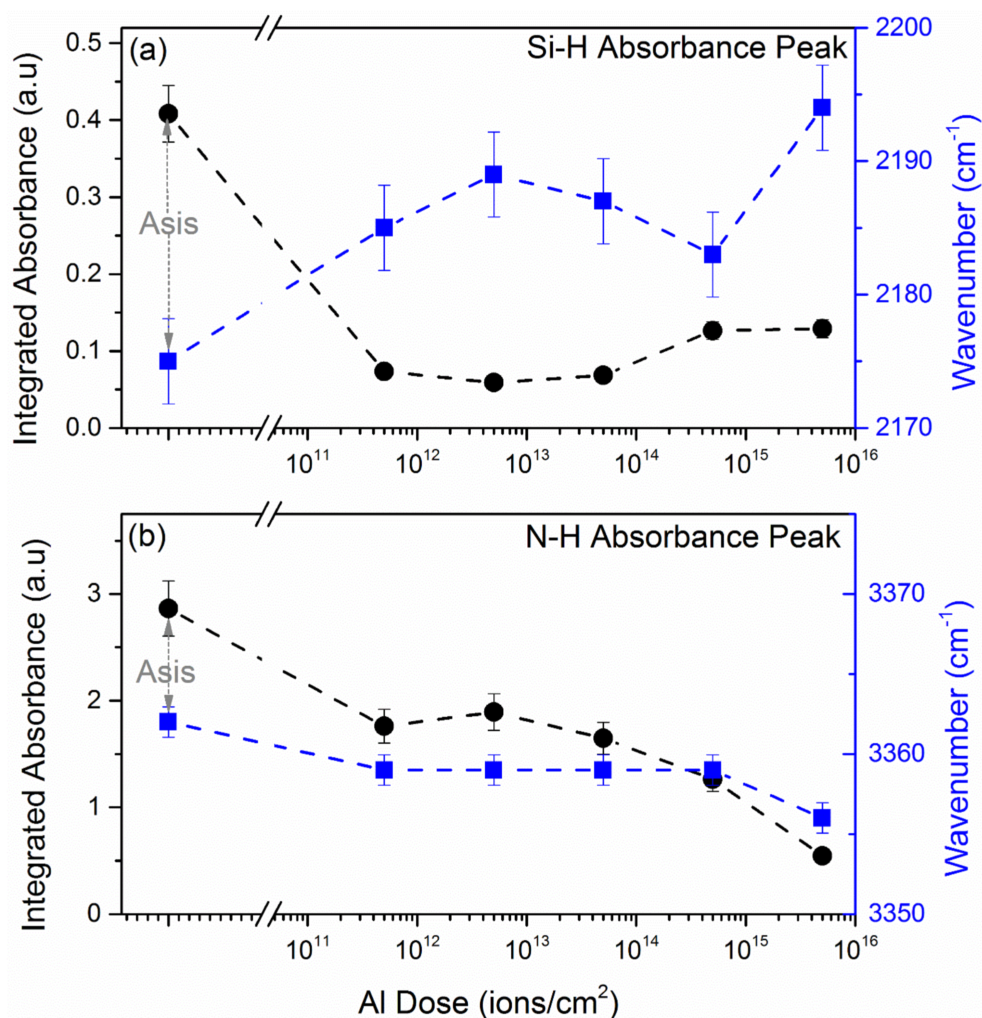


**Fig.4.4:** Integrated absorbance (black dots) and wavenumber (blue squares) of the (a) Si-H and (b) N-H absorbance peak as a function implantation dose. Error bars for integrated absorbance is 9% based on the signal-to-noise ratio while the error bars for wavenumber are $\pm 0.5 cm^{-1}$.

XANES measurements were carried out to examine the change in chemical composition for samples implanted with different doses of Al. The FLY XANES spectra at the Si L-edge is shown in Fig.4.5(a) with the Si-N peak located at 104.8 eV and Fig.4.5(b) shows the first derivative of the XANES spectra for samples annealed, 5e13, 5e14 and 5e15. In Fig.4.5(a), we observe that after annealing $Si_3N_4$ (sample annealed) there is a slight

upshift in the Si-N peak location to 104.9 eV. We use our annealed sample as our reference as it allows us to isolate changes due to annealing from those caused by Al.

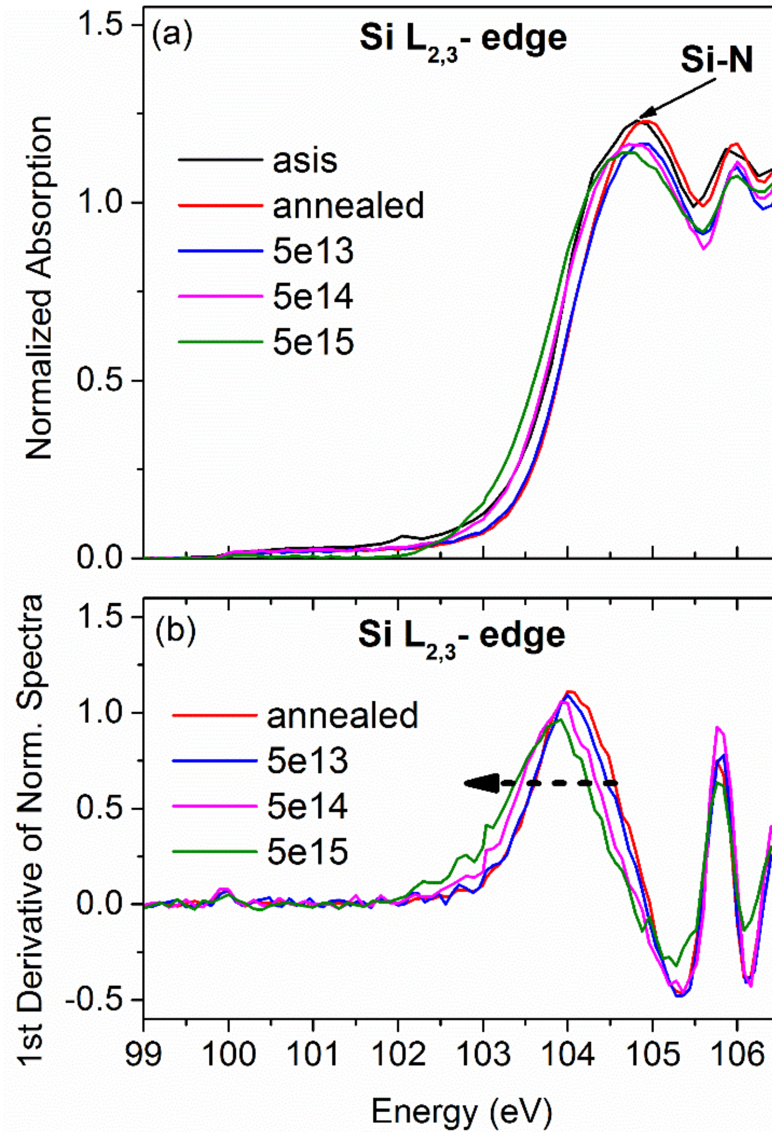


**Fig.4.5:** (a) FLY XANES spectra at the Si $L_{2,3}$-edge from 99 to 106.5 eV for asis, annealed, and implanted (implanted with Al doses of $5\times10^{13}$, $5\times10^{14}$ and $5\times10^{15}$ atom/cm$^2$) silicon nitride samples. (b) 1$^{st}$ derivative of the normalized spectra that are shown in (a).

As shown in Fig.4.5(a), we observe that the Si-N signal decreases for samples 5e13, 5e14 and 5e15 in comparison to the annealed and unimplanted sample (denoted annealed).

The increase in implantation dose corresponds to a decrease in the Si-N signal. A gradual downshift in the Si-N peak position is also observed with increasing Al dose from 104.9eV (for sample annealed) to 104.7eV (for sample 5e15).

The XANES spectra at the N K-edge in TEY mode are shown in Fig.4.6. As shown in Fig.4.6, the Si-N peak is located around 405 eV and there is a decrease in Si-N bonds after Al implantation. Also highlighted in Fig.4.6 is a feature attributed to the presence of $SiO_xN_y$ on the surface of the films which decreases with implantation dose.[18]

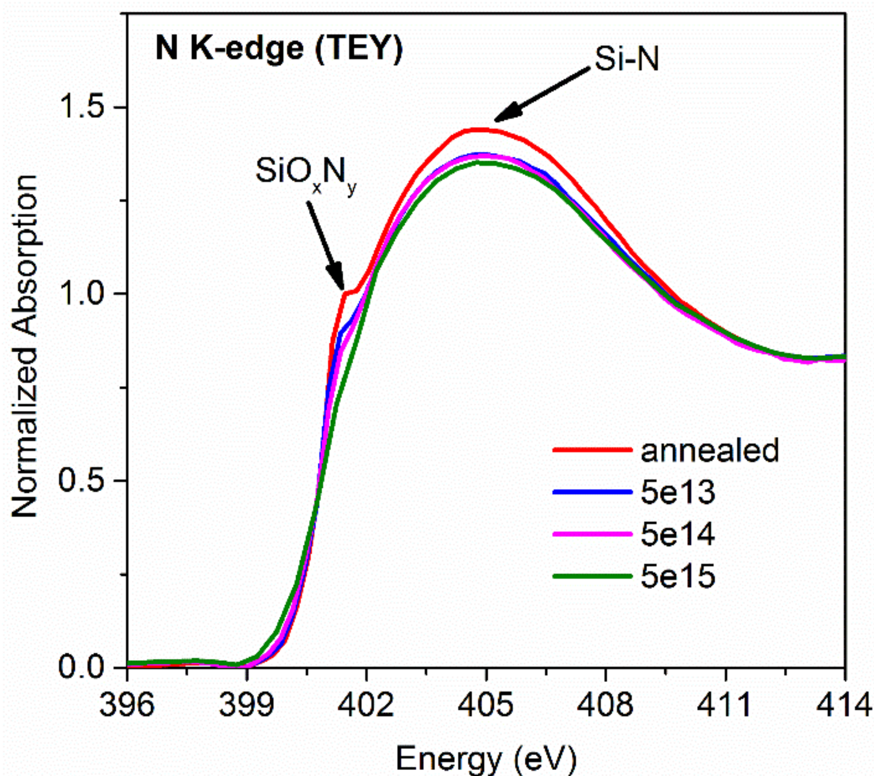


**Fig.4.6:** TEY XANES spectra at the N K-edge for annealed $Si_3N_4$ and $Si_3N_4$ films implanted with Al doses of $5\times10^{13}$, $5\times10^{14}$ and $5\times10^{15}$ atom/cm$^2$.

XANES measurements at the Al K-edge were collected for samples 5e11, 5e13 and 5e15, in order to examine the changes in composition at the lowest, median and highest

doses of Al. Fig.4.7(a) shows the normalized absorption spectra for sample 5e15 while Fig.4.7(b) shows the absorption spectra for samples 5e11 and 5e13. The sample with the highest dose (sample 5e15) dose displays a very distinct peak around 1565eV. No Al related features are observed for samples 5e11 and 5e13.

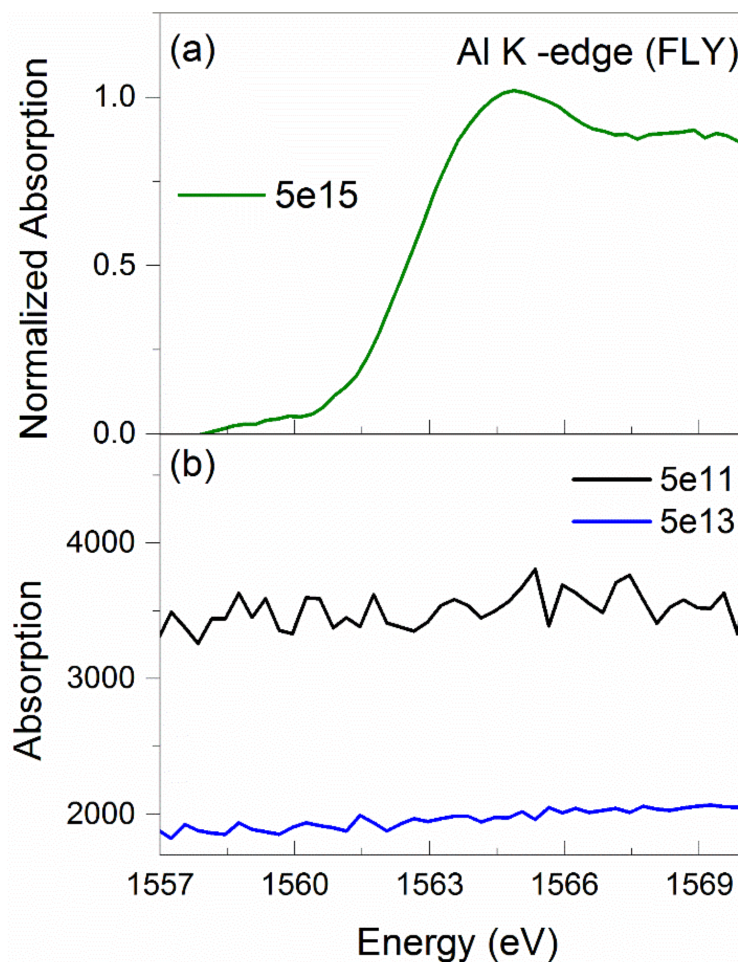


**Fig.4.7:** (a) Normalized XANES spectra of $Si_3N_4$ implanted with $5\times10^{15}$ ions/cm$^2$ of Al. (b) Raw XANES spectra at the Al K-edge for $Si_3N_4$ implanted with a dose of $5\times10^{11}$ and $5\times10^{13}$ ions/cm$^2$ of Al.

## 4.4 Discussion

The relatively wide bandgap of stoichiometric $Si_3N_4$ makes it an inherently poor light emitter. This is shown in Fig.4.1 by the nearly zero light emission from our 'asis' and 'annealed' stoichiometric $Si_3N_4$ samples. This lack of PL is also observed in samples implanted with Al doses ranging from $5\times10^{11}$ to $5\times10^{13}$ atoms/cm$^2$. In Fig.4.1, we observe that the PL intensity increases for $Si_3N_4$ implanted with an Al dose that is equal to or greater than $5\times10^{14}$ ions/cm$^2$ followed by annealing at 600°C.

As the annealing temperature increases, the PL intensities for Al-implanted $Si_3N_4$ samples, and S parameter is going up consistently. From the S parameter difference spectra shown in Fig.4.3, we observe that this increase in the S parameter is due to the formation of positronium. This increase in positronium may be due to any number of changes in the material including hydrogen loss and impurity related defects. The loss of hydrogen is expected due to the loss of Si-H and N-H bonds within the material.[19] This is further supported by FTIR data, shown in Fig.4.4, which shows a loss of Si-H and N-H bonds after annealing. Other researchers have also partially attributed the increase in S parameter to the loss of hydrogen from the film.[19]

Also observed in FTIR data is a shift in the Si-H absorbance peak for samples implanted with $5\times10^{15}$ ions/cm$^2$ of Al dose followed by 600°C annealing. The increase in the wavenumber of the Si-H absorbance band after Al implantation and annealing can be explained based on changes in local coordination and electronegativity. The fact the electronegativity of Al is less than that of Si causes the bond length to decrease which in turn causes an increase in the Si-H absorbance band frequency. Furthermore, we perform

a rough estimation of the location of the Si-H and Al-H stretching frequencies using the following equations:

$$\bar{\upsilon} = \frac{1}{2\pi c}\sqrt{\frac{k(m_1 + m_2)}{m_1 m_2}} \quad (4.\ 2)$$

where *c* is the speed of light, $k$=5 × $10^5$ dyne/cm is the force constant for a single bond and $m_1$ and $m_2$ are the masses of the elements in the molecule. For Si-H and Al-H we get an estimate of 2956 $cm^{-1}$ and 2966 $cm^{-1}$, respectively, for the stretching frequencies. This estimate indicates that the location of the Al-H vibration peak should be slightly higher in wavenumber than that of Si-H. This suggests that the shift in wavenumber observed in FTIR data is most likely the result of Al-H bond formation. The loss of Si-H after implantation and annealing may indicate that more Si-dangling bonds are present in the film. The major defects found in $Si_3N_4$ are the Si-dangling bonds back-bonded to N, known as K centres ($Si{\equiv}N_3$ which can have three charge states), N- dangling bonds that are back-bonded to Si ($*N{=}Si_2$ which are known as $N_2$ centres and have three charge states), Si-Si, Si- and N- dangling bonds.[20, 21] Theoretical predictions made by Warren *et al*. indicate that when Si-Si bonds are present in the film they form both $\sigma^*$ states close to the $Si_3N_4$ conduction band and $\sigma$ states close to the valence band. Whereas Si- dangling bonds form a band state in the middle of the band gap.[21] The presence of this Si-dangling bond mid-gap state has been attributed to PL peak located around 2.5±0.1 eV.[5] This suggests that the luminescence seen at a dose of $5{\times}10^{14}$ atoms/$cm^2$ may partially be caused by the presence of Si-dangling bonds. The shift at the highest dose ($5{\times}10^{15}$ atoms/$cm^2$) maybe partly due to an increased number of Al-H bonds. Other bonds which may also be contributing to changes in the PL spectra as implantation dose increases are Si-Al and N-Al. These bonds

may arise from an increasing number of dangling bonds created as a result of ion implantation that then maybe capped by the implanted Al. The increase in PL intensity for samples annealed in vacuum compared to those annealed in forming gas may be the result of fewer Si-dangling bonds and a lower probability of Al-H, Si-Al and N-Al bonds being present in those annealed in forming gas.

The incorporation of Al into the $Si_3N_4$ matrix is also likely responsible for the downshift observed in the XANES measurements at the Si $L_{2,3}$-edge. The decrease in Si-N observed after implantation indicates a loss of Si-N bonds after implantation and annealing, also contributing to the increase in the S parameter. The loss of Si-N bonds further contributes to the formation of Si- and N- dangling bonds which increase the probability of recombination due to these dangling bonds. The incorporation of Al causes changes in the local environment around the Si-N bonds which results in the downshift seen in the Si-N peak with increasing Al dose that was observed in Fig.4.5. We observe that of the three Al doses measured at the Al K-edge, a signal was only measured for the sample with the highest dose (sample 5e15) which suggests that the peak observed at 1565 eV may be related to N-Al, Si-Al or Al-H bonds. The origin this peak will be discussed further in chapter 5.

FTIR results indicate that Al-H bonds are likely present in the film. These measurements also indicate that after implantation and annealing a large number of Si- and N- dangling bonds are present in the material. Furthermore, as implantation dose increases the number of Si- and N- dangling bonds also increases. Therefore, the probability of Si-Al and N-Al bonds forming in the material increases with increasing dose.

## 4.5 Conclusion

We have examined the optical properties of Al-implanted $Si_3N_4$ with for doses in the $5\times10^{11}$ to $5\times10^{15}$ ions/cm$^2$ range using photoluminescence (PL), positron annihilation spectroscopy (PAS), Fourier transform infrared spectroscopy (FTIR) and X-ray absorption near edge spectroscopy (XANES). We have shown that PL intensity increases for $Si_3N_4$ implanted with Al doses equal to or greater than $5\times10^{14}$ ions/cm$^2$ followed by annealing at 600°C. PL measurements for $Si_3N_4$ implanted with $5\times10^{15}$ ions/cm$^2$ of Al and annealed at different temperatures ranging from 200°C to 600°C showed an increase in PL intensity with an increase in annealing temperature.

A correlation between the increase in PL intensity and increase in S parameter value has been observed. The loss of hydrogen from the film appears to contribute to the increase in positronium observed for samples annealed at different temperatures and increase in the PL intensity. The loss of hydrogen from the films and the damage caused by ion implantation is observed to increase the number of Si and N dangling bonds present in the films. The presence of these Si and N dangling bonds appear to play a significant role in the increase in PL intensity observed for samples implanted with high doses of Al.

## 4.6 References

[1] P. Calta, P. Šutta, R. Medlín, and M. Netrvalová, "Impact of sublayer thickness and annealing on silicon nanostructures formation in a-Si:H/a-$SiN_x$:H superlattices for photovoltaics," *Vacuum,* vol. 153, pp. 154-161, 2018.

[2] A. Zelenina, S. A. Dyakov, D. Hiller, S. Gutsch, V. Trouillet, M. Bruns*, et al.*, "Structural and optical properties of size controlled Si nanocrystals in $Si_3N_4$ matrix: The nature of photoluminescence peak shift," *Journal of Applied Physics,* vol. 114, p. 184311, 2013.

[3] S. Kluska, K. Hejduk, K. Drabczyk, and M. Lipiński, "Optical properties and passivation effects of silicon nitride three layer stacks deposited by plasma enhanced chemical vapor deposition," *Physica status solidi (a),* vol. 213, pp. 1839-1847, 2016.

[4] N.-M. Park, C.-J. Choi, T.-Y. Seong, and S.-J. Park, "Quantum Confinement in Amorphous Silicon Quantum Dots Embedded in Silicon Nitride," *Physical Review Letters,* vol. 86, pp. 1355-1357, 2001.

[5] S. V. Deshpande, E. Gulari, S. W. Brown, and S. C. Rand, "Optical properties of silicon nitride films deposited by hot filament chemical vapor deposition," *Journal of Applied Physics,* vol. 77, pp. 6534-6541, 1995.

[6] H. R. Philipp, "Optical Properties of Silicon Nitride," *Journal of The Electrochemical Society,* vol. 120, pp. 295-300, 1973.

[7] Y.-N. Xu and W. Y. Ching, "Electronic structure and optical properties of a and b phases of silicon nitride, silicon oxynitride, and with comparison to silicon dioxide," *Physical Review B,* vol. 51, pp. 17379-17389, 1995.

[8] M. Akiharu, T. Yoshinori, K. Minoru, and S. Tatsuo, "Properties of Hydrogenated Amorphous Si-N Prepared by Various Methods," *Japanese Journal of Applied Physics,* vol. 24, p. 1394, 1985.

[9] X. J. Hao, E. C. Cho, G. Scardera, Y. S. Shen, E. Bellet-Amalric, D. Bellet*, et al.*, "Phosphorus-doped silicon quantum dots for all-silicon quantum dot tandem solar cells," *Solar Energy Materials and Solar Cells,* vol. 93, pp. 1524-1530, 2009.

[10] N. Garcia-Castello, S. Illera, J. D. Prades, S. Ossicini, A. Cirera, and R. Guerra, "Energetics and carrier transport in doped Si/$SiO_2$ quantum dots," *Nanoscale,* vol. 7, pp. 12564-12571, 2015.

[11] J. Liu, W. Zhang, and S. Liu, "$H_2$-Ar dilution for improved c-Si quantum dots in P-doped $SiN_x$:H thin film matrix," *Applied Surface Science,* vol. 396, pp. 235-242, 2017.

[12] F. Munakata, K. Matsuo, K. Furuya, Y. Akimune, J. Ye, and I. Ishikawa, "Optical properties of β-$Si_3N_4$ single crystals grown from a Si melt in $N_2$," *Applied Physics Letters,* vol. 74, pp. 3498-3500, 1999.

[13] Z. Mao, Y. Zhu, Y. Zeng, F. Xu, Z. Liu, G. Ma*, et al.*, "Investigation of Al-doped silicon nitride-based semiconductor and its shrinkage mechanism," *CrystEngComm,* vol. 14, pp. 7929-7933, 2012.

[14] Z. Huang, Z. Wang, F. Chen, Q. Shen, and L. Zhang, "Band structures and optical properties of Al-doped α-$Si_3N_4$: theoretical and experimental studies," *Ceramics International,* vol. 42, pp. 3681-3686, 2016.

[15] C. C. Cadogan, L. V. Goncharova, P. J. Simpson, P. H. Nguyen, Z. Q. Wang, and T. K. Sham, "Influence of hydrogen passivation on the luminescence of Si

quantum dots embedded in $Si_3N_x$," *Journal of Vacuum Science and Technology B: Nanotechnology and Microelectronics,* vol. 34, 2016.

[16] G. Dlubek and N. Meyendorf, "Positron Annihilation Spectroscopy (PAS)," in *Nondestructive Materials Characterization: With Applications to Aerospace Materials*, N. G. H. Meyendorf, P. B. Nagy, and S. I. Rokhlin, Eds., ed Berlin, Heidelberg: Springer Berlin Heidelberg, 2004, pp. 374-411.

[17] P. J. Schultz and K. G. Lynn, "Interaction of positron beams with surfaces, thin films, and interfaces," *Reviews of Modern Physics,* vol. 60, pp. 701-779, 1988.

[18] W.-Y. Ching, S.-D. Mo, and Y. Chen, "Calculation of XANES/ELNES Spectra of All Edges in $Si_3N_4$ and $Si_2N_2O$," *Journal of the American Ceramic Society,* vol. 85, pp. 11-15, 2004.

[19] D. Landheer, G. C. Aers, G. I. Sproule, D. W. Lawther, P. J. Simpson, G. R. Massoumi*, et al.*, "Positron beam study of annealed silicon nitride films," *Journal of Applied Physics,* vol. 79, pp. 2458-2462, 1996.

[20] W. L. Warren, J. Kanicki, and E. H. Poindexter, "Paramagnetic point defects in silicon nitride and silicon oxynitride thin films on silicon," *Colloids and Surfaces A: Physicochemical and Engineering Aspects,* vol. 115, pp. 311-317, 1996.

[21] W. L. Warren, J. Robertson, and J. Kanicki, "Si and N dangling bond creation in silicon nitride thin films," *Applied Physics Letters,* vol. 63, pp. 2685-2687, 1993.

# Chapter 5

# Optical Properties of Al- and P- Implanted Silicon-Rich Silicon Nitride

## 5.1 Introduction

Silicon nitride ($Si_3N_4$) has been explored as an alternative host for silicon quantum dots (Si-QDs) due to its smaller bandgap in comparison to silicon dioxide ($SiO_2$).[1, 2] Researchers have demonstrated that Si-rich $Si_3N_4$ can be used to producing Si-QDs/$Si_3N_4$ systems with the light emission spectrum strongly dependent on growth conditions.[3-5] While photoluminescence (PL) and, in some cases, electroluminescence (EL) can be obtained when $Si_3N_4$ is used as the host matrix, the emission intensity is still to low for a commercial product. [1, 2] As a result, various means of increasing the luminescence and charge carrier concentrations of this type of system has been a subject of exploration in the last decade.

To increase charge carrier concentration and modify optical properties of Si-QDs systems, researchers have explored doping Si-QDs using n- and p-dopants. However, most of these studies have focused on Si-QDs/$SiO_2$ systems doped with B and/or P.[6-8] The use of B and P dopants is very common in these studies as these dopants are typically used for doping bulk Si. These studies observed that dopant-induced defects and Auger processes in the Si-QDs resulted in PL quenching.[9-11]

Quenching effects have also been observed in studies investigating the use of B and Sb dopants in Si-QDs/$Si_3N_4$ systems.[12-14] Authors in these studies argue that this observation is evidence of Si-QD doping. As many studies have focused primarily on B and P dopants, there is still room to explore the effects other dopant elements would have on the optical properties of Si-QDs/$Si_3N_4$ systems and the mechanisms responsible for these observed properties.

Here we focus on the potential for Al and P ions to be incorporated into a Si-QDs/$Si_3N_4$ system and examine the mechanisms responsible for the changes in PL intensity. In chapter 4, we discussed the optical properties of stoichiometric PECVD $Si_3N_4$ implanted with Al as a function of implantation dose as well as annealing temperature. We show that the luminescence of $Si_3N_4$ was significantly increased at a high implantation dose and an annealing temperature of 600°C. Considering these findings, we now seek to explore the behaviour of Si-rich $Si_3N_4$, to examine the influence Al and P ions have on the optical properties of Si-rich $Si_3N_4$ films.

This chapter will examine the various mechanisms that may be contributing to the increased luminescence observed in our PL spectra for Al and P implanted Si-rich $Si_3N_4$. These include: (1) $Si_3N_4$ matrix doping, (2) doping of Si-QDs and (3) Si-QDs being passivated by the Al and P. The use of p-type and n-type elements will also allow us to examine the role the type of dopant has on the light emission of the samples.

## 5.2 Experimental

Silicon-rich silicon nitride (denoted SRSN) and stoichiometric silicon nitride (SiN, reference) films were deposited on Si (100) wafers ($\rho = 0.01$-$0.025\ \Omega$cm) using plasma enhanced chemical vapour deposition (PECVD) in an Edwards STS310 system at 750 mTorr and 300°C. Films were deposited using $SiH_4$ and $NH_3$ gas flow rates of 600:35sccm for SRSN films (with stoichiometry $Si_3N_3$) and 400:90 sccm for $Si_3N_4$ films. Selection of these growth conditions and stoichiometry of the resulting films was discussed previously.[3, 15] From our previous analysis of these films, stoichiometric composition corresponds to a N/Si ratio of 1.33, the H content is constant (15-20%), and the major change in properties is due to the N/Si ratio. Film thicknesses were measured to be $200 \pm 20$ nm using spectroscopic ellipsometry.

For ion implantation, we selected Al and P ions, as these elements have similar masses and implantation profiles, but have different chemical properties, solid state solubility, and diffusivity. SRIM-2008 was used to estimate the displacements per atom (dpa) for Al and P, as well as the target damage for the ions and energies used in this study.[16] For SRIM Monte Carlo simulations, the depth of the maximum damage for Al and P-implanted samples was found to be 44nm and 36nm respectively, with an assumed SRSN density of 3.00g/cm$^3$.[17, 18] At these depths using full cascade and knock-on calculations, the damage levels were found to be ~0.083±0.001 and ~0.095±0.001 vacancies/(Å ion). The percentage difference in target damage (dpa) was calculated to be ~5%, with Al- implanted dpa at 212 and P-implanted dpa at 201 for the implantation dose of $5\times10^{15}$ atoms/cm$^2$. All samples were implanted with Al ions using a 1.7MeV Tandem accelerator, at an incident energy of 50keV at 7° tilt at room temperature. The implantation doses were ranging from

$5\times10^{11}$ to $5\times10^{15}$ ions/cm$^2$ (denoted 5e11 to 5e15 which corresponds to the implantation dose). To compare the effects of ion bombardment on the observed optical properties, we also implanted SRSN samples with P ions with the same doses and implantation energy (denoted as SRSN_P_5e11 to SRSN_P_5e15). After implantation, all samples were annealed at 600°C in forming gas (95% $H_2$: 5% $N_2$) for 30 mins. These conditions were found to be optimal in our previous study of photoluminescence (PL) intensity vs. annealing temperature/time discussed in chapter 3.[3]

Room temperature PL measurements were carried out using a 405nm laser diode with 120mW power input, and a Mightex HRS-BD1-200 spectrometer. Fourier transform infrared (FTIR) (FTS 7000 Series DigiLab) spectrometry was used to evaluate chemical bonding. The characteristic IR peaks were analysed using the integrated absorbance of FTIR spectra.

X-ray absorption near-edge spectroscopy (XANES) measurements at the Si, N and Al K-edges, and Si $L_{2,3}$ -edge were carried out at the Canadian Light Source (CLS). Si, N and Al K-edge measurements were collected using the High Resolution Spherical Grating Monochromator (SGM) 11ID-1 beamline with a 45mm planar undulator (E= 0.25 to 2 keV, and an energy resolution of $2\times10^{-4}$ $\Delta E/E$). At the Si and Al K-edges, the total electron yield (TEY) was collected using a high energy (1700 lines/mm) grating to maximize photon flux. TEY and fluorescence yield (FLY) at the N K-edge were obtained using the low energy (600 lines/mm) grating. FLY measurements at the Si $L_{2,3}$-edge were collected using the variable line spacing plane grating monochromator (VLS PGM) 11ID-2 beamline. XANES spectra were normalized to the incident X-ray intensity ($I_0$) using Athena software.[19]

Elastic recoil detection (ERD) measurements were conducted with 2.9MeV $^{4}He^{+}$ ions at the Western Tandem accelerator. ERD spectra were collected for a dose of 3µC and detector angle of 30°. ERD spectra were calibrated using poly-oxydiphenylene-pyromellitimide, ($C_{22}H_{10}N_2O_5$, Kapton®) tape and data was fitted using SIMNRA software[20] to determine composition and film thickness.

## 5.3 Results

Fig.5.1(a) compares the PL spectra of the SRSN samples following annealing and implantation steps. The PL intensities shown in this figure have been normalized to a common but arbitrary scale. The PL peak position of our unannealed SRSN sample (SRSN_asis) is 2.00 eV while our annealed sample (SRSN_annealed) PL maximum shifted to 1.89 eV. We will use SRSN_annealed as our reference to help distinguish changes in the PL spectra caused by hydrogen passivation from those due to other processes.

We observe an ~40% increase in the PL intensity for sample SRSN_5e13 in comparison to SRSN_annealed, with no significant change in intensity and peak locations. When we increase the Al dose to $5\times10^{14}$ atoms/cm$^2$ (sample SRSN_5e14), we observe a ~50% increase in PL intensity compared to SRSN_annealed. At the highest dose of $5\times10^{15}$ atoms/cm$^2$ (sample SRSN_5e15), PL intensity decreases compared to sample SRSN_5e14; however, it is still 13% greater than SRSN_annealed.

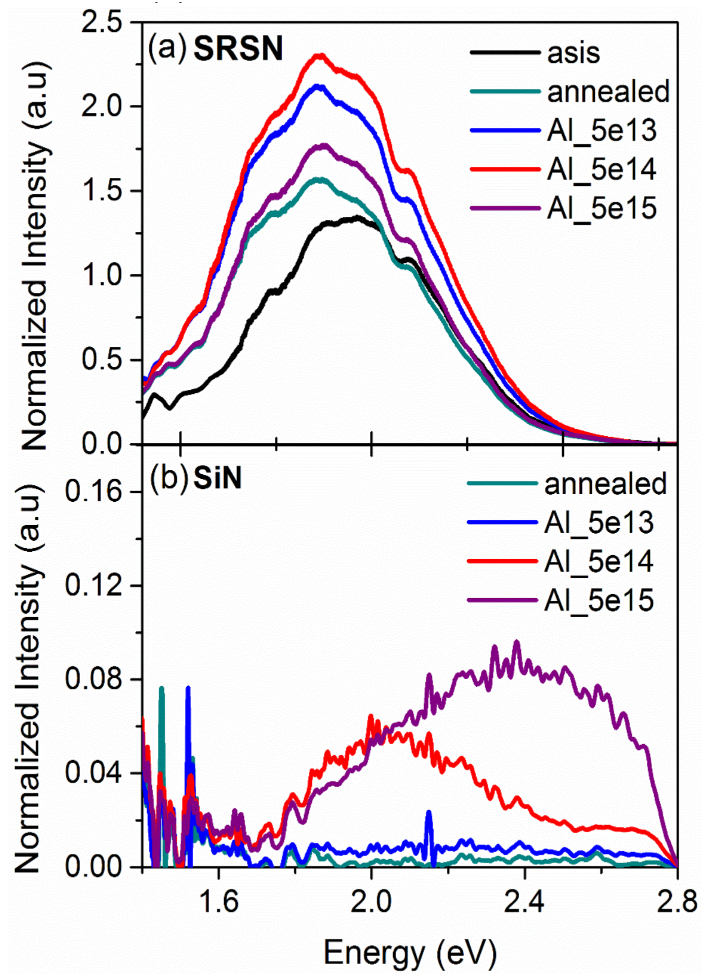


**Fig.5.1:** Photoluminescence spectra of Si-rich silicon nitride (SRSN) and stoichiometric silicon nitride (SiN) samples. PL intensity has been normalised to a common but arbitrary scale. (a) Shows the PL spectra of SRSN before and after annealing at 600°C in forming gas in comparison to SRSN samples that have been implanted with different doses of Al ranging from $5\times10^{13}$ to $5\times10^{15}$ ions/cm$^2$ (labeled Al_5e13, Al_5e14 and Al_5e15, respectively) followed by annealing at 600°C in forming gas. (b) PL spectra of SiN samples after annealing at 600°C in forming gas compared to SiN samples that have been implanted using the same Al dose range as SRSN samples followed by annealing at 600°C in forming gas.

For comparison, we have also implanted stoichiometric $Si_3N_4$ (denoted SiN) with Al using the same dose range as with SRSN samples. This set of samples is discussed in detail in chapter 4. As we can see in Fig.5.1(b), the PL intensity of all SiN samples is very low compared to SRSN. From this figure, we observe that at an implantation dose of $5\times10^{14}$ ions/cm$^2$ there is an increase in PL intensity with a PL peak position of 2.1 eV. A further improvement is observed when we increase the dose to $5\times10^{15}$ atoms/cm$^2$, with a shift in PL peak position to 2.4 eV.

To compare the luminescence of p-type and n-type dopants, we have also implanted SRSN samples with P. As mentioned above the use of P ions also help us to isolate, to an extent, effects due to ion bombardment. The PL spectra of P implanted SRSN samples (spectra presented in Appendix A3) were found to have a similar shape to those of Al-implanted samples. However, the PL intensity is different between Al and P, as presented in Fig.5.2, with lower PL intensity for P implanted samples compared to Al-implanted samples. The uncertainties presented in this plot are based on the difference of the intensity for several measurements taken at different regions of the same sample (~1%).

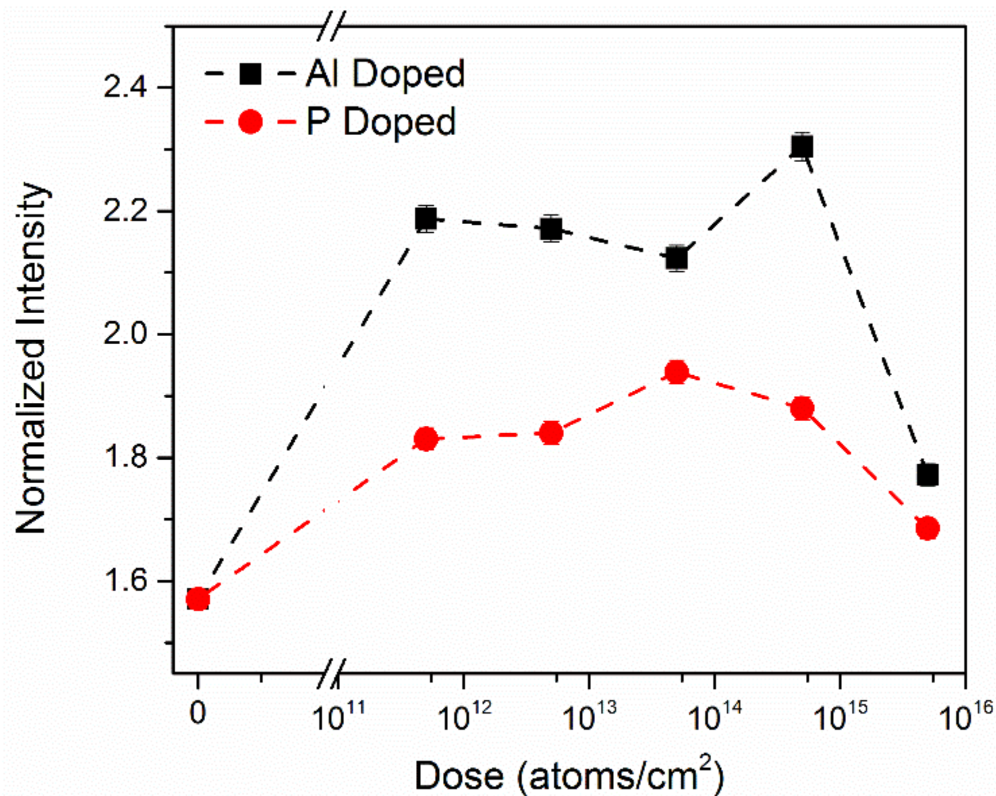


**Fig.5.2:** Maximum PL intensity for SRSN samples implanted with Al (black squares) and P (red dots) followed by 600°C anneal in forming gas compared to SRSN that is unimplanted but annealed under the same conditions (0 atoms/cm$^2$).

From our PL results, we observe that the incorporation of Al or P into the SRSN samples increases the PL intensity of the system. As shown in Fig.5.1(b) and discussed in chapter 4, the implantation of $Si_3N_4$ with Al ions, at a dose of $5\times10^{14}$ and $5\times10^{15}$ ions/cm$^2$, increases the PL intensity and may be contributing to the increase in PL intensity observed in Si-rich $Si_3N_4$ samples. X-ray absorption near-edge spectroscopy (XANES) measurements were conducted to examine the influence of the implanted ions on the electronic structure and local chemical environment of the SRSN samples. XANES

measurements at the Si and N K-edges showed slight decreases in the Si-N bonds (see Appendix A3).

The fluorescence yield (FLY) XANES spectra at the Si $L_{2,3}$-edge is shown in Fig.5.3(a). In Fig.5.3(a), we observe that after annealing SiN samples (sample SiN_annealed) there is an upshift in the Si-N peak location to 105 eV. For implanted samples, we observe that there is an increase in Si-N bonds along with a downshift in the position of the Si-N peak.

The FLY XANES spectra at the Si $L_{2,3}$-edge for SRSN samples implanted with $5\times10^{13}$, $5\times10^{14}$ and $5\times10^{15}$ atoms/cm$^2$ of Al and P are shown in Fig.5.3(b) and 5.3(c), respectively. In these figures, the XANES spectra of annealed SRSN is included as a reference. The Si $L_{2,3}$-edge spectra of our SRSN samples all possess a pre-edge feature at 100eV, which is attributed to Si-Si bonds and is found in literature related to Si-rich silicon nitride samples.[21] The Si-N peak is located around ~104.9eV, as highlighted by the dotted grey line in Fig.5.3(b) and 5.3(c). We observe that the Si-N peak is higher for P implanted samples than Al implanted samples. The Si-N peak position shifts to lower energy with increasing dose for both Al and P implantations.

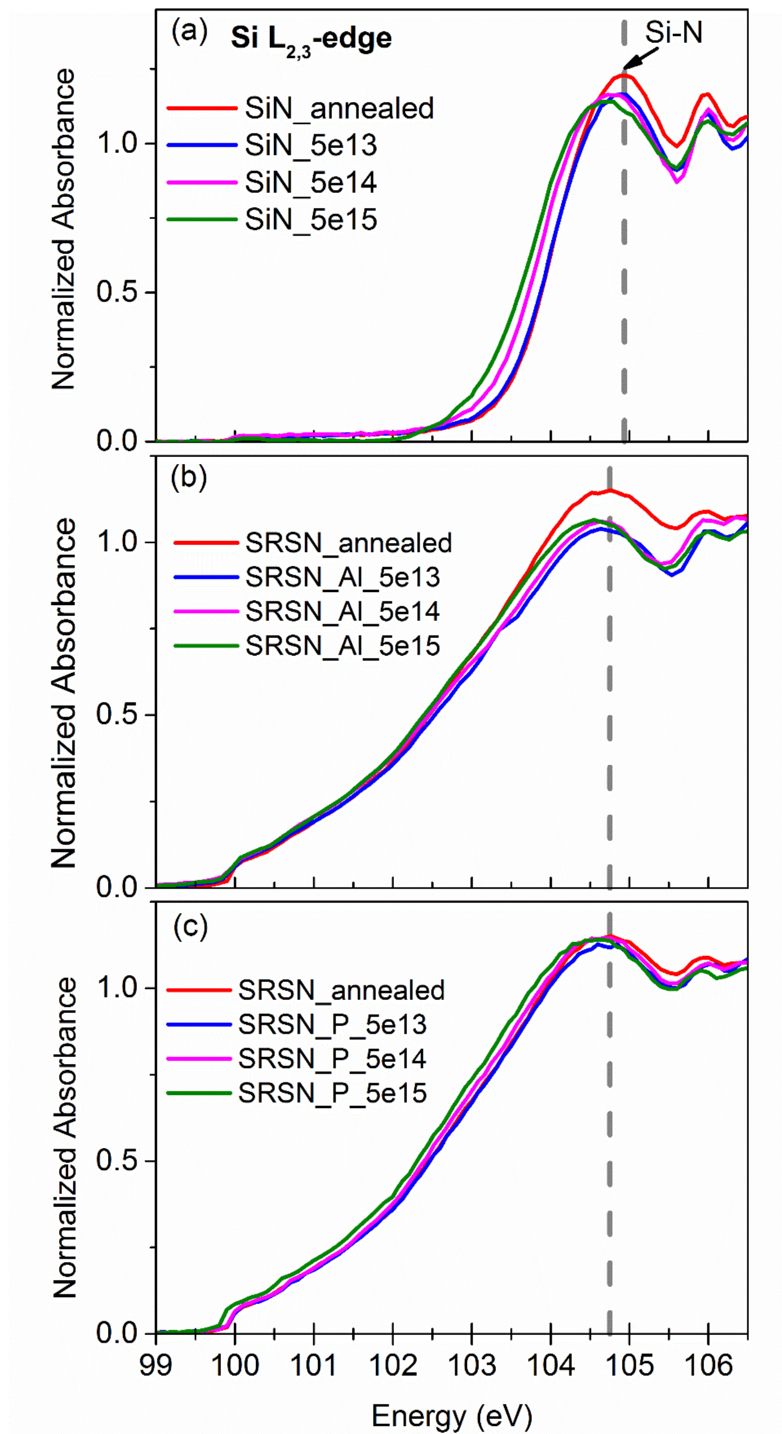


**Fig.5.3:** Fluorescence yield (FLY) XANES at the Si $L_{2,3}$-edge for SiN and SRSN samples. The Si-N peak at the Si $L_{2,3}$ edge is highlighted using grey dashed line, and the dose range of implanted samples is $5\times10^{13}$ to $5\times10^{15}$ atoms/cm$^2$. (a) The FLY XANES spectra of Al

implanted and annealed SiN samples are compared to the unimplanted and annealed SiN. The XANES of (b) Al implanted and (c) P implanted SRSN samples compared to unimplanted and annealed SRSN.

The XANES spectra at the Al K-edge for samples SRSN_Al_5e11, SRSN_Al_5e13, SRSN_Al_5e15 and SiN_5e15 are shown in Fig.5.4, and were chosen to compare changes at low, medium and high implantation doses. From this figure, we observe a pre-edge feature at ~1558eV for samples SRSN_Al_5e11 to SRSN_Al_5e13 and peak at ~1566 eV for all samples. At a dose of $5\times10^{15}$atoms/cm$^2$, we observe a significant decrease in this peak in addition to a shoulder around 1563eV. From XANES measurements carried out on SiN samples, we observed that no signal was observed for SiN_5e11 and SiN_5e13 (spectra are shown in chapter 4). However, an absorbance peak was observed for SiN_5e15, which is shown in Fig.5.4.

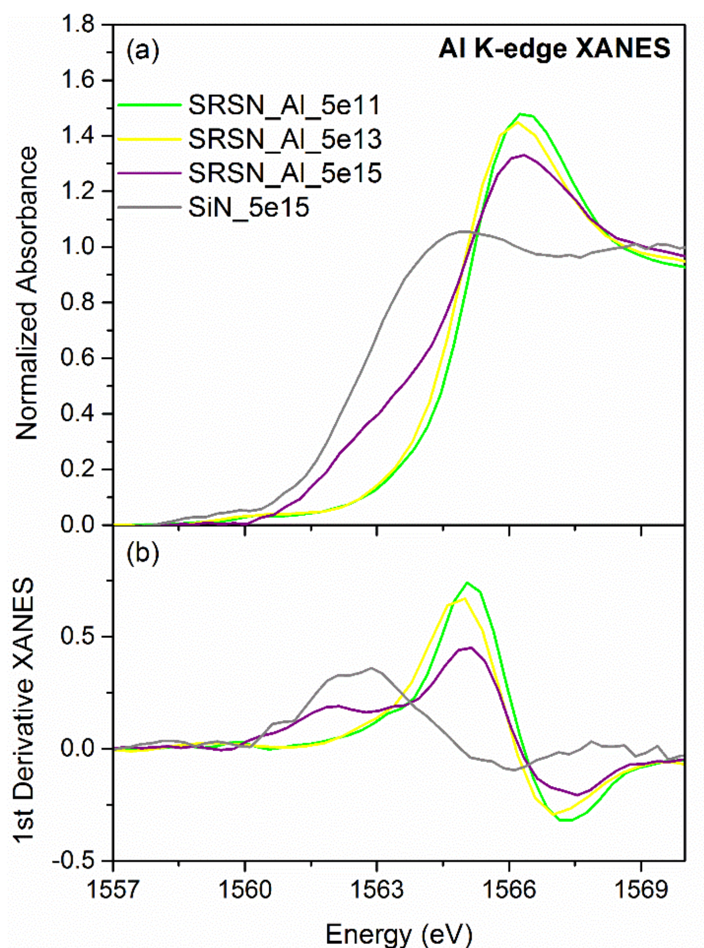


**Fig.5.4:** (a) The TEY XANES of Al implanted SRSN samples and SiN implanted with Al dose of $5\times10^{15}$atoms/cm$^2$ at the Al K-edge with inset showing the peak at 1566eV. (b) The first derivative of XANES spectra shown in (a).

FTIR measurements were also taken to complement XANES results. These measurements allow us to probe N-H, Si-H and Si-N bonds and how their concentration is affected by the incorporation of Al. The FTIR spectrum of SRSN_asis is shown as an example in Fig.5.5 (insert) where we observe the Si-N stretching mode between 700 and 1050cm$^{-1}$. The N-H bending mode is detected between 1050 and 1200cm$^{-1}$. While the Si-H stretching and N-H stretching modes are located at 2176 and 3346 cm$^{-1}$, respectively. The FTIR spectra of Al-implanted SRSN samples do not show any Al-related absorption

band due to the low concentration of Al used or Al staying at interstitial sites. To estimate the bond density, $N$, of Si-H and N-H from the FTIR absorption spectrum the following equation was used:[22]

$$N(X-H) = K(X-H) \times \int \alpha(v)dv \tag{5.1}$$

where $X$ = Si or N, $\alpha(v)$ is the absorption coefficient and $v$ is the wavenumber. The calibration factor $K(X-H)$ – values of the Si–H and N–H stretching modes are $1.7 \times 10^{20}$ and $2.8 \times 10^{20}$ $cm^{-1}$, respectively.[23] We observe that the bond density of Si-H and N-H decrease after samples are annealed, as shown in Fig.5.5.

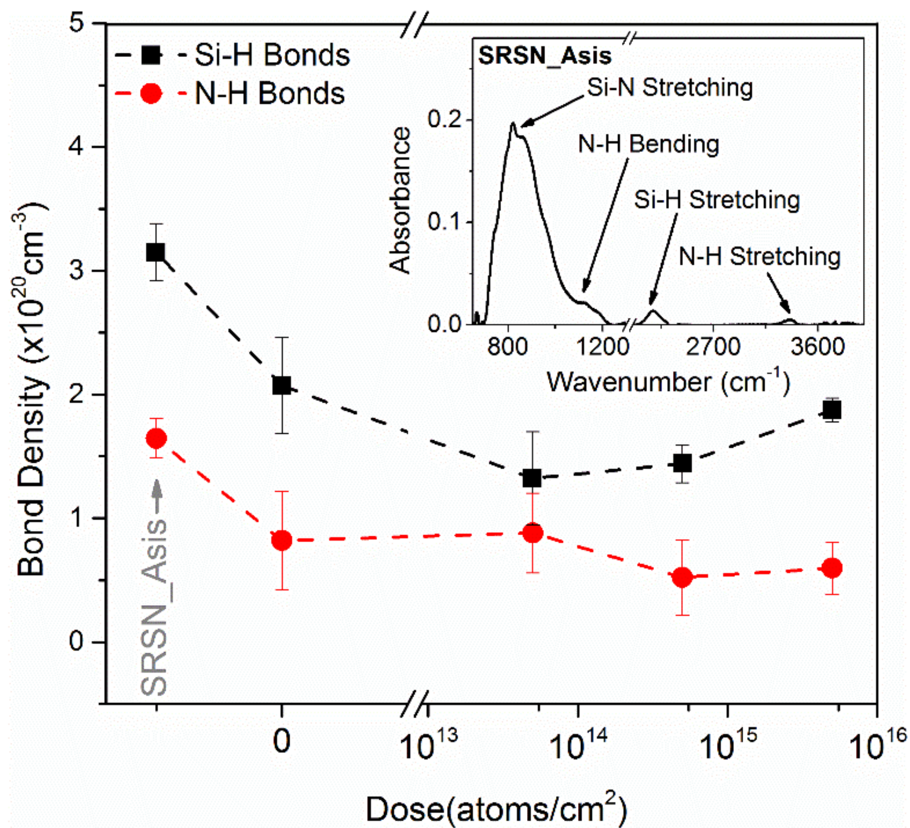


**Fig.5.5:** Bond density of Si-H (squares) and N-H (dots) for implanted and unimplanted samples. FTIR spectra for unimplanted and unannealed sample SRSN_Asis. (insert) The first point on both curves is for SRSN_Asis which is an unannealed and unimplanted SRSN

sample. All other points are for samples that have been annealed at 600°C in forming gas for 30mins.

Elastic recoil detection (ERD) analysis results showed that the hydrogen content for annealed samples, whether implanted or unimplanted, were roughly the same. The ERD results for samples implanted with $5\times10^{15}$ atoms/cm$^2$ of Al and P are shown in Table.5.1, along with asis and annealed SRSN samples. ERD spectra can be found in Appendix A3. As shown in Table.5.1, the hydrogen content (in at. %) in SRSN_asis samples was estimated to be 23.9±1.4% and 16.4±1.0% for SRSN_annealed. For Al and P implanted SRSN samples annealed to 600°C, the hydrogen content was found to be 16.3±1.0% and 16.8+1.0%, respectively. From table.5.1, it is clear to see that the hydrogen content of all annealed SRSN samples, implanted and unimplanted, are equal within experimental uncertainty.

| Sample | **HYDROGEN CONTENT (at. %)** |
|---|---|
| SRSN_asis | 23.9 ± 1.4 |
| SRSN_annealed | 16.4 ± 1.0 |
| SRSN_Al_5E15 | 16.3 ± 1.0 |
| SRSN_P_5E15 | 16.8 ± 1.0 |

**Table.5.1:** Hydrogen content (in at. %) based on elastic recoil detection measurements for SRSN_asis and SRSN_annealed in comparison to SRSN samples implanted with Al and P. SRSN_annealed, SRSN_Al_5e15 and SRSN_P_5e15 were all annealed in forming gas at 600°C for 30mins.

## 5.4 Discussion

PL results, shown in Fig.5.1(a), show a redshift between SRSN_asis and SRSN_annealed. This is consistent with an increase in the average Si-QDs size that has also been reported in the literature.[24] Furthermore, evidence of the presence of Si-QDs is provided by XANES results taken at the Si $L_{2,3}$ -edge, which shows the presence of the Si-Si bonds located at 100 eV. The presence of $Si^{o}$ phase has been used as evidence to support the formation of Si-QDs in $Si_3N_4$ films by other authors.[21]

From PL results, we also observe an increase in the PL intensity after annealing (see Fig.5.1). This increase in PL intensity is a known effect caused by the reduction of Si dangling bonds by hydrogen passivation.[3] An increase in PL intensity was observed for Al and P implanted samples. The following examines the role of matrix doping, the doping of Si-QDs and passivation on the PL intensity of implanted samples.

(1) **Matrix doping**. As shown in greater details in chapter 4, we have examined the band modification of $Si_3N_4$ by implanting Al of different doses and the effect of annealing temperatures on the optical properties of the material. PL results similar to those shown in Fig.5.1(b) have been reported by Huang *et al.*[25] with the PL maximum at 2.03 eV (610 nm) for 1.9-2.5% Al-doped $\alpha$-$Si_3N_4$ samples. This group also reported density-functional theory (DFT) calculations for Al in substitutional and interstitial positions in $\alpha$-$Si_3N_4$, and the PL peak at 610 nm was attributed to the electron transitions from the Al-Si states to Al-N and Si-N states. It was shown by the same group that the substitutional Al defects mainly affects the relative locations of the valence band and conduction band, with the band-gap reduction to 1.99eV. A correlation between the decrease of Si-H and N-H bonds and an increase in PL intensity was observed, suggesting that an abundance of Si-

and N- dangling bonds play a notable role in the PL intensity of Al implanted SiN. The low PL intensity of Al-implanted SiN samples suggests that although matrix doping may take place in our implanted SRSN samples, the contribution of this process to PL intensity is minimal in comparison to the overall increase observed in our implanted SRSN samples.

(2) **Doping of Si-QDs**. To explore the contribution of Si-QD doping to the PL intensity of our implanted samples, we examined theoretical studies on the doping of self-assembled Si-QDs. In a theoretical study conducted by R. Guerra *et al.*, which examined the preferential positioning of dopants and co-dopants in embedded and freestanding Si-QDs in $SiO_2$, the position of dopants was found to be highly dependent on the type of dopant introduced into the system.[26] Their study shows that dopants like Al and B prefer to be positioned at interfacial sites while dopants such as P and As prefer to migrate into the core of the Si-QDs, due to the higher solid state solubility. R. Guerra's study, therefore, suggests that the migration of Al into the Si-QD core is energetically unfavourable and is unlikely to be a contributing factor to the increase in PL intensity observed.[26] Since Si-QD doping would cause an increase in Auger recombination, we believe that the increase in PL intensity means that Si-QD doping is unlikely occurring in our Al implanted system.[11, 27-29] On the other hand, Guerra's findings, if extrapolated to a Si-QDs/$Si_3N_4$ system, do suggest that doping of Si-QDs is possible using P dopants. This may also explain why the PL intensity of P implanted is lower overall than Al implanted samples. In P doped samples, the competition between the PL quenching effect of Si-QD doping and radiative recombination processes may partially be responsible for the lower PL intensity observed for P implanted samples.

(3) **Passivation**. The next mechanism that may be responsible for the increase in PL intensity of implanted Si-QDs is impurity passivation of the Si-QDs. ERD and FTIR measurements were collected to investigate the role of this mechanism. The aim of these measurements was to determine whether there are any changes in hydrogen content between the implanted and unimplanted samples. The role which hydrogen passivation plays in increasing the PL intensity of self-assembled Si-QDs has been explored by our group and by other groups.[3, 30, 31] It has been found that the luminescence of SRSN samples decreases significantly with increased annealing temperature due to a loss of hydrogen from the sample, details found in chapter 3.[3]

If it is that the hydrogen content of implanted and unimplanted SRSN samples is the same even though there is an increase in PL intensity for implanted SRSN samples, then this helps to indirectly support the possibility that impurity passivation may be at play. This is because if the hydrogen content is the same, then one would expect the PL intensity to be roughly the same or even lower in the case of implanted samples because of implantation damage. If instead there is an increase in PL intensity for implanted samples even though the hydrogen content is the same, there must be some other element that is passivating the dangling bonds.

From ERD and FTIR results of SRSN samples, we observed that the hydrogen content for implanted and unimplanted samples after annealing at the same temperature were roughly the same. From the PL data presented in Fig.5.1 and 5.2, we observe that though the hydrogen content after annealing for implanted and unimplanted samples is the same, these samples do not have similar PL intensities. Instead, we see an increase in PL intensity for implanted samples which suggests that another mechanism is aiding in the

increase of luminescence. By considering the findings of R. Guerra *et al.*[26] and the increased luminescence of our implanted samples, we believe that some level of dopant passivation is occurring within our samples. Dopant passivation is further supported by D. I. Tetelbaum *et al.* who explored the influence of P and H on the PL of Si-QDs in $SiO_2$ and reported that P impurities did passivate many of the Si- dangling bonds.[32] This suggests both P and Al atoms are likely passivating the Si-QDs in our samples.

It was also observed that P implanted samples do not obtain a PL intensity as high as those implanted with Al. This is likely due to more non-radiative sites present in these samples which were caused by damage during implantation. This is supported by the fact that PL intensity is a maximum at a dose of $5\times10^{13}$ atoms/$cm^2$, which is a dose ten times lower than for Al implanted samples. Also from SRIM calculations, the damage levels were found to be ~$0.083\pm0.001$ and ~$0.095\pm0.001$ vacancies/(Å ion) for Al and P implantations, respectively. This, in addition to the difference in chemical bonding, would explain the difference in PL intensity observed for the different implanted species.

From Fig.5.4(a), we observe all Al implanted (implanted at low, medium and high Al doses) SRSN samples have a peak around 1566 eV, which is not the case for SiN samples. For SiN samples, this feature is only observed in the highest dose sample. In SRSN samples, we know that there is an excess amount of Si while in SiN samples there is not. We also know from chapter 4 that Si-H and N-H bonds are lost after implantation and annealing. Therefore, after implantation and annealing SiN would have a higher number of Si and N dangling bonds. The fact the peak in the XANES at Al K-edge is only observed at the highest dose for SiN suggests that the abundance of Si and N dangling bonds is what is interacting with the implanted Al to form Al-Si bonds, which are likely

what is observed in Fig.5.4(a) for the SiN sample. We argue this peak at the Al K-edge is observed even for SRSN samples implanted with the lowest dose of Al and the significant difference between SRSN and SiN sample is the concentration of Si in the film. This suggests that Si-Al bonds are likely being formed in SRSN samples implanted with Al. We infer that Si-P bonds are being formed in P implanted SRSN which causes the PL intensity of these samples to increase. This result helps us to attribute the peak seen in at the Al K-edge for our high dose SiN sample to Si-Al bonds. Therefore, our XANES measurements taken at the Al K-edge provide evidence that Al-Si (or P-Si for P implanted SRSN) bonds are forming in our implanted SRSN samples. These XANES results suggest that it is likely that the Si-QDs undergo some level of passivation by Al (or P). We acknowledge that there is a probability that Al-N (or P-N) bonds may also be forming in the samples, but we do not have any evidence of this from our measurements.

The shoulder seen for SRSN_Al_5e15 around 1562eV indicates that there is a significant change in our sample structure at the highest Al dose. This change in sample structure also correlates to the decrease in PL intensity observed for sample SRSN_5e15 in comparison to the lower dose samples. This structural change is likely causing an increase in non-radiative recombination sites, which causes a decrease in this sample's PL intensity.

## 5.5 Conclusion

The optical properties of Al-and P-implanted Si-rich silicon nitride (SRSN) has been examined using photoluminescence (PL), Fourier transfer infrared (FTIR) spectroscopy, X-ray absorption near-edge (XANES) spectroscopy and elastic recoil detection (ERD). We have shown that the PL intensity of P and Al implanted SRSN films increased in comparison to unimplanted SRSN samples, with larger increase for Al in comparison to P. We have also demonstrated that PL intensity is at a maximum using an Al dose of $5\times10^{14}$ atoms/cm$^2$, above which an increase in non-radiativative recombination sites causes PL intensity to decrease. For P- implanted SRSN films, the maximum PL intensity is achieved at a dose of $5\times10^{13}$ atoms/cm$^2$ and then decreases, possibily due to greater damage caused during the implantation of P compared to Al.

We infer that the increase in PL intensity for Al implanted SRSN is not attributed to the doping of Si-QDs while for P implanted SRSN samples this possibility can not be ruled out. We concluded that the mechanism that is contributing the most to the increase in PL intensity for our implanted SRSN samples is impurity atoms passivating the Si-QDs as impurity atoms migrate to the Si-QDs/$Si_3N_4$ interface. Doping of the nitride matrix is not as significant according to our findings. Further studies on the impact of annealing temperature on the optical properties of Al and P implanted Si-rich nitride are needed to obtain optimum concentration and annealing temperatures required for effective doping of Si-QDs embedded in silicon nitride.

## 5.6 References


[1] D. Li, J. Huang, and D. Yang, "Electroluminescence of silicon-rich silicon nitride light-emitting devices," in *2008 5th IEEE International Conference on Group IV Photonics*, 2008, pp. 119-121.

[2] O. Debieu, R. P. Nalini, J. Cardin, X. Portier, J. Perrière, and F. Gourbilleau, "Structural and optical characterization of pure Si-rich nitride thin films," *Nanoscale Research Letters,* vol. 8, pp. 31-31, 2013.

[3] C. C. Cadogan, L. V. Goncharova, P. J. Simpson, P. H. Nguyen, Z. Q. Wang, and T. K. Sham, "Influence of hydrogen passivation on the luminescence of Si quantum dots embedded in $Si_3N_x$," *Journal of Vacuum Science and Technology B: Nanotechnology and Microelectronics,* vol. 34, 2016.

[4] B.-H. Kim, C.-H. Cho, T.-W. Kim, N.-M. Park, G. Y. Sung, and S.-J. Park, "Photoluminescence of silicon quantum dots in silicon nitride grown by $NH_3$ and $SiH_4$," *Applied Physics Letters,* vol. 86, p. 091908, 2005.

[5] N.-M. Park, C.-J. Choi, T.-Y. Seong, and S.-J. Park, "Quantum Confinement in Amorphous Silicon Quantum Dots Embedded in Silicon Nitride," *Physical Review Letters,* vol. 86, pp. 1355-1357, 2001.

[6] S. Gutsch, A. M. Hartel, D. Hiller, N. Zakharov, P. Werner, and M. Zacharias, "Doping efficiency of phosphorus doped silicon nanocrystals embedded in a SiO2 matrix," *Applied Physics Letters,* vol. 100, p. 233115, 2012.

[7] D. Li, Y. Jiang, P. Zhang, D. Shan, J. Xu, W. Li*, et al.*, "The phosphorus and boron co-doping behaviors at nanoscale in Si nanocrystals/SiO2 multilayers," *Applied Physics Letters,* vol. 110, p. 233105, 2017.

[8] S. Gutsch, J. Laube, D. Hiller, W. Bock, M. Wahl, M. Kopnarski*, et al.*, "Electronic properties of phosphorus doped silicon nanocrystals embedded in SiO2," *Applied Physics Letters,* vol. 106, p. 113103, 2015.

[9] X. Hao, E. Cho, C. Flynn, Y. Shen, G. J. Conibeer, and M. Green, "Effects of boron doping on the structural and optical properties of silicon nanocrystals in a silicon dioxide matrix," *Nanotechnology,* vol. 19, p. 424019, 2008.

[10] D. Hiller, J. López-Vidrier, S. Gutsch, M. Zacharias, M. Wahl, W. Bock*, et al.*, "Boron-Incorporating Silicon Nanocrystals Embedded in $SiO_2$: Absence of Free Carriers vs. B-Induced Defects," *Scientific Reports,* vol. 7, 2017.

[11] A. Mimura, M. Fujii, S. Hayashi, and K. Yamamoto, "Quenching of photoluminescence from Si nanocrystals caused by boron doping," *Solid State Communications,* vol. 109, pp. 561-565, 1999.

[12] G. Shujuan Huang and Yong Heng So and Gavin Conibeer and Martin, "Doping of Silicon Quantum Dots Embedded in Nitride Matrix for All-Silicon Tandem Cells," *Japanese Journal of Applied Physics,* vol. 51, p. 10NE10, 2012.

[13] L. Jia Liu and Bin Liu and Xisheng Zhang and Xiaojia Guo and Shengzhong, "Effect of argon flow on promoting boron doping for in-situ grown silicon nitride thin films containing silicon quantum dots," *Nanotechnology,* vol. 28, p. 285202, 2017.

[14] D.-H. Ma, W.-J. Zhang, Z.-Y. Jiang, Q. Ma, X.-B. Ma, Z.-Q. Fan*, et al.*, "Effect of Si nanoparticles on electronic transport mechanisms in P-doped silicon-rich silicon nitride/c-Si heterojunction devices," *Materials Science in Semiconductor Processing,* vol. 50, pp. 20-30, 2016.

[15] L. V. Goncharova, P. H. Nguyen, V. L. Karner, R. D'Ortenzio, S. Chaudhary, C. R. Mokry*, et al.*, "Si quantum dots in silicon nitride: Quantum confinement and defects," *Journal of Applied Physics,* vol. 118, p. 224302, 2015.

[16] J. F. Ziegler, "SRIM - The Stopping and Range of Ions in Matter," ed, 2008.

[17] J. A. Taylor, "The mechanical properties and microstructure of plasma enhanced chemical vapor deposited silicon nitride thin films," *Journal of Vacuum Science & Technology A: Vacuum, Surfaces, and Films,* vol. 9, pp. 2464-2468, 1991.

[18] B. K. Yen, R. L. White, R. J. Waltman, Q. Dai, D. C. Miller, A. J. Kellock*, et al.*, "Microstructure and properties of ultrathin amorphous silicon nitride protective coating," *Journal of Vacuum Science & Technology A,* vol. 21, pp. 1895-1904, 2003.

[19] B. Ravel and M. Newville, "ATHENA, ARTEMIS, HEPHAESTUS: data analysis for X-ray absorption spectroscopy using IFEFFIT," *Journal of Synchrotron Radiation,* vol. 12, pp. 537-541, 2005.

[20] M. Mayer, *SIMNRA user's guide*. Garching, Germany: Max-Planck-Institut fur Plasmaphysik, 1997.

[21] P. R. J. Wilson, T. Roschuk, K. Dunn, E. N. Normand, E. Chelomentsev, O. H. Y. Zalloum*, et al.*, "Effect of thermal treatment on the growth, structure and luminescence of nitride-passivated silicon nanoclusters," *Nanoscale Research Letters,* vol. 6, p. 168, 2011.

[22] W. A. Lanford and M. J. Rand, "The hydrogen content of plasma-deposited silicon nitride," *Journal of Applied Physics,* vol. 49, pp. 2473-2477, 1978.

[23] F. Demichelis, F. Giorgis, and C. F. Pirri, "Compositional and structural analysis of hydrogenated amorphous silicon—nitrogen alloys prepared by plasma-enhanced

chemical vapour deposition," *Philosophical Magazine B,* vol. 74, pp. 155-168, 1996.

[24] B. Dridi Rezgui, A. Sibai, T. Nychyporuk, M. Lemiti, and G. Bremond, "Luminescence mechanisms in Si quantum dots-$SiN_x$ nanocomposite structures," *Journal of Vacuum Science & Technology B,* vol. 27, pp. 2238-2241, 2009.

[25] Z. Huang, Z. Wang, F. Chen, Q. Shen, and L. Zhang, "Band structures and optical properties of Al-doped α-$Si_3N_4$: theoretical and experimental studies," *Ceramics International,* vol. 42, pp. 3681-3686, 2016.

[26] R. Guerra and S. Ossicini, "Preferential Positioning of Dopants and Co-Dopants in Embedded and Freestanding Si Nanocrystals," *Journal of the American Chemical Society,* vol. 136, pp. 4404-4409, 2014.

[27] M. Fujii, S. Hayashi, and K. Yamamoto, "Photoluminescence from B-doped Si nanocrystals," *Journal of Applied Physics,* vol. 83, pp. 7953-7957, 1998.

[28] B. Puthen Veettil, L. Wu, X. Jia, Z. Lin, T. Zhang, T. Yang*, et al.*, "Passivation effects in B doped self-assembled Si nanocrystals," *Applied Physics Letters,* vol. 105, p. 222108, 2014.

[29] M. Lannoo, C. Delerue, and G. Allan, "Theory of radiative and nonradiative transitions for semiconductor nanocrystals," *Journal of Luminescence,* vol. 70, pp. 170-184, 1996.

[30] A. I. Yakimov, V V Kirienko, V A Armbrister, and A. V. Dvurechenskii, "Hydrogen passivation of self-assembled Ge/Si quantum dots," *Semiconductor Science and Technology,* vol. 29, p. 085011, 2014.

[31] P. C. Spruijtenburg, S. V. Amitonov, F. Mueller, W. G. van der Wiel, and F. A. Zwanenburg, "Passivation and characterization of charge defects in ambipolar silicon quantum dots," *Scientific Reports,* vol. 6, p. 38127, 2016.

[32] D. I. Tetelbaum, S. A. Trushin, V. A. Burdov, A. I. Golovanov, D. G. Revin, and D. M. Gaponova, "The influence of phosphorus and hydrogen ion implantation on the photoluminescence of $SiO_2$ with Si nanoinclusions," *Nuclear Instruments and Methods in Physics Research Section B: Beam Interactions with Materials and Atoms,* vol. 174, pp. 123-129, 2001.

# Chapter 6

# The Influence of Matrix Crystallinity on the Optical Properties of Si Implanted Aluminium Oxide

## 6.1 Introduction

Embedded silicon quantum dots (Si-QDs) in a host material have been the focus of many studies due to their potential use in optical and photovoltaic devices.[1-5] As mentioned previously, to qualify as a host the band gap of the material must be large enough for quantum confinement while at the same time permittivity should allow for dielectric amplification. As mentioned in chapter 1, $Si_3N_4$ is a matrix which has gain a lot of interest as a host material for Si-QDs as it satisfies the above criteria. In chapter 3-5, we have examined properties of Si-QDs embedded in $Si_3N_4$ and doped $Si_3N_4$.

Another dielectric satisfying these criteria is $Al_2O_3$, which has the added advantage of optically transparency, an important property for transparent devices.[6] Unlike $Si_3N_4$, the publication record for Si-QDs in $Al_2O_3$ is very low because of difficulty in producing Si-QDs in this material.[7-9] The cases where Si-QDs formation has been reported, the luminescence from these Si-QDs has been either very low or not present. Various hypotheses have been proposed for both the lack of Si-QDs formation and the lack of luminescence observed. For instance, Kovalev *et al.* have researched the optical and structural properties of Si-QDs in crystalline and amorphous $Al_2O_3$. Kovalev *et al.* concluded that Si-QDs did not form in their crystalline $Al_2O_3$ film but did form in amorphous $Al_2O_3$ films. Instead of photoluminescence (PL) peaks related to Si-QDs, this

group observed that only oxygen defect-related PL peaks were present. Similar PL results were obtained by Yerci *et al.*, who argued that the lack of PL from the Si-QDs was due to mechanical stress on the Si-QDs at the interface caused by lattice mismatch.[8, 10]

In this chapter, we focus on effects of $Al_2O_3$ crystallinity on the growth and optical properties of Si-QDs. As noted in chapters 4 and 5, defects in the matrix can strongly impact the optical properties of the Si-QDs. Different crystallographic forms of $Al_2O_3$ were reviewed in section 1.3.2 of this thesis. Remarkably, crystalline $Al_2O_3$ material has optical properties that can be modified by introduction of defects, or colour centres. Fig.6.1 illustrates the main types of oxygen defects, which are F (oxygen vacancies with two electrons, $e^-$), $F^+$ (oxygen vacancies with one $e^-$), $F_2$ (oxygen divacancies with four $e^-$,s), $F_2^+$ (oxygen divacancies with three $e^-$,s) and $F_2^{2+}$ (oxygen divacancies with two $e^-$,s) centres.

.

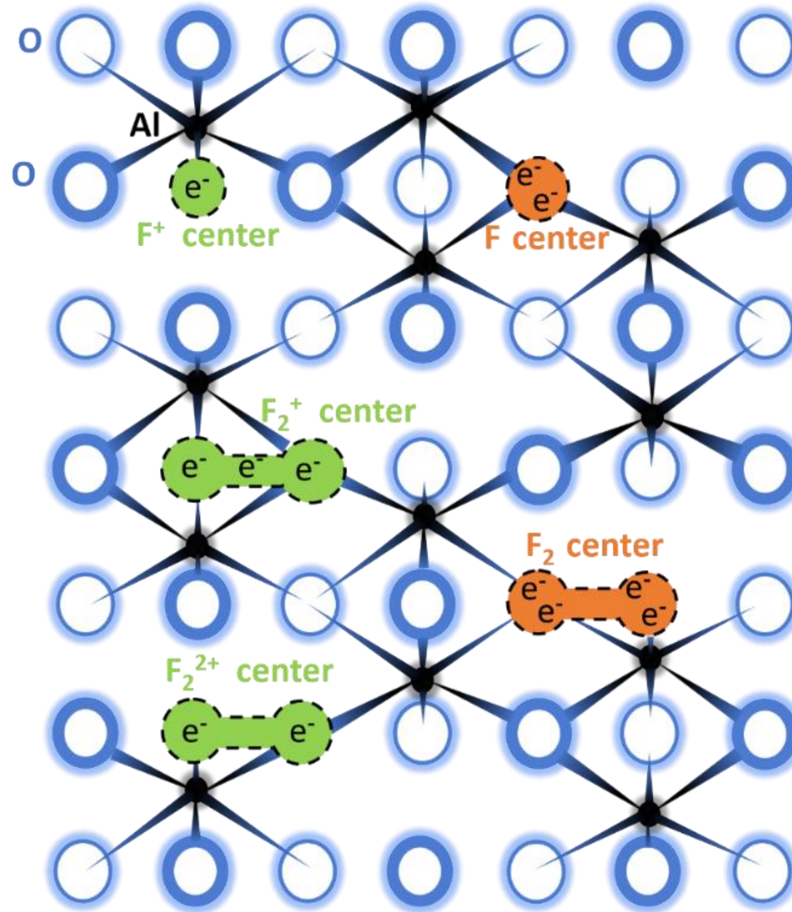


**Fig.6.1:** Structure of α-$Al_2O_3$, projected on (2110) plane with oxygen monovacancies ($F^+$ and F centres) and the oxygen divacancies ($F_2$, $F_2^+$ and $F_2^{2+}$ centres). All Al (filled small circles) are in the plane of the paper, while the oxygen atoms are located above (thick open circles) or below (thin open large circles) this plane. Adapted from reference 11.[11]

These oxygen defects can be found in the intrinsic $Al_2O_3$ film or can be introduced by bombarding the film with particles (such as neutrons, electrons or energetic ions). Furthermore, these defects have latent excitation and recombination luminescence bands which are summarized in table.6.1.[8, 12-14]

**Table 6.1:** Table of defect centres found in $Al_2O_3$

| Defect Center | Description | Luminescence | |
|---|---|---|---|
| | | Latent excitation (in nm) | Recombination (in nm) |
| F | One oxygen vacancy with two electrons | 204 | 413 |
| $F^+$ | One oxygen vacancy with one electron | 232; 256 | 326 |
| $F_2$ | Two oxygen vacancy with four electrons | 303 | 516 |
| $F_2^+$ | Two oxygen vacancy with three electrons | 357 | 380 |
| $F_2^{2+}$ | Two oxygen vacancy with two electrons | 450 | 563 |

To study the impact of crystallinity on the optical properties of Si-implanted $Al_2O_3$ and the impact crystallinity has on the formation of Si-QDs, we compare anodized amorphous $Al_2O_3$, disordered $Al_2O_3$ produced by implanting oxygen ions into crystalline $\alpha$-$Al_2O_3$, and crystalline $\alpha$-$Al_2O_3$. There is an interesting interplay between defect luminescence channels observed in our PL and time-resolved PL (TRPL) measurements. Based on X-ray absorption near edge spectroscopy (XANES) and X-ray excited optical luminescence (XEOL) measurements, Si-QDs are less readily formed in an amorphous $Al_2O_3$ matrix, in comparison to disordered and crystalline $Al_2O_3$. Our findings contradict previous studies which showed that amorphous $Al_2O_3$ is a better candidate for Si-QDs formation than crystalline $Al_2O_3$.[8] We also have found the lack of luminescence from Si-QDs is mainly due to competing de-excitation pathways provided by defects (mainly oxygen and $Cr^{3+}$ impurities) within the matrix. However, the characteristic lifetimes of our samples, merit exploration for optoelectronic or radiation dosimetry devices where switching at characteristic lifetimes is necessary.

## 6.2 Experimental Details

Amorphous aluminium oxide films (denoted *a*-$Al_2O_3$) were produced by the electrochemical growth of amorphous nanoporous $Al_2O_3$ in phosphoric acid. First, 99.997% purity Al foil was electropolished in a 1:9 $HClO_4$ (70% in ethanol)/$C_2H_5OH$ (anhydrous) solution at 20V for 5 minutes at 10°C using a tantalum cathode. For anodization, a 5cm$^2$ circular area of the Al foil was exposed to 0.4M phosphoric acid ($H_3PO_4$) at 10$^0$C, for 5 hours at 100V, then rinsed with distilled water. To separate the $Al_2O_3$ film from the Al foil, the $Al_2O_3$ films were covered in two coats of a commercial lacquer before immersion in an etching solution (3 g of $CuCl_2{\cdot}2H_2O$, 100 mL of $H_2O$ and 100 mL of concentrated HCl) for 2 hours. Films were rinsed with distilled water then immersed in acetone for half an hour to remove the lacquer. To minimize $PO_4^{3-}$ groups trapped in the $Al_2O_3$ film, films were soaked in an ammonium solution then rinsed in distilled water. A schematic diagram of the electropolishing and anodization process is shown in Fig.6.2.

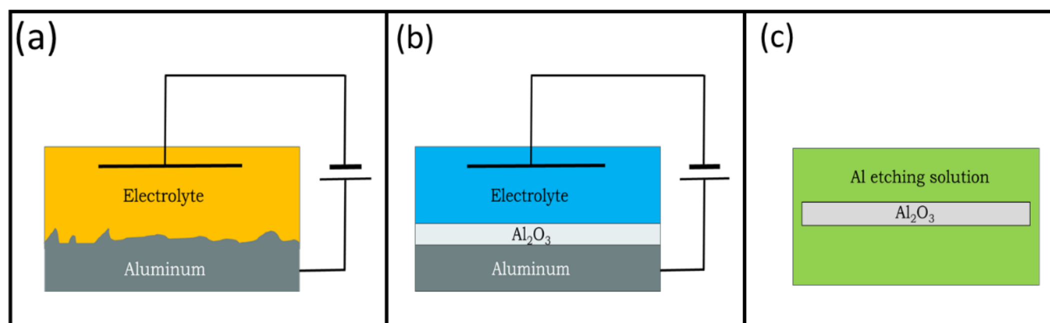


**Fig.6.2:** Schematic of the (a) electropolishing, (b) anodization, and (c) Al etching processes used for growing the amorphous aluminium oxide film.

To characterize thickness and porosity, scanning electron microscope (SEM) images of amorphous films were taken using a LEO 1530 Field Emission Scanning Electron Microscope. The films were found to have a pore diameter of 85±5 nm, an interpore distance of 110±10 nm, and a film thickness of 400±30 nm. Fig.6.3(a) and (b) show cross-sectional and top views of the amorphous aluminium oxide film. To confirm that the anodized films were indeed amorphous, powder X-ray diffraction measurements were conducted. The results of XRD measurements are shown in Appendix A4. These measurements confirmed that the films were amorphous.

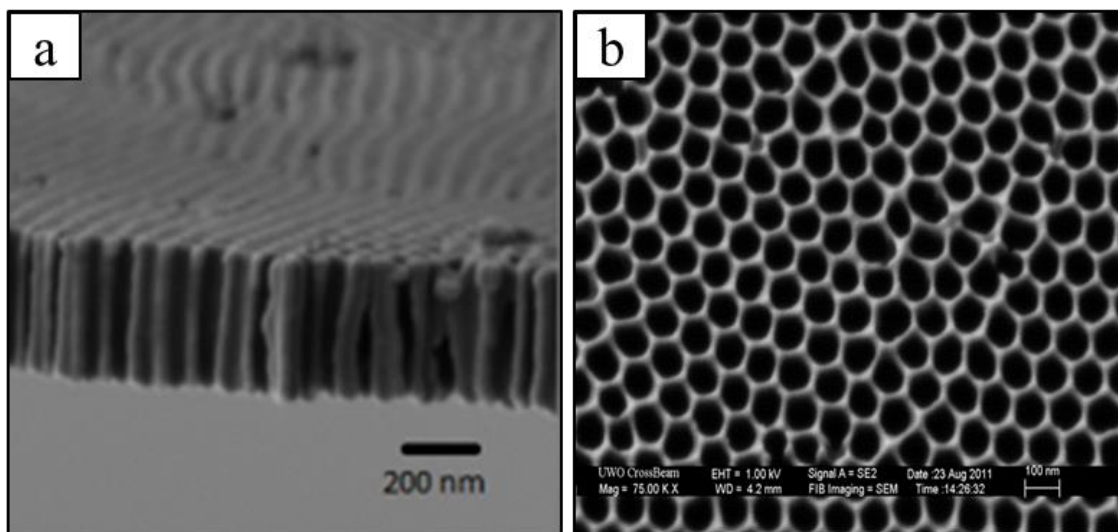


**Fig.6.3:** Scanning electron microscopy (SEM) images of anodized nanoporous aluminium oxide films. (a) The cross-sectional view of the film. (b) The top view of the film with the outline of the pores in grey.

Disordered samples (denoted *d*-$Al_2O_3$) were made by implanting single-side-polished crystalline $Al_2O_3$ samples with oxygen ions at an incident angle of 7°, energy of 90keV, and a dose of $8\times10^{16}$ ions/cm$^2$ at 300K. A crystalline-to-amorphous phase transition was achieved at this implantation condition with the surface layer (~350nm thick) becoming

disordered (amorphous). The diffusivity of oxygen in $\alpha$-$Al_2O_3$ is $4.2\times10^{-20}$ $cm^2$ $s^{-1}$ at 1473K, and the diffusion distance of oxygen does not exceed 2-3Å/hour. Single-side-polished sapphire samples ($\alpha$-$Al_2O_3$, MTI Corporation) were also studied and are denoted *c*-$Al_2O_3$.

All samples (*a*-$Al_2O_3$, *d*-$Al_2O_3$ and *c*-$Al_2O_3$) were implanted with Si ions at an incident angle of 7°, an energy of 90keV and dose of $8\times10^{16}$ ions/$cm^2$; and annealed at 1000°C in $N_2$ gas for 1 hour. Note that formation of Si-QDs was observed at similar implantation doses and annealing temperatures by Yerci, *et al.* and Kovalev *et al.*[8, 9] Additionally, the recrystallization of the damaged near-surface layer was reported at temperatures of 873K and higher.[10]

Photoluminescence (PL) spectra were measured using a 405±10 nm wavelength laser diode with a power input of 120mW. The laser diode was band-pass filtered (405 nm) and the emitted photons from the sample were high-pass filtered (> 450 nm). In our experimental setup, the incident beam was at 45° to the sample, and emitted photons were collected normal to the sample surface using a Mightex HRS-BD1-200 spectrometer with a wavelength range of 300-1050 nm. PL measurements were complemented with XANES and XEOL measurements, conducted at the Canadian Light Source using the High Resolution Spherical Grating Monochromator beamline (E= 0.25 to 2 keV and an energy resolution of $2\times10^{-4}$ E/ΔE). Details of XANES and XEOL experiments are described in Chapter 2. To briefly summarize here, in order to maximize photon flux, a low energy (600 lines/mm) grating was used for Al K-edge and O K-edge measurements while a high energy (1700 lines/mm) grating was used for Si K-edge measurements. Partial fluorescence yield was measured using a four Si drift detector array. XEOL was measured with the excitation

energy below, on and above the absorption edge. The step at the absorption edge was normalized to a value of 1.0 using Athena software.[15] All XANES and XEOL spectra were normalized to the incident photon flux collected on a refreshed Au grid ($I_0$).

## 6.3 Results

Fig.6.4 shows the photoluminescence ( PL) spectra for samples *a*-$Al_2O_3$, *d*-$Al_2O_3$ and *c*-$Al_2O_3$ before and after Si implantation and annealing. We observe that all samples show a peak that begins at the lower end of the detection limit (450 nm) and has a tail that extends up to 600 nm. Comparing the PL spectra between 450 and 600 nm for blank (unimplanted and unannealed) samples to samples after Si implantation and annealing, we observed that the PL intensity in this wavelength range decreases for samples *d*-$Al_2O_3$ and *c*-$Al_2O_3$. On the other hand, for *a*-$Al_2O_3$ only the $F_2$ centre component of the peak is reduced after implantation and annealing. As highlighted in Fig.6.4, this peak consists of several defect-related peaks, which are $F_2^{2+}$ and $F_2$ centres.

PL spectra for samples *d*-$Al_2O_3$ and *c*-$Al_2O_3$ both exhibits a sharp peak at 694 nm with a full width half maximum (FWHM) around 5 nm. This peak has been assigned to chromium ($Cr^{3+}$) impurities which are typically found in $Al_2O_3$ films and emit at this wavelength.[16] This luminescence is due to the d→d optical transition of $Cr^{3+}$ impurities with a $d^3$ electronic configuration. The optical transition leading to the emission is $^4A_{2g} \leftarrow ^4T_{2g}$, where $Cr^{3+}$ ions are sitting in vacant octahedral sites in the $Al_2O_3$ matrix or substitute for $Al^{3+}$ in octahedral sites.[17] Based on our particle-induced X-ray emission (PIXE) measurements (see Appendix A4), and supplier information on the *α*-$Al_2O_3$ substrates used in this study, trace amounts of $Cr^{3+}$ impurities are present. This suggests

that the peak seen in *d*-$Al_2O_3$ and *c*-$Al_2O_3$ at 694 nm is due to $Cr^{3+}$. From Fig.6.1, we observe that the peak intensity for $Cr^{3+}$ is most intense for c-$Al_2O_3$ and less intense for *d*-$Al_2O_3$. No PL peak related to this impurity is observed for sample *a*-$Al_2O_3$. However, this impurity was found in the unimplanted anodized $Al_2O_3$ films (*a*-$Al_2O_3$(blank)) using PIXE.

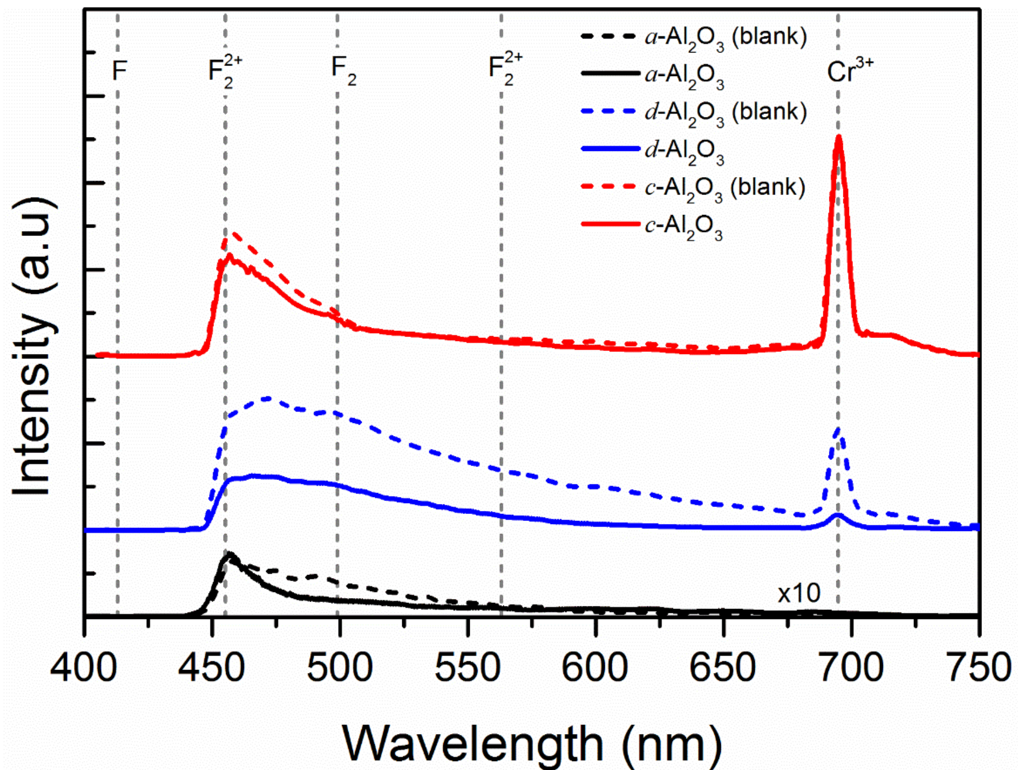


**Fig.6.4:** Photoluminescence spectra of *a*-$Al_2O_3$ (solid black line), *d*-$Al_2O_3$ (solid blue line) and *c*-$Al_2O_3$ (solid red line) samples implanted with Si ions and annealed at 1000°C (with a vertical offset and magnified where indicated for clarity). The matrix before implantation and anneal are labelled blank.

Time-resolved PL (TRPL) measurements were taken for all samples and the TRPL spectra of all these samples are shown in Appendix A4. It was found that samples *a*-$Al_2O_3$ and *d*-$Al_2O_3$ exhibited only short lifetimes, i.e., shorter than the time resolution of our system. Fig.6.5 shows the TRPL spectrum for sample *c*-$Al_2O_3$ fitted with multiple

exponentials decay function. The shortest lifetime component of sample *c*-$Al_2O_3$ was found to be 110 ns or shorter, i.e. the system resolution, and the longest lifetime component of the system was determined to be about 3 ms.

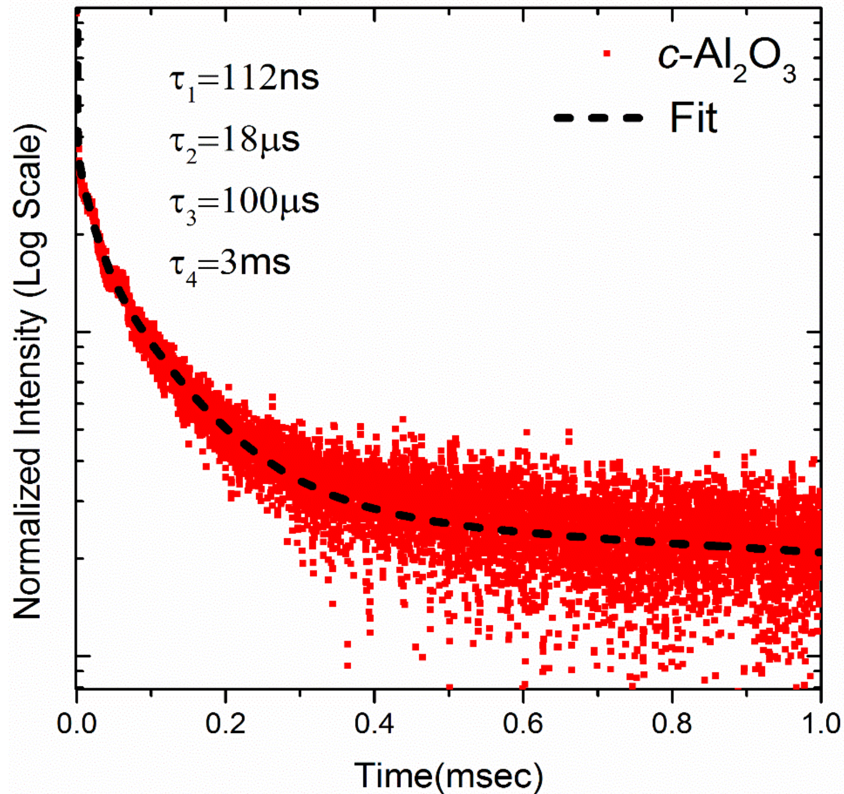


**Fig.6.5:** PL lifetime curve for samples *c*-$Al_2O_3$ fitted with a multi-exponential decay function.

Fig.6.6 shows the X-ray excited optical luminescence (XEOL) spectra of *a*-$Al_2O_3$, *d*-$Al_2O_3$ and *c*-$Al_2O_3$ excited at 540 eV (O K-edge), 1566 eV (Al K-edge) and 1841 eV (Si K-edge). In XEOL, the optical luminescence produced by either the radiative recombination of the electron-hole pairs or by energy transfers to defects was measured. We first examine the XEOL spectra between 200 and 550 nm, shown in Fig.6.6(a), (c) and (e). There is a broad low-intensity peak centered around 331 nm for all samples at an

excitation energy of 540 eV. This peak is attributed to $F^+$ centre emission and the low intensity at the O K-edge indicates that transfer from O sites to $F^+$ centres is very inefficient.[11]

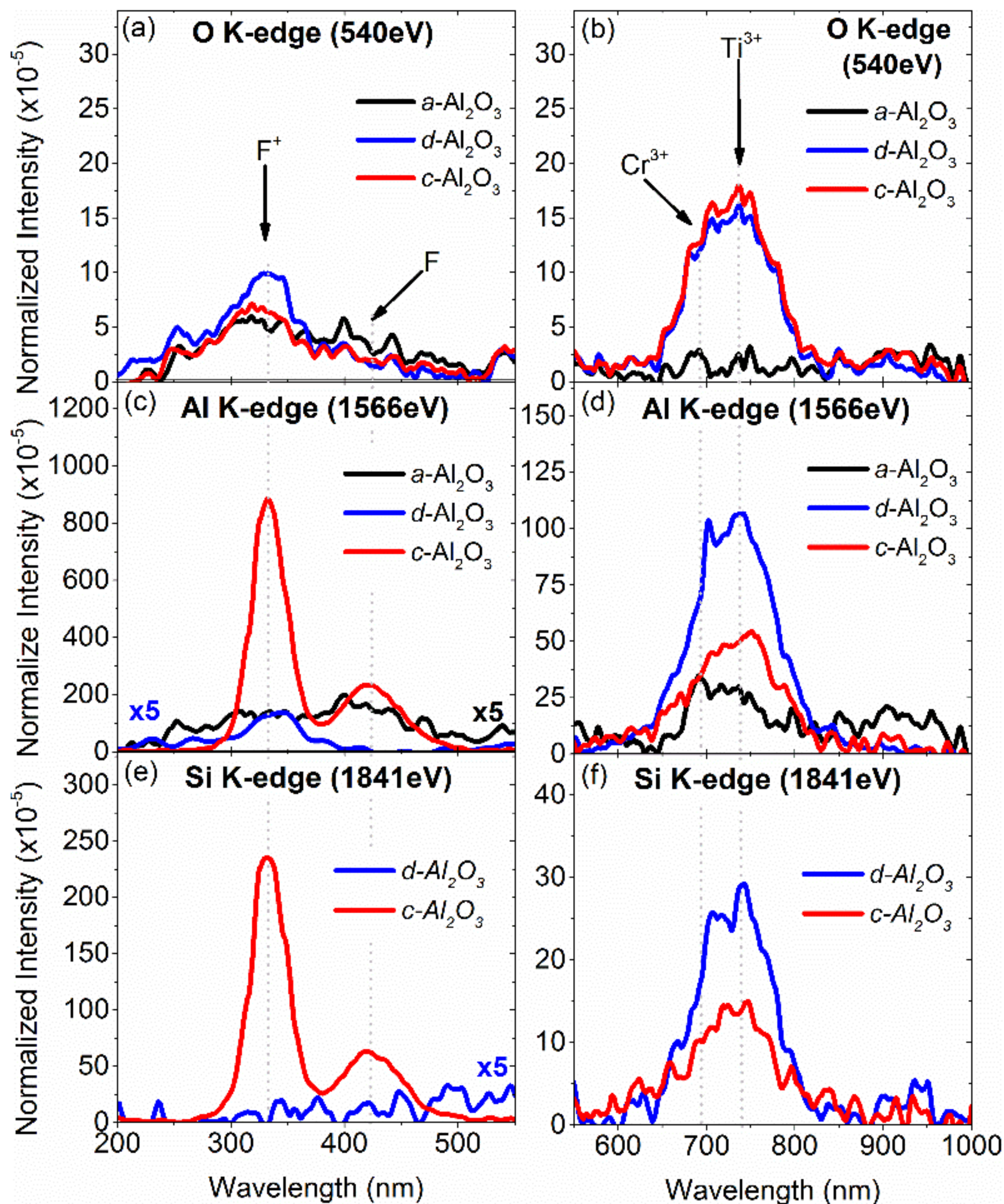


**Fig.6.6:** XEOL spectra at (a, b) 540eV and (c, d) 1566eV for samples *a*-$Al_2O_3$, *d*-$Al_2O_3$ and *c*-$Al_2O_3$. In (c) the XEOL spectra for *a*-$Al_2O_3$ and *d*-$Al_2O_3$ have been magnified by a factor 5 for the clarity. While at (e, f) 1841eV only the XEOL spectra for samples *d*-$Al_2O_3$

and *c*-$Al_2O_3$ are presented since *a*-$Al_2O_3$ had no XEOL emission at the Si K-edge. In (e), the XEOL spectra of *d*-$Al_2O_3$ is magnified by a factor of five for clarity.

At 1566 eV (Al K-edge), there is a significant increase in the 331 nm peak intensity for *c*-$Al_2O_3$, as shown in Fig.6.6(c). A less intense peak at 422nm, which is attributed to the presence of F centres, was also observed.[11, 13, 18] In contrast, the XEOL intensity of samples *a*-$Al_2O_3$ and *d*-$Al_2O_3$, between 200 and 500 nm, were lower than *c*-$Al_2O_3$ at the Al K-edge. No peak related to F centres was observed for sample *d*-$Al_2O_3$. When the beam energy was increased to 1841 eV (Si K-edge), there was a decrease in absolute XEOL intensity for sample *c*-$Al_2O_3$, which suggests that the Si K-edge de-excitation channel is less efficient for this sample. For this sample, it should be noted that the ratio of the two peaks in XEOL spectra in this wavelength range is consistent with that at the Al K-edge. There is also a decrease in XEOL intensity for sample *d*-$Al_2O_3$ when we move to the Si K-edge. No XEOL emission was observed for *a*-$Al_2O_3$ at the Si K-edge, which indicates that there was no energy transfer to Si sites and this supports argument that no Si-QDs are formed in this sample.

We now examine the XEOL spectra between 550 and 1000 nm. In this wavelength range, *a*-$Al_2O_3$ has virtually no XEOL signal at the O K-edge (540 eV) and Si K-edge (1841 eV) but a low intensity XEOL peak at the Al K-edge (1566 eV). The location of the peak observed with excitation at 1566 eV (Al K-edge) corresponds to the wavelength of emission for $Cr^{3+}$ impurities. This indicates that $Cr^{3+}$ impurities are also present in *a*-$Al_2O_3$, as they are in *d*-$Al_2O_3$ and *c*-$Al_2O_3$, even though it was not observed in PL measurements.

The XEOL spectra for samples *d*-$Al_2O_3$ and *c*-$Al_2O_3$ both display a peak centred at 726 nm at the O, Al and Si K-edges, with the highest intensity recorded at the Al K-edge. We have performed deconvolution on this peak (an example of this fit can be found in Appendix A4) and it was found to be made up of two peaks centred at 694 and 740nm. Based on the literature, and as seen in PL spectra, the peak located at 694nm is attributed to $Cr^{3+}$. The peak located at 740nm in the XEOL spectra was also observed in the XEOL spectra of samples before Si implantation (plots are shown in Appendix A4). This suggests that this peak is likely due to some matrix impurity and not due to Si nanoclusters being formed in the matrix. Based on the literature, the most likely impurity responsible for this emission is Ti.[19, 20] The fact that the intensity of this peak has a maximum along the Al K-edge, suggests that energy transfer from Al sites to $Cr^{3+}$ and Ti impurities is more efficient than from O sites. For XEOL at the Si K-edge, a significant decrease in peak intensity is observed and again no XEOL is detected for sample *a*-$Al_2O_3$.

XANES spectroscopy was used to examine the changes in the electronic structure and chemical composition of our samples. We first examine the XANES spectra at the O K-edge, shown in Fig.6.7(a). The O K-edge spectra originate from transitions from the O 1s state to the unoccupied states in the conduction band formed by the mixing of O 2p states with Al $t_{2g}$ and Al $e_g$ states, and also with Al 3p, 3s and 3p states.[21] The peaks at 542eV and 546eV (labelled 1 and 2) are attributed to the transition to unoccupied states formed by the mixing of O 2p with Al $t_{2g}$ and $e_g$ states. Peaks found at 554eV and 564eV (labelled 3 and 4) are assigned to transitions to states formed by O 2p mixing with Al 3p, 3s and 3p states. The presence of these spectral features is attributed to the $\gamma$-$Al_2O_3$ phase, which suggests that samples undergo recrystallization after annealing. This is examined in more detail

below. For all samples, there is also a significant pre-edge feature at ~525 eV up to the rising edge at ~537 eV. This pre-edge is attributed to beam-induced O defects and is typical of O K-edge XANES taken at this beamline.[22, 23] We also observed that the intensity of the peak at 546 eV (labelled 2) is greatest for sample *d*-$Al_2O_3$. It is known that the intensity of this peak (at 546 eV) corresponds with the concentration of oxygen in the film.[24, 25] Thus we conclude that the increase in intensity at 546 eV for sample *d*-$Al_2O_3$ is due to excess oxygen in the film.

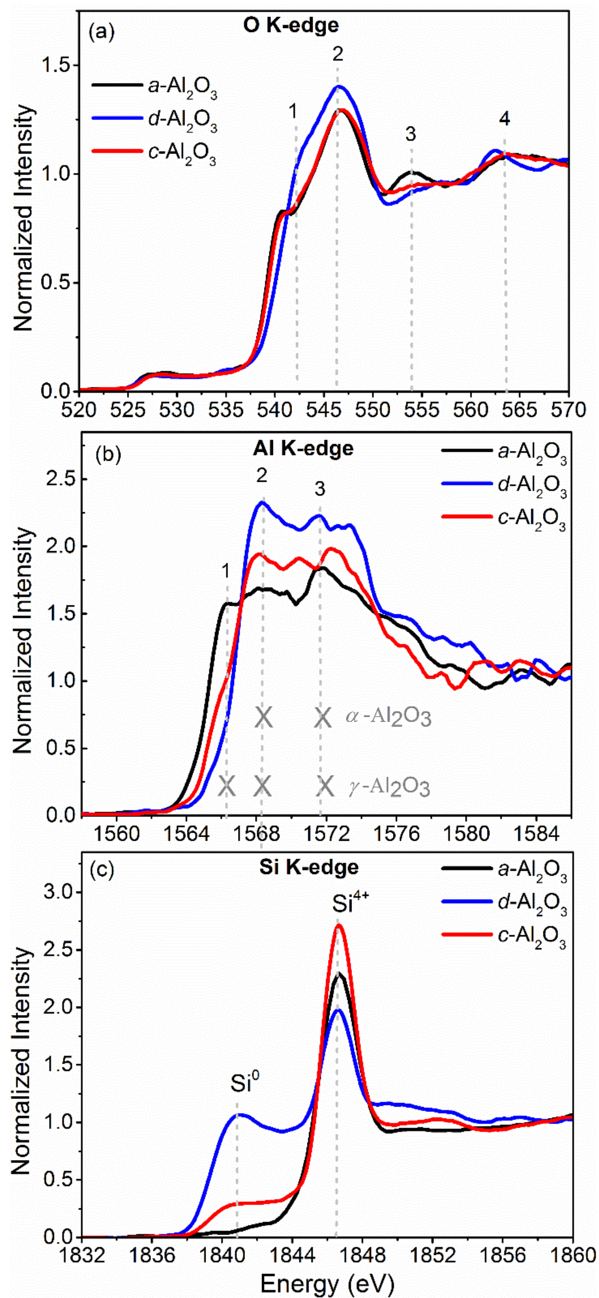


**Fig.6.7:** XANES spectra at (a) O K-edge, (b) Al K-edge and (c) Si K-edge, for *a*-$Al_2O_3$, *d*-$Al_2O_3$ and *c*-$Al_2O_3$ implanted with Si and annealed at 1000°C.

We also examined the XANES spectra at the Al K-edge, shown in Fig.6.7(b). We first examine the XANES spectrum of *a*-$Al_2O_3$ which has peaks at 1566, 1568 and 1572eV,

respectively, that are labelled 1, 2 and 3 in Fig.6.7(b). As discussed in chapter 1, $Al_2O_3$ has several different crystallographic phases with α and γ being most common.[26, 27] The presence of different phases of $Al_2O_3$ change the XANES spectra. By comparing the spectra of different phases, the phase or mixture of phases present in our samples can be identified. The three peaks located around 1565, 1567 and 1571 eV are characteristic of γ-$Al_2O_3$, which contains both 4-coordinated ($AlO_4$) and 6-coordinated ($AlO_6$) Al with a 1:2 ratio.[28, 29] In contrast, the XANES spectrum of $\alpha$-$Al_2O_3$ has two characteristic features found around 1568 and 1571 eV, which are due to the presence of only 6-coordinated Al.[30] Based on this interpretation, our samples indicate that varying degrees of recrystallization have occurred in the different samples annealed at the same temperature. The presence of the three characteristic peaks after annealing indicates that the *a*-$Al_2O_3$ samples possess the metastable γ phase. The *d*-$Al_2O_3$ and *c*-$Al_2O_3$ samples exhibit the crystalline α phase (based on XANES at the Al K-edge) and γ phase (based on XANES at the O K-edge) after annealing. The expected transformation of the amorphous structure to the crystalline one occurs in the following manner:[29, 31]

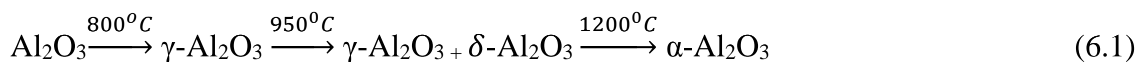

$$Al_2O_3 \xrightarrow{800^{o}C} \gamma\text{-}Al_2O_3 \xrightarrow{950^{0}C} \gamma\text{-}Al_2O_3 + \delta\text{-}Al_2O_3 \xrightarrow{1200^{0}C} \alpha\text{-}Al_2O_3 \quad (6.1)$$

For XANES measurements taken at the Si K-edge, we observe that all samples display two peaks located at 1841 and 1847 eV, labelled 1 and 2 in Fig.6.7(c). The first peak is attributed to the presence of $Si^0$ which indicates that Si-Si bonds are present in all three samples.[32, 33] Though the intensity of this peak varies between samples, the presence of this peak does suggest that Si-QDs (or Si clusters) are formed.[9, 34-36] The difference in intensity of $Si^0$ peak indicates that the samples contain different amounts of the $Si^0$ phase,

with sample *a*-$Al_2O_3$ containing the lowest amount even though the implantation dose was the same for all samples. We also observe that the $Si^0$ phase is greatest for sample *d*-$Al_2O_3$ in comparison to the other samples. For sample *c*-$Al_2O_3$, we observe that there was the less of the $Si^0$ phase than *d*-$Al_2O_3$ but much greater than the *a*-$Al_2O_3$ median. The second peak in Fig.6.7(c), located at 1847eV is attributed to the presence of $Si^{4+}$ phase. This phase is much greater in sample *a*-$Al_2O_3$ than the $Si^0$ phases. [37]

## 6.4 Discussion

Photoluminescence ( PL) results do not indicate the presence of Si-QDs as oxygen and impurity defects dominate the spectra.[11, 38, 39] We observed that the $Cr^{3+}$ impurity was the most intense in the PL spectra for sample *c*-$Al_2O_3$. The high PL intensity of $Cr^{3+}$ in this sample may help explain why the time-resolved PL (TRPL) de-excitation curves of the different samples were so vastly different. As mentioned in section 6.3, the TRPL de-excitation curves for samples *a*-$Al_2O_3$ and *d*-$Al_2O_3$ displayed very short lifetimes while sample *c*-$Al_2O_3$ possessed a long lifetime component of approximately 3ms. The origin of the fast lifetime observed for samples *a*-$Al_2O_3$ and *d*-$Al_2O_3$ is likely caused by $F^+$ center defects, which exhibit PL lifetimes below 70ns.[40]

On the other hand, the long lifetime component exhibited by sample *c*-$Al_2O_3$ is attributed to the presence of $Cr^{3+}$, for which other researchers have reported a PL lifetime between 3-4.3ms.[41, 42] This would mean that the long lifetime observed for sample *c*-$Al_2O_3$ is directly related to the dominance of $Cr^{3+}$ impurities. We recognize that there may be other unidentified defects in the system which may also be responsible for the long lifetime observed in our crystalline samples as we have found other unassigned lifetime components

(18 µs and 100µs) in our fit. Lifetimes on the µs scale have been observed for other Si-QDs systems.[43, 44]

Though evidence of Si-QDs emission was not observed in PL or XEOL measurements, evidence of the presence of Si-QDs was found in XANES spectra at the Si K-edge. Based on Si K-edge XANES of *d*-$Al_2O_3$, Si-QDs appear to form more readily in a disordered matrix in comparison to crystalline and amorphous matrices. This is inferred from the abundance of the $Si^0$ phase in the sample. Si-QDs may more readily form in the disordered matrix because of the radiation-damage-enhanced diffusion of the Si atoms: a similar effect has been reported for Si-QDs formed in $SiO_2$ films.[45]

Also found in XANES data was the presence of the $Si^{4+}$ phase. This phase is attributed to the formation of a $SiO_2$ layer at the Si-QDs/$Al_2O_3$ interface and/or the formation $SiO_2$ in the film.[37] The amount of interfacial verses stand-alone $SiO_2$ would likely be dependent on the abundance of Si-QDs formed in the film. In films with more Si-QDs, $SiO_2$ forming at the interface is more probable than with those with fewer. If we consider the ratio of peak intensities (at 1847 eV for $SiO_2$ and 1841 eV for $Si^0$) we can infer the likelihood of interfacial $SiO_2$ forming.[46] For sample *a*-$Al_2O_3$, the lack of Si-QD formation suggests that the $SiO_2$ formed in this sample is likely caused by $SiO_2$ forming in the film and not around the interface of Si-QDs. While for samples *d*-$Al_2O_3$ and *c*-$Al_2O_3$ the interfacial $SiO_2$ and $SiO_2$ forming in the bulk of the matrix are both probable. For sample *d*-$Al_2O_3$, the high abundance of the $Si^0$ suggests that the likelihood of Si-O bonds forming at that the interface of these clusters is more probable than $SiO_2$ forming in the bulk of the film. While for sample *c*-$Al_2O_3$, $SiO_2$ forming in either region (interfacial or matrix) is equally probable. This is because the high $Si^{4+}$ signal for sample *c*-$Al_2O_3$ may be caused by

many small Si clusters forming which would increase the number of interfacial Si-O bonds present in the film or by a few large Si clusters forming and the majority of Si-O bonds being formed in the matrix. Either of these scenarios is equally likely considering that no PL signal from cluster formation is observed in PL spectra of this sample. This would mean either too few Si-QDs are formed are too many small Si-QDs are formed and the incident energy of the laser used in PL measurements is not great enough to energize these Si-QDs.

In addition to oxidation, the recrystallization evident in XANES at the Al K-edge partially explains why there are no features due to Si-QDs in the PL spectra of our samples. Si-QDs tend to align with the matrix, which causes stress on the Si-QDs and this has been hypothesized to negatively affect the luminescence of Si-QDs.[8, 10] Furthermore, Si-dangling bonds formed at the Si-QDs/$Al_2O_3$ interface can negatively impact luminescence.[47, 48] These results, together with XEOL and PL data, suggest that though Si-QDs can be formed in both disordered and crystalline $Al_2O_3$, the Si-QDs luminescence in these materials is strongly impacted by the presence of oxygen vacancies and impurity ions, as well as transition/interface regions between Si-QDs and the $Al_2O_3$ matrix.

## 6.5 Conclusion

In summary, we have found that though Si-QDs are formed in $Al_2O_3$ films of varying crystallinity, the process of formation is strongly dependent on the crystallinity of the matrix. We have observed from XANES and XEOL measurements that the formation of Si-QDs is least favourable in an amorphous $Al_2O_3$ matrix, in comparison to disordered and crystalline matrices. The formation of Si-QDs was found to be highest in our disordered matrix, which was enhanced by radiation damage caused during the production of this host

matrix. Evidence of Si-QD formation was observed based on XANES measurement taken at the Si K-edge.

Though the presence of Si-QDs was observed in both our disordered and crystalline $Al_2O_3$ films, no luminescence from these QDs was observed in PL measurements. The lack of luminescence from the Si-QDs was found to be due to the presence of oxygen vacancies and impurities. The de-excitation pathways from these impurities and defects were found to be dominant, based on XEOL measurements. We note the luminescence due to $Cr^{3+}$ and F centres in $Al_2O_3$ can be applied for instance in the areas of environmental and space dosimetry.[49]

## 6.6 References

[1] E. G. Barbagiovanni, D. J. Lockwood, P. J. Simpson, and L. V. Goncharova, "Quantum confinement in Si and Ge nanostructures: Theory and experiment," *Applied Physics Reviews,* vol. 1, p. 47, 2014.

[2] E. G. Barbagiovanni, D. J. Lockwood, P. J. Simpson, and L. V. Goncharova, "Quantum confinement in Si and Ge nanostructures," *J. Applied Physics,* vol. 111, p. 034307, 2012.

[3] M. Araya, D. E. Díaz-Droguett, M. Ribeiro, K. F. Albertin, J. Avila, V. M. Fuenzalida*, et al.*, "Photoluminescence in silicon/silicon oxide films produced by the Pulsed Electron Beam Ablation technique," *Journal of Non-Crystalline Solids,* vol. 358, pp. 880-884, 2012.

[4] A. J. Kenyon, P. F. Trwoga, C. W. Pitt, and G. Rehm, "The origin of photoluminescence from thin films of silicon-rich silica," *Journal of Applied Physics,* vol. 79, pp. 9291-9300, 1996.

[5] T. Shimizu-Iwayama, K. Fujita, S. Nakao, K. Saitoh, T. Fujita, and N. Itoh, "Visible photoluminescence in Si+-implanted silica glass," *Journal of Applied Physics,* vol. 75, pp. 7779-7783, 1994.

[6] J. Robertson, "High dielectric constant oxides," *Eur. Phys. J. Appl. Phys.,* vol. 28, pp. 265-291, 2004.

[7] S. Yanagiya and M. Ishida, "Optical and electrical properties of Al2O3 films containing silicon nanocrystals," *Journal of Electronic Materials,* vol. 28, pp. 496-502, 1999.

[8] A. Kovalev, D. Wainstein, D. Tetelbaum, A. Mikhaylov, L. Pavesi, A. Ershov*, et al.*, "The electron and crystalline structure features of ion-synthesized nanocomposite of Si nanocrystals in $Al_2O_3$ matrix revealed by electron spectroscopy," *Journal of Physics: Conference Series,* vol. 100, p. 072012, 2008.

[9] S. Yerci, U. Serincan, I. Dogan, S. Tokay, M. Genisel, A. Aydinli*, et al.*, "Formation of silicon nanocrystals in sapphire by ion implantation and the origin of visible photoluminescence," *Journal of Applied Physics,* vol. 100, p. 074301, 2006.

[10] S. Yerci, I. Yildiz, M. Kulakci, U. Serincan, M. Barozzi, M. Bersani*, et al.*, "Depth profile investigations of silicon nanocrystals formed in sapphire by ion implantation," *Journal of Applied Physics,* vol. 102, p. 024309, 2007.

[11] M. Itou, A. Fujiwara, and T. Uchino, "Reversible Photoinduced Interconversion of Color Centers in $\alpha$-$Al_2O_3$ Prepared under Vacuum," *The Journal of Physical Chemistry C,* vol. 113, pp. 20949-20957, 2009.

[12] S. Yin, E.-q. Xie, C.-h. Zhang, Z.-g. Wang, L.-h. Zhou, Y.-Z. Ma*, et al.*, "Photoluminescence character of Xe ion irradiated sapphire," *Nuclear Instruments and Methods in Physics Research Section B: Beam Interactions with Materials and Atoms,* vol. 266, pp. 2998-3001, 2008.

[13] B. D. Evans and M. Stapelbroek, "Optical properties of the $F^+$ center in crystalline $Al_2O_3$," *Physical Review B,* vol. 18, pp. 7089-7098, 1978.

[14] B. D. Evans, G. J. Pogatshnik, and Y. Chen, "Optical properties of lattice defects in $\alpha$-$Al_2O_3$," *Nuclear Instruments and Methods in Physics Research Section B: Beam Interactions with Materials and Atoms,* vol. 91, pp. 258-262, 1994.

[15] B. Ravel and M. Newville, "ATHENA, ARTEMIS, HEPHAESTUS: data analysis for X-ray absorption spectroscopy using IFEFFIT," *Journal of Synchrotron Radiation,* vol. 12, pp. 537-541, 2005.

[16] E. R. Dobrovinskaya, L. A. Lytvynov, and V. Pishchik, "Properties of Sapphire," in *Sapphire: Material, Manufacturing, Applications*, V. Pishchik, L. A. Lytvynov, and E. R. Dobrovinskaya, Eds., ed Boston, MA: Springer US, 2009, pp. 55-176.

[17] M. N. Taran, K. Langer, A. N. Platonov, and V. Indutny, "Optical absorption investigation of Cr3+ ion-bearing minerals in the temperature range 77–797 K," *Physics and Chemistry of Minerals,* vol. 21, pp. 360-372, 1994.

[18] R. Jankowiak, K. Roberts, P. Tomasik, M. Sikora, G. J. Small, and C. H. Schilling, "Probing the crystalline environment of α-alumina via luminescence of metal ion impurities: an optical method of ceramic flaw detection," *Materials Science and Engineering: A,* vol. 281, pp. 45-55, 2000.

[19] L. E. Bausa, I. Vergara, F. Jaque, and J. G. Sole, "Ultraviolet laser excited luminescence of Ti-sapphire," *Journal of Physics: Condensed Matter,* vol. 2, p. 9919, 1990.

[20] D. I. Tetelbaum, O. N. Gorshkov, A. V. Ershov, A. P. Kasatkin, V. A. Kamin, A. N. Mikhaylov*, et al.*, "Influence of the nature of oxide matrix on the photoluminescence spectrum of ion-synthesized silicon nanostructures," *Thin Solid Films,* vol. 515, pp. 333-337, 2006.

[21] W.-Y. Ching and Y. N. Xu, *First-Principles Calculation of Electronic, Optical, and Structural Properties of α-*$Al_2O_3$ vol. 77, 2005.

[22] N. Jiang and J. C. H. Spence, "Interpretation of Oxygen K pre-edge peak in complex oxides," *Ultramicroscopy,* vol. 106, pp. 215-219, 2006.

[23] G. S. Henderson, D. R. Neuville, and L. Cormier, "An O K-edge XANES study of calcium aluminates," *Canadian Journal of Chemistry,* vol. 85, pp. 801-805, 2007.

[24] N. H. Tran, R. N. Lamb, L. J. Lai, and Y. W. Yang, "Influence of Oxygen on the Crystalline−Amorphous Transition in Gallium Nitride Films," *The Journal of Physical Chemistry B,* vol. 109, pp. 18348-18351, 2005.

[25] E. O. Filatova, A. A. Sokolov, Y. V. Egorova, A. S. Konashuk, O. Y. Vilkov, M. Gorgoi*, et al.*, "X-ray spectroscopic study of $SrTiO_x$ films with different interlayers," *Journal of Applied Physics,* vol. 113, p. 224301, 2013.

[26] I. Levin and D. Brandon, "Metastable Alumina Polymorphs: Crystal Structures and Transition Sequences," *Journal of the American Ceramic Society,* vol. 81, pp. 1995-2012, 1998.

[27] W. H. Gitzen, *Alumina as a ceramic material*. Columbus, Ohio: American Ceramic Society, 1970.

[28] T. H. Yoon, S. B. Johnson, K. Benzerara, C. S. Doyle, T. Tyliszczak, D. K. Shuh*, et al.*, "In Situ Characterization of Aluminum-Containing Mineral−Microorganism Aqueous Suspensions Using Scanning Transmission X-ray Microscopy," *Langmuir,* vol. 20, pp. 10361-10366, 2004.

[29] S. Cava, S. M. Tebcherani, I. A. Souza, S. A. Pianaro, C. A. Paskocimas, E. Longo*, et al.*, "Structural characterization of phase transition of $Al_2O_3$ nanopowders obtained by polymeric precursor method," *Materials Chemistry and Physics,* vol. 103, pp. 394-399, 2007.

[30] S. B. J. Tae Hyun Yoon , Karim Benzerara , Colin S. Doyle ,Tolek Tyliszczak ,David K. Shuh and Gordon E. Brown , Jr., "In Situ Characterization of Aluminum-

Containing Mineral−Microorganism Aqueous Suspensions Using Scanning Transmission X-ray Microscopy," 2004.

[31] Y.-I. Jung, H.-G. Kim, J.-Y. Park, D.-J. Park, and J.-H. Park, "Effect of heat-treatment on phase formation and crystallization of sol–gel derived $Al_2O_3$, $ZrO_2$–$Y_2O_3$, and $Ta_2O_5$ oxide coatings," *Journal of Asian Ceramic Societies,* vol. 3, pp. 217-220, 2015.

[32] P. Wilson, T. Roschuk, K. Dunn, E. Normand, E. Chelomentsev, O. Zalloum*, et al.*, "Effect of thermal treatment on the growth, structure and luminescence of nitride-passivated silicon nanoclusters," *Nanoscale Research Letters,* vol. 6, p. 168, 2011.

[33] P. R. Wilson, T. Roschuk, K. Dunn, M. Betti, J. Wojcik, and P. Mascher, "The Influence of Structural Ordering on Luminescence from Nitride- and Oxynitride-Passivated Silicon Nanoclusters," *ECS Transactions,* vol. 19, pp. 19-28, 2009.

[34] T.-K. Sham, "Nanoparticles and nanowires: synchrotron spectroscopy studies," *International Journal of Nanotechnology,* vol. 5, pp. 1194 - 1246, 2008.

[35] C. Meier, S. Lüttjohann, V. G. Kravets, H. Nienhaus, A. Lorke, and H. Wiggers, "Raman properties of silicon nanoparticles," *Physica E: Low-dimensional Systems and Nanostructures,* vol. 32, pp. 155-158, 2006.

[36] N. Daldosso, M. Luppi, S. Ossicini, E. Degoli, R. Magri, G. Dalba*, et al.*, "Role of the interface region on the optoelectronic properties of silicon nanocrystals embedded in $SiO_2$," *Physical Review B,* vol. 68, p. 085327, 2003.

[37] I. Coulthard , W. J. Antel Jr. , J. W. Freeland , T. K. Sham , S. J. Naftel , and a. P. Zhang, "Influence of sample oxidation on the nature of optical luminescence from porous silicon," *Applied Physics Letters,* vol. 77, pp. 498-500, 2000.

[38] Y. Song, C. H. Zhang, Z. G. Wang, Y. M. Sun, J. L. Duan, and Z. M. Zhao, "Photoluminescence of inert-gas ion implanted sapphire after 230-MeV Pb ion irradiation," *Nuclear Instruments and Methods in Physics Research Section B: Beam Interactions with Materials and Atoms,* vol. 245, pp. 210-213, 2006.

[39] B. S. Gourary and F. J. Adrian, "Wave Functions for Electron-Excess Color Centers in Alkali Halide Crystals11Work supported by the Bureau of Ordnance, Department of the Navy, under NORD 7386," *Solid State Physics,* vol. 10, pp. 127-247, 1960.

[40] B. D. Evans and M. Stapelbroek, "Optical properties of the $F^+$ center in crystalline $Al_2O$ 3," *Physical Review B,* vol. 18, pp. 7089-7098, 1978.

[41] H. Aizawa, E. Toba, T. Katsumata, S. Komuro, and T. Morikawa, "Chromium doped phosphor based fiber-optic thermometer," in *SENSORS, 2003 IEEE*, 2003, pp. 88-91 Vol.1.

[42] S. M. Borisov, K. Gatterer, B. Bitschnau, and I. Klimant, "Preparation and Characterization of Chromium(III)-Activated Yttrium Aluminum Borate: A New Thermographic Phosphor for Optical Sensing and Imaging at Ambient Temperatures," *The Journal of Physical Chemistry C,* vol. 114, pp. 9118-9124, 2010.

[43] H. Jayatilleka, D. Diamare, M. Wojdak, A. J. Kenyon, C. R. Mokry, P. J. Simpson, *et al.*, "Probing energy transfer in an ensemble of silicon nanocrystals," *Journal of Applied Physics,* vol. 110, p. 033522, 2011.

[44] L. V. Goncharova, P. H. Nguyen, V. L. Karner, R. D'Ortenzio, S. Chaudhary, C. R. Mokry*, et al.*, "Si quantum dots in silicon nitride: Quantum confinement and defects," *Journal of Applied Physics,* vol. 118, p. 224302, 2015.

[45] C. R. Mokry, P. J. Simpson, and A. P. Knights, "Role of vacancy-type defects in the formation of silicon nanocrystals," *Journal of Applied Physics,* vol. 105, p. 114301, 2009.

[46] Y. F. Zhang, L. S. Liao, W. H. Chan, S. T. Lee, R. Sammynaiken, and T. K. Sham, "Electronic structure of silicon nanowires: A photoemission and x-ray absorption study," *Physical Review B,* vol. 61, pp. 8298-8305, 2000.

[47] J. L. Cantin and H. J. von Bardeleben, *An electron paramagnetic resonance study of the Si(100)/$Al_2O_3$ interface defects* vol. 303, 2002.

[48] A. R. Wilkinson and R. G. Elliman, "Passivation of Si nanocrystals in SiO2: Atomic versus molecular hydrogen," *Applied Physics Letters,* vol. 83, pp. 5512-5514, 2003.

[49] L. Boetter-Jensen, S.W.S. McKeever, and A. G. Wintle, *Optically Stimulated Luminescence Dosimetry*: Elsevier Science, 2003.

# Chapter 7

# Conclusion and Future Work

## 7.1 Conclusion

The focus of this thesis is to examine the optical properties of Si-QDs embedded in $Si_3N_4$ as well as to determine the impact of $Al_2O_3$ film crystallinity on the formation and optical properties of Si-QDs. For Si-QDs embedded in silicon nitride ($Si_3N_4$), the role of various mechanisms on the PL intensity of the system were examined including: (1) the effect of annealing temperature and the film composition of non-stoichiometric silicon nitride films, (2) the role of Al doping of the host $Si_3N_4$ film, (3) doping Si-QDs and (4) the role of Al and P passivation of Si-QDs.

In chapter 3, the luminescence of Si-QDs embedded in $Si_3N_4$ was examined. To study the impact of sample composition and annealing temperature on the luminescence of Si-QDs, silicon nitride films of compositions ranging from $Si_3N_{2.72}$ to $Si_3N_{3.21}$ were investigated. The PL intensity of Si-QDs in $Si_3N_4$ was found to be a function of both composition and annealing temperature. Maximum PL intensity for the $Si_3N_{2.72}$ film was achieved after annealing at 400°C, while films with a composition of $Si_3N_{3.00}$ and $Si_3N_{3.15}$ showed maximum intensity after annealing at 600°C, and for a film composition of $Si_3N_{3.21}$ only slight variations in PL intensity were observed for annealing temperatures ranging from 400°C to 600°C. The reason for the increase in luminescence at lower temperatures (600°C or lower) for samples $Si_3N_{2.72}$, $Si_3N_{3.00}$ and $Si_3N_{3.15}$ was determined to be the result of a high Si content and hydrogen passivation of Si and N dangling bonds.

At high annealing temperatures (greater than 600°C), a significant decrease in the PL intensity of the system was observed for samples $Si_3N_{2.72}$, $Si_3N_{3.00}$ and $Si_3N_{3.15}$ while for sample $Si_3N_{3.15}$ (which was the sample with highest N content) this decrease was found to be less significant. Based on Fourier transform infrared (FTIR) spectroscopy measurements, it was found that there was a considerable decrease in Si-N, Si-H and N-H bonds at high annealing temperatures. We determined that the loss of hydrogen and nitrogen from the film caused the formation of Si- and N- dangling bonds within the system. These dangling bonds act as non-radiative recombination sites causing a decrease in the PL intensity of the system.

This thesis also explored the use of Al and P dopants in the Si-QDs/$Si_3N_4$ structure to improve the PL intensity of Si-QDs in $Si_3N_4$. In chapter 4, we examined the impact of Al implantation on the PL spectra for stoichiometric $Si_3N_4$. These results are important to determine the extent to which matrix doping might affect the PL spectra of a Si-QD/$Si_3N_4$ system. We found that PL intensity increased using an Al dose equal to or greater than $5\times10^{14}$ ions/cm$^2$ followed by annealing at 600°C. A correlation between the number of Si- and N- dangling bonds and the increase in the PL intensity of the system was established. It was determined that a high number of Si-and N- dangling bonds increased the probability of forming Si-Al and N-Al bonds, which based on the literature is reported to be responsible for the formation of colour centres in Al-doped $Si_3N_4$.

Chapter 5 was focused on the optical properties of Al and P implanted Si-rich $Si_3N_4$ films. We found that formation of Si-Al bonds played a significant role in increasing the PL intensity of Al implanted stoichiometric $Si_3N_4$ and Si-rich $Si_3N_4$ films. In this chapter,

it was also determined that the passivation of Si-QDs by Al and P ions was primarily responsible for the increase in PL intensity observed for Al and P implanted Si-rich $Si_3N_4$.

As mentioned in chapter 1, research into alternative host matrix to $SiO_2$ has gain traction with $Al_2O_3$ being a viable candidate for such applications. In chapter 6, the influence of $Al_2O_3$ crystallinity on the formation and optical properties of Si-QDs was examined. We found that though Si-QDs were formed in $Al_2O_3$ films of varying crystallinity, the process of formation is strongly dependent on the matrix. Our XANES and XEOL results indicate that Si-QDs formed more readily in disordered and crystalline $Al_2O_3$ films. The formation of Si-QDs in our disordered matrix was concluded to be enhanced by transient diffusion due to radiation damage caused during the production of the disordered film. The results of this study appear to contradict previous studies which report that Si-QDs were best formed in an amorphous $Al_2O_3$ film instead of a crystalline one.[1] Furthermore, it was found that no luminescence from Si-QDs was observed. This lack of luminescence from the Si-QDs was explained to be due to the presence of competitive radiative sites, such as oxygen vacancies and impurities. The de-excitation pathways from these impurities and defects dominate our XEOL and PL spectra.

## 7.2 Future Work

The results presented in this thesis demonstrate that an increase in PL intensity is achieved for Al and P implanted Si-rich silicon nitride ($Si_3N_4$). These results could be applied to the fabrication of Si-based luminescent devices. The findings of this research can be used to study the electrical and electroluminescence properties of Al and P implanted Si-rich $Si_3N_4$ as well as combining the mechanisms studied in this thesis with other light enhancing mechanisms such as plasmonic enhancement.

As discussed in this thesis, the doping of Si-QDs systems modifies the optical and electrical properties of the system. This modification can be advantageous for producing high-efficiency optoelectronic devices by increasing charge carrier concentration in the doped material. This thesis has demonstrated that the doping of stoichiometric and Si-rich $Si_3N_4$ samples can be used to increase the material's PL intensity. As a next step of understanding optical properties, an investigation into the behaviour of Al and P implanted Si-rich $Si_3N_4$ films at higher annealing temperatures (greater than 600°C) holds merit. This would allow for a study of the behaviour of these dopants in Si-rich $Si_3N_4$ films at high annealing temperatures. This type of study would allow for an examination of the migration of Al and P throughout the host matrix as well as their incorporation into the Si-QDs/$Si_3N_4$ or even into the core of the Si-QD.

The results presented in this thesis also open many opportunities for studies on the electrical properties of doped Si-QDs/$Si_3N_4$ systems. Some electrical measurements are included in Appendix B1 of this thesis, which shows the current-voltage characteristics of Al-implanted Si-rich $Si_3N_4$ films. Al implanted Si-rich $Si_3N_4$ films implanted with $5\times10^{14}$ and $5\times10^{15}$ atom/cm$^2$ show that the forward voltage value decreases with increasing Al

dose. Future work in this area can include a study on the effect of annealing temperature on different implantation doses, and charge mobility as a function of dose and annealing temperature.

Current research in Si photonics using plasmonic materials have been with Si-QDs embedded in $SiO_2$, with the majority using silver (Ag) or gold (Au) NPs.[2-4] There exist far fewer papers exploring the use of alternative plasmonic materials.[5] There have been even fewer papers which have examined the coupling of the luminescence of Si-QDs embedded $Si_3N_4$ with alternatives such as Al. The high abundance of Al makes it a very attractive candidate for use as a plasmonic material for luminescence enhancement. However, the optimization of Al nanostructure dimensions in order to observe such enhancements does prove a challenge. Both nanostructure shape and size need to be optimized for maximum PL enhancement.[6]

Preliminary studies which we have carried out have demonstrated that plasmonic enhancement can be used to increase the PL intensity of Si-QDs in $Si_3N_4$ films. We have examined the use of Al nanostructures deposited on the surface of Si-QDs/$Si_3N_4$ films. In this preliminary study, Al nanostructures were produced by depositing Al films that were 50 and 100nm thick through a polystyrene microsphere mask. More details can be found in Appendix B2. From PL measurements it was found that when 50 and 100 nm high Al nanostructures were deposited on the surface of Si-QDs/$Si_3N_4$ films, the PL intensity increased 2-fold. PL results can be found in Appendix B2.

These results show great promise for the coupling of plasmonic effects with the luminescence from Si-QDs/$Si_3N_4$ films. However, there is still a need to optimize the deposition method of the polystyrene mask, as forming a uniform monolayer of the

polystyrene beads has proved difficult using our current air-liquid method. Possible solutions to this issue may be: (1) varying the concentration of microspheres used in the deposition method, (2) the deposition rate of the microspheres on to the $Si_3N_4$ surface and (3) optimizing microsphere adhesion to the film surface through pre-treating the film with some kind of tailored adhesive. Combining this plasmonic effect with the increased luminescence of Al or P implanted Si-rich $Si_3N_4$ merits investigation as a potential avenue for further increasing the luminescence of Si-QDs/$Si_3N_4$ films.

## 7.3 References

[1] A. Kovalev, D. Wainstein, D. Tetelbaum, A. Mikhaylov, L. Pavesi, A. Ershov*, et al.*, "The electron and crystalline structure features of ion-synthesized nanocomposite of Si nanocrystals in $Al_2O_3$ matrix revealed by electron spectroscopy," *Journal of Physics: Conference Series,* vol. 100, p. 072012, 2008.

[2] A. Benami, A. López-Suárez, L. Rodríguez-Fernández, A. Crespo-Sosa, J. C. Cheang-Wong, J. A. Reyes-Esqueda*, et al.*, "Enhancement and quenching of photoluminescence from silicon quantum dots by silver nanoparticles in a totally integrated configuration," *AIP Advances,* vol. 2, p. 012193, 2012.

[3] F. Wang, C. Ren, D. Li, and D. Yang, "Effect of scattering from localized surface plasmon resonance on improving the luminescence efficiency of silicon nitride light-emitting devices," *Journal of Nanoparticle Research,* vol. 15, pp. 1-7, 2013.

[4] R. Philip, P. Chantharasupawong, H. Qian, R. Jin, and J. Thomas, "Evolution of nonlinear optical properties: from gold atomic clusters to plasmonic nanocrystals," *Nano Lett,* vol. 12, pp. 4661-7, 2012.

[5] G. V. Naik, V. M. Shalaev, and A. Boltasseva, "Alternative Plasmonic Materials: Beyond Gold and Silver," *Advanced Materials,* vol. 25, pp. 3264-3294, 2013.

[6] C. Zhu, S. Misawa, S. Tsukahara, and S. Fujiwara, "Growth kinetics of aluminum on the Si(100) surface studied by scanning tunneling microscopy," *Surface Science,* vol. 357–358, pp. 926-930, 1996.

# Appendix A1

## A1.1: Partial Fluorescence Yield X-ray Absorption Near-edge (XANES) Spectra

Fig.A1.1 shows the partial fluorescence yield at the Si K-edge for Si rich $Si_3N_{3.00}$ samples annealed from 400 to 1000°C. Samples are denoted SiN and are not the same in composition as those discussed in chapter 4, where this notation was used for $Si_3N_4$ samples.

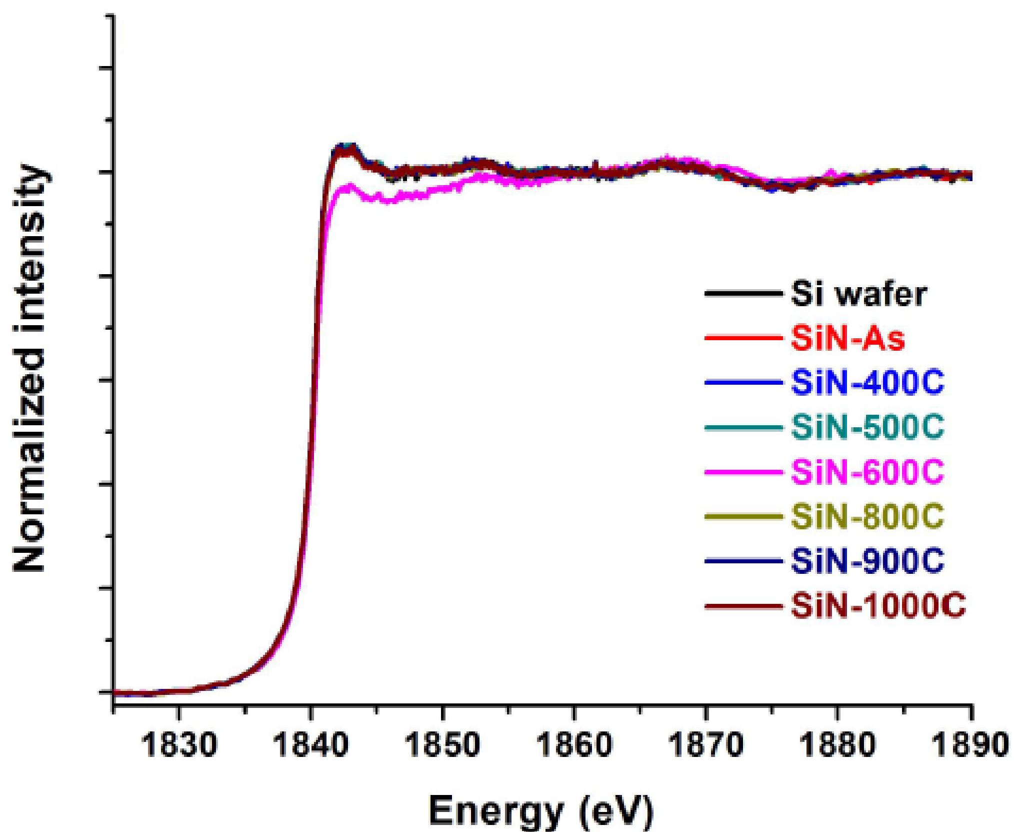


**Fig.A1.1:** Partial fluorescence yield X-ray absorption near edge spectroscopy (PFY-XANES) for the Si-K edge for $Si_3N_{3.00}$ annealed from 400 to 1000°C. The XANES spectra for a Si wafer is included as a reference.

# Appendix A2

## A2.1: Raw FTIR spectra for implanted and unimplanted $Si_3N_4$

Fig.A2.1 shows the FTIR spectra of asis $Si_3N_4$ in black and Al implanted $Si_3N_4$ using a dose of $5x10^{11}$ atoms/cm$^2$. Spectra are plotted with a y-offset of 0.1 for clarity. In Fig.A2.1 the location of the peaks are as follows: the Si-N peak at ~870 cm$^{-1}$, the Si-H peak at ~2180 cm$^{-1}$ and the N-H peaks at ~3360 cm$^{-1}$.

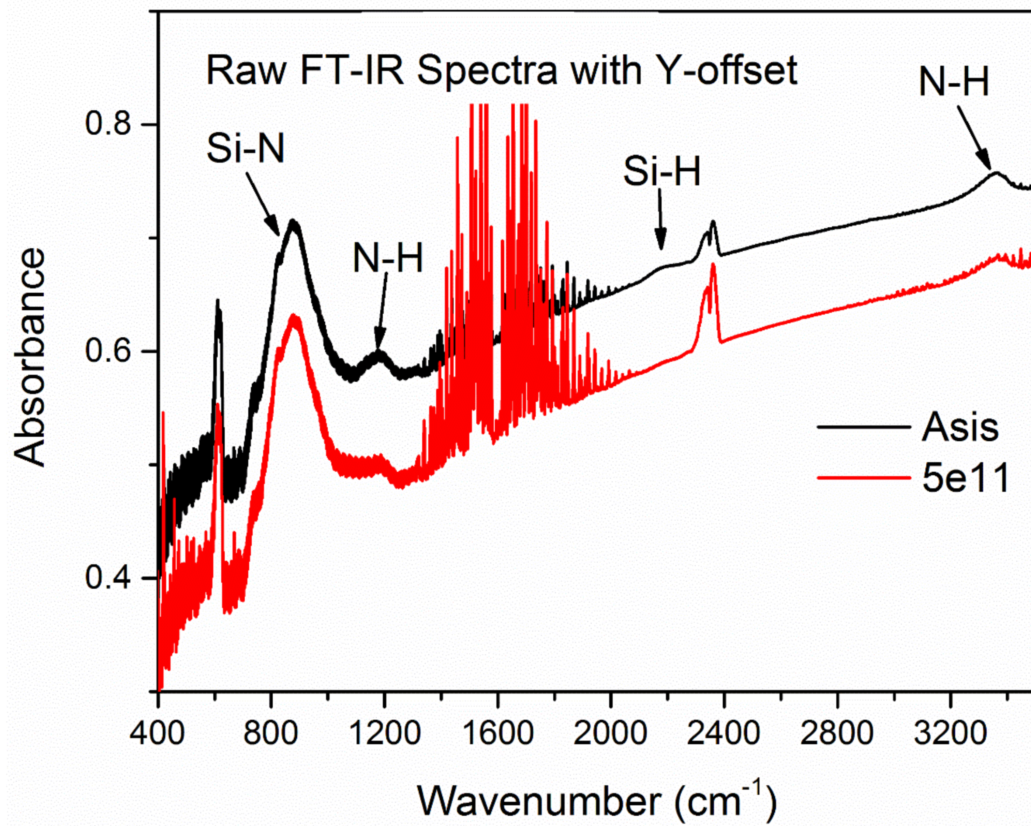


**Fig.A2.1:** FT-IR spectra for asis $Si_3N_4$ and $Si_3N_4$ implanted with $5\times10^{11}$ atoms/cm$^2$ (labelled 5e11). For clarity, a y-offset of 0.1 is applied to the spectra.

## A2.2: XANES spectra at Si K-edge for implanted and unimplanted $Si_3N_4$

Fig.A2.2 shows the total electron yield (TEY) XANES spectra at the Si K-edge for our annealed sample and doped samples using Al doses of $5x10^{13}$, $5x10^{14}$ and $5x10^{15}$ atoms/cm$^2$. From this measurement, a decrease in the Si-N peak as a function of implantation dose is observed. No consistent trend is observed for the Si-Si feature after Al implantation.

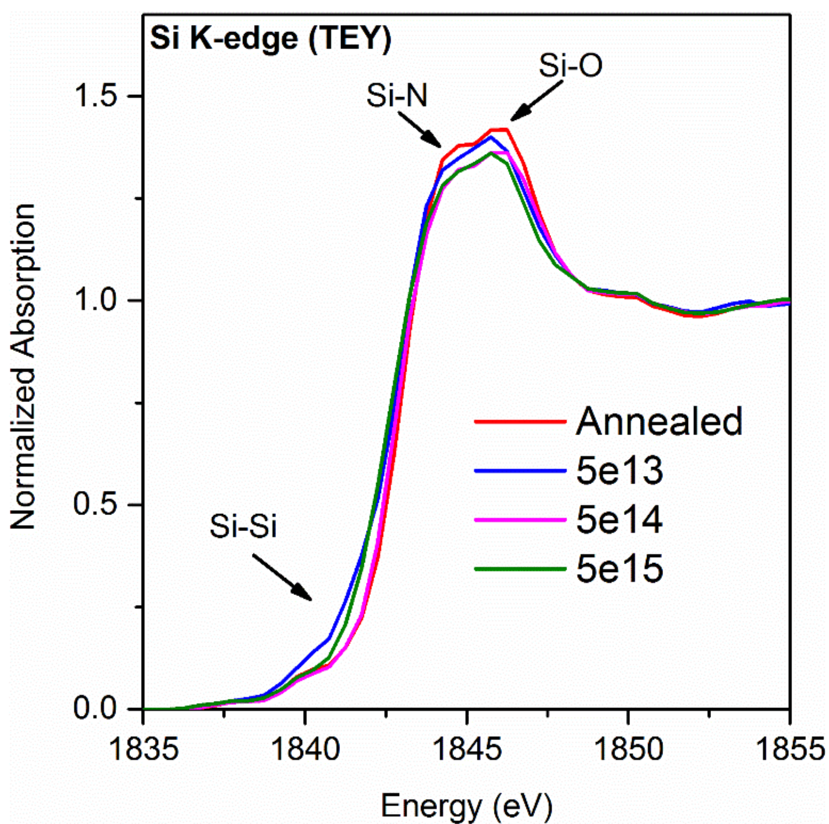


**Fig.A2.2:** XANES spectra at the Si K-edge in TEY mode for implanted and unimplanted samples annealed at the same temperature.

# Appendix A3

## A3.1: Photoluminescence Spectra for P implanted SRSN samples

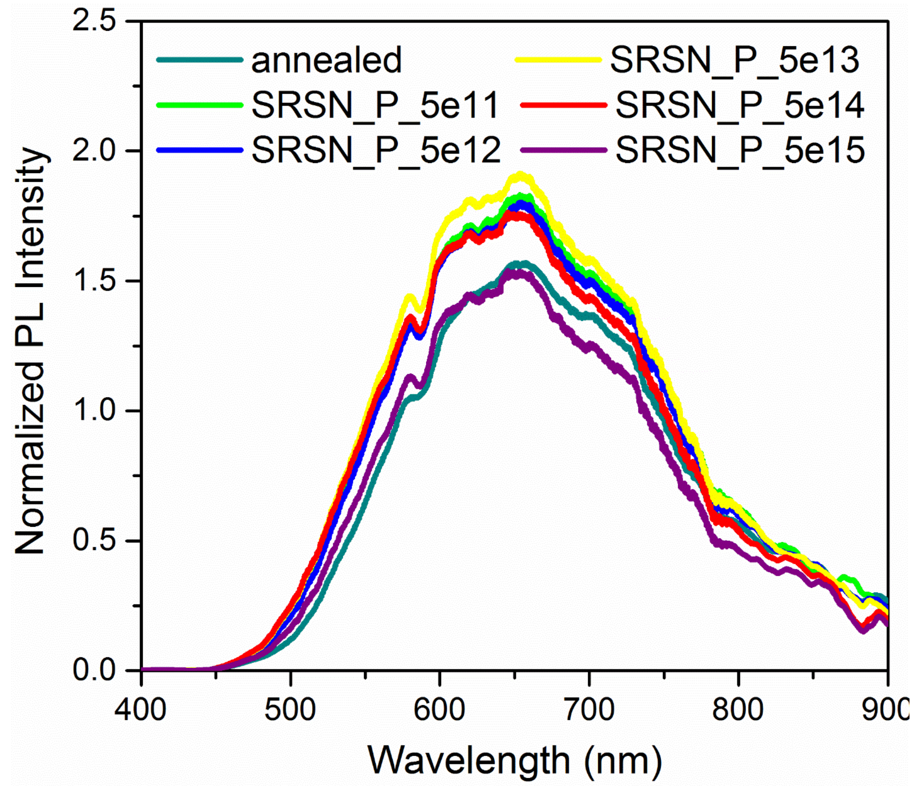


**Fig.A3.1:** Normalized PL spectra for annealed SRSN and P doped SRSN samples.

## A3.2: X-ray Absorption Near-edge structure Data Si K-edge Spectra for SRSN Samples

The XANES spectra of Al implanted SRSN taken at the Si K-edge are shown in Fig.A3.2. For clarity, the spectra for SRSN_5e11 and SRSN_5e12 are omitted from this plot. We examine the total electron yield (TEY) at the Si K-edge because the maximum sampling depth for this measurement mode is approximately 70nm.[1] This helps to minimize any contributions from the Si(001) substrate. In Fig.A3.2, the shoulder observed around 1840eV is due to Si-Si bonding. At the Si-Si peak, all samples have no distinguishable difference. As highlighted in Fig.A3.2, there are Si-N and Si-O peaks located at 1844 and 1846eV respectively. The presence of the Si-O peak is most likely due to oxygen contamination on the SRSN film surface. However, there is the possibility that recoil oxygen atoms may have been incorporated in the film bulk during the Al implantation process.[2] Therefore, we expect oxygen incorporation to be minimal. By monitoring the Si-O resonance peak, we observe that the Si-O peak is unaffected by implantation or annealing which indicates that the Si-O resonance peak is most likely due to a thin $SiO_2$ layer forming on the sample surface. The insert of Fig.A3.2 shows that the slight loss of Si-N bonds after implantation which is consistent with FTIR results shown in chapter 5.

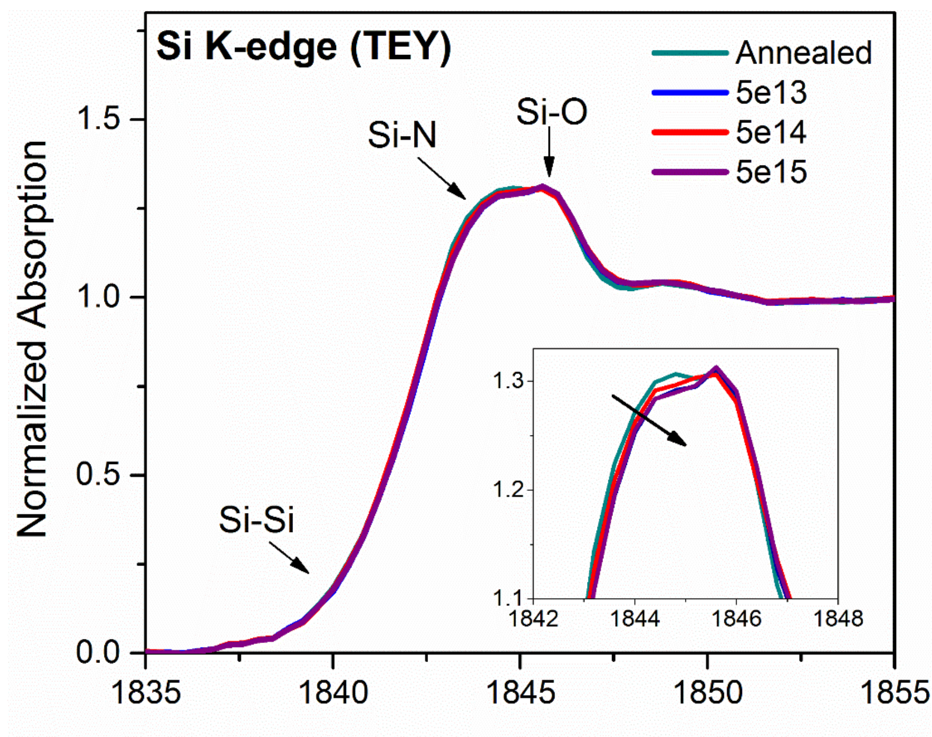


**Fig.A3.2:** TEY XANES at the Si K-edge for SRSN_Annealaed,SRSN_5e13,SRSN_5e14 and SRSN_5e15 samples. For clarity the spectra for SRSN_5e11 and SRSN_5e12 are omitted from this plot.

## A3.3: XANES spectra at Si K-edge for SiN and SRSN samples

As a comparison, Fig.A3.3(a) shows the TEY XANES at the Si K-edge for SiN and SRSN samples after annealing. We observe that the rising edge of SRSN_Annealed is at a lower energy than SiN_Annealed. This shift in the rising edge is due to the excess Si-Si bonds in SRSN_Annealed in comparison to SiN_Annealed. The intensity of the Si-N peak is greater for SiN_Annealed than SRSN_Annealed, because SiN samples possess more Si-N bonds than SRSN samples.[3] Similar results are observed when we compare our implanted samples. As an example, the Si K-edge of SiN and SRSN samples implanted with $5\times10^{15}$

atoms/cm$^2$ of Al are shown in Fig.A3.3(b). We observe, in Fig.A3.3(b) a decrease in the Si-N peak for SiN_5e15, compared with the unimplanted sample (SiN_Annealed), which indicates a decrease of Si-N bonds. This may be due to Si-Al or Al-N bonds being formed when SiN samples were implanted. However, this decrease in Si-N bonds is not as significant in our implanted SRSN samples shown in Fig.A3.3(a).

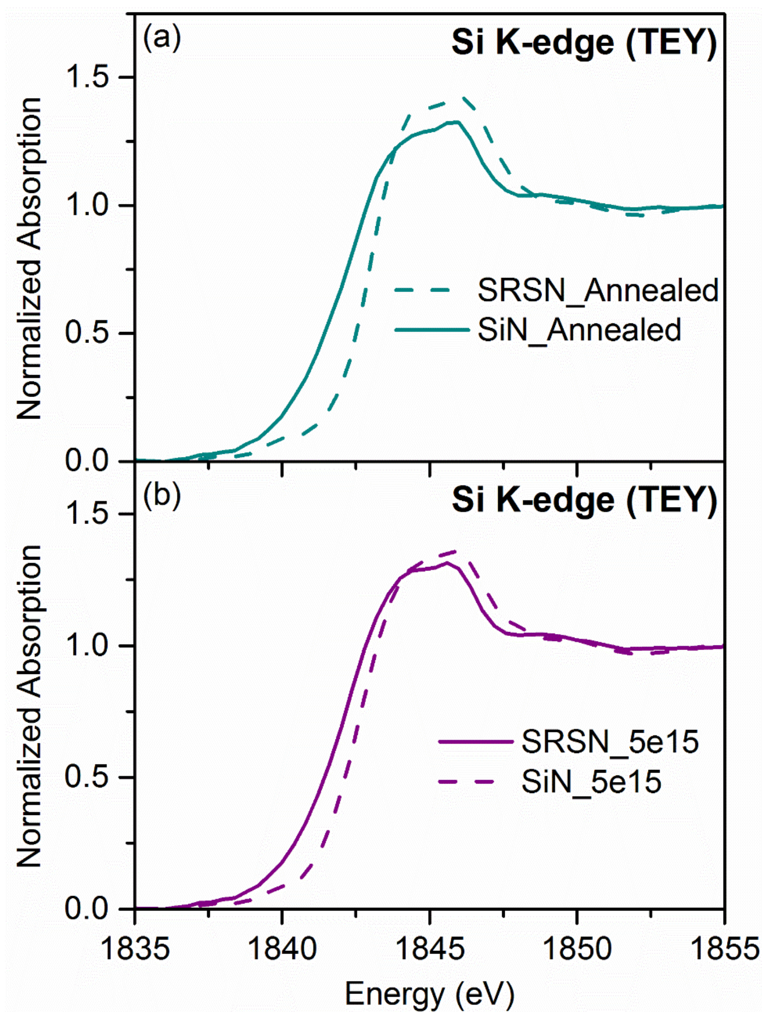


**Fig.A3.3:** TEY XANES at the Si K-edge of (a) SiN_Annealed and SRSN_Annealed are compared to (b) SiN_5e15 and SRSN_5e15. The spectra of SRSN samples are plotted using solid lines and SiN samples are plotted using dash lines.

## A3.4: XANES Spectra at the N K-edge for SRSN Samples

In FLY mode, there is no significant difference in the XANES spectra at the N K-edge for implanted samples in comparison to our unimplanted sample, as shown in Fig.A3.4(a). We also observe that the FLY signal is weaker than our TEY signal (shown in Fig.A3.4(b)) this is because the Auger electron yield is typically higher than fluorescence yield for elements with a low atomic number. We also observe that there is an increase in the Si-N peak located around 405eV for P implanted samples which is likely due to matrix rearrangement after implantation.

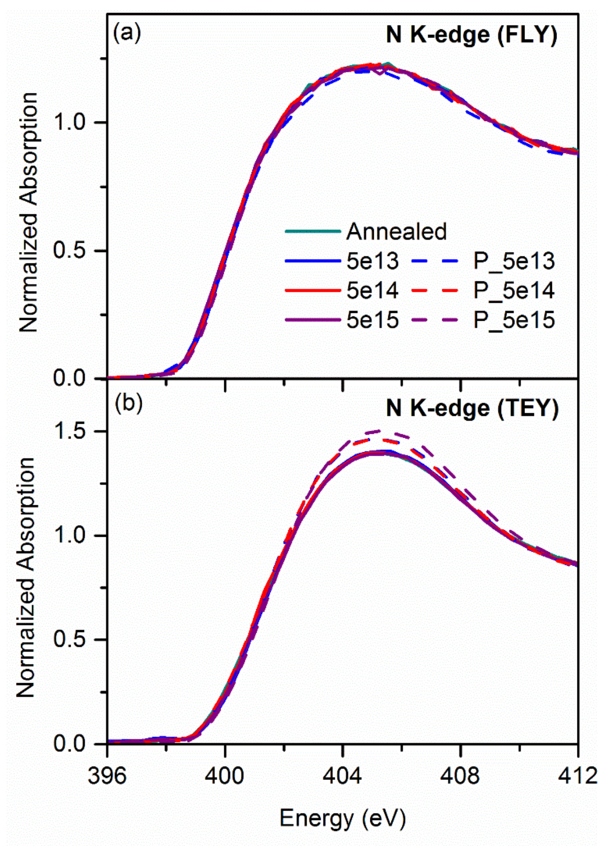


**Fig.A3.4:** The XANES spectra at the N K-edge in (a) TEY mode and (b) FLY mode for Al and P imlplanted SRSN samples. The spectra for Al implanted samples are plotted using

solid lines while for P implanted samples the spectra are plotted using dashed line. The XANES spectra of our unimplanted and annealed sample is plotted for comparison. The spectra for samples 5e11 and 5e12 are not plotted for clarity as the N K-edge spectra for all implanted samples the same.

## A3.5: Elastic Recoil Detection (ERD)Spectra for SRSN Samples

Fig.A3.5 shows the ERD spectra for implanted and unimplanted SRSN samples. After annealing a decrease in hydrogen content is clearly observed. The amount of hydrogen present in all annealed samples whether implanted or not is the same.

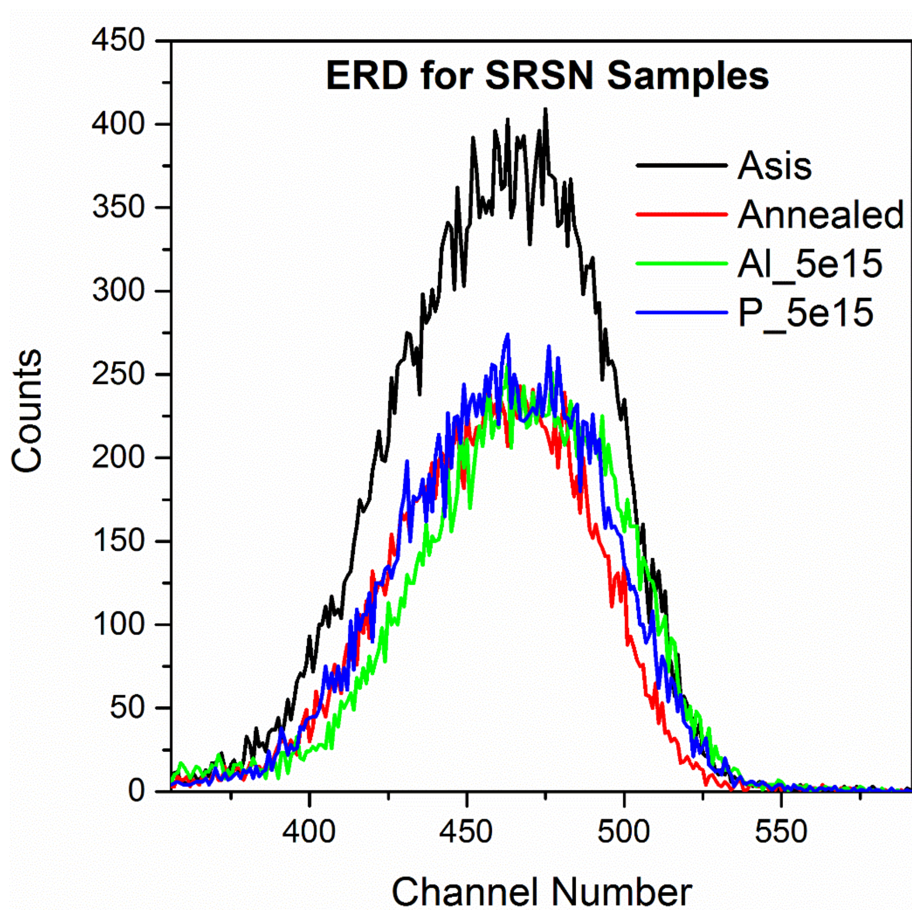


**Fig.A3.5:** Elastic recoil detection spectra for SRSN samples.

# Appendix A4

## A4.1: Particle-Induced X-ray Emission Spectra

PIXE spectra were collected at the Tandetron Facility at the University of Western Ontario using 1 MeV $H^+$ at 45° incident angle. At this energy range, the ion range for alumina was 9.4μm. Measurements were conducted using a liquid nitrogen cooled HPGe detector located at an angle of 90° relative to the incident beam. Fig.A4.1 shows the PIXE spectra for the Al film used for producing anodized alumina, as well as the anodized alumina film with and without the Al film attached to the back of the oxide film. Fig.A4.2 shows the PIXE spectra for polished and unpolished sapphire films used for our disorder and crystalline alumina.

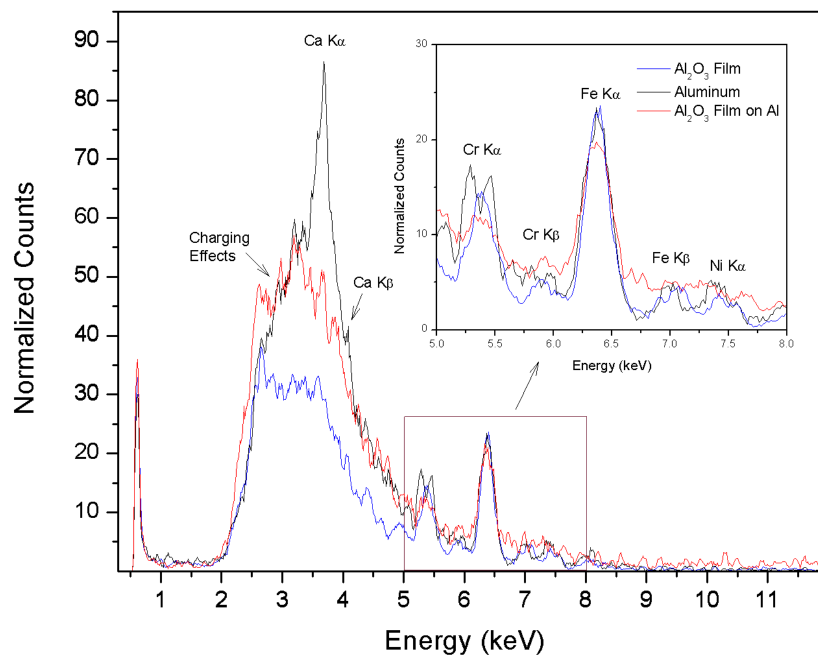


**Fig.A4.1:** PIXE spectra for (a) $Al_2O_3$ film after removal from the Al film, (b) Al film, and (c) $Al_2O_3$ film on Al.

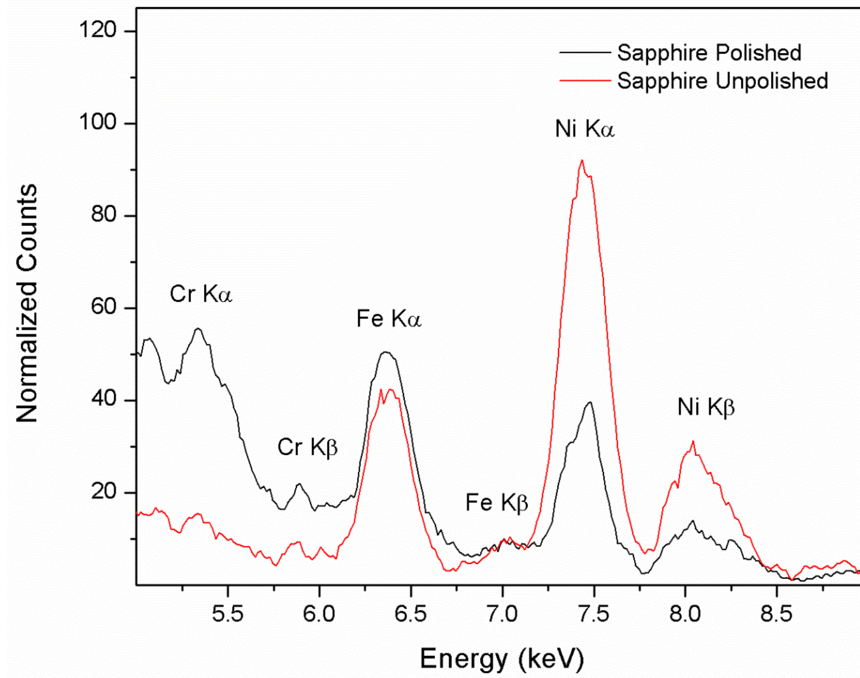


Fig.A4.2: PIXE Spectra for (a) 5×5 mm sapphire (polished side), and (b) 5×5 mm sapphire (unpolished side).

## A4.2: X-ray Absorption Near-Edge Structure Spectra

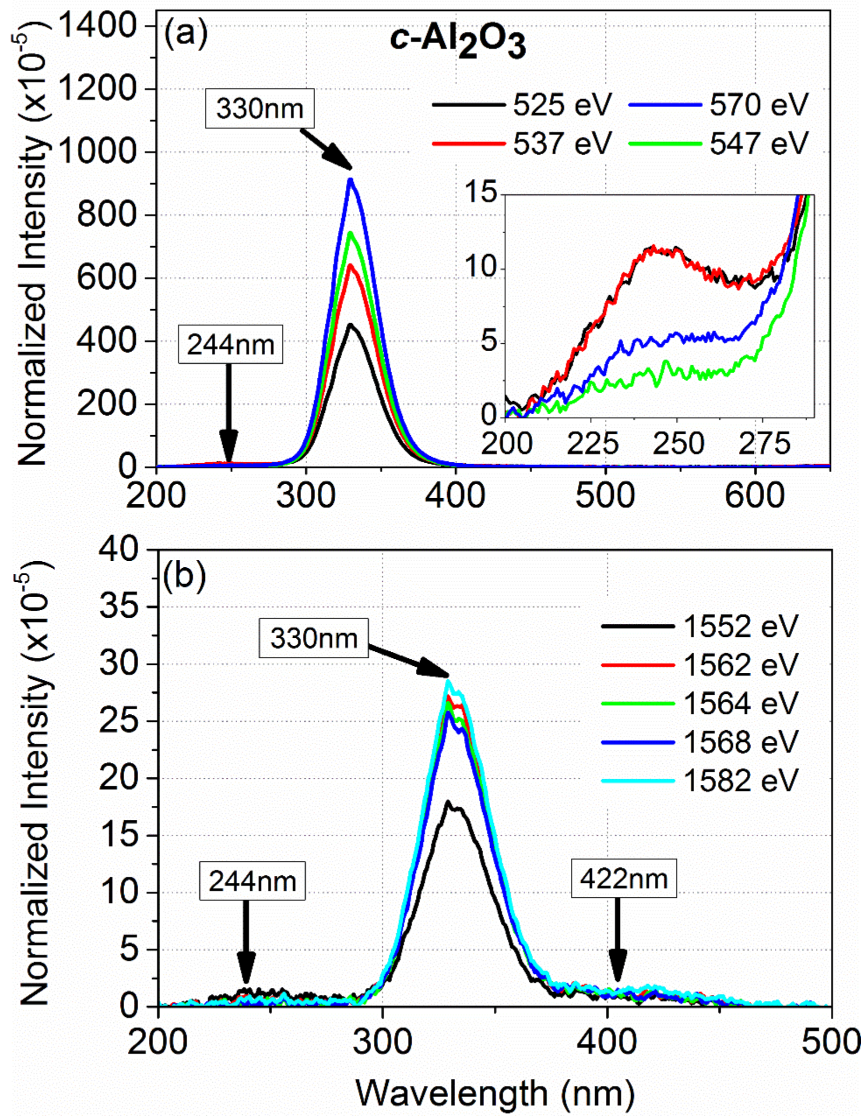


**Fig.A4.3:** XEOL spectra of $c$-$Al_2O_3$ before Si implantation from 200 to 650nm along the (a) O K-edge and from 200 to 500nm along (b) Al K-edge.

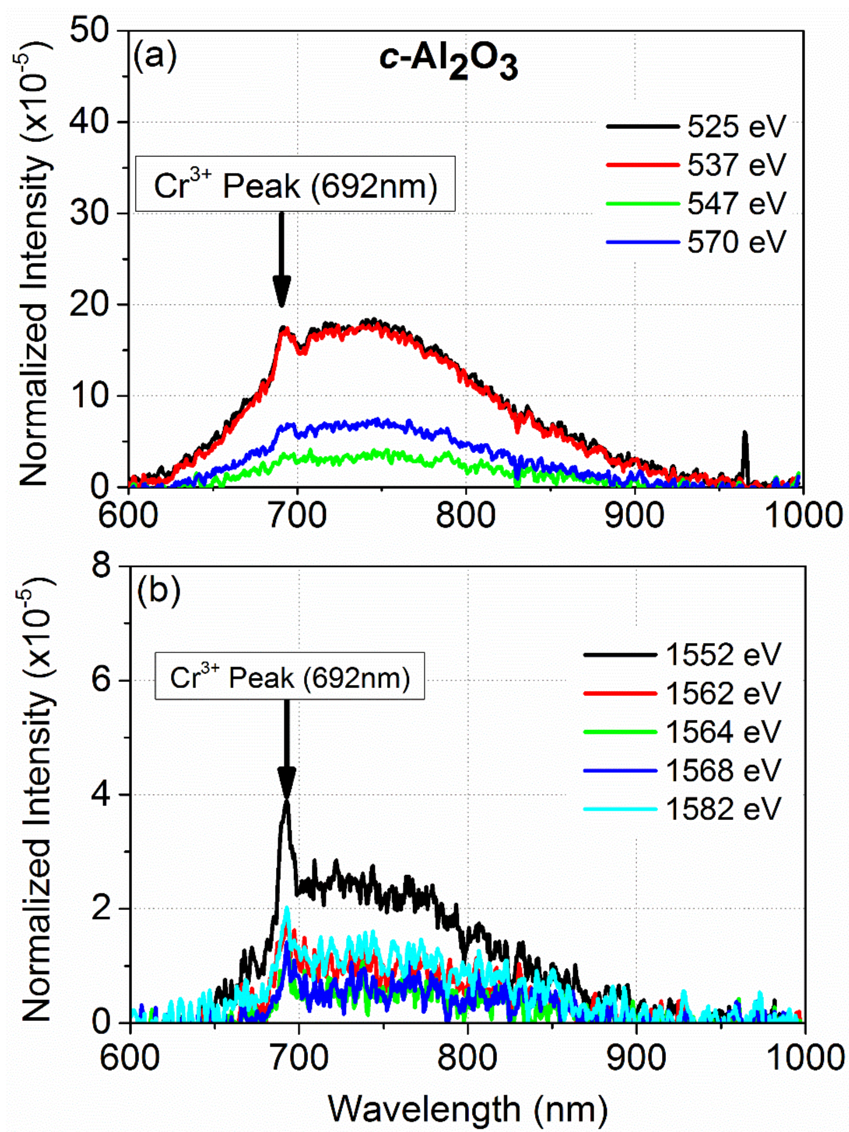


**Fig.A4.4:** XEOL spectra of *c*-$Al_2O_3$ prior to Si implantation from 600 to 1000nm along the (a) O K-edge and (b) Al K-edge.

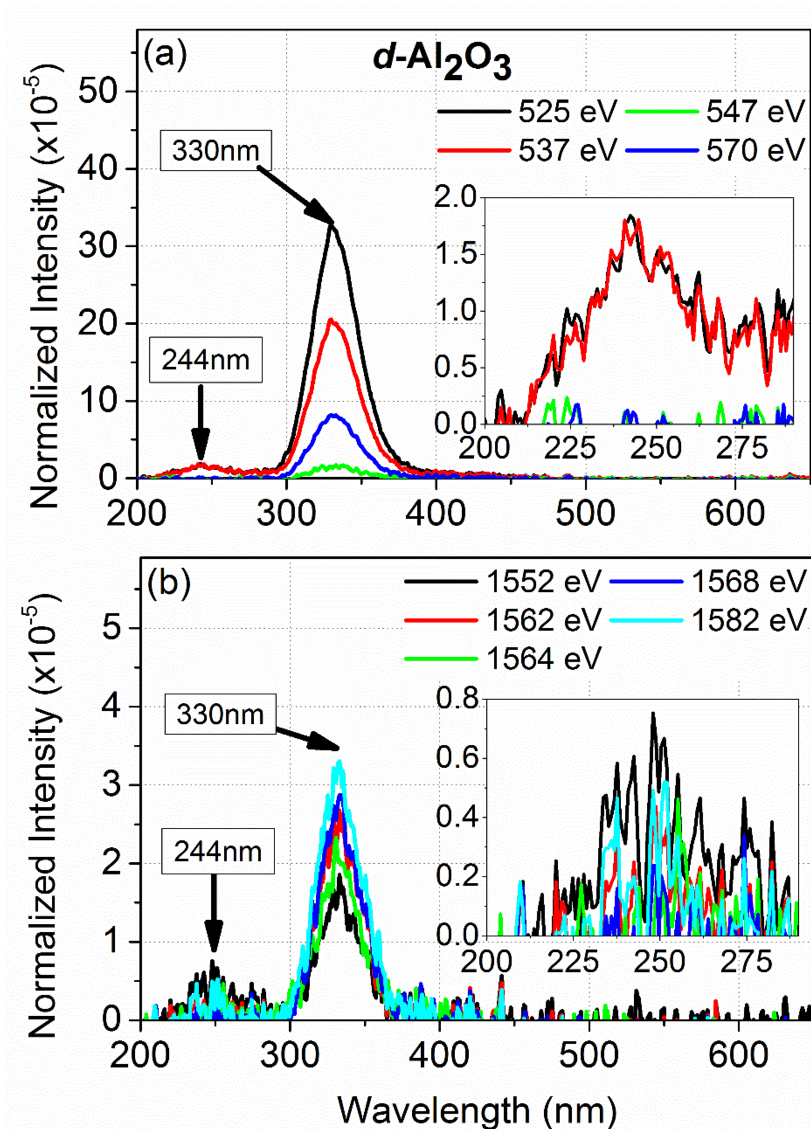


**Fig.A4.5:** XEOL spectra of *d*-$Al_2O_3$ prior to Si implantation from 200 to 650nm along (a) O K-edge and (b) Al K-edge.

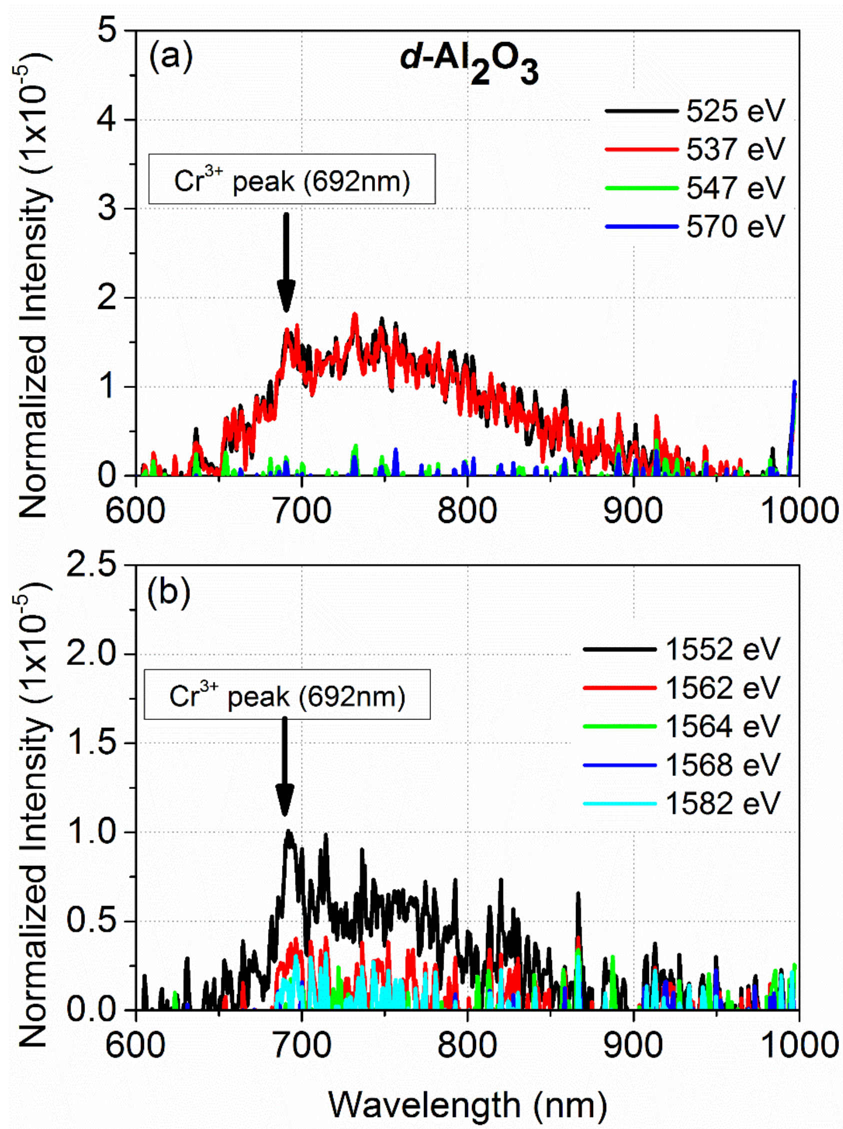


**Fig.A4.6:** XEOL spectra of $d$-$Al_2O_3$ before Si implantation from 600 to 1000nm along the (a) O K-edge and (b) Al K-edge.

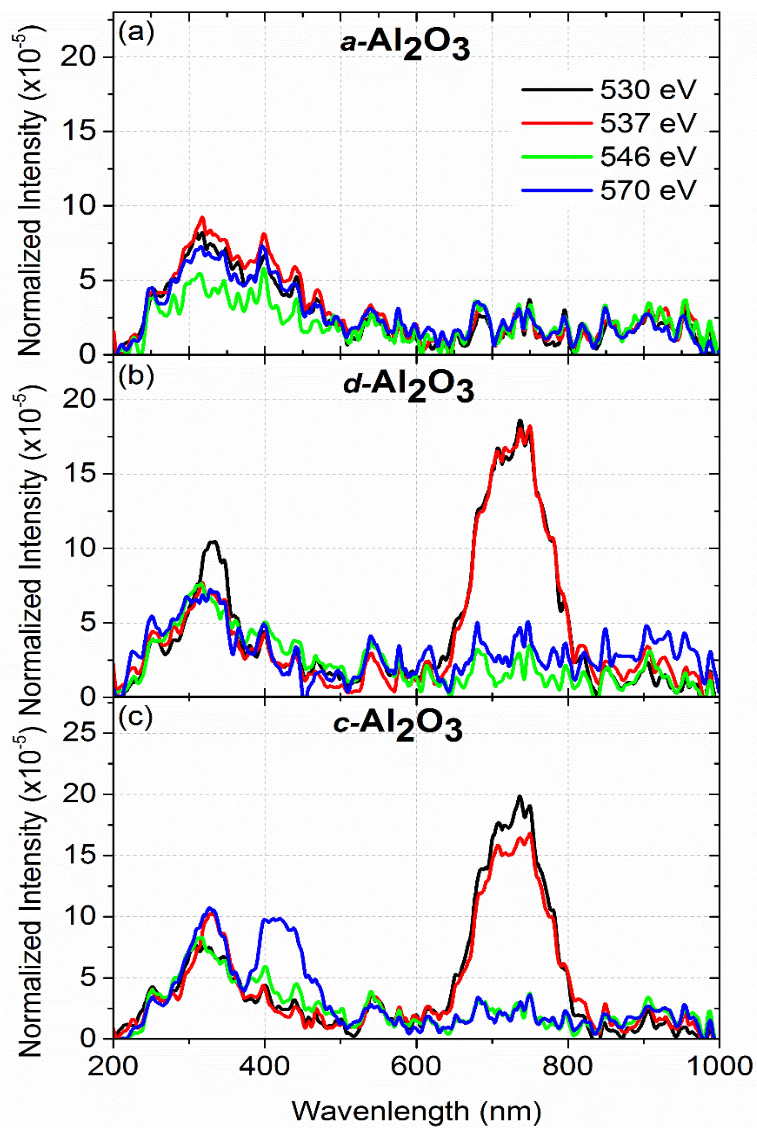


**Fig.A4.7:** XEOL spectra of Si-implanted (a) *a*-$Al_2O_3$. (b) *d*-$Al_2O_3$ and (c) *c*-$Al_2O_3$ along the O K-edge.

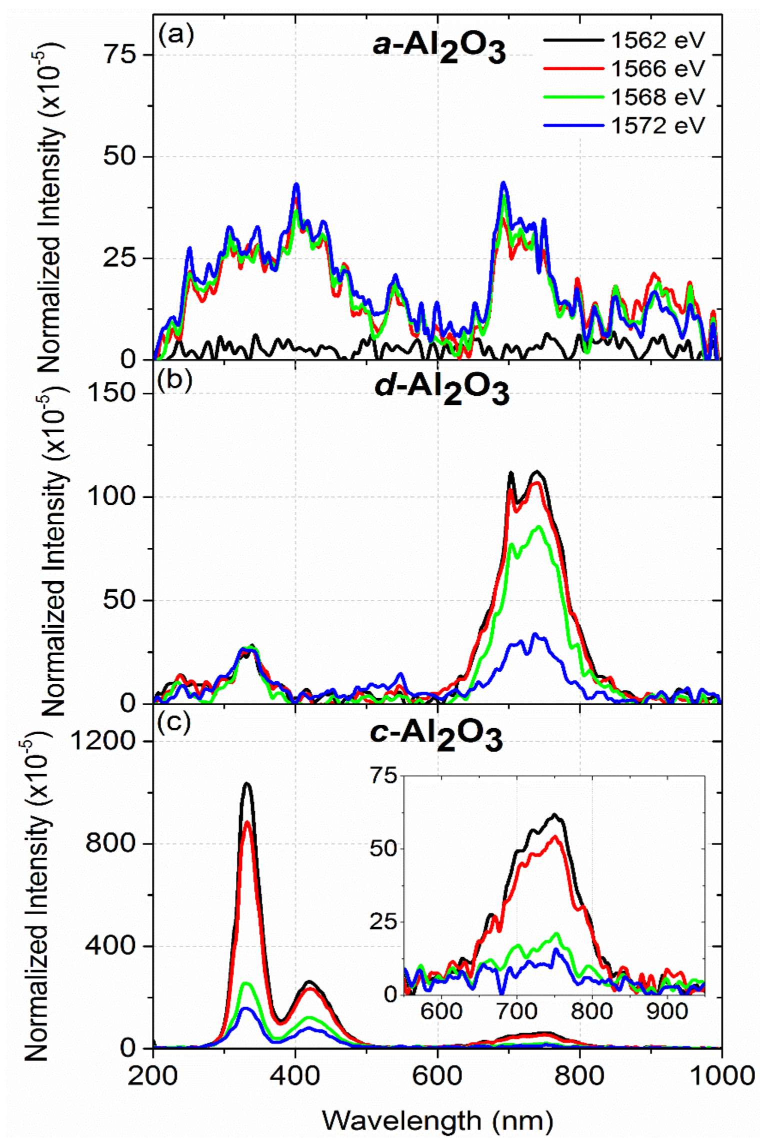


**Fig.A4.8:** XEOL spectra of Si-implanted (a) *a*-$Al_2O_3$. (b) *d*-$Al_2O_3$ and (c) *c*-$Al_2O_3$ along the Al K-edge.

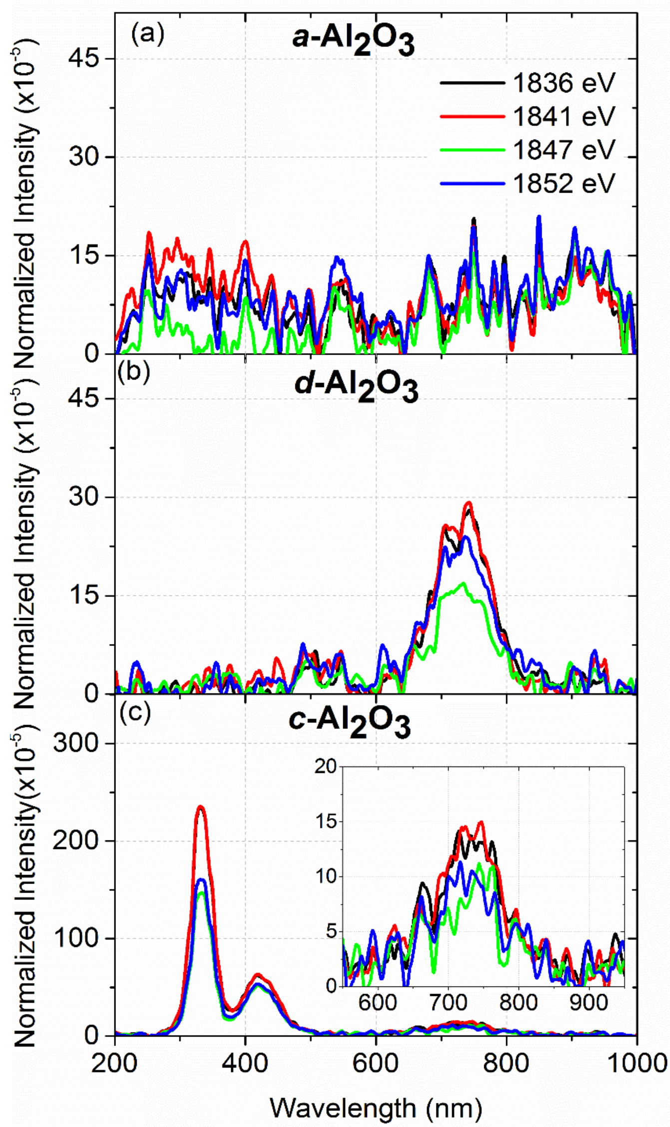


**Fig.A4.9:** XEOL spectra of Si-implanted (a) *a*-$Al_2O_3$ (b) *d*-$Al_2O_3$ and (c) *c*-$Al_2O_3$ along the Si K-edge.

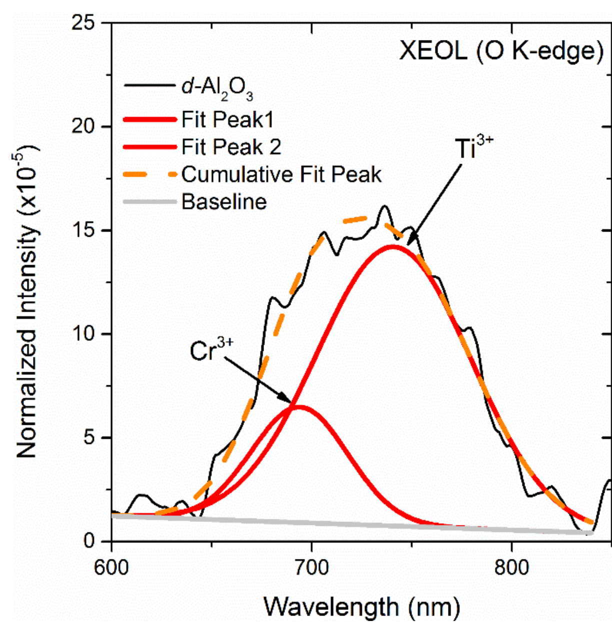


**Fig.A4.10:** XEOL spectra of Si-implanted *d*-$Al_2O_3$ along the O K-edge. This spectrum is fitted using two gaussian peaks centred at 694nm and 740nm. The cumulative fit of these two peaks is shown with an orange dashed line.

# A4.3: Partial Fluorescence Yield X-ray Absorption Near-edge (XANES) Spectra

Fig.A4.11 shows X-ray diffraction (XRD) spectra for implanted and unimplanted $Al_2O_3$ compared to a reference sapphire sample. If $Al_2O_3$ films were crystalline, then the XRD spectra for the material would possess sharp peaks similar to those seen for our sapphire sample. Instead, in Fig.A4.11, we only observe broad peaks in the XRD spectra which indicate that the implanted and unimplanted $Al_2O_3$ films are amorphous.

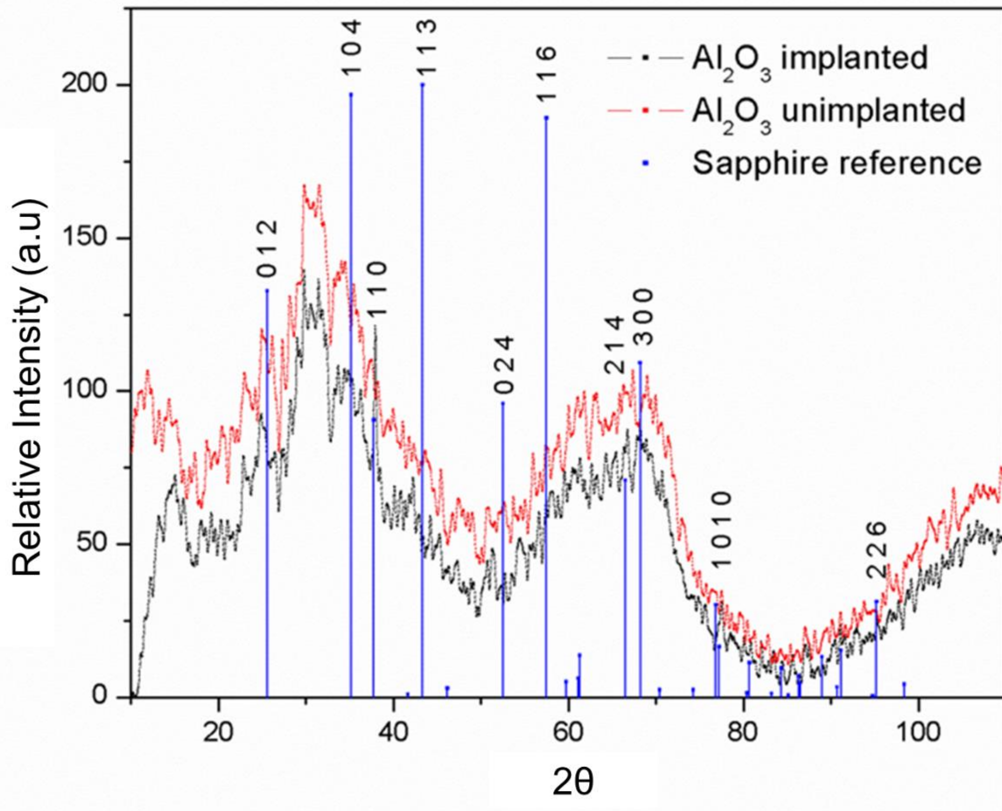


**Fig.A4.11:** X-ray diffraction spectra for unimplanted (black) and unimplanted (red) amorphous $Al_2O_3$ films. Sapphire reference points are included to compare the amorphous $Al_2O_3$ sample with crystalline $Al_2O_3$.

## A4.4: Images of $Al_2O_3$ Samples Before and After Annealing

Due to the fragile nature of amorphous $Al_2O_3$ films, to anneal the samples in the tube furnace these $Al_2O_3$ films needed to be sandwiched between two pieces of Quartz glass. Fig.A4.12 shows images of samples before and after annealing in the tube furnace.

Before Annealing

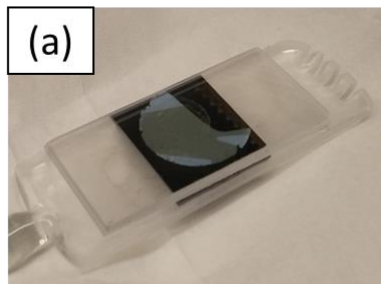


After Annealing

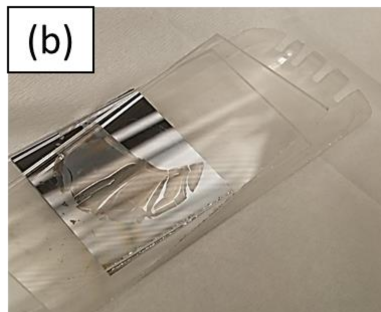


**Fig.A4.12:** Images of amorphous$Al_2O_3$ samples (a) before and (b) after annealing. Samples were supported on a Si wafer to reduce material fractures caused by annealing.

## A4.5: Time-Resolved Photoluminescence Spectra

Time-resolved PL (TRPL) measurements were collected using a 405 nm laser diode that was pulsed using a 3310A HP function generator. The time resolution of our setup was 100 nsec. Decay curves were acquired using a R7400U-20 Hamanatsu photomultiplier tube (PMT) with a spectral range of 300-900 nm and peak sensitivity of 630nm. Decay curves were analysed using OriginLab and fitted using exponential decay curve.

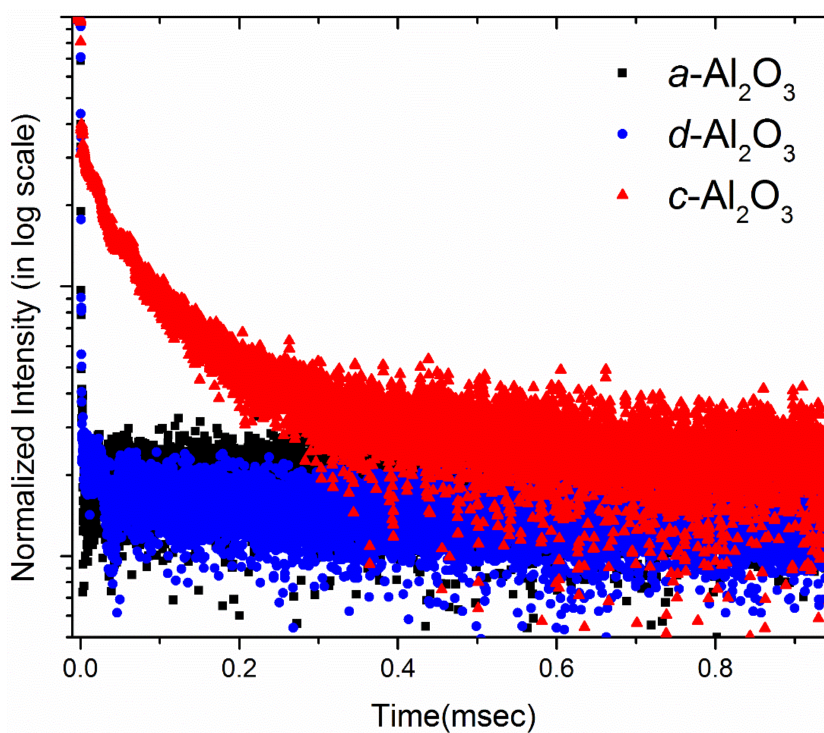


**Fig.A4.13:** PL Lifetime curve for samples *a*-Al2O3 (black), *d*-Al2O3 (blue) *c*-al2O3 (red).

# Appendix B1

## B1.1: Contact Mask and Contacts

For electrical measurements, Al front contacts were deposited by depositing 100nm of Al through the deposition mask shown in Fig.B1.1(a). The deposition mask was designed such that electrical measurements, photocurrent and electroluminescence measurements could be measured in future work. For back contacts, silver paste was used and allowed to dry overnight.

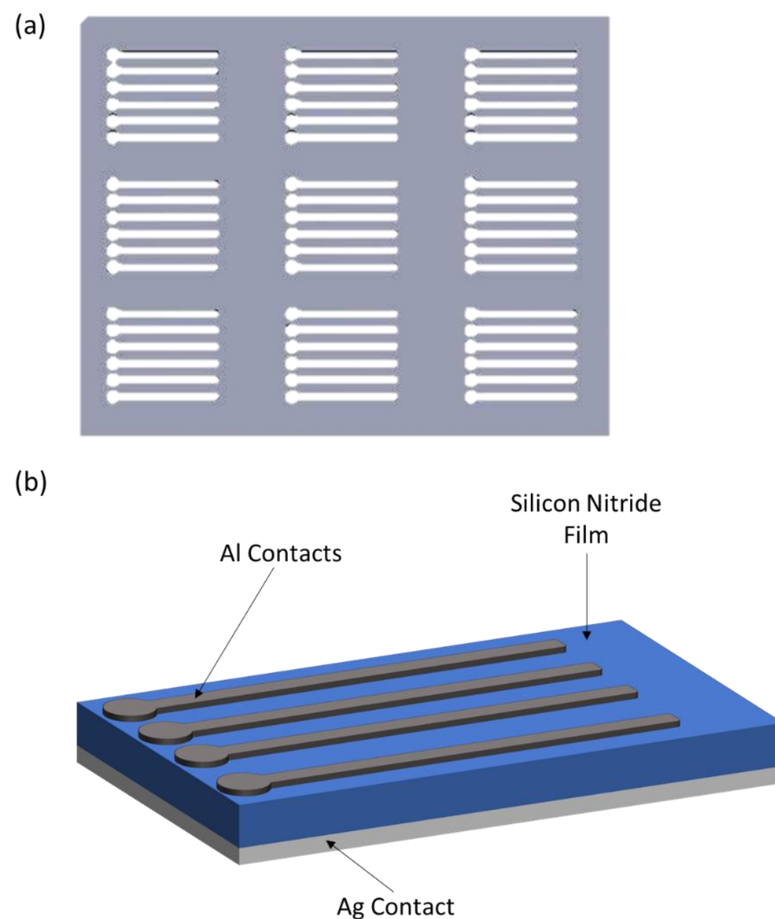


**Fig.B1.1:** Schematic of (a) Al deposition mask used for depositing Al front contacts and (b) silicon nitride films with front Al contacts and Ag back contact.

## B1.2: Current-Voltage Curves

Current-voltage measurements were conducted for Si-rich silicon nitride (SRSN) samples that were implanted with $5\times10^{14}$ and $5\times10^{15}$ atoms/cm$^2$ of Al followed by annealing at 600°C for 30 mins in forming gas. As shown in Fig.B1.2, the resistivity for unimplanted Si-rich $Si_3N_4$ was very high, which was expected as $Si_3N_4$ is a dielectric material with high resistivity. On the other hand, for Al implanted SRSN samples there was a significant decrease in the forward voltage with increasing Al dose.

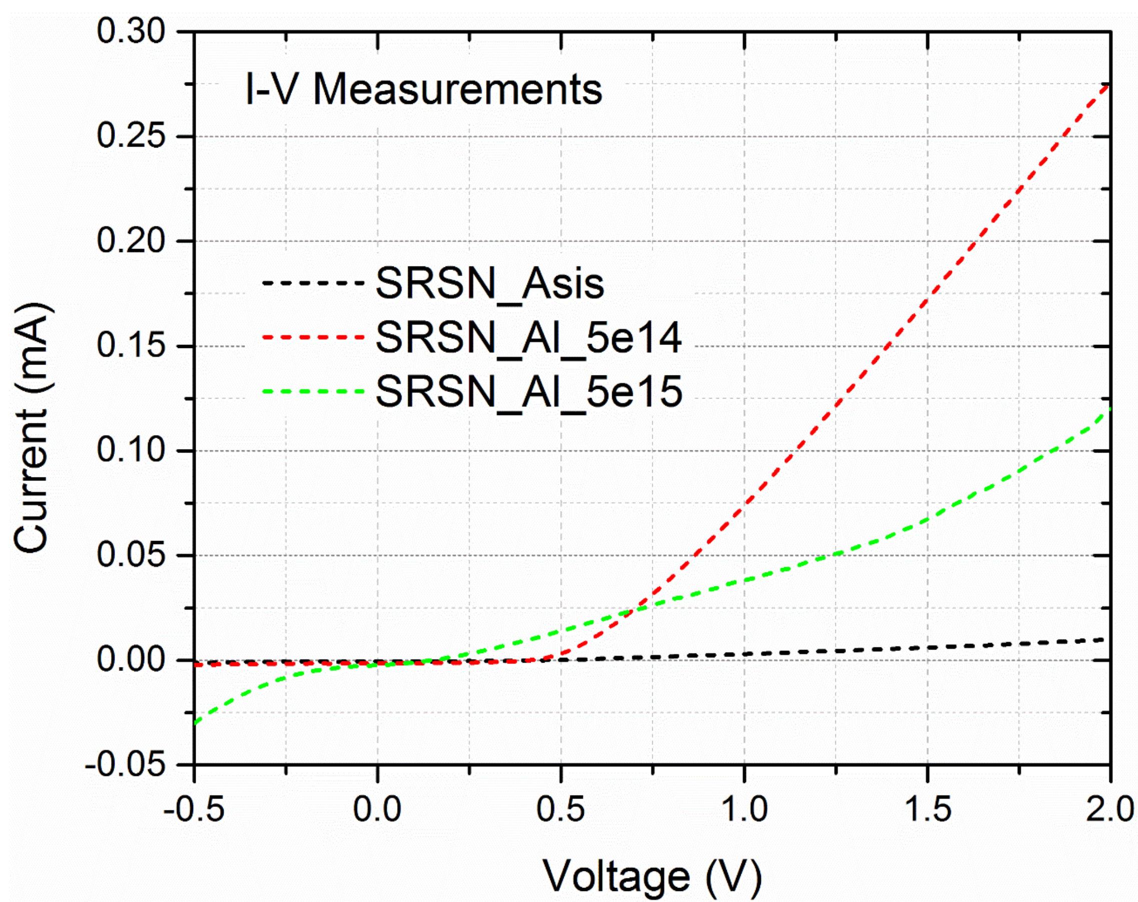


**Fig.B1.2:** Current-voltage curves for Si-rich silicon nitride (SRSN) samples asis (black dash) and implanted samples with Al doses of $5\times10^{14}$atoms/cm$^2$ (red dash) and $5\times10^{15}$atoms/cm$^2$.

# Appendix B2

## B2.1: Al Nanostructure Fabrication

To produce Al nanostructures, a polystyrene microsphere mask was deposited on the surface of Si-rich silicon nitride ($Si_3N_4$) samples using the air-liquid method. This method is illustrated in Fig.B2.1. In this method, a mixture of ethanol and polystyrene microspheres (diameter of 430 nm) suspension solution was dispersed on a water surface to produce a monolayer of the spheres. To push the microspheres closer together one to two drops of a surfactant (in our case 2% sodium dodecyl sulfate (SDS) solution) were added to the surface of the water. Once the microspheres were given time to disperse, the Si-rich $Si_3N_4$ films were immersed in the water and lifted slowly to allow the microspheres to be deposited on the film surface.

To maximize the adheres, Si-rich $Si_3N_4$ were cleaned using an ultrasonic acetone bath followed by a methanol bath and dried using purified nitrogen gas. The nitride films were then cleaned using an UV-Ozone system. This UV-Ozone treatment increased the hydrophilicity of the nitride surface.  After microspheres were deposited on the surface of the nitride film, the films were then allowed to dry overnight to allow for all solvents too dry.

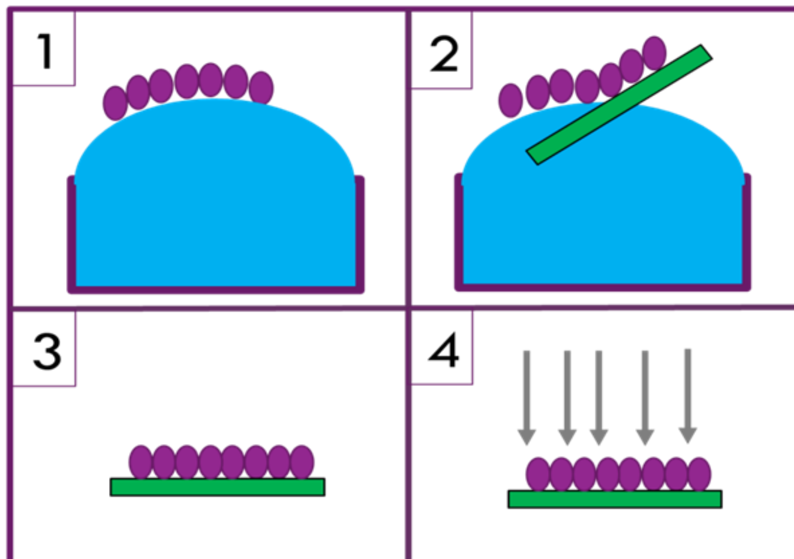


**Fig.B2.1:** Diagram illustrating the fabrication of Al nanostructures. (1) Polystyrene microspheres are dispersed on the water surface, (2) microspheres are deposited on to the sample surface, (3) microsphere mask is allowed to dry and (4) Al film is deposited through the microsphere mask.

After the mask was dried, the Al film was deposited using Edwards Auto500 sputtering system at the University of Western Ontario Nanofabrication facility. After Al film deposition, the microsphere mask was removed by sonicating samples in ethanol.

## B2.2: Photoluminescence Results using Al nanostructures

Photoluminescence measurements were collected for Al nanostructures made using Al film thicknesses of 50±7 and 100±7 nm deposited on the surface of 400nm thick Si-rich silicon nitride films with stoichiometry of $Si_3N_3$. As shown in Fig.B2.2, the PL intensity increased around 2-fold for both Al film thicknesses.

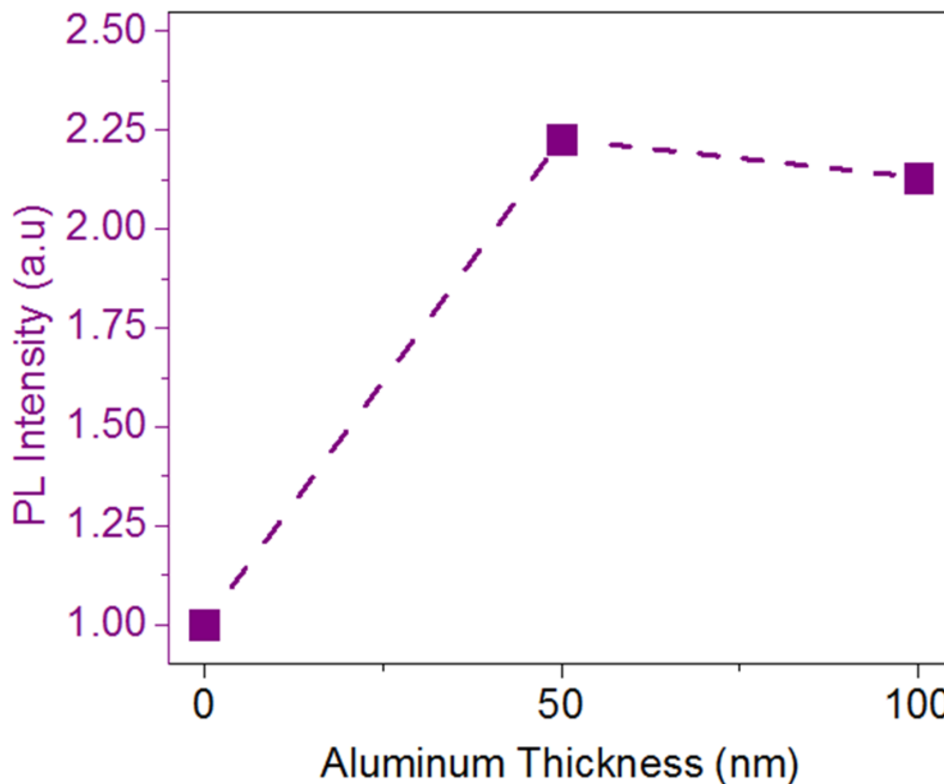


**Fig.B2.2:** Photoluminescence intensity of Si-rich silicon nitride sample with Al nanostructure deposited on the surface. Al nanostructures were produced using different Al film thicknesses.

## B2.3: Scanning Electron Microscope (SEM) Images

Scanning electron microscope (SEM) images were taken using LEO (Zeiss) 1530 SEM system. Fig.B2.3(a) shows the SEM images for Si-rich silicon nitride sample with Al nanostructures while Fig.B2.3(b) shows a region of the sample where the microspheres were not fully removed by the ethanol sonication. The major issue with producing Al nanostructures using our method is that a periodic monolayer of microsphere is difficult to produce. We can see that there were several regions where the periodicity of the

microsphere mask was lost. This lack of periodicity in the microsphere film has a negative impact on the plasmonic effect of the Al nanostructures produced.

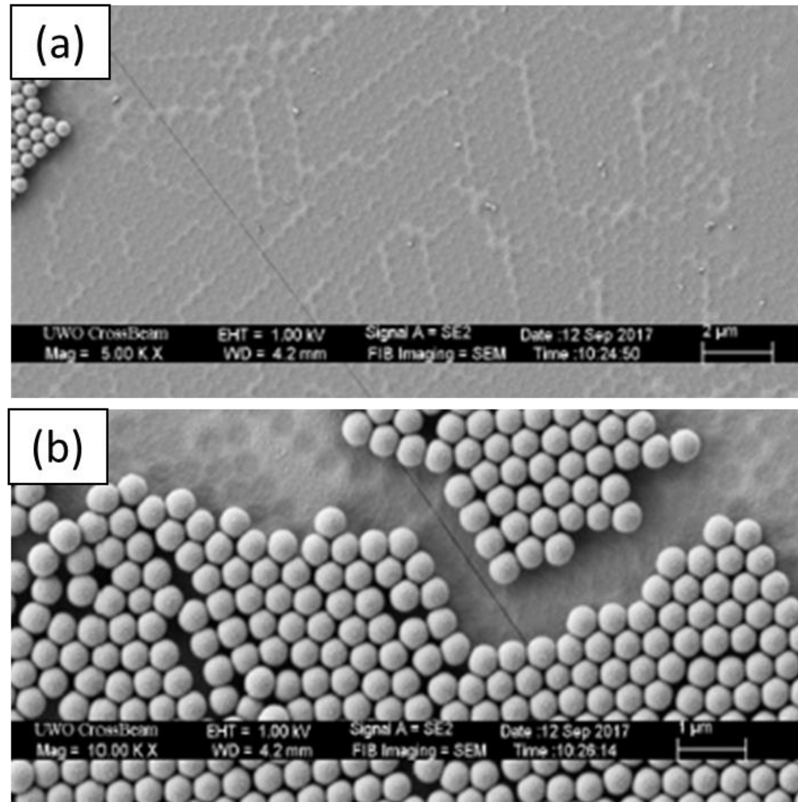


**Fig.B2.3:** SEM images of Si-rich silicon nitride films with Al nanostructures where (a) shows the region that clearly shows the type of Al nanostructures formed. In (a) we observe that there are regions where the microsphere film had gaps as we can observe elevated regions of Al. A region where microspheres were not completely removed is shown in (b).

# Carolyn Cadogan

## Academic studies

Sept. 2014–present **Doctor of Philosophy**, *Experimental Condensed Matter Physics*, Western University.
Investigating the luminescence of silicon nanoparticles (Si-NPs) embedded in silicon nitride ($Si_3N_4$)
Investigating the formation and luminescence of Si-NPs in anodized $Al_2O_3$ films and crystalline $Al_2O_3$ films
Enhancing the luminescence of Si-NPs using Al dopants and the localized plasmonic resonance of Al nanostructures

Sept. 2013–Sept. 2014 **Master of Science**, *Experimental Condensed Matter Physics*, Western University, transfer to Ph.D. program.

Sept. 2010–May. 2013 **Bachelor of Science**, *Physics with Mathematics, First Class Honours*, The University of the West Indies.
Investigated the temperature and field dependence of smectic phases of AIS178 liquid crystals

## Relevant work experience

### Western University

Aug. 2016–May 2017 **Lead teaching assistant for the Department of Physics and Astronomy**.
Conducted departmental evaluation to identify and address training requirements for TAs
Designed and facilitated training workshops for TAs

June 2016–present **Teaching Assistant Training Program (Instructor) Teaching Support Center**.
Taught introductory course on teaching for TAs
Facilitated microteaching sessions for trainees

Sep. 2015–May 2016 **Learning Development Graduate Fellowship for the Faculty of Science**.
Consulting with faculty to organize student events
Promotion of faculty events to faculty members and students

Sep. 2013–present **Graduate Research Assistant for Interface Science Western**.
Collect and analyse data; designing and troubleshooting experiments
Preparing publications,reports and presentations on research findings
Training graduate and undergraduate students on lab equipment
Performing measurements and data analysis for collaborators in various departments and external industry users

Sep. 2013–present **Teaching Assistant (TA) for the Physics and Astronomy Department**.
Teaching assistant for introductory physics and graduate level courses
Lab demonstrator for first and upper year lab courses
Designed and facilitated graduate student TA training

# Awards

## Conference Awards

June 2017 **Second Place, Talk**, *2017 Canadian Association of Physicists (CAP) Congress*, Best Student Paper Oral Competition (DCMMP).

Aug. 2016 **Third Place, Poster**, *8th International Workshop on High Resolution Depth Profiling*.

June 2016 **First Place, Talk**, *2016 Canadian Association of Physicists (CAP) Congress*, Best Student Paper Oral Competition (DCMMP).

June 2016 **Finalist, Talk**, *2016 Canadian Association of Physicists (CAP) Congress*, Best Student Paper Oral Competition (overall).

June 2015 **Third Place, Poster**, *Photonics North Conference 2015*.

# Publicatoins

## Publications


[1] T. I. Levchenko, C. Kübel, B. Khalili Najafabadi, P. D. Boyle, **C. Cadogan**, L. V. Goncharova, A. Garreau, F. Lagugné-Labarthet, Y. Huang, and J. F. Corrigan. *"Luminescent CdSe superstructures: A nanocluster superlattice and a nanoporous crystal"*. *J. Am. Chem. Soc.*, **139**:1129–1144, (2017).

[2] **C. C. Cadogan**, L. V. Goncharova, P. J. Simpson, P. H. Nguyen, Z. Q. Wang, and T.-K. Sham. *"Influence of hydrogen passivation on the luminescence of Si quantum dots embedded in $Si_3N_x$"*. *J. Vac. Sci. Technol., B: Nanotechnol. Microelectron.: Mater., Process., Meas., Phenom.*, **34**:061202, (2016).

[3] A. M. Polgar, C. B. Khadka, M. Azizpoor Fard, B. Nikkel, T. O'Donnell, T. Neumann, K. Lahring, K. Thompson, **C. Cadogan**, F. Weigend, and J. F. Corrigan. *"A controlled route to a luminescent $3d^{10}$–$5d^{10}$ sulfido cluster containing unique $AuCu_2(\mu_3$-S) motifs"*. *Chem. Eur. J.*, **22**:18378–18382, (2016).

[4] M. Azizpoor Fard, T. I. Levchenko, **C. Cadogan**, W. J. Humenny, and J. F. Corrigan. *"Stable -$ESiMe_3$ complexes of $Cu^I$ and $Ag^I$ (E=S, Se) with NHCs: Synthons in ternary nanocluster assembly"*. *Chem. Eur. J.*, **22**:4543–4550, (2016).